Neutrino Interactions in the ND280 Upgrade Era and Beyond: Theoretical Modelling and Experimental Observations at T2K

Jake McKean

Blackett Laboratory, Department of Physics
Imperial College London
September 2025

A thesis submitted to Imperial College London for the degree of Doctor of Philosophy

Abstract

The Tokai-to-Kamioka (T2K) experiment is a long-baseline neutrino oscillation experiment designed to make measurements of neutrino oscillation parameters. A muon (anti)neutrino beam is produced at the Japan Proton Accelerator Research Complex (J-PARC) in Tokai-mura, Ibaraki. The beam is first measured by near detectors ND280 and INGRID at J-PARC, 280 m downstream of the target, then travels 295 km to Kamioka-machi, Gifu, where the far detector Super Kamiokande (SK) samples it again.

To reduce systematic and statistical uncertainties in T2K analyses, the ND280 detector at J-PARC has been upgraded. Its central component, the Super Fine-Grained Detector (SFGD), is built from segmented scintillator cubes. This thesis presents the construction, commissioning, calibration and characterisation of the SFGD, along with real-time monitoring and visualisation software.

Nuclear modelling is one of the largest sources of systematic uncertainty in T2K analyses. T2K uses the NEUT neutrino interaction event generator, which models nuclear effects through different approximations. The dominant interaction channel in T2K is the charged-current quasi-elastic (CCQE) channel.

This thesis introduces the implementation of a CCQE neutrino- and electron–nucleus scattering model beyond the plane wave impulse approximation, which is currently used in NEUT, using relativistic mean field (RMF) theory, implemented in an event generator for the first time. The model implementation, validation and benchmarking against current NEUT CCQE models and various neutrino scattering cross section datasets are shown. This work resulted in a publication to Physical Review D.

Finally, the potential for investigating nuclear effects with the SFGD is introduced. NEUT samples using the RMF-based model are simulated within the SFGD and the results are shown. This highlights the key differences between different CCQE models that can be differentiated with the SFGD.

Declaration

The work presented in this thesis is my sole work, unless otherwise stated. No part of this work has been previously submitted for a higher degree to any other university.

The SFGD construction work was performed with the SFGD working group at J-PARC. The calibration and commissioning work was performed in collaboration with the SFGD working group. While I led the initial calibration and software group, I wrote several initial pieces of software that were built on by the entire group.

The electron- and neutrino-nucleus interaction model has been a continuous development by the nuclear theory groups at Universidad Complutense de Madrid and Universidad de Seville for many years. The implementation, validation and benchmarking of the model within the NEUT event generator framework was my sole work.

Jake McKean

Copyright declaration

Acknowledgments

I have had the great privilege to live out my dream-not just to undertake a Ph.D., but to travel to many countries, meet many amazing people and form lifelong friendships. I have wanted to study for a Ph.D. since the age of twelve when my interest in physics was sparked after reading George's Secret Key to the Universe by Lucy and Stephen Hawking. I have also wanted to live in Japan since the age of sixteen and have studied Japanese since then in order to do so. The years of my undergraduate period had a lot of anxiety in trying to come up with a way to combine these two important parts of my life. My Ph.D. offer at Imperial College London was an opportunity that provided a route to do just that.

My time at Imperial College London has been a whirlwind-in every positive meaning. From my first year living in London to living in Tokai-mura in Japan for the remainder of my time, the experiences I have had have held me in good stead for the rest of my life and career. I would not have been able to become the physicist I am without the support of my supervisor, Professor Yoshi Uchida, and my co-supervisor, Dr. Monireh (Minoo) Kabirnezhad. My first year was fraught with anxiety and uncertainty over whether I was doing well enough, but Yoshi and Minoo helped me see my potential and would always put me back on track with more gusto than before. I would also like to thank all of my colleagues at Imperial College London. While I did not see most of you for many years, we would still have many laughs at every T2K collaboration meeting. I would also like to thank Dr. Raul González-Jiménez who, without the countless hours explaining lepton scattering theory to me, this work would not have been possible.

My time in Japan was nothing less than a dream come true. Constructing the SFGD detector and getting hands on in every way I could has given me a priceless experience. I would like to thank all my colleagues that I met there. I would like to especially thank Joel Elias, Tristan Doyle and Tristan Schefke. Through our time constructing and commissioning the SFGD and spending over twelve-hour days in the ND280 control room, I like to think that we have built up a decade of friendship. Thanks to us spending many days shopping at Hard Off and hanging out at our many secret places in and around Tokai-mura: "the spot", "the place" and 'the location", I have stories to tell for years to come.

Away from my work, I have met some amazing people in Tokai-mura. I was lucky enough to integrate into the local community and be a part of many events. To Fujita-san, the owner of Fujita Coffee, without your amazing coffee and relaxed coffee shop, I would not have finished most of my work. I spent almost every day drinking a coffee or two there and met many people and was lucky to get involved in many community events. To Yamazaki-san, the Yakitori chef at Papaya, the countless hours I have spent sitting at the counter speaking to you and being introduced to so many people have given me amazing stories and memories. To Satou-san, an amazing local carpenter who I met at kickboxing, you introduced me to many people and gave me the opportunity to help out

at the Sweet Potato Festival and the Marche at the shrine two years in a row. While out and about alone in Tennouji, Osaka, where I found myself spending a lot of time toward the end of my time in Japan, I would always get a coffee at Tully's and sit. For the first five minutes, I would always sit and think how lucky I am to be where I am.

I would also like to thank my parents. No amount of thanks is enough to show my appreciation. To my Mum, you would always pretend to know what I was talking about and, even now, I am not convinced you know exactly what I do, but you always say how proud of me you are and support me every step of the way. To my Dad, you would always listen to me talking about work or any other problem I have, no matter what time it was in the UK or Japan, and always push me to do the right thing. Thank you. To my Grandma Pat, who passed shortly before the submission of this thesis, you always wanted to see me graduate with a Ph.D. and I regret not being able to show you sooner. I know you will be watching down that day.

Contents

Part I

Introduction To Neutrino Physics

Chapter 1

Introduction to the Neutrino Oscillations and Interactions

In this chapter, the history of the neutrino and how it fits into the Standard Model of particle physics is explained. The history and theoretical framework of neutrino oscillations is then described and the current state of neutrino oscillation experiments is explained. Finally, neutrino interactions and their role in neutrino oscillations experiments are introduced including the focus of this work, the charged-current quasi-elastic interaction.

1.1 The history of the neutrino

In 1914, James Chadwick investigated the β decay of radium B and C [1]. At that time, the process was assumed to be a two-body decay, emitting only an electron.

$$ {}^{A}_{Z}X \rightarrow {}^{A}_{Z+1}Y + e^{-}. \tag{1.1} $$

Because it was a two-body decay, the energy of the electron can be found by energy and momentum conservation:

$$ E_e = \frac{M_X^2 - M_Y^2 + M_e^2}{2M_X}. \tag{1.2} $$

Therefore, for every beta decay, the emitted electron should have the same energy. However, it was found that the emitted electron energy formed a distribution rather than a single value. This, at the time, posed many problems as it appeared to violate key principles in which physics is built: energy and angular momentum conservation. In 1930, Wolfgang Pauli proposed the idea of an additional particle, referred to at the time as a "neutron", which would have a very low mass, zero charge, and had spin-1/2 [2]. This particle, if it existed, would solve the problems seen by Chadwick in 1914. After Chadwick discovered the neutron we know today (the nucleon) in 1932 [3], Enrico Fermi formulated a theoretical description of β decay using the new particle, now called the "neutrino" meaning "little neutral one", in 1934 [4]. This description wrote β decay as

$$ {}^{A}_{Z}X \rightarrow {}^{A}_{Z+1}Y + e^{-} + \bar{\nu}_e, \tag{1.3} $$

where $\bar{\nu}_e$ is the electron antineutrino. The antiparticle nature of the neutrino in β decay is necessary to conserve lepton number. Being more specific and writing β decay in terms of the particles that actually take part in the interaction,

$$n \rightarrow p + e^- + \bar{\nu}_e. \tag{1.4}$$

Here, p and n represent a proton and neutron respectively. The framework also allows for the inverse process, inverse beta decay, to occur. Inverse beta decay is induced by the antineutrino,

$$\bar{\nu}_e + p \rightarrow e^+ + n. \tag{1.5}$$

The process defined in Equation 1.5 introduces a possible route to the neutrino detection.

In 1956, Cowan and Reines [5] used this idea to discover the neutrino with a detector composed of two large tanks of water doped with cadmium chloride ($CdCl_2$) with three tanks of liquid scintillator between them. The detector was placed close to a nuclear reactor providing the required antineutrino flux. In order to detect the neutrino, the positron, when annihilating with an electron, produces two photons of energy > 1.02 MeV (the rest mass of an electron-positron pair) that must be detected. Additionally, the neutron produced is captured by the cadmium nucleus, producing an excited state. The excited state then de-excites, producing an additional photon roughly 5 μs later. These two coincidences would prove the discovery of the neutrino.

One year before this, in 1955, Davis conducted an experiment around the Brookhaven National Laboratory nuclear reactor in which neutrinos interact with ^{37}Cl and become ^{37}Ar that is removed and counted [6]. The neutrinos produced by reactors are antineutrinos; such an experimental method is sensitive only to neutrinos. The result of this experiment showed that the neutrino and antineutrino were distinct in nature and their nuclear interactions.

After the electron antineutrino was discovered, the muon neutrino was later discovered in 1962 at Brookhaven National Laboratory by Lederman, Schwartz, Steinberger, and others [7]. The muon neutrino was produced by impinging protons onto a target, producing mesons that later decay to muon neutrinos via

$$\pi^{\mp} \rightarrow \mu^{\mp} + \overset{(-)}{\nu}_{\mu} \, . \tag{1.6}$$

The fact that muons, not antimuons, were observed further reinforced the fact that neutrinos and antineutrinos are distinct.

In 1975, the electron-positron collider at the Stanford linear accelerator (SLAC) proved the existence of the τ lepton [8]. This immediately sparked a search for its neutrino counterparts such as the (e^-, ν_e) and (μ^-, ν_μ) doublets. With the τ meson being so much heavier than its electron and muon counterparts, the lifetime is around $(290.3 \pm 0.5) \times$

10^{-15} s [9]. This is roughly 7.5 million times shorter than the lifetime of the muon. As a result, τ leptons are difficult to detect, which means that it took until 2000 before the tau neutrino was detected by the DONUT experiment [10].

1.2 Neutrinos and the Standard Model

1.2.1 An overview of the Standard Model

The Standard Model (SM) of particle physics is a unified quantum field theory which describes matter and its interactions. The SM unifies the three forces: electromagnetism (EM), the weak force, and the strong force. Within the SM, particles are divided into two categories: fermions and bosons. A fermion is a spin-1/2 particle, such as an electron or a proton, and bosons have integer spin. The SM is often written as a direct product of the underlying gauge symmetry groups, $SU_C(3) \times SU_L(2) \times U_Y(1)$ whose associated gauge fields mediate the forces. The $SU_C(3)$ group describes quantum chromodynamics (QCD), which is the theory that describes the strong force. The group has eight generators that correspond to the eight massless gluon gauge bosons that mediate the force. The "C" in $SU_C(3)$ is the "colour" charge; the strong force acts only on particles that have colour. The $SU_L(2) \times U_Y(1)$ group describes the unified electroweak (EW) force. The group has three $SU_L(2)$ generators corresponding to the $W^{1,2,3}$ gauge bosons and one $U_Y(1)$ generator corresponding to the B gauge boson. The quantum fields associated with these gauge symmetry groups are described by a Lagrangian $\mathcal{L}$.

The chirality, or "handedness" of a particle is an intrinsic property in the SM. For charged leptons, they can exist in both the left-handed or right-handed chiralities. The elementary fermions, given in Table 1.1, are split into quarks, of which there are six: up, down, charm, strange, top and bottom, and leptons. Quarks that exist in the "left-handed" chiral state form doublets under the $SU_L(2)$ group and have weak isospin $T = \frac{1}{2}$: (u_L, d_L), (c_L, s_L) and (t_L, b_L). Quarks that are in the "right-handed" chiral state form singlets and are different fields with a weak hypercharge, Y. In addition to quarks, there are three generations (also called "flavours") of leptons which exist only in the left-handed chiral state and are arranged in doublets, (e^-, ν_e), (μ^-, ν_μ) and (τ^-, ν_τ). Quarks are not found as free particles, but as bound states. This is called quark confinement. The quarks have a "colour" charge; all bound particles have neutral colour. The quarks can then only exist in two forms: qqq, a triplet quark configuration called a baryon, or $q\bar{q}$, a quark-antiquark pair called a meson.
The bosons are shown in Table 1.2. The $W^\pm$ bosons mediate the charged-current weak force, the Z^0 boson mediates the neutral-current weak force and the photon γ mediates the EM force. The gluon, g, exists in eight distinct colour states. This leads to a total of 12 unique gauge bosons in the SM. The Higgs boson, H^0 is a scalar boson and does not mediate a force in the SM. It couples massive particles to the Higgs field and is responsible for the mass generation of particles. The $W^\pm$ and H^0 bosons are massive while the Z^0 boson, the gluon and the photon are massless. The gauge bosons have spin-1 and are

Particle	$SU(2)_L$ Rep.	T	T_3	Y	Q
u_L	Doublet (u_L, d_L)	$\frac{1}{2}$	$+\frac{1}{2}$	$\frac{1}{3}$	$+\frac{2}{3}$
u_R	Singlet	0	0	$\frac{4}{3}$	$+\frac{2}{3}$
d_L	Doublet (u_L, d_L)	$\frac{1}{2}$	$-\frac{1}{2}$	$\frac{1}{3}$	$-\frac{1}{3}$
d_R	Singlet	0	0	$-\frac{2}{3}$	$-\frac{1}{3}$
c_L	Doublet (c_L, s_L)	$\frac{1}{2}$	$+\frac{1}{2}$	$\frac{1}{3}$	$+\frac{2}{3}$
c_R	Singlet	0	0	$\frac{4}{3}$	$+\frac{2}{3}$
s_L	Doublet (c_L, s_L)	$\frac{1}{2}$	$-\frac{1}{2}$	$\frac{1}{3}$	$-\frac{1}{3}$
s_R	Singlet	0	0	$-\frac{2}{3}$	$-\frac{1}{3}$
t_L	Doublet (t_L, b_L)	$\frac{1}{2}$	$+\frac{1}{2}$	$\frac{1}{3}$	$+\frac{2}{3}$
t_R	Singlet	0	0	$\frac{4}{3}$	$+\frac{2}{3}$
b_L	Doublet (t_L, b_L)	$\frac{1}{2}$	$-\frac{1}{2}$	$\frac{1}{3}$	$-\frac{1}{3}$
b_R	Singlet	0	0	$-\frac{2}{3}$	$-\frac{1}{3}$
ν_{eL}	Doublet (ν_{eL}, e_L)	$\frac{1}{2}$	$+\frac{1}{2}$	-1	0
e_L	Doublet (ν_{eL}, e_L)	$\frac{1}{2}$	$-\frac{1}{2}$	-1	-1
$\nu_{\mu L}$	Doublet $(\nu_{\mu L}, \mu_L)$	$\frac{1}{2}$	$+\frac{1}{2}$	-1	0
μ_L	Doublet $(\nu_{\mu L}, \mu_L)$	$\frac{1}{2}$	$-\frac{1}{2}$	-1	-1
$\nu_{\tau L}$	Doublet $(\nu_{\tau L}, \tau_L)$	$\frac{1}{2}$	$+\frac{1}{2}$	-1	0
τ_L	Doublet $(\nu_{\tau L}, \tau_L)$	$\frac{1}{2}$	$-\frac{1}{2}$	-1	-1

Table 1.1: The elementary fermions in the Standard Model. The electric charge, $Q = T_3 + \frac{Y}{2}$, weak isospin T, the third component of weak isospin T_3, and weak hypercharge Y are given for the six quarks and three generations of leptons. The upper section shows the quarks and the lower section shows the fermions. Only left-handed leptons exist in the SM but quarks can exist in the left-handed doublet states or right-handed singlet states.

therefore vector bosons, whereas H^0 is spin-0.

Particle	Boson type	Q	S
W^+	Gauge	+1	1
W^-	Gauge	-1	1
Z^0	Gauge	0	1
γ	Gauge	0	1
g	Gauge	0	1
H^0	Scalar	0	0

Table 1.2: The Gauge and scalar bosons in the Standard Model. The electric charge, Q and spin, S are given.

1.2.2 Neutrinos in the SM

It has been experimentally observed that (anti)neutrinos only exist in the (right)left-handed chiral state. This has implications in the mass-generating terms in the Lagrangian and so are massless in the SM. As explained in Section 1.3, this contradicts experimental observations in how neutrinos propagate through spacetime. Neutrinos have been experimentally observed violating parity [11]. Parity is the symmetry whereby if all position vectors are inverted, the physics should remain invariant.

Neutrinos also have implications for the properties of other particles, such as the decay width, Γ, of the Z boson. The Z boson can decay through three main channels: $\Gamma_{Z\to l^+l^-}$, $\Gamma_{Z\to\text{hadrons}}$ and $\Gamma_{Z\to\nu\bar{\nu}}$. Before it was certain that there were three neutrino flavours, the neutrino partial decay width had a factor of N_ν representing the number of neutrino flavours. In 2006, data containing 17 million Z decays accumulated by the ALEPH, DELPHI, L3 and OPAL experiments at the Large Electron Positron collider (LEP) at CERN, and 600 thousand Z decays by the Stanford Linear Detector (SLD) experiment at SLAC, was used to get the a precise measurement of the Z boson decay width [12]. The result showed that $N_\nu = 2.9840 \pm 0.0082$ and is therefore consistent with three flavours of neutrinos.

1.3 History and theoretical framework of neutrino oscillations

Neutrino oscillation is the process in which a neutrino can change its flavour between its production and detection. Neutrino oscillation was first postulated by Pontecorvo [13] in 1957. In Pontecorvo's paper, he postulated that, similar to neutral Kaon particles oscillating between its antiparticle $K^0 \leftrightarrow \bar{K}^0$, neutrinos can also undergo $\nu \leftrightarrow \bar{\nu}$ since is it not explicitly forbidden. In 1967, Pontecorvo expanded on his previous ideas [14]

proposing $\nu_\mu \leftrightarrow \nu_e$ oscillations. The theory describing such a process was developed by Maki, Nakagawa and Sakata in 1962 [15]. Despite the theoretical framework being developed in the 1960s, it was not until 1998 that the Super Kamiokande experiment first observed neutrino oscillation [16]. This section first introduces the theoretical framework of neutrino oscillations before going through the history of oscillation experiments. The current state of the neutrino oscillation field is then described.

1.3.1 Neutrino oscillation theoretical framework

As postulated by Pontecorvo [13], neutrino oscillations of the type $\nu_\mu \leftrightarrow \nu_e$ or similar require diagonal states $\nu_1,\ \nu_2$ that are related to ν_μ and ν_e. Nowadays, the $\nu_{1,2,3}$ states are referred to as the "mass eigenstates"; neutrinos propagate in its mass eigenstate. $\nu_{e,\mu,\tau}$ are referred to as the 'weak eigenstates"; neutrinos interact in its weak eigenstate. The left-handed components of the fields describing the weak eigenstates are related to the left-handed component of the fields describing the mass eigenstates by [17, 18]

$$\nu_{\alpha L} = \sum_k U_{\alpha k}\nu_{kL} \quad ;\ (k = 1, 2, 3)(\alpha = e, \mu, \tau). \tag{1.7}$$

The elements $U_{\alpha k}$ describe the amount of mixing between, or the projection of the mass eigenstate onto the weak eigenstate. In matrix notation, this is known as the Pontecorvo-Maki-Nakagawa-Sakata (PMNS) matrix, and is given by

$$\begin{pmatrix}\nu_e\\ \nu_\mu\\ \nu_\tau\end{pmatrix} = U \begin{pmatrix}\nu_1\\ \nu_2\\ \nu_3\end{pmatrix} = \begin{pmatrix}U_{e1} & U_{e2} & U_{e3}\\ U_{\mu 1} & U_{\mu 2} & U_{\mu 3}\\ U_{\tau 1} & U_{\tau 2} & U_{\tau 3}\end{pmatrix} \begin{pmatrix}\nu_1\\ \nu_2\\ \nu_3\end{pmatrix}. \tag{1.8}$$

Here, the subscript "L" is dropped. Therefore, the neutrino that interacts via the weak CC is a coherent superposition of mass eigenstates. Since the PMNS matrix is a change of basis, the matrix itself is unitary [18], therefore $U^\dagger U = UU^\dagger = \mathbb{I}$. It is important to note that there are active investigations in the experimental community on whether the PMNS matrix is unitary or not [19].

$$\begin{aligned}\sum_i U_{\alpha i}U^*_{\beta i} &= \delta_{\alpha\beta} \quad ;\ (\alpha, \beta = e, \mu, \tau)\\ \sum_\alpha U^*_{\alpha i}U_{\alpha j} &= \delta_{ij} \quad ;\ (i, j = 1, 2, 3).\end{aligned} \tag{1.9}$$

A 3×3 unitary matrix can be parameterised by three mixing angles and six phases. The three mixing angles allows for the decomposition of U into three rotation matrices. The six phases are not all physical and some can be removed by rephasing the lepton fields. If neutrinos are assumed to be Dirac fermions, meaning that they are distinct particles from their antiparticle counterparts, then the lepton and neutrino fields can be rephased such that $\nu_i \to e^{i\phi_i}\nu_i$. This is a symmetry in the EW Lagrangian provided that the PMNS matrix is redefined as

$$U_{\alpha i} \to e^{i(\phi_\alpha - \phi_i)}U_{\alpha i}. \tag{1.10}$$

There are five independent values for the phase differences; these values can be removed leaving behind a single physical CP-violating phase. With this, the PMNS matrix can be written as a product of three unitary rotation matrices through angles θ_{12}, θ_{13} and θ_{23} with an additional CP-violating phase, δ_{CP}.

$$\begin{aligned} U &= \begin{pmatrix} U_{e1} & U_{e2} & U_{e3} \\ U_{\mu 1} & U_{\mu 2} & U_{\mu 3} \\ U_{\tau 1} & U_{\tau 2} & U_{\tau 3} \end{pmatrix} = \begin{pmatrix} 1 & 0 & 0 \\ 0 & c_{23} & s_{23} \\ 0 & -s_{23} & c_{23} \end{pmatrix} \begin{pmatrix} c_{13} & 0 & s_{13}e^{-i\delta_{\mathrm{CP}}} \\ 0 & 1 & 0 \\ -s_{13}e^{-i\delta_{\mathrm{CP}}} & 0 & c_{13} \end{pmatrix} \begin{pmatrix} c_{12} & s_{12} & 0 \\ -s_{12} & c_{12} & 0 \\ 0 & 0 & 1 \end{pmatrix} \\ &= \begin{pmatrix} c_{12}c_{13} & s_{12}c_{13} & s_{13}e^{-i\delta_{\mathrm{CP}}} \\ -s_{12}c_{23} - c_{12}s_{13}s_{23}e^{i\delta_{\mathrm{CP}}} & c_{12}c_{23} - s_{12}s_{13}s_{23}e^{i\delta_{\mathrm{CP}}} & c_{13}s_{23} \\ s_{12}s_{23} - c_{12}s_{13}c_{23}e^{i\delta_{\mathrm{CP}}} & -c_{12}s_{23} - s_{12}s_{13}c_{23}e^{i\delta_{\mathrm{CP}}} & c_{13}c_{23} \end{pmatrix}. \end{aligned} \tag{1.11}$$

Here, s_{ij} and c_{ij} correspond to $\sin(\theta_{ij})$ and $\cos(\theta_{ij})$ respectively.

Neutrino oscillations in a vacuum

In a vacuum, neutrinos produced in a pure weak eigenstate are a coherent superposition of the mass eigenstates [18]

$$|\nu(t=0)\rangle = |\nu_\alpha\rangle = \sum_i U^*_{\alpha i} |\nu_i\rangle . \tag{1.12}$$

Note that in Equation 1.7, it is given in terms of field operators. Therefore, when describing neutrino states, creation operators are required to create the single-particle state and so the complex conjugates of the PMNS matrix elements are used. The mass eigenstate is an eigenstate of a free Hamiltonian, $\hat{H}$, as it propagates through the vacuum. Therefore, it evolves as

$$|\nu(t)\rangle = e^{-i\hat{H}t} |\nu(t=0)\rangle = e^{-i\hat{H}t} \sum_i U^*_{\alpha i} |\nu_i\rangle \tag{1.13}$$

with $E_i = \sqrt{p^2 + m_i^2}$. Here, m_i is the mass of the i-th mass eigenstate. The operator $\hat{H}$ acting on the mass eigenstates will produce the eigenvalue E_i,

$$|\nu(t)\rangle = \sum_i U^*_{\alpha i} e^{-iE_i t} |\nu_i\rangle . \tag{1.14}$$

Once the neutrino has travelled through the vacuum and is detected again, it is in a weak eigenstate

$$|\nu(t)\rangle = \sum_i U^*_{\alpha i} e^{-iE_i t} \sum_\beta U_{\beta i} |\nu_\beta\rangle . \tag{1.15}$$

Here, ν_β is a different weak eigenstate (a different neutrino flavour) to when it started. The probability amplitude for a neutrino of flavour α to oscillate into flavour β after time t is given as

$$P(\nu_\alpha \to \nu_\beta) = \Big| \langle \nu_\beta | \nu(t) \rangle \Big|^2 = \Big| \sum_i U^*_{\alpha i} U_{\beta i} e^{-E_i t} \Big|^2 . \tag{1.16}$$

The above expression can be simplified by assuming that neutrinos are travelling ultra-relativistically, therefore $E_i \approx p + \frac{m_i^2}{2E_i}$. This yields

$$P(\nu_\alpha \to \nu_\beta) = \delta_{\alpha\beta} - 4\sum_{i<j} \mathrm{Re}[U_{\alpha i}U_{\beta i}^* U_{\alpha j}^* U_{\beta j}] \sin^2\left(\frac{\Delta m_{ij}^2 L}{4E_i}\right) + 2\sum_{i<j} \mathrm{Im}[U_{\alpha i}U_{\beta i}^* U_{\alpha j}^* U_{\beta j}] \sin\left(\frac{\Delta m_{ij}^2 L}{2E_i}\right). \tag{1.17}$$

Here, Δm_{ij}^2 is the squared mass difference between two mass eigenstates, $L \approx ct$ is the distance travelled by the neutrino, also called the "baseline" and Re and Im represent the real and imaginary parts respectively. An important point to notice about neutrino oscillation is that Δm_{ij}^2 cannot be 0. There are two distinct Δm_{ij}^2 and they are taken to be Δm_{21}^2 and Δm_{31}^2. Neutrino oscillation also depends on δ_{CP} through the terms in the PMNS matrix. In fact, CP violation, i.e. $P(\nu_\alpha \to \nu_\beta) \neq P(\bar{\nu}_\alpha \to \bar{\nu}_\beta)$, is only possible in channels where $\alpha \neq \beta$; this is called the "appearance channel". The case where $\alpha = \beta$ is called the "disappearance channel". The same appearance probability, in the case of antineutrinos, is the same but with $U \to U^*$ [17]. The disappearance probability is given as

$$P(\nu_\alpha \to \nu_\alpha) = 1 - 4\sum_{i<j} \left|U_{\alpha i}U_{\alpha j}\right|^2 \sin^2\left(\frac{\Delta m_{ij}^2 L}{2E_i}\right) = P(\bar{\nu}_\alpha \to \bar{\nu}_\alpha). \tag{1.18}$$

Two-flavour neutrino oscillations

Using a two-flavour approximation, instead of the full three-flavour case as in the previous section, can be informative. Neutrinos coming from the sun, "solar neutrinos", and from the decay of cosmic rays, "atmospheric neutrinos", turned out to be well described by the two-flavour approximation before experiments became sensitive to subleading contributions. In the two-flavour case, the unitary mixing matrix reduces to a simpler rotation matrix:

$$U_{\text{two-flavour}} = \begin{pmatrix} \cos(\theta) & \sin(\theta) \\ -\sin(\theta) & \cos(\theta) \end{pmatrix}. \tag{1.19}$$

There is now just a single mixing angle, θ, between the two flavours, α and β. The appearance probability simplifies to

$$P(\nu_\alpha \to \nu_\beta) = \sin^2(2\theta)\sin^2\left(\frac{\Delta m^2 L}{4E}\right). \tag{1.20}$$

The amplitude of the neutrino oscillation is controlled by $\sin^2(2\theta)$. This probability is not sensitive to the sign of Δm^2 or the octant of θ. In the case of solar and atmospheric neutrinos, the parameters used are $(\Delta m_{\mathrm{sol}}^2, \theta_{\mathrm{sol}})$ and $(\Delta m_{\mathrm{atm}}^2, \theta_{\mathrm{atm}})$ respectively. The value of $\Delta m_{\mathrm{sol}}^2 \ll \Delta m_{\mathrm{atm}}^2$ and the mixing angles are large.

To put these results in the context of three-flavour neutrino oscillations, $\Delta m_{\mathrm{sol}}^2$ is taken to be the mass splitting between the ν_1 and ν_2 mass eigenstates, i.e. Δm_{21}^2. Since Δm_{21}^2

was found to be > 0, $m_2 > m_1$. Δm^2_{atm} is therefore identified with $|\Delta m^2_{31}|$ or $|\Delta m^2_{32}|$.

The last point leaves us with two possibilities [18]:

1. $m_1 < m_2 < m_3$, this is known as the "normal hierarchy". This requires $\Delta m^2_{31} > 0$.
2. $m_3 < m_1 < m_2$, this is known as the "inverted hierarchy". This requires $\Delta m^2_{31} < 0$.

CP violation in neutrino oscillations

In Equation 1.17, the oscillation probability in appearance channels is dependent on δ_{CP}. Here, the different symmetries and their effect on the appearance probability are discussed.

- $P(\nu_\alpha \to \nu_\beta) \xrightarrow{T} P(\nu_\beta \to \nu_\alpha)$
- $P(\nu_\alpha \to \nu_\beta) \xrightarrow{CP} P(\bar{\nu}_\alpha \to \bar{\nu}_\beta)$
- $P(\nu_\alpha \to \nu_\beta) \xrightarrow{CPT} P(\bar{\nu}_\beta \to \bar{\nu}_\alpha)$

The above discrete symmetries have an effect on the appearance probability. The CPT theorem is that any system under the CPT transformation is invariant. This means that CP and T must be violated in equal and opposite amounts. The quantity $A_{\alpha\beta}$ is introduced to quantify the amount of violation.

$$A_{\alpha\beta} = \frac{P(\nu_\alpha \to \nu_\beta) - P(\bar{\nu}_\alpha \to \bar{\nu}_\beta)}{P(\nu_\alpha \to \nu_\beta) + P(\bar{\nu}_\alpha \to \bar{\nu}_\beta)}. \tag{1.21}$$

Often, the quantity $\Delta P_{\alpha\beta} = P(\nu_\alpha \to \nu_\beta) - P(\bar{\nu}_\alpha \to \bar{\nu}_\beta)$ is defined. It can be further expressed using the Jarlskog invariant, a quantity that remains unchanged after the rephasing of the lepton fields, as

$$\Delta P_{\alpha\beta} = \pm 16 J \sin\left(\frac{\Delta m^2_{21} L}{4E}\right) \sin\left(\frac{\Delta m^2_{31} L}{4E}\right) \sin\left(\frac{\Delta m^2_{32} L}{4E}\right), \tag{1.22}$$

where $J = \mathfrak{Im}(U_{\alpha i}\, U_{\beta j}\, U^*_{\alpha j}\, U^*_{\beta i}) = \frac{1}{8}\cos(\theta_{13})\sin(2\theta_{12})\sin(2\theta_{13})\sin(\delta_{\text{CP}})$. The parameterisation of J this way shows that for CP violation to occur, all mixing angles must be non zero and δ_{CP} must not be 0 or π.

Matter effects in neutrino oscillations

In reality, neutrinos do not travel through a vacuum. As neutrinos travel through matter, they interact with it via the EW force. Neutrinos interact via the NC with the Z boson equally in all matter. However, in the CC, a neutrino interacts with its charged counterpart. Because matter is made up of protons, neutrons and electrons, electron (anti)neutrinos will have more interactions in matter through the CC channel. This effect was first investigated by Wolfenstein in 1978 [20] and later built upon by Mikheyev and

Smirnov [21] becoming known as the Mikheyev-Smirnov-Wolfenstein (MSW) effect. The MSW effect manifests itself as an additional potential given by

$$V_{\mathrm{MSW}} = \pm\sqrt{2}\, G_F n_e, \tag{1.23}$$

where G_F is the Fermi constant and n_e is the electron density in the matter through which the neutrino travels. The MSW effect affects the neutrino oscillation probabilities and must be taken into account to get a complete picture.

1.3.2 History of neutrino oscillation experiments

Neutrinos are produced across a wide range of energies, and the way they interact with matter depends strongly on this energy. At low energies, typical of reactor and solar neutrinos, they can only induce transitions to a few low-lying excited states of the final nucleus. At higher energies, characteristic of atmospheric and accelerator neutrinos, they can penetrate the nucleus and interact directly with constituent nucleons. Understanding these different interaction regimes is essential for developing appropriate experiments to measure them. There have been many neutrino oscillation experiments that have been carried out over the past several decades.

The Sun is kept in hydrostatic equilibrium by the outward pressure force from nuclear fusion counteracting the Sun's inward gravitational force. The nuclear fusion processes within the Sun are an abundant source of neutrinos. In 1964, the standard solar model (SSM) was developed by Bahcall [22] and this gave a prediction for the solar neutrino flux. In 1968, Davis measured this solar neutrino flux using tanks of ^{37}Cl in the Homestake mine in South Dakota [23]. The neutrinos are captured by the ^{37}Cl via inverse beta decay as proposed by Pontecorvo in 1946 [24]. The process is

$$\bar{\nu}_e + {}^{37}\mathrm{Cl} \rightarrow e^- + {}^{37}\mathrm{Ar}. \tag{1.24}$$

The argon is then removed from the tanks and counted. Davis found that the measured solar neutrino flux was a factor of seven lower than the predictions from the SSM. This became known as the "solar neutrino problem". It was not until 1989 that the Kamiokande-II experiment in Japan also found that the solar neutrino flux was less than the prediction, however, they found it to be half the expected value [25]. In the 1990s, the SAGE [26] and GALLEX [27] experiments corroborated this measurement when they also reported about half of the expected flux. The SAGE and GALLEX experiments used a process similar to that of Davis but with ^{71}Ga instead. This change lowered the threshold for inverse beta decay and increased their sensitivity to solar neutrinos. The different experiments, due to different neutrino detection techniques, were sensitive to different amounts of the true solar neutrino flux; this made it even more difficult to attribute the deficit to a single cause.

The idea of neutrino oscillations, originally suggested by Pontecorvo in 1967 [14], was a potential solution to the solar neutrino problem and in 1998, the Super-Kamiokande

(SK) experiment showed that atmospheric neutrinos oscillated in flavour [16]. This was a major step forward in neutrino physics. The fact that neutrinos can oscillate in their flavour means that they must experience time and therefore have mass; this breaks the SM in which they are assumed to be massless. It also meant that neutrino oscillations as a solution to the solar neutrino problem could be true.

In 2002, the Sudbury Neutrino Observatory (SNO), a spherical-tank Cherenkov detector filled with heavy water, showed that the solar neutrino flux in the CC channel has a deficit, but the NC channel, which is equally sensitive to all neutrino flavours, is in line with the SSM [28]. The neutrino flux from each channel is shown in Figure 1.1. The NC contour agrees with the SSM meaning that the total number of neutrinos is as expected. The CC contour shows a deficit, indicating that the number of electron neutrinos is lower than expected.

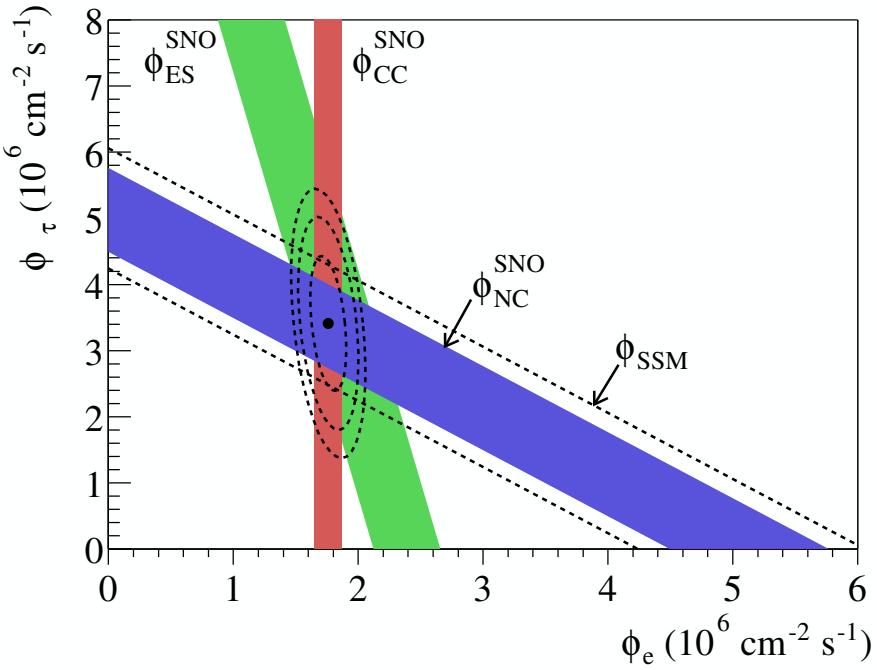

Figure 1.1: Solar neutrino flux from the charged current (CC), neutral current (NC) and elastic scattering (ES) channels in the SNO detector. The NC channel is equally sensitive to all neutrino flavours and is in line with the SSM. The CC channel shows a clear deficit. Figure from Ref. [28].

The solar parameters, Δm^2_{21} and the solar mixing angle θ_{21}, were first measured using these solar neutrino analyses. However, neutrino detectors placed near nuclear reactors (called "reactor experiments") are also sensitive to these parameters. The KamLAND experiment provided one such constraint to the solar parameters [29]. Together with SNO and SK, constraints on the solar parameters were calculated by combining all results.

Atmospheric neutrinos are produced by solar rays entering the Earth's atmosphere. The protons in the solar rays collide with nuclei in the upper atmosphere producing hadronic showers consisting mostly of pions. The charged pions decay to muons which then decay to neutrinos.

$$\begin{aligned} \pi^+ &\to \mu^+ + \nu_\mu \to e^+ + \nu_e + \bar{\nu}_\mu + \nu_\mu \\ \pi^- &\to \mu^- + \bar{\nu}_\mu \to e^- + \bar{\nu}_e + \nu_\mu + \bar{\nu}_\mu \end{aligned} \tag{1.25}$$

From this, the expected ratio of muon neutrinos to electron neutrinos is 2. However, the Kamiokande experiment consistently found this ratio to be less than this [30, 31]. The result from SK in 1998, however, found that the atmospheric neutrino oscillation agreed with $\nu_\mu \to \nu_\tau$ oscillations; this provided a solution to the atmospheric neutrino flux deficit. The atmospheric parameters, Δm^2_{32} and the atmospheric mixing angle θ_{32}, were initially measured using these atmospheric neutrino experiments, but more recent accelerator neutrino experiments, such as T2K [32] and NOνA [33], also provide high-statistics constraints. More recent results from SK [34], shown in Figure 1.2, show a 2D contour of the atmospheric parameters using data from accelerator neutrino experiments, MINOS+ [35], NOνA [36], T2K [37] and IceCube [38].

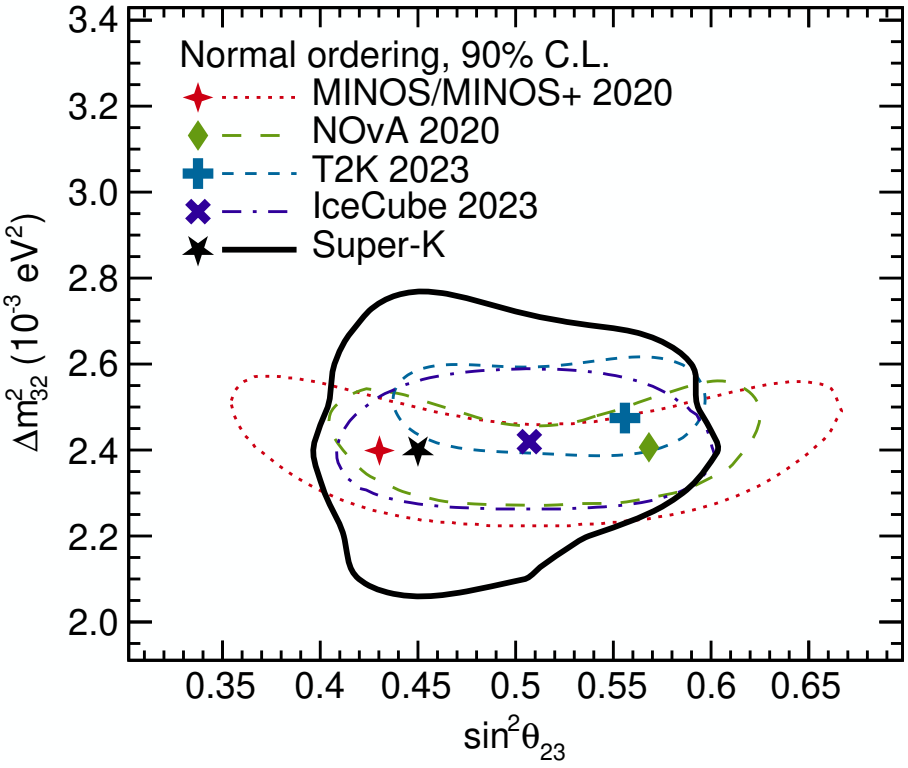

Figure 1.2: Constraints on the atmospheric neutrino oscillation parameters, Δm^2_{32} and θ_{32} from Ref. [34] showing data from MINOS+ [35], NOνA [36], T2K [37] and IceCube [38].

1.3.3 Current state of the field

Current accelerator-based long-baseline neutrino experiments, such as T2K in Japan [32] and NOνA in the US [33] continue to provide up-to-date neutrino oscillation results, continually tightening the constraints on the PMNS parameters, including δ_{CP} [39, 40, 36]. Atmospheric neutrinos from cosmic rays are produced in a wide range of energies (MeV-TeV) and they propagate a range of baselines (from 15 km to around 13,000 km). This increases the sensitivity to the neutrino mass ordering as a result of matter effects. In the normal hierarchy, these effects enhance ν_e appearance. The opposite is true for the inverted hierarchy. For these reasons, the SK experiment has increased sensitivity to the neutrino mass ordering and continues to measure oscillation [41]. Conversely, with T2K having an increased sensitivity to δ_{CP} but not to mass ordering, a joint fit of T2K and SK data was performed and recently published [42]. The results show no strong preference for the octant of θ_{23} and that a CP-conserving $J = 0$ is excluded at 1.9–2.0σ.

Another joint fit between T2K and NOνA data is being prepared for publication [43]. The two experiments have different baselines and therefore different oscillation probabilities. This helps lift degeneracies seen by both experiments. Next-generation experiments, such as Hyper-Kamiokande (HK) [44] and the Deep Underground Neutrino Experiment (DUNE) [45] are currently being constructed with HK on-track for turning on in 2027. These next-generation experiments aim to provide much more neutrino interactions which are needed to reduce the statistical uncertainties on the PMNS parameters. This is often called the "high-precision era" of neutrino physics and aims to measure δ_{CP} with a significance of 5σ. The JUNO experiment [46] has recently begun taking data and aims to measure the neutrino mass hierarchy. The most up-to-date values for the PMNS parameters can be found in Ref. [47]. The current limitation in neutrino oscillation experiments comes from nuclear mismodelling. For the 5σ significance goal to be achieved by next-generation experiments, advancements in nuclear modelling in neutrino interaction models are necessary.

1.4 Introduction to Neutrino Interactions

In experimental settings, neutrinos interact with a single nucleus within a detector. Depending on the neutrino energy, the energy transferred in the interaction is different and, therefore, the interaction channel is different. At energy transfers up to around 100 MeV, the neutrino interacts coherently with the nucleus as a whole via $\nu + {}^{A}_{Z}X \rightarrow \nu + {}^{A}_{Z}X^{*}$, where the nucleus, X, can be left in an excited state, X^{*}. Beyond this energy, the neutrino can begin to resolve the nucleons within the nucleus and can interact via different channels. The quasi-elastic (QE) channel, as shown in Figure 1.3, is dominant for neutrino energies between approximately 200 MeV and 1000 MeV. The QE channel can be a neutral-current interaction (NCQE) or a charged-current interaction (CCQE). The NCQE interaction is mediated by the neutral Z boson and can be written as

$$\nu_l + N \rightarrow \nu_l + N, \tag{1.26}$$

where N is a nucleon in the nucleus and l is the flavour of the neutrino. The CCQE interaction, however, is mediated by the W^{+} boson for the neutrino case and the W^{-} boson for the antineutrino case. As a result, the CCQE interaction involves a $d \rightarrow u$ quark transition increasing the third component of isospin (I_3) by a single unit for neutrino interactions, and a $u \rightarrow d$ quark transition decreasing I_3 by a single unit for antineutrino interactions. In this section, the CKM mixing interactions, while they exist in the SM, are ignored due to the suppression by the CKM mixing elements, and only the leading interactions are shown. In CCQE interactions, charge conservation requires neutrinos to scatter from neutrons and antineutrinos to scatter from protons. The two CCQE interaction channels are written as

$$\begin{aligned} \nu_l + n &\rightarrow l^{-} + p, \\ \bar{\nu}_l + p &\rightarrow l^{+} + n. \end{aligned} \tag{1.27}$$

Here, the final state contains a nucleon with the opposite I_3 to the initial state. In reality, the target nucleons are not free and are bound within a nucleus. The analogous interactions can therefore be written as

$$\begin{aligned} \nu_l + {}^{A}_{Z}X &\rightarrow l^{-} + p + {}^{A-1}_{Z-1}Y, \\ \bar{\nu}_l + {}^{A}_{Z}X &\rightarrow l^{+} + n + {}^{A-1}_{Z}Y, \end{aligned} \tag{1.28}$$

where the final-state nucleus, Y, is written explicitly and can be in an excited state. The CCQE interaction with a target neutron is shown in Figure 1.4a.

At neutrino energies from around 400 MeV, the energy transfer in the interaction is large enough to create a Δ baryon which then decays via resonance into a nucleon and a pion. As shown in Figure 1.3, neutrino energies from around 1000 MeV, this pion production interaction is the dominant interaction.

Pion production is a more complex interaction because there are a lot of baryon resonances (excited nucleons) and non-resonant interactions that produce a single pion in the region $M_{\text{nucleon}} + m_\pi < W < 2$ GeV, where W is the hadron invariant mass. At low W, the Δ resonance contributes and is at a maximum at $W = 1232$ MeV. At higher W and higher neutrino energy, heavier resonances are produced. These resonant processes overlap and also interfere with non-resonant backgrounds, leading to significant interference effects that are not directly distinguishable in experiments.

Due to the isospin structure of the weak CC interaction, neutrino interactions are mediated by the W^+ boson and increase I_3 by a single unit by the $u \to d$ quark transition. Unlike CCQE interactions, where charge conservation restricts neutrinos to interacting on neutrons and antineutrinos on protons, the neutrino can interact on a proton or a neutron target. An interaction on a proton target, will change the quark structure to be uuu and create the Δ^{++} baryon. An interaction on a neutron target, however, will create a uud, which is a Δ^+ resonance. These two processes are written as

$$\begin{aligned} &\nu_l + p \to l^- + \Delta^{++} \to l^- + p + \pi^+, \\ &\nu_l + n \to l^- + \Delta^{+} \to l^- + n + \pi^+. \\ &\nu_l + n \to l^- + \Delta^{+} \to l^- + p + \pi^0. \end{aligned} \tag{1.29}$$

Here, the neutrino interaction on a neutron target can also produce a proton and π^0 in the final state. The Δ^{++} resonance interaction is shown in Figure 1.4b.

The analogous antineutrino interactions are mediated by the W^- boson and therefore involve a $u \to d$ quark transition, reducing I_3 by a single unit. Therefore, different states of the Δ baryon resonance multiplet are accessible. For antineutrino interactions on a proton target, the $u \to d$ transition produces an udd state that is a Δ^0 resonance. For interactions on a neutron target, however, a ddd state is produced; this is the Δ^- resonance. These two processes are written as

$$\begin{aligned} &\bar{\nu}_l + p \to l^+ + \Delta^{0} \to l^+ + p + \pi^-, \\ &\bar{\nu}_l + p \to l^+ + \Delta^{0} \to l^+ + n + \pi^0, \\ &\bar{\nu}_l + n \to l^+ + \Delta^{-} \to l^+ + n + \pi^-. \end{aligned} \tag{1.30}$$

Here, the antineutrino interaction on a proton target, analogous to the neutrino case, can also produce a neutron and a π^0 in the final state.

Therefore, there are several resonant pion production configurations that can produce $\pi^\pm$, π^0 or even multiple πs in a single neutrino interaction. Final states that contain a single pion are denoted as a CC1π interaction, while final states that contain multiple pions are denoted as a CC$N\pi$ interaction.

At neutrino energies from around 2000 MeV, the deep-inelastic scattering (DIS) interaction begins to contribute to the total cross section. In DIS interactions, the neutrino

resolves the quarks within the nucleus. They can be written as

$$\nu_l + {}^{A}_{Z}X \rightarrow l^{-} + Y. \tag{1.31}$$

Here, Y is a final state consisting of hadrons and mesons.

Resonant pion production and DIS scattering are closely related through quark-hadron duality [48] which states that if one averages over the CC resonances, the structure functions that describe the interaction tend to the DIS structure functions for the same Bjorken x and momentum transfer. This implies that the nucleon- and quark-level descriptions are dual representations of the same underlying physics. This has been used in previous work by Bodek and Yang to modify the DIS structure functions that are used in current neutrino scattering simulations [49].

Neutrino oscillation experiments use accelerator neutrinos that are in the GeV energy range. In this work, we focus on the QE interaction, specifically the CCQE interaction. Figure 1.3 shows the total interaction cross section for different interaction channels as a function of the incident neutrino energy, E_ν.

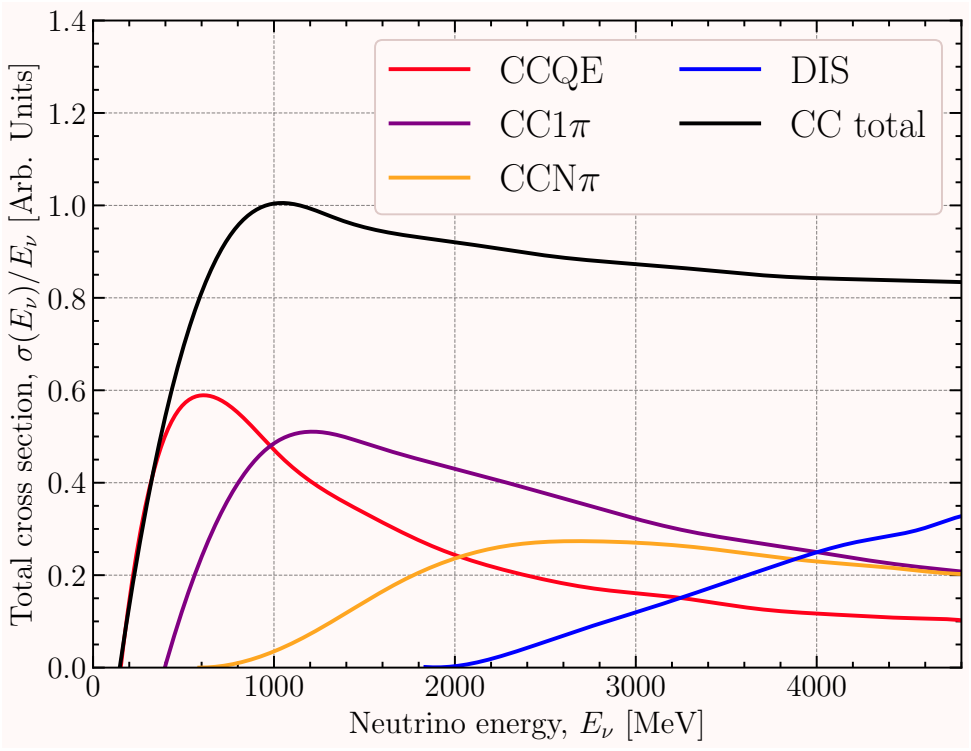

Figure 1.3: The total interaction cross section for the charged-current quasi-elastic (CCQE), charged-current single pion production (CC1π), charged-current N-pion production (CC$N\pi$), deep inelastic scattering (DIS) and charged-current total (CC total, it is the sum of all CC channels) channels as a function of incident neutrino energy E_ν. The distributions are normalised to the peak of the CC total channel. Produced using NEUT 5.8.0.

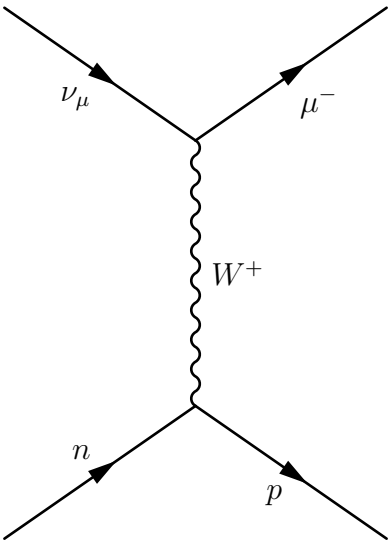

(a) Charged-current quasi-elastic (CCQE) interaction channel between a neutrino of flavour l and a nucleus (in this Figure it is a neutron, but the analogous antiparticle is possible). The interaction produces a charged lepton of the same flavour and ejects a nucleon of opposite third component of isospin.

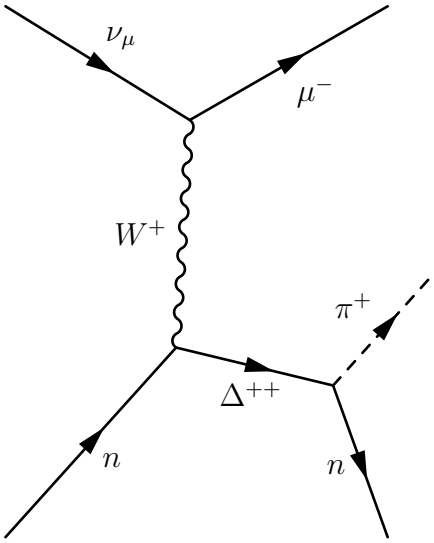

(b) Single pion production through a Δ^{++} baryon resonance. Analogous interactions exist for different baryonic resonances and antineutrinos.

Figure 1.4: Neutrino-nucleon interaction diagrams for the CCQE channel and an example of a resonant pion production interaction.

1.4.1 The role of neutrino interactions in oscillation experiments

In neutrino experiments, detectors cannot observe neutrinos directly. Instead, the detectors capture the visible final-state particles that are produced when a neutrino interacts with a nuclear target within the detector. Neutrino interaction models are used to infer the original properties of the neutrino. Specifically, the neutrino energy, which cannot be measured directly, is inferred using neutrino interaction models. This is shown graphically in Figure 1.5.

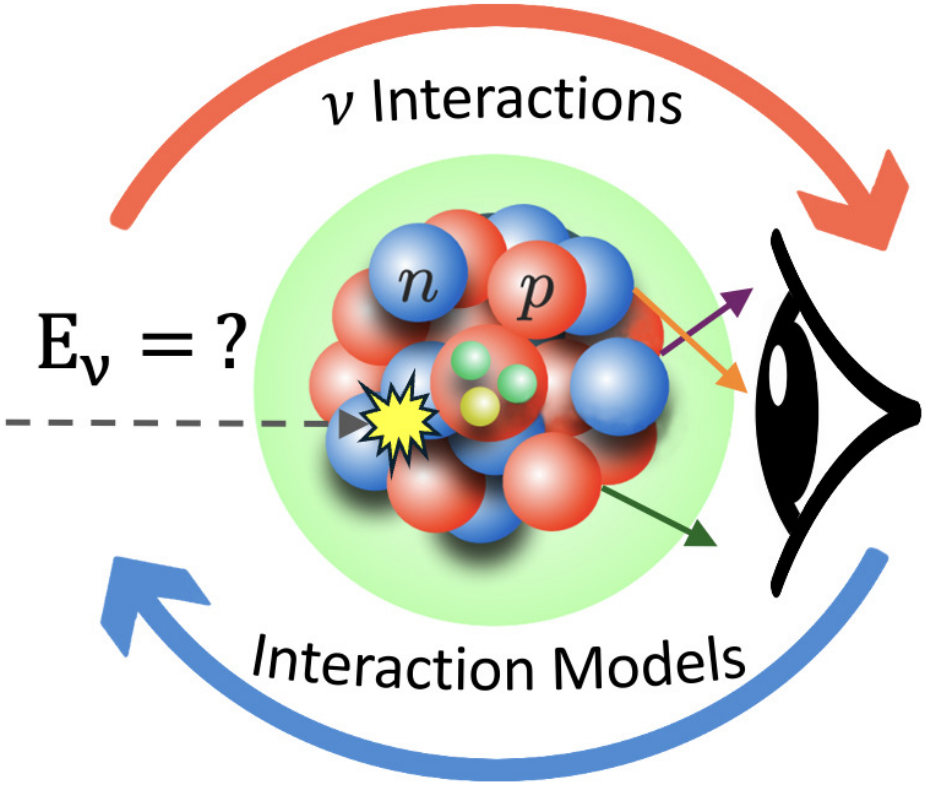

Figure 1.5: A graphical representation showing how neutrino energy is reconstructed in current detectors in accelerator-based neutrino experiments by detecting visible particles in the final state and using neutrino interaction models. Figure from M. Kabirnezhad.

Neutrino oscillation experiments commonly use wide-band accelerator neutrino beams, which span a broad energy range (typically from hundreds of MeV to a few GeV). This variability introduces another complication and removes the ability to detect neutrinos event-by-event. Therefore, interaction models are used even more. As a result, these experiments rely heavily on detailed neutrino interaction models, encapsulated in sophisticated neutrino event generators.

Since the neutrino energy cannot be measured directly and must be inferred from the final-state configuration and neutrino interaction models, there can be a direct bias to neutrino energy reconstruction. This will then bias neutrino cross-section and oscillation parameter measurements [50, 51]. For water Cherenkov experiments, such as SK (and T2K neutrino oscillation studies) detect the final-state lepton directly from its Cherenkov light. The neutrino energy is then reconstructed using only lepton kinematics via

$$E_\nu^{\mathrm{QE}} = \frac{2E_l(M_{N,i} - E_b) - M_l^2 + M_{N,f}^2 - (M_{N,i} - E_b)^2}{2\big((M_{N,i} - E_b) - E_l + k_l\cos(\theta_l)\big)}. \tag{1.32}$$

Here, E_b is the binding energy that is approximated for different target nuclei. If $E_b = 0$,

this is the exact neutrino energy from scattering off a free on-shell nucleon. The lack of nucleon information in the final state in E_ν^{QE} indicates that this method is especially susceptible to bias due to misidentification of interaction channel that mimic the QE channel after final-state interactions.

For liquid argon experiments, such as MicroBooNE [52], more final-state particles can be measured. Therefore, a calorimetric approach can be employed to reconstruct the neutrino energy. This approach is given in Equation 1.33,

$$E_\nu^{\mathrm{Cal}} = E_l + E_B + \sum_{i \in \mathrm{nucleon}} T_i + \sum_{j \in \mathrm{meson}} E_j, \tag{1.33}$$

where l is the ejected lepton, E_B is the binding energy, T_i are the kinetic energies of each knocked out nucleon and E_j is the total energy of each knocked out meson. This approach utilises nucleon information in the neutrino energy estimator, and therefore encodes more information about the interaction. However, neutrino interaction models are required in order to predict how many nucleons or mesons should be in the final state. This introduces a bias in the neutrino energy reconstruction.

The neutrino energy is required to estimate the neutrino interaction event rate at the far detector. This is given by Equation 1.34.

$$R(\nu_i \rightarrow \nu_j \ ; E_\nu^{\mathrm{obs}}) = \phi(E_\nu)\sigma(E_\nu, E_\nu^{\mathrm{obs}})\epsilon(E_\nu^{\mathrm{obs}})P(\nu_i \rightarrow \nu_j \ ; E_\nu). \tag{1.34}$$

Here R is the observed far detector neutrino event spectrum, P is the probability to oscillate between neutrino flavours i and j, E_ν is the neutrino energy at the near detector, E_ν^{obs} is the observed (reconstructed) neutrino energy at the far detector, ϕ is the near detector flux, σ is the cross section of a given neutrino interaction, and ϵ is the detection efficiency.

Early neutrino experiments used bubble chambers in which the interaction is on hydrogen gas. Interactions on hydrogen are clean because the interaction is on a free nucleon. Modern detectors are made of composite materials, such as water and hydrocarbon (SK, T2K), or of pure larger nuclei, such as liquid argon (MicroBooNE, DUNE). This is more complicated than hydrogen because the presence of a nuclear medium means that there are many nuclear effects that need to be taken into account.

The main nuclear effects are as follows: Fermi motion, the motion of the nucleon within the nucleus before the interaction; final-state interactions (FSI), re-interaction of the scattered nucleon with the residual nucleus; short-ranged correlations (SRC), two nucleons are "correlated" within the nucleus and a neutrino interacting with one also ejects the correlated nucleon. These nuclear effects also significantly bias E_ν^{QE}.

Nuclear mismodelling, as is known in experiments, is one of the largest contributors to the overall systematic error in neutrino oscillation experiments [53]. For experiments

such as T2K and MicroBooNE, the dominant interaction channel is CCQE, while for the MINERvA experiment [54] with the low-energy (LE) flux, the dominant channel would be CC1π, CC$N\pi$ and DIS. This can be seen from the flux peak in Figure 1.6 when compared with the total cross section for an interaction channel in Figure 1.3. Therefore, it is imperative to reduce this nuclear mismodelling for the CCQE channel in order to reduce overall systematic uncertainties for the T2K experiment. This is even more true when next-generation experiments, such as DUNE and HK begin to take data.

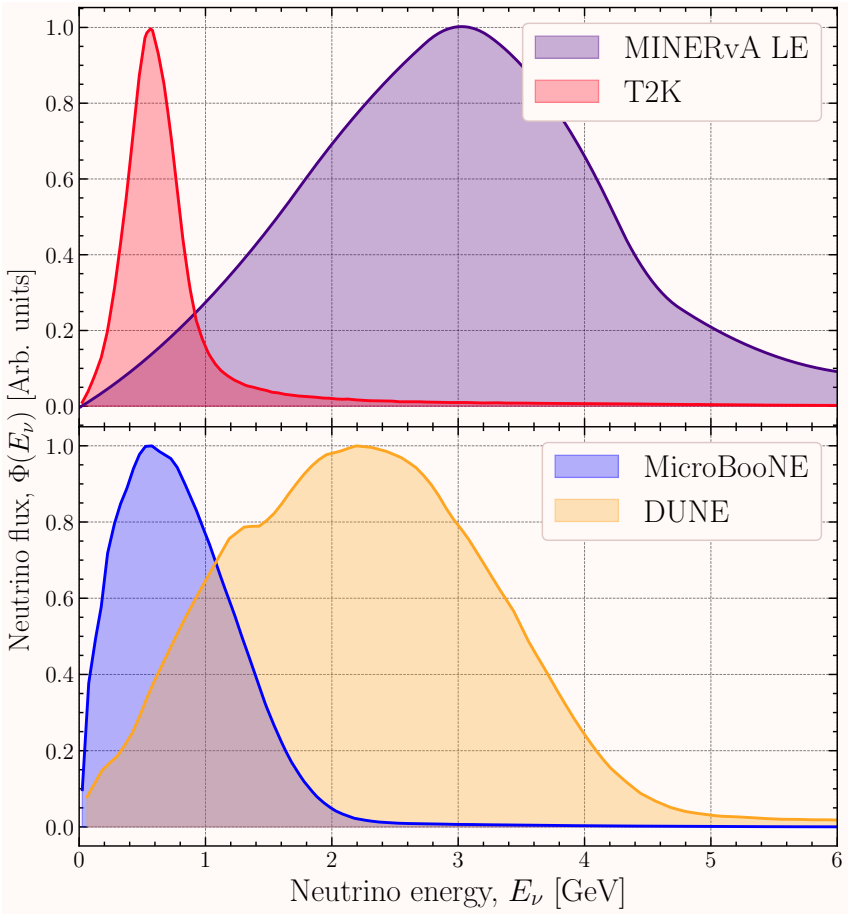

Figure 1.6: Comparison of the neutrino fluxes for the T2K, MINERvA (LE flux), MicroBooNE and DUNE experiments. The fluxes are peak normalised for shape comparison. The T2K and MINERvA (top) target is hydrocarbon while MicroBooNE and DUNE (bottom) is on argon.

For nuclear mismodelling to be improved, sophisticated neutrino-nucleus models must be developed. More importantly, they need to be integrated into neutrino Monte Carlo (MC) event generators (EGs). These EGs are used directly in experiments to produce MC for analyses. For theorists to develop sophisticated models, data with which to compare and fit are paramount.

Electron-nucleus scattering offers a unique insight into neutrino-nucleus scattering because most of the theoretical framework (including nuclear effects) is the same [50]. Electron-nucleus scattering using a monochromatic beam is also cleaner data to compare theoretical models with, since the incident electron energy is known and the scattering angle of the lepton and other final-state particles is also often known. However, in neutrino-nucleus scattering, the incident neutrino energy is not known, and the flux must be integrated over, producing a "flux-averaged" cross section. Electron-nucleus scattering provides constraints for the vector component of the interaction. This is explained in more detail in Section 6.

Different reaction channels which can be measured, each offering us different information. The reaction channels are:

1. Inclusive cross section: in this interaction, only the final-state lepton is detected. This is often denoted as (e, e') in electron scattering.

2. The semi-inclusive cross section: in this interaction, the final-state lepton is detected in coincidence with another final-state particle or set of particles.

3. The exclusive cross section: in this interaction, the final state is completely determined. That is, if the interaction is kept below the two-nucleon-knockout threshold, the final state is completely determined because the excited state of the residual nucleus is also known.

It is important to note that $(e, e'p)$ experiments, which denote experiments in which particles are detected in coincidence with a lepton, can be semi-inclusive or exclusive. All neutrino-nucleus scattering models can model the inclusive cross section well since the physics of the lepton is less complex than that of the final-state nucleons. Semi-inclusive data provides an insight into the different models and how they describe the physics of the final-state nucleon. As will be described in later chapters, some models model SRC effects but neglect FSI. Exclusive data would provide all the information required to fully test theoretical models. However, this provides a challenge to experiments since it requires all particles to be detected simultaneously regardless of detection thresholds.

Part II

The T2K Experiment, ND280 Upgrade and The Super Fine-Grained Detector

Chapter 2

The T2K Experiment

The Tokai-to-Kamioka (T2K) experiment is a long-baseline neutrino experiment which is based in Japan [32]. A $\nu_\mu/\bar{\nu}_\mu$ beam is produced at the Japan Proton Accelerator Research Complex (J-PARC) and is sent towards SK roughly 295 km away. The experiment utilises a two-detector configuration: a near detector suite and a far detector. The near detector suite contains two main near detectors, ND280, the 2.5° off-axis detector used to constrain systematics on parameters such as flux and cross section, and Interactive Neutrino GRID (INGRID), the on-axis detector that is used to profile the beam and measure the beam quality. The far detector, SK, is 1 km underground in the Kamioka mine in Gifu, Japan [32]. The T2K experiment measures $\nu_\mu \to \nu_e$ oscillations (ν_e appearance) and $\nu_\mu \to \nu_\mu$ disappearance, and from this measures aforementioned PMNS matrix parameters. The ν_μ disappearance probability enables the measurement of $\sin^2(\theta_{23})$ and Δm^2_{32}; while the ν_e appearance probability allows access to the θ_{13} parameter and thus to the value of δ_{CP}.

T2K began in 2010 and presented evidence of non-zero value of θ_{13} at 2.5 σ confidence one year later [55]. Since then, T2K has published world-leading results on the allowed values of δ_{CP}, such as a 3 σ confidence limit (CL) published in Nature in 2020 [56]. In addition to neutrino oscillation parameter measurements, T2K also publishes a breadth of cross-section measurements allowing for a better understanding of the neutrinos with the nuclei in detectors.

The neutrino beam is produced by accelerating protons to 30 GeV and impinging them onto a graphite target [57]. This subsequently produces $\pi^\pm$ and $K^\pm$ mesons through deep inelastic scattering. These pions and kaons then travel through magnetic horns where the polarity of charged particles can be selected for the decay volume. Then, the mesons travel through the decay volume where, due to helicity preferences, they decay to muons and muon neutrinos. However, around 1% of the neutrino flux is ν_e as a result of the $\mu^+ \to e^+\bar{\nu}_\mu\nu_e$, $K^+ \to \pi^0 e^+\nu_e$ and $K^0_L \to \pi^- e^+\nu_e$ decays with branching ratios of 100%, 5.1% and 40.5% respectively [58].

This process results in an almost pure neutrino beam that is then sent to the detectors. The neutrino beam flux is a narrow-band beam and has a peak neutrino energy at around 0.6–0.7 GeV in order to maximise the oscillation probability at SK. The beam can be used in neutrino mode (known as forward horn current, FHC) or antineutrino mode (known as reverse horn current, RHC). A schematic is shown in Figure 2.1 below.

This chapter describes the experimental setup of T2K, including beam production, near detector suite, SK and recent upgrade efforts to the beam and ND280.

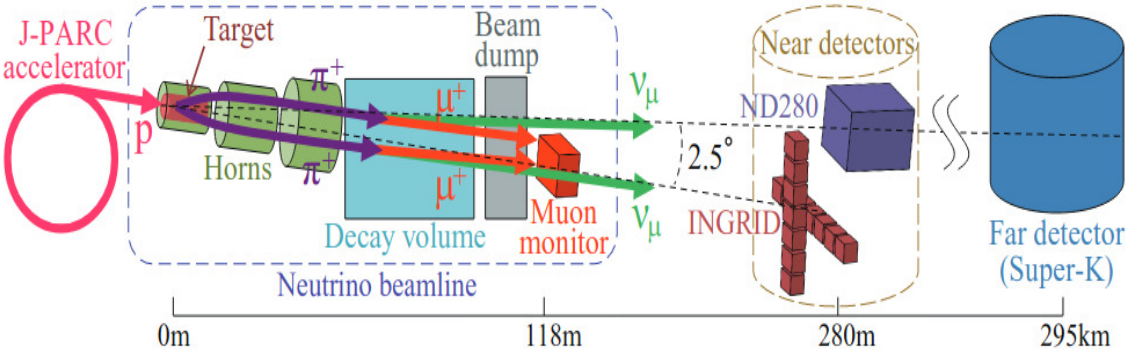

Figure 2.1: Schematic layout of the T2K beamline showing the pion production target, magnetic horns for focusing, decay volume and near detectors [59].

2.1 J-PARC neutrino beam

The T2K beamline is composed of an initial linear accelerator, a rapid cycling synchrotron and a main ring (MR) synchrotron. The beam is fast-extracted from the MR into the neutrino beamline at a design power of 750 kW. The protons in the MR are accelerated to 30 GeV/c and are fast-extracted in "spills", where each spill contains 2.5×10^{14} protons in eight bunches. A spill window is 0.5 μs. The repetition cycle of the MR was designed to be 2.46 s. Over upgrade work during 2021–2022, the repetition cycle was reduced to 1.36 s, providing more protons in a given time window. In December 2023, stable running was achieved at 760 kW for the first time [60]. The future beam uprgade plan aims to operate at a beam power of 1.3 MW with a repetition time of 1.16 s and 3.2×10^{14} protons per pulse [57].

The neutrino beamline, shown in Figure 2.2 is comprised of two segments: the primary and secondary beamline. The primary beamline is bent towards the direction of SK and guides the protons into a graphite target. Protons collide with the graphite target to produce predominantly $\pi^{\pm}$ and $K^{\pm}$ mesons through deep-inelastic scattering (DIS) interactions. The graphite target is housed within a magnetic horn which focus right-sign mesons and deflects wrong-sign mesons which will contribute to a background in the neutrino beam. Downstream of the target and initial magnetic horn, are two more magnetic horns. The initial horns, while designed to operate at 320 kA, operated at 250 kA due to choices related to power supplies. However, after a power supply and design upgrade, they now operate at 320 kA, creating a more pure beam [61]. The $\pi^{\pm}$ and $K^{\pm}$ then travel down a 96 m decay volume in which most mesons decay into muons and other particles. Any undecayed mesons and low momentum muons then collide with a beam dump. Muons with momentum above 5.0 GeV/c pass through the beam dump and travel to the muon monitor [62].

Neutrinos are produced by three main mesonic decay channels and one leptonic decay channel. Specifically,

$$\begin{aligned}
\pi^{\pm} &\to \mu^{\pm} + \overset{(-)}{\nu}_{\mu}, \\
K^{\pm} &\to \mu^{\pm} + \overset{(-)}{\nu}_{\mu}, \\
K^{+} &\to \pi^{0} + \mu^{+} + \nu_{\mu} \\
&\quad\ \pi^{0} + e^{+} + \nu_{e} \\
K^{0}_{\mathrm{L}} &\to \pi^{-} + e^{+} + \nu_{e}, \\
&\quad\ \pi^{-} + \mu^{+} + \nu_{\mu}.
\end{aligned} \tag{2.1}$$

For the mesonic decay channels and

$$\mu^{+} \to e^{+} + \bar{\nu}_{\mu} + \nu_{e} \tag{2.2}$$

for the leptonic decay. Decay rates [9]:

Decay channel	Decay rate
$\pi^{\pm} \to \mu^{\pm} + \overset{(-)}{\nu}_{\mu}$	99.9877%
$K^{\pm} \to \mu^{\pm} + \overset{(-)}{\nu}_{\mu}$	63.56%
$K^{+} \to \pi^{0} + \mu^{+} + \nu_{\mu}$	3.35%
$K^{+} \to \pi^{0} + e^{+} + \nu_{e}$	5.07%
$K^{0}_{\mathrm{L}} \to \pi^{-} + e^{+} + \nu_{e}$	40.55%
$K^{0}_{\mathrm{L}} \to \pi^{-} + \mu^{+} + \nu_{\mu}$	27.04%
$\mu^{+} \to e^{+} + \bar{\nu}_{\mu} + \nu_{e}$	100%

Table 2.1: Decay rates of particles produced in a neutrino beamline that produce neutrinos.

118 m downstream of the graphite target and almost immediately downstream of the beam dump is the MUMON detector [62]. The MUMON detector consists of two detector arrays: ionisation chambers and silicon PIN photodiodes. Beam Monte Carlo (MC) simulations predict a muon beam profile that is roughly Gaussian with a width of 1 m. As such, the MUMON detector is fitted with 49 sensors in a 1.5×1.5 m^2 array. The aims of MUMON are to measure the neutrino beam intensity to a precision of 3% and to measure the neutrino beam direction to 0.25 mrad. This informs the beam group about the status of the beam and also provides important validations to the beam MC, which is important for providing flux predictions at ND280 and SK.

The T2K experiment utilises the off-axis (OA) technique which produces a neutrino beam with a narrower energy spectrum with a peak that ensures the principle oscillation maximum occurs when the beam reaches SK [63]. The OA technique refers to the opening angle between the decaying meson and neutrino, often called the "OA angle", θ_{OA}. Assuming the neutrinos come from a decay such as $A^{\pm} \to \mu^{\pm} + \overset{(-)}{\nu}_{\mu}$, where A is either $\pi^{\pm}$ or $K^{\pm}$, the neutrino energy can be approximated assuming massless neutrinos.

$$\begin{aligned} P_A^{\lambda} &= P_{\mu}^{\lambda} + P_{\nu}^{\lambda} \\ \begin{pmatrix} E_{\pi} \\ \mathbf{p}_{\pi} \end{pmatrix} &= \begin{pmatrix} E_{\mu} \\ \mathbf{p}_{\mu} \end{pmatrix} + \begin{pmatrix} E_{\nu} \\ \mathbf{p}_{\nu} \end{pmatrix} \end{aligned} \tag{2.3}$$

which can be rearranged to give

$$\begin{aligned} m_{\pi}^2 - 2\mathbf{p}_{\nu} \cdot \mathbf{p}_{\pi} &= m_{\mu}^2 \\ \frac{m_{\pi}^2 - m_{\mu}^2}{2} &= E_{\nu}\big(E_{\pi} - p_{\pi}\cos(\theta_{\mathrm{OA}})\big) \\ \Rightarrow E_{\nu} &= \frac{m_{\pi}^2 - m_{\mu}^2}{2\big(E_{\pi} - p_{\pi}\cos(\theta_{\mathrm{OA}})\big)}. \end{aligned} \tag{2.4}$$

Here, λ is a covariant index, P_X^λ is a four vector for particle X, m indicates the mass of a particle and p indicates the magnitude of the three momentum. The available neutrino energy spectrum decreases as θ_{OA} increases. Figure 2.3 shows the maximum neutrino energy spectra for an energy of 4 GeV. As θ_{OA} increases, the neutrino energy quickly drops off. The maximum neutrino energy is given as

$$E_\nu^{\max} = \frac{m_\pi^2 - m_\mu^2}{2E_\pi \sin^2(\theta_{\mathrm{OA}})}. \tag{2.5}$$

The NA61/SHINE experiment used a T2K replica target to reduce uncertainties on neutrino beam flux and modelling [64]. Figure 7 in Ref. [64] shows the momentum spectra for pions leaving the end of the T2K replica target. The momentum spectra peaks at 2–4 GeV/c. Figure 2.3 shows the maximum neutrino energy at the T2K OA angle of 2.5°. Figure 2.6 shows the neutrino flux at ND280 for different OA angle. It also shows the neutrino oscillation prediction as a function of baseline. The T2K neutrino flux is tuned such that SK is placed at the oscillation maxima.
Figure 2.4 shows the Protons-on-Target (POT) accumulated per beam run from the start of T2K until now. Figure 2.5 shows the accumulated POT in the beam run over November and December 2024. In that run, the neutrino beam operated at 810 kW stably, surpassing the previous 750 kW achieved the year before.

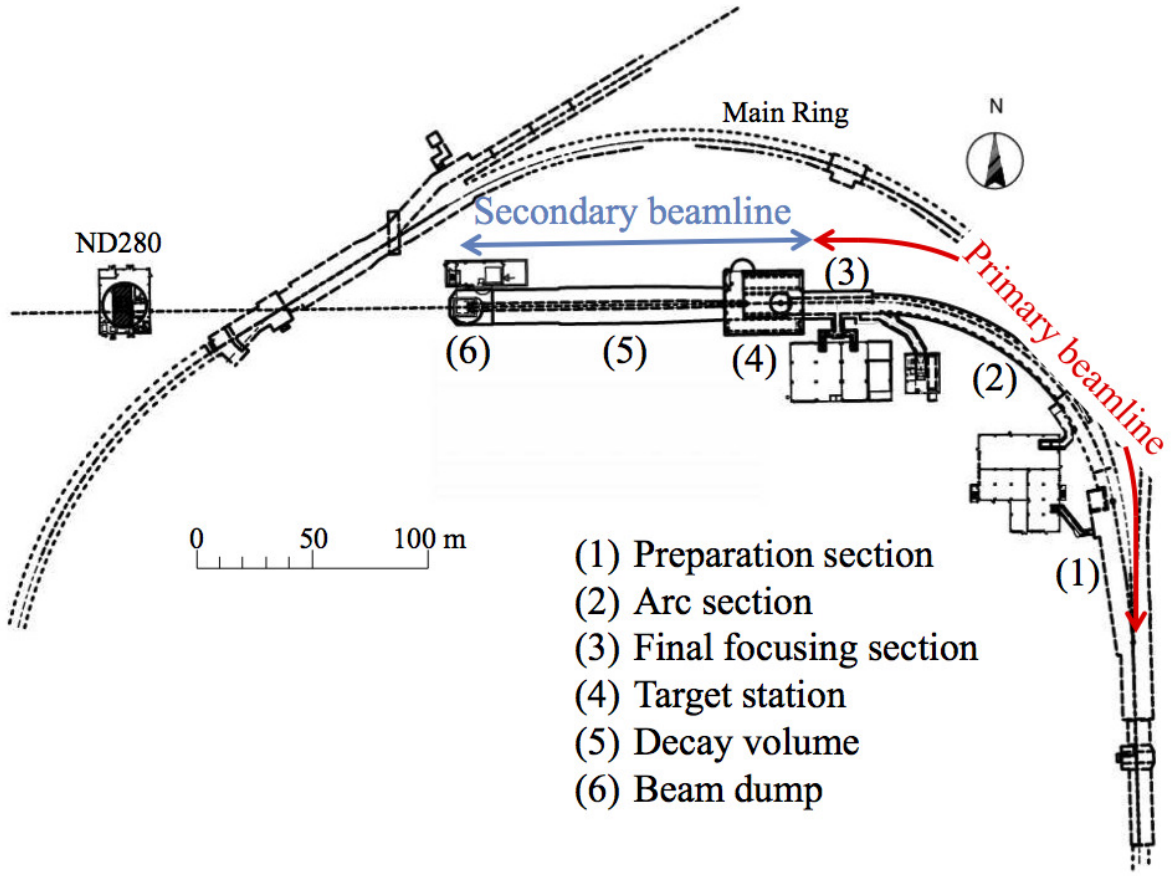

Figure 2.2: Schematic layout of the T2K neutrino beamline. Figure taken from Ref. [57].

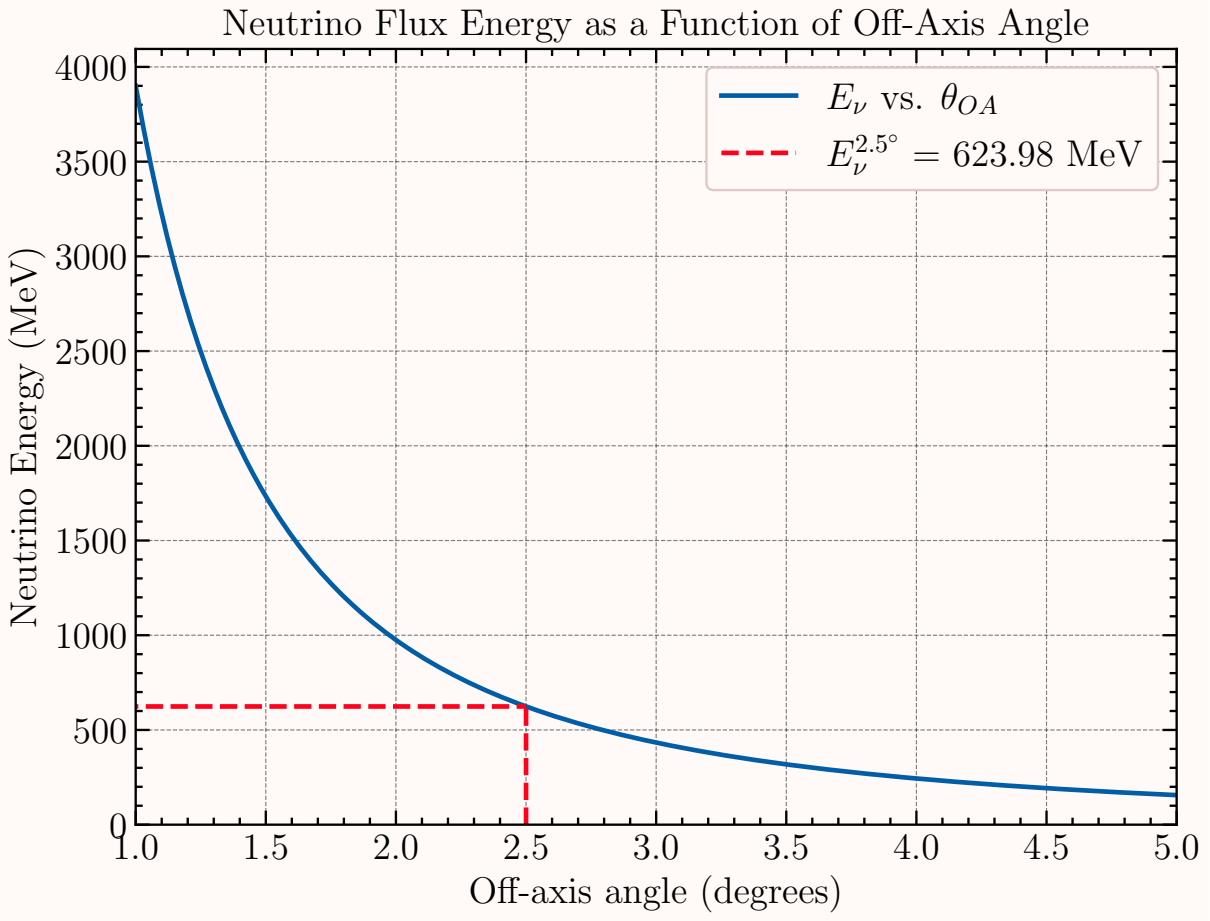

Figure 2.3: Maximum neutrino energy as a function of θ_{OA} for a pion with energy 4 GeV decaying into a muon and a neutrino. The neutrino energy at 2.5°, the T2K OA angle, is shown by the red dotted line.

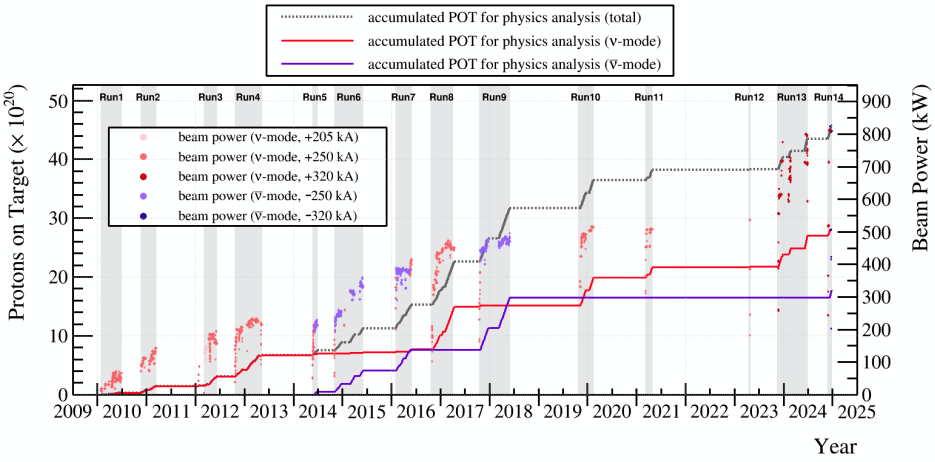

Figure 2.4: Accumulated POT by year for the J-PARC neutrino beam for use for physics analysis by T2K. Both neutrino and antineutrino modes, as well as different magnetic horn currents, are shown.

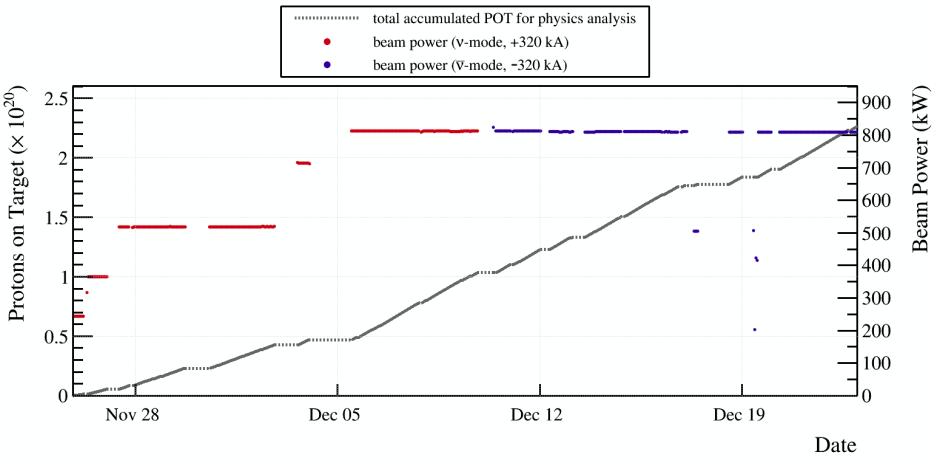

Figure 2.5: Accumulated POT for the J-PARC neutrino beam, November–December 2024, showing both neutrino and antineutrino modes. During this period, the beam power reached a record 810 kW.

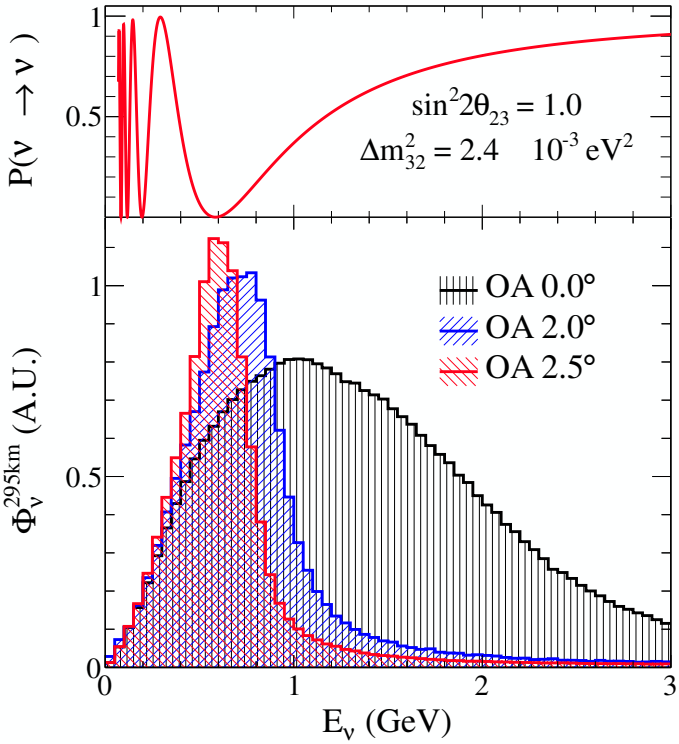

Figure 2.6: T2K flux at different OA angles. Shows neutrino oscillation probability as a function of baseline. Figure from Ref. [65].

2.2 INGRID

The INGRID detector, shown in Figure 2.7 from a head-on perspective, is located in the ND280 pit roughly 25 m below ground level and is the on-axis detector, meaning it is centred on the beam. At a distance of 280 m from the meson production target, the spatial width, 1 σ, of the neutrino beam is approximately 5 m. In order to span this width, INGRID is composed of 14 identical modules, shown in Figure 2.8, arranged in two transverse sections arranged in a cross spanning 10 m $\times$ 10 m [66]. Each module consists of 9 iron plates and 11 scintillator tracking planes and are surrounded by veto scintillator planes [32]. The iron plates are 124 cm $\times$ 124 cm in the transverse planes and 6.5 cm along the beam direction. This allows for the total iron target mass for neutrinos to be 7.1 tonnes per module and enables accurate measurements of neutrino interactions on iron with sufficient statistics. Each scintillator tracking plane consists of 48 scintillator bars (24 in each transverse direction, arranged perpendicularly) which have a wavelength shifting fibre (WLS) running through it. The WLSs are mirrored on one end, and the other end is read out by a Multi-Pixel Photon Counter (MPPC) [67, 68]. There are also two separate modules placed at opposite off-axis positions along the main cross; this allows measurements of beam asymmetry [32]. The INGRID detector is used to provide measurements for beam position, stability monitoring and neutrino event rate. INGRID has measured the neutrino event rate to within 1.7% of the expected rate and the beam direction with respect to the expected direction to better than 0.1 mrad in the y-direction and 0.01 mrad in the x-direction [66].

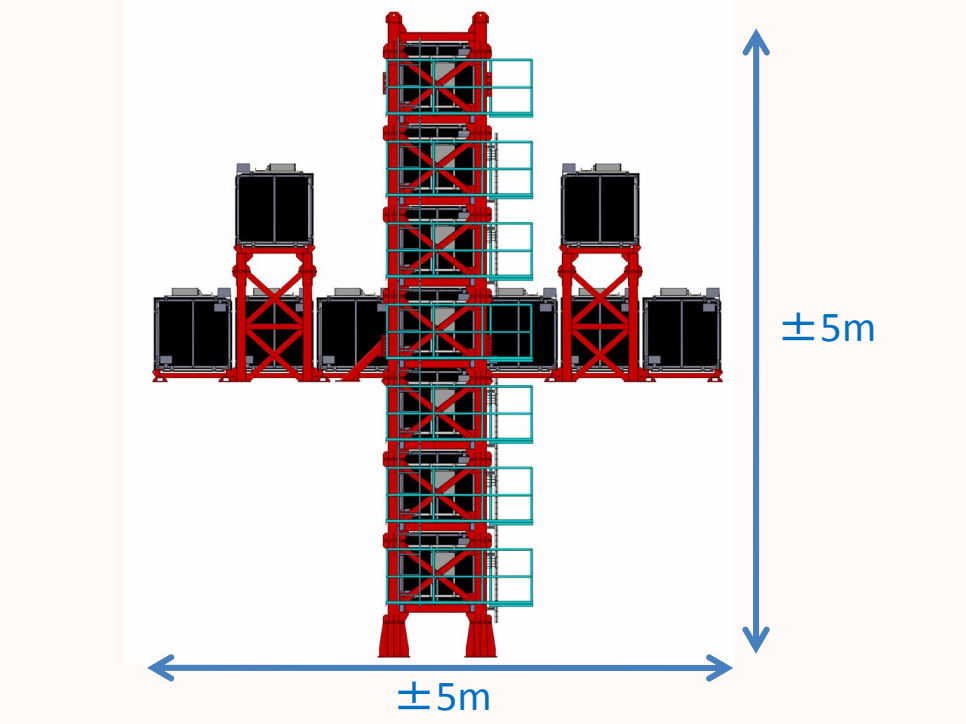

Figure 2.7: The on-axis INGRID detector from the point of view of the neutrino beam. It spans 10 m vertically and 10 m horizontally to span the width of the beam which is roughly 5 m in the ND280 pit. The centre of the two modules rows is the beam center. Two modules are offset from the main cross and are used to measure beam asymmetry. Figure taken from Ref. [66].

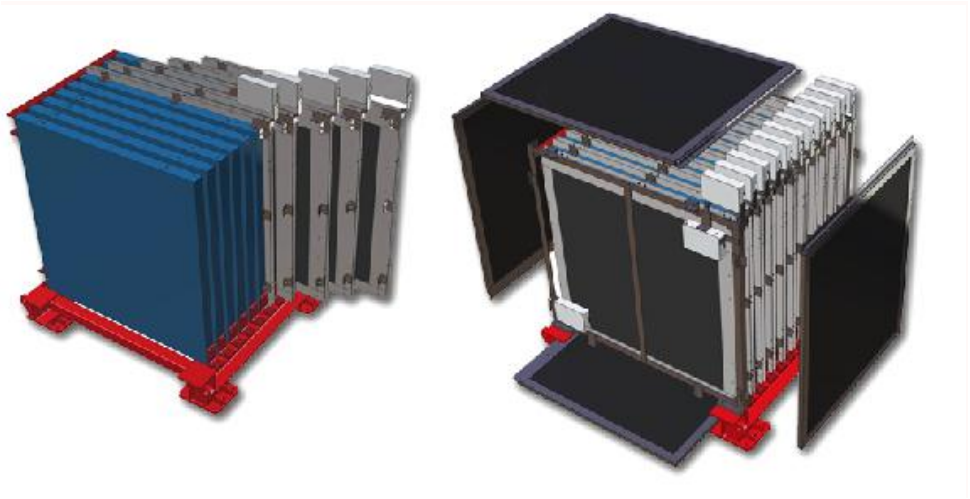

Figure 2.8: A close-up view of the INGRID modules. Each module consists of 11 scintillator tracking planes and 9 iron plates between them. There are also veto planes (shown as the black planes on the right) on each face to veto events where particles come from outside an expected beam event. Figure from Ref. [66].

2.3 ND280

ND280 is the off-axis detector and contains multiple sub-detectors that are each used for specific purposes; each sub-detector is explained in Section 2.3.1 . It has dimensions 6.5 m $\times$ 2.6 m $\times$ 2.5 m. The general purpose of ND280 is to: measure the ν_μ and ν_e fluxes before oscillation occurs; their respective energy spectrum through quasi-elastic and charged current interactions, and measure the π^0 production as this provides an estimate of the background from such processes at SK and constrains systematic uncertainties [69]. Additionally, ND280 is used to calculate a range of neutrino-nucleus interaction cross sections. In 2018 [70], an upgrade to ND280 was proposed for the T2K experiment. Before the upgrade, ND280 could constrain systematic errors up to the order of 6%, while after the upgrade it is projected to be reduced to around 4% [71]. The ND280 upgrade detector configuration is explained in Section 2.5. The pre- and post-upgrade ND280 are shown in Figure 2.9 and Figure 2.10.

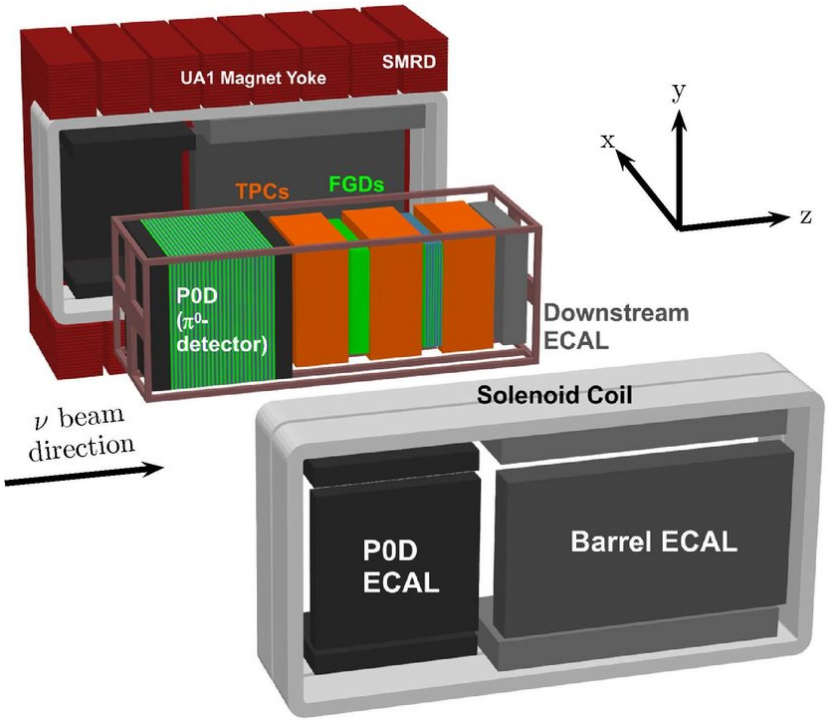

Figure 2.9: Schematic diagram of ND280 before the upgrade [32]. ND280 contained a π^0-detector (PØD), two fine-grain detectors (FGDs), three time projection chambers (TPCs), a barrel, PØD, downstream and upstream electromagnetic calorimeter (ECal), a side range muon detector (SMRD) all enclosed in a magnetic yoke from the UA1 experiment.

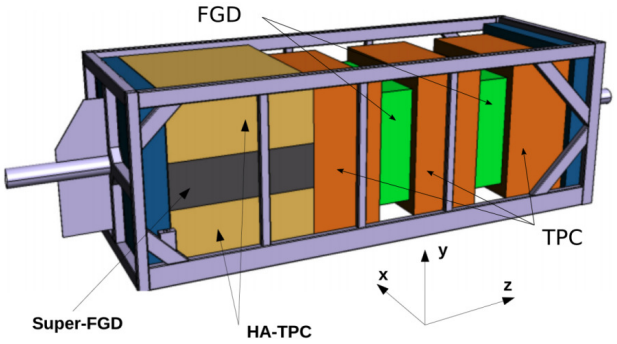

Figure 2.10: Schematic diagram of the proposed ND280 upgrade. The upgrade is comprised of a super fine-grain detector (SFGD), two high-angle TPCs (HA-TPCs) and 6 time-of-flight (TOF) planes in place of the PØD. The SFGD is installed upstream of the TPCs and FGDs. Above and below the SFGD will be the two HA-TPCs. The TOF planes, not shown here, but will encompass the SFGD and HA-TPCs [71].

2.3.1 ND280 pre-upgrade detector configuration

ND280 pre-upgrade contained central tracking detectors, namely two fine-grain detectors (FGDs) and three time projection chambers (TPCs) which are placed between the FGDs. This is called the "inner tracker". Upstream of the inner tracker is the π^0-detector, the PØD, and an upstream electromagnetic calorimeter (ECal) which was historically part of the PØD. Downstream of the inner tracker is a downstream ECal. All of this is enclosed by a barrel ECal, which encloses the inner tracker, and a PØD-ECal, which encloses the PØD. Around all of this is a magnetic yoke with a side muon range detector (SMRD) interleaves between the magnetic yoke fingers [32]. The magnetic yoke surrounding the detector is from the UA1 experiment and provides a 0.2 T field used for the identification of the particles. Each sub-detector is described below.

PØD

A main background at SK is the neutrino-induced production of π^0 mesons. π^0 mesons decay through $\pi^0 \to \gamma\gamma$ 98.82% of the time [9]. The photons produced in this decay can initiate electromagnetic showers and mimic an electron signal from an electron neutrino. Therefore, π^0 production is a background in the $\nu_\mu \to \nu_e$ appearance signal. The PØD [72], shown in Figure 2.11, is used to detect and characterise π^0 production processes via the NC process $\nu_\mu + N \to \nu_\mu + N + \pi^0 + X$ where N and X are nuclei. The PØD contains a water target which is fillable to provide a subtraction method for the π^0 production on water for SK background estimation. The PØD consists of four main sections, an upstream ECal, an upstream water target, a central water target, and a central ECal. The ECals are made up of seven planes of perpendicular triangular scintillator bars and 4.5 mm thick lead sheets interleaved between them. The upstream water target contains 13 modules of plastic scintillator-water bag-brass sheet planes. Figure 2.12 shows an expanded view of a plane. Each scintillator plane contains two perpendicular arrays of triangular scintillator bars. Per module, there are 134 vertical bars of length 2133 mm and 126 horizontal bars of length 2272 mm. The water bags are 28 mm thick and the brass sheets are 1.28 mm thick. The central water target is of the same design but contains 12 modules. The active target of the PØD is $2103 \times 2239 \times 2400$ mm^3 (width $\times$ height $\times$ length) and has a target mass of 15.8 T with water and 12.9 T without water. The scintillator bars have WLSs running through them with one end mirrored and the other end is connected to an MPPC for readout, similarly to INGRID [66, 68].

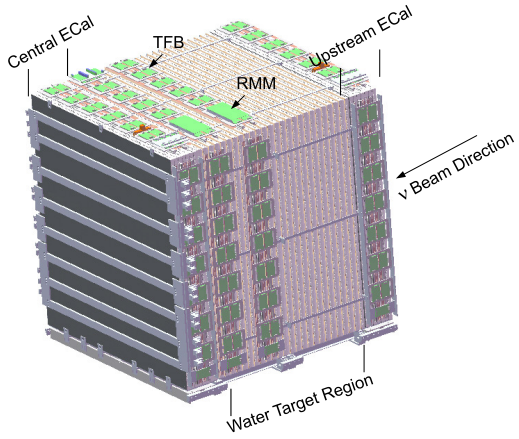

(a) Schematic diagram of the PØD. The downstream face is shown.

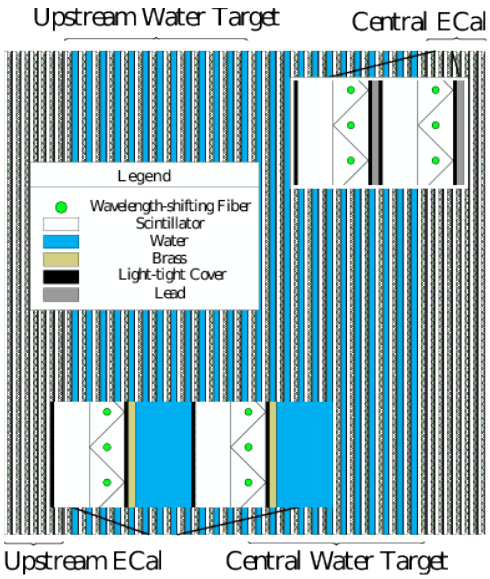

(b) A close-up view of the PØD showing the modules and four main sections: upstream ECal, upstream water target, central water target and central ECal. Also shown are the triangular scintillator plane.

Figure 2.11: Schematic diagrams of the PØD.

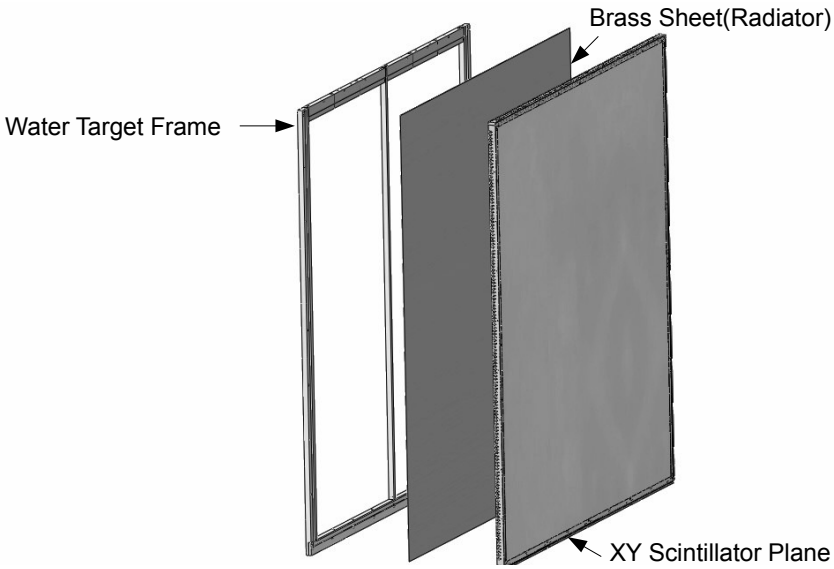

Figure 2.12: An expanded view of a PØD plane consisting of a water bag, a brass sheet and a scintillator plane.

ECal

The ND280 ECal is made up of three main sections: the PØD ECal, which encompasses the PØD and is adhered to the inner face of the magnet, the barrel ECal, which encompasses the inner tracker and is adhered to the inner face of the magnet, and the downstream ECal, which is the most downstream detector of the inner tracker [73]. The structure of the ECals can be seen in Figure 2.9. The ECals are polystyrene scintillator - lead sampling calorimeters. The purpose of the barrel and downstream ECals are to provide support in tagging and reconstructing π^0 mesons which leave the inner tracker. The PØD ECal is designed to distinguish between electromagnetic showers and muon tracks and so has a different design to the other two ECals.

The barrel ECal is composed of six modules, two vertical (side) and four horizontal modules (two top and two bottom). The horizontal modules are $4140 \times 462 \times 1676$ mm^3 (width $\times$ depth $\times$ length) and the vertical modules are $4140 \times 462 \times 2500$ mm^3. Each module is composed of 31 layers of rectangular polystyrene scintillator bars with a cross-sectional area of 40×10 mm^2 interleaved with 1.75 mm thick lead sheets. The plastic scintillator bars are arranged perpendicularly to adjacent bars to provide for 3D reconstruction. The electron radiation length (X_0) in lead is 5.6 mm [74] and so the barrel ECal provides roughly 9.7 X_0, enough to contain 50% of the energy of an electromagnetic shower. The top and bottom horizontal modules contain 38 bars parallel to the beam direction and 96 bars perpendicular to the beam direction. The side vertical modules have 57 bars parallel to the beam direction and 96 bars perpendicular to the beam direction. The scintillator bar length for the bars parallel to the beam direction is 3840 mm, while the bars perpendicular to the beam direction in the top and bottom horizontal modules are 1520 mm long and 2280 mm long in the vertical side modules.

The downstream ECal is a single module of dimension $2300 \times 500 \times 2300$ mm^3 and contains 34 layers of the same rectangular polystyrene scintillator interlaced with 1.75 mm thick lead sheets. This corresponds to roughly 10.6 X_0 for an electron. The scintillator bars are arranged in an x, y fashion such that adjacent bars are perpendicular while all being perpendicular to the beam direction. There are 50 scintillator bars per layer of length 2000 mm.

The PØD ECal composed of six modules similar to the barrel ECal. The two vertical (side) modules have dimensions $2898 \times 155 \times 2454$ mm^3 and the four top and bottom horizontal modules have dimensions $1584 \times 155 \times 2454$ mm^3. Each module is composed of 6 layers of scintillator bars interlaced with 4.0 mm thick lead sheets. This corresponds to 4.3 X_0. All scintillator bars are parallel to the beam direction and are 2340 mm long. Each layer contains 38 bars for the top and bottom horizontal modules and 69 bars in the side vertical modules.

All scintillator bars have a 2 mm hole with a WLS inserted through it that is connected to

an MPPC, much like INGRID and the PØD [67, 68]. The WLSs for the downstream ECal are read out on both ends. The barrel ECal is read out on both ends for scintillator bars that are parallel to the beam direction while bars perpendicular to the beam direction are read out on a single end. The bars in the PØD ECal are read out on a single end.

Magnet and SMRD

ND280 is enclosed by the UA1 dipole magnet which is operated at 3 kA and delivers a horizontal magnetic field of 0.2 T [75]. The magnet is divided into two halves. Each half has eight C-shaped return yokes and each return yoke consists of sixteen iron plates with 17 mm air gaps between them. Each iron plate is 48 mm thick. When closed, each pair of return yokes forms a ring around the ND280 detector and each ring is numbered one to eight from upstream to downstream. Figure 2.13 shows one return yoke of the ND280 magnet. The nominal outer dimensions of each return yoke is $6150 \times 2815 \times 876$ mm^3 (height $\times$ width $\times$ depth). Each yoke has a nominal enclosed dimension measuring $4040 \times 3600 \times 7568$ mm^3.

The SMRD is constructed by multiple layers of plastic scintillator which are placed in the air gaps between the magnet iron plates. The main purpose is to measure momenta of muons which escape the inner tracker at high angles. It also provides a trigger for cosmic rays passing through the detector. The data taken by the cosmic triggers are used for ND280 calibration purposes such as detector alignment. Cosmic samples can be taken with the magnet on and off, a configuration called "flat cosmics" which provides straight cosmic tracks which are more ideal for detector alignment studies.

The SMRD consists of 440 polystyrene scintillator modules (192 horizontal and 248 vertical) that are placed in air gaps of 1.7 cm between the steel plates of the magnet. The horizontal scintillator modules have dimensions $9 \times 686 \times 955$ mm^3 and the vertical modules have dimensions $9 \times 892 \times 955$ mm^3. Figure 2.14 shows the scintillation counters which makes up each SRMD scintillator module. Each horizontal module has four scintillation counters with dimensions $7 \times 167 \times 875$ mm^3 and each vertical module has five scintillation counters with dimensions $7 \times 175 \times 875$ mm^3. This gives a total of 768 horizontal and 1240 vertical scintillation counters. Each scintillation counter has a WLS running through it in an S-shape. The WLS is read out on both ends by an MPPC like other sub-detectors in ND280. Starting from the upstream end, there are three layers of SMRD modules in the first to the fifth magnetic yoke ring, four layers in the sixth ring and six layers in the seventh and eighth ring. The increased number of modules in the downstream section of the detectors helps with the tagging of more forward angle muons which will have increased momenta.

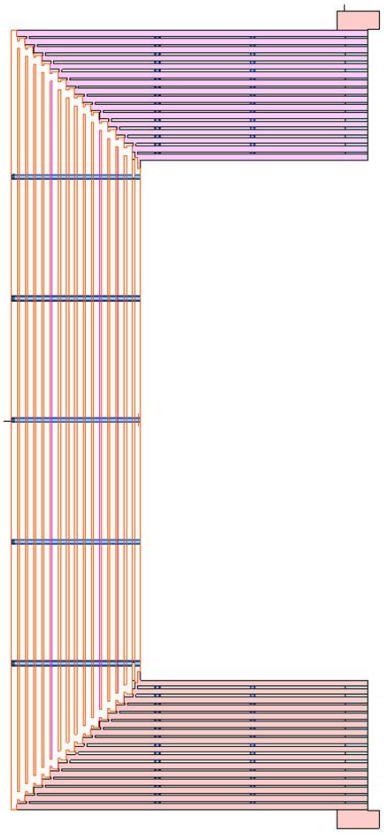

Figure 2.13: Schematic of one return yoke of the ND280 magnet. Each yoke consists of sixteen iron plates with air gaps between them. The SMRD is made of scintillator planes and is placed between each iron plate in the air gaps.

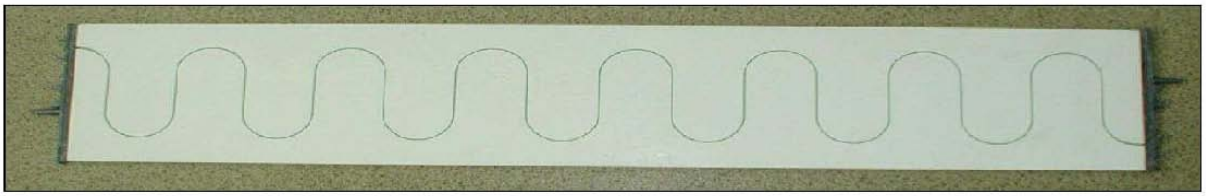

Figure 2.14: Picture of a scintillator counter that is used in the SMRD. It is made of polystyrene and has a WLS running through is in an S-shape. The WLS is connected to an MPPC on both ends.

FGD

ND280 has two FGDs that form part of the ND280 "inner tracker" [76] and can be seen in Figure 2.9. The FGDs are between the three TPCs to allow for tracks to be matched between the TPCs and FGDs. The two FGDs measure neutrino flux, particle energy spectra and also ν_e contamination in the beam. This contamination is important to constrain the

irreducible background rates at SK. Each FGD has dimensions $2300 \times 2400 \times 365$ mm^3 (width $\times$ height $\times$ depth) and has an active target mass of 1.1 T. The FGDs can also be used for particle identification for particles that stop entirely inside the FGD. In this case, low-momentum particles will deposit more energy per unit track length according to the Bethe-Bloch equation for particle "stopping power". The deposited energy can be summed and thus can be used to differentiate between protons, pions and minimal ionising particles (MIPs). Figure 2.15 shows how the deposited energy per unit track length for different particles can be used to differentiate between protons, muons and pions. Timing information is also used between the FGD and TPC matched tracks in order to differentiate between forward-going positive particles and backwards-going negative particles, as both particles would bend in the same direction in a magnetic field.

The most upstream FGD, called FGD1, is entirely polystyrene scintillator and is made up of 30 layers of scintillator bars arranged such that each adjacent bar is perpendicular (15 XY planes). Each XY plane has dimensions $1864 \times 1864 \times 202$ mm^3 and contains 192 horizontal and 192 vertical scintillator bars, each with dimensions $961 \times 1864 \times 961$ mm^3. Each scintillator bar has a hole in the centre with a WLS running through it, which is read out by an MPPC on one end. Each scintillator bar is chemically etched with TiO_2 in order to minimise bar-to-bar cross-talk (where light from one scintillator bar leaks into the adjacent bar. Each WLS is read out by a single photosensor and so there is no optical cross talk between the photosensors.

The second, downstream FGD, FGD2, is made up of alternating modules of scintillator planes and water targets. The water target provides interactions on water and is important for predicting event rate on water at SK. FGD2 is made of seven XY scintillator planes and six 254 mm thick water targets.

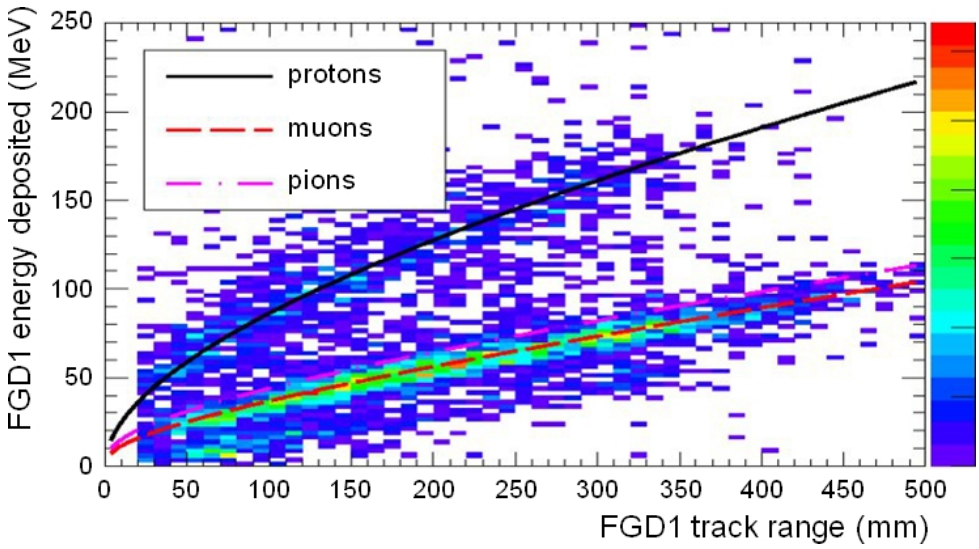

Figure 2.15: Different particles stopping entirely inside an FGD, in this case FGD1, deposit different amounts of energy per unit track length. This can be used to differentiate between protons, muons and pion.

TPC

ND280 contains three TPCs (numbered from upstream to downstream as TPC1, 2 and 3, which are placed between the two FGDs and provide the majority of the tracking, momentum measurement, PID and energy loss measurements [77, 32]. The three TPCs are identical and the design can be seen in Figure 2.16. Each TPC is made of an "inner box" and an "outer box". The inner box provides the electric field cage and the outer box provides the grounding and ground potential. Each field cage has outer dimensions $1808 \times 2230 \times 854$ mm^3 (width $\times$ height $\times$ depth). The inner dimensions has depth (along neutrino beam direction) of 772 mm with an active tracking region of 720 mm after the exclusion of 15 mm closest to the field cage walls where the electric field is not uniform. The outer box has dimensions $2302 \times 2400 \times 974$ mm^3.

The field cage is filled with a gas mixture of $^{40}\mathrm{Ar} : \mathrm{CF}_4 : \mathrm{iC}_4\mathrm{H}_{10}$ with a 95 : 3 : 2 percent proportion. This gas ionises when charged particle pass through it; the ionised electron drift with the electric field to bulk Micromegas readout planes. Each plane contains 12 bulk Micromegas tiles of dimensions 342×359 mm^2 and these amplify the charge. Each plane is made of 1728 rectangular 7.0×9.8 mm^2 (vertical $\times$ horizontal) pads which provide horizontal and vertical position tracking. The drift velocity is also used with the horizontal and vertical tracking to produce a full 3D readout. A max drift distance for each field cage is 897 mm. The electric field in each TPC is 275 V/cm. The electric field, as seen in Figure 2.16 is aligned with the magnetic field. Using the equations

$$\begin{aligned} \mathbf{F}_\mathrm{B} &= q\ (\mathbf{v} \times \mathbf{B}), \\ \mathbf{F}_\mathrm{E} &= q\mathbf{E}, \end{aligned} \tag{2.6}$$

$\mathbf{F}_{\mathrm{B}}$ is proportional to the velocity of the particle, $\mathbf{v}$. Therefore, particles passing through the TPC are subjected to a centripetal force given by $\mathbf{F}_{\mathrm{B}}$ and the direction of curvature can be found. For electrons ionised in the TPC, the force $\mathbf{F}_{\mathrm{E}}$ is dominant and is used to find the drift direction. The energy resolution for a MIP is 7.8 $\pm$ 0.2% meaning a mis-ID of an electron as a muon has a probability of $\approx 0.2\%$ for muons with less than 1 GeV/c momentum. Energy loss per unit track length can also be measured using the Bethe-Bloch formula like for the FGD. Figure 2.17 shows the deposited energy per unit track length as a function of particle momentum for positive and negatively charged particles. The simulation matches the data well and provides excellent separation for muons and protons.

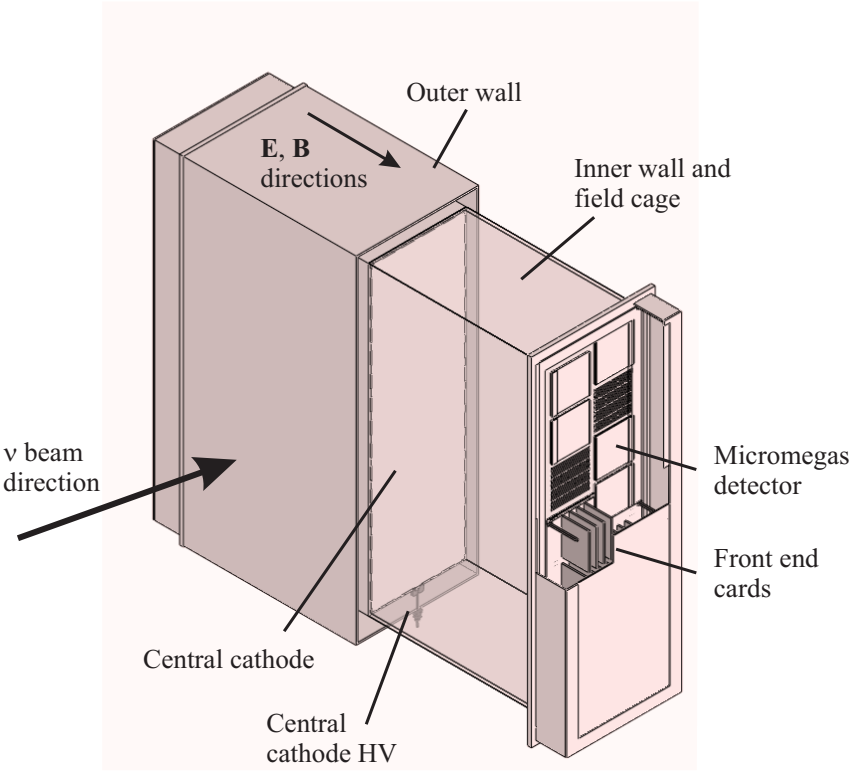

Figure 2.16: Design of the TPCs used in ND280. The electric field is aligned with the magnetic field in order to provide particle identification and momentum measurements. Each TPC is made of an inner box providing the field cage and an outer box which provides the ground potential. Each field cage uses a gas mixture of $^{40}\mathrm{Ar} : \mathrm{CF}_4 : \mathrm{C}_4\mathrm{H}_{10}$ with a 95 : 3 : 2 percent proportion. The electric field produced is 275 V/cm.

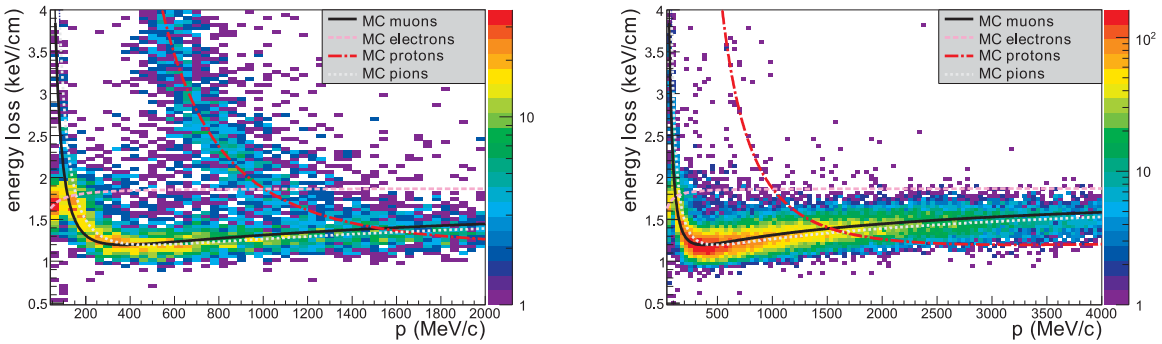

(a) Positively charged particle energy deposition (stopping power) curve. The simulation is shown as solid curves alongside the data.

(b) Negatively charged particle energy deposition (stopping power) curve. The simulation is shown as solid curves alongside the data.

Figure 2.17: Energy deposited per unit track length for (a) positively charged particles and (b) negatively charged particles.

2.3.2 Other near detectors

The T2K near detector complex also houses smaller detectors, which are placed below INGRID and ND280 and are 1.5° off axis. These detectors include the WAter-Grid-And-SCIntillator (WAGASCI) detector [78], the Magnetised Iron Neutrino Detector (Baby MIND) [79] and a liquid emulsion detector, NINJA [80]. The WAGASCI detector has two water modules and one scintillator module with muon range detectors (wall MRDs) on both sides parallel to the beam direction. The water module is designed as a 3D grid of scintillator bars with the space between being filled with water. The scintillator module is the "proton module" from INGRID [66], which uses slightly thinner scintillator bars than other INGRID modules in order to help with resolution. The wall MRDs are made of alternating iron and scintillator bars, similar to the SMRD in ND280. Downstream of WAGASCI is the Baby MIND detector which has 33 magnetised iron planes which are 30 mm thick and 18 scintillator planes. The Baby MIND magnet produces a 1.5 T field in order to help with particle identification and momentum measurements. The NINJA detector is placed between two WAGASCI modules.

2.4 Super Kamiokande

The Super-Kamiokande (SK) detector [81] is the far detector for the T2K experiment and is also an experiment by itself which has been running since 1996 producing results on proton decay [82] and atmospheric neutrino oscillations [83, 84]. SK, shown in Figure 2.18, is located roughly 1 km deep in a mine under Mt. Ikenoyama in Gifu, Japan. This is roughly 295 km west of J-PARC and sits 2.5° off-axis to the J-PARC neutrino beam, the same angle as ND280. The detector is a cylinder with a height of 41.2 m and a diameter of 38.8 m and contains 50 kT of ultra-pure water. The detector cylinder is split into an "inner detector" (ID) and an "outer detector" (OD) and can be seen in Figure 2.19. The ID has a height of 36.2 m and a diameter of 33.8 m which houses a fiducial volume of 25 kT of ultra-pure water. The ID is equipped with 11,146 inward-facing photomultiplier tubes (PMTs) each with a diameter of 0.5 m. This provides roughly 40% photo-coverage of the internal surface of the ID. The OD extends 2 m radially from the ID contains 1,885 outward-facing PMTs with a diameter of 0.2 m which acts as a veto for cosmic rays or other muons entering the detector which do not come from neutrino interactions. The OD has much less photo-coverage but is ample for acting as a veto with an efficiency of almost 100% [32]. The ID and OD are separated by a 0.5 m stainless steel cylinder which is covered in black sheets. The walls of the OD are also lined with Tyvek, a highly reflective material in order to further optically isolate the ID and OD.

SK detects neutrino interactions through the detection of Cherenkov light produced by particles inside the ultra-pure water. When charged particles pass through a medium, in this case, the ultra-pure water, the molecules in the medium can be ionised. These molecules then relax and emit photons. However, if the charged particle is moving faster than the speed of light in the medium, these wavefronts constructively interfere and a single coherent wavefront is produced at a fixed angle to the particle direction [85]. The refractive index of ultra-pure water is 1.33 and so light travels at around $0.75c$ with SK. The angle of the produced Cherenkov light is emitted at

$$\cos(\theta_c) = \frac{1}{n\beta}, \tag{2.7}$$

where $\beta = v/c$ and n is the refractive index of the medium. Cherenkov light produced by charged particles in SK produce characteristic rings of light which is detected by the PMTs. Since the T2K neutrino beam has an average peak energy of around 0.6 GeV, the main interaction channel is a CCQE interaction.

In a CCQE interaction, a neutrino interacts with a bound nucleon and the nucleon is subsequently ejected after it changes into its isospin doublet (proton to neutron and neutron to proton). A lepton is also produced with a flavour which matches the flavour of the initial neutrino. The speed of the lepton is often above this Cherenkov threshold of $0.75c$. The characteristics of the Cherenkov rings of muons and electrons are different since the electron mass is approximately 206 times lighter than the muon. As a result, the electron

undergoes many scattering events as it emits the Cherenkov light. This causes the cone of Cherenkov light to become "fuzzy" when detected by the PMTs. The muon however, scatters much less and produces a sharp ring of light on the ID inner wall. Figure 2.20 shows a muon and electron Cherenkov light ring as detected by the PMTs.

CCQE interactions are not the only interactions in SK. A neutral current (NC) reaction is a coherent reaction with a nucleus as a whole which can produce a π^0 . The π^0 decays to two photons which are back-to-back if the π^0 is stationary. Since it is not produced at rest, the photons are produced back-to-back in the boosted rest frame of the π^0 and so in the lab frame, these two photons are collinear. A photon produces a similar Cherenkov ring to an electron and so if two photon rings are detected in coincidence, then it is ruled as a π^0 decay. However, if the angle of the photons is such that the two rings overlap, then this can appear like an electron ring from an electron neutrino CCQE interaction producing a background in electron neutrino appearance searches.

In SK, the ejected nucleon cannot be directly observed since it is often emitted below the Cherenkov threshold. As a result, SK is unable to differentiate between neutrino and antineutrino interactions. In 2015, SK began being doped with a Gadolinium-based salt, $Gd_2(SO_4)_3 \cdot 8H_2O$, which enhanced neutron capture from antineutrino interactions. This neutron capture reaction produces γ rays which total to an energy of 8 MeV with a time constant of around 20 μs. This signal is distinguishable from electron rings due to the short time frame of the interaction. The original plan is to dope the ultra-pure water with the Gadolinium salt until it is 0.2% of the fiducial mass [31] and Ref. [86] quotes a 0.01% fiducial mass of Gadolinium salt.

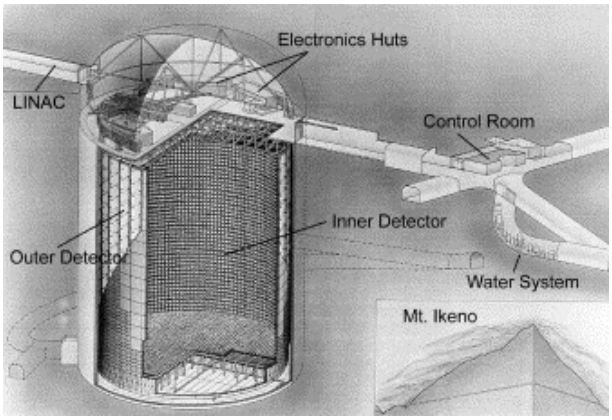

Figure 2.18: Schematic design of the SK detector in the Kamioka mine.

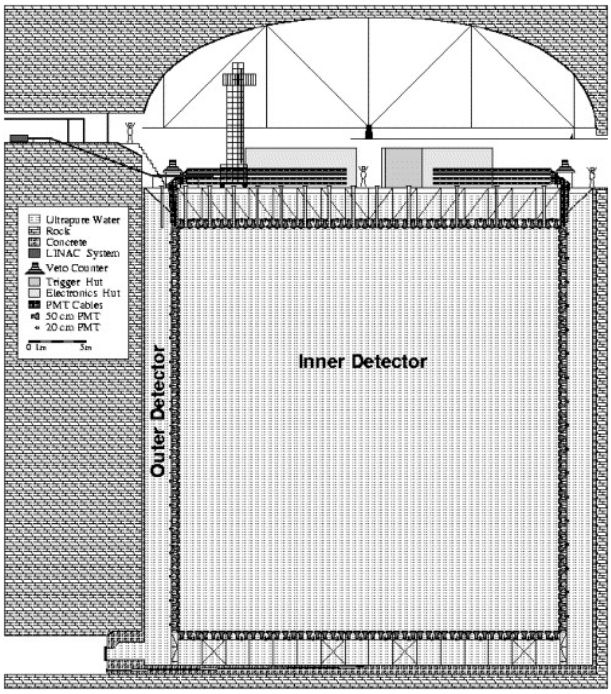

Figure 2.19: Schematic design of the SK detector showing the inner and outer detector volumes.

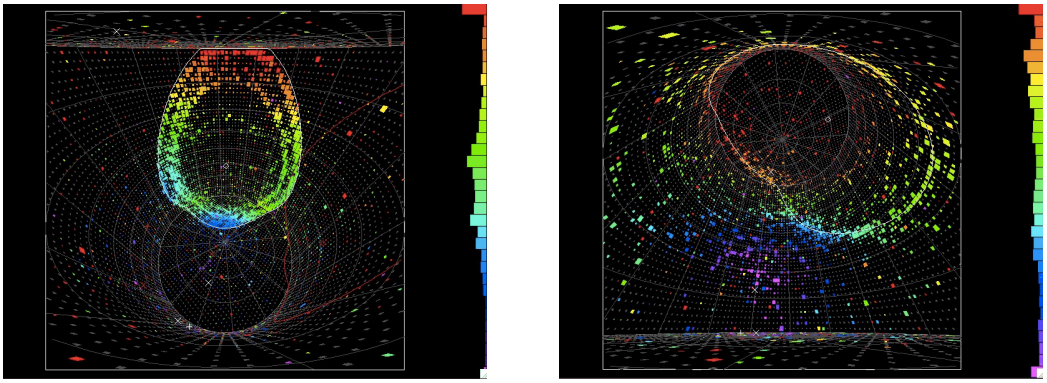

(a) Muon Cherenkov ring. (b) Electron Cherenkov ring.

Figure 2.20: Event display for (a) a muon neutrino CCQE event and (b) electron neutrino CCQE event.

2.5 The ND280 Upgrade

The ND280 upgrade, situated upstream of the tracking detectors, where the PØD was located. This new block contains three new sub-detectors: two high-angle TPCs (HA-TPC); a Super Fine-Grained Detector (SFGD); and six time-of-flight (TOF) planes to protect the HA-TPCs and SFGD [71]. The current installation schedule is to install and commission the SFGD by April 2023, while the HA-TPCs are expected to be delayed. This section briefly details the HA-TPC and TOF planes. The SFGD is explained in more detail in Chapter 3.

2.5.1 HA-TPC

The TPCs used in ND280 provide T2K with important measurements of particle charge, momentum and allow for particle identification when combining $\mathrm{d}E/\mathrm{d}x$ measurements. A requirement of T2K is to have the TPCs provide a momentum (or charge deposition) resolution of 10% at 1 GeV/c. This provides ND280 with enough e^-/μ^- separation to measure ν_e interactions and provide a constraint on the ν_e background at SK [71]. This momentum resolution translates to a spatial resolution of roughly 800 μm using a magnetic field of 0.2 T.

As shown in Figure 2.10, in ND280, the original TPCs, are positioned, along with the FGDs, to detect mostly forward-going particles. The HA-TPCs are placed above and below the SFGD and are designed to track particles that leave the SFGD at high angles.

There are two HA-TPCs, each of dimension $2000\times820\times1800$ mm^3 (width×depth×height). A schematic of a HA-TPC is shown in Figure 2.21. Each HA-TPC has two major design differences compared to the original TPCs [71].

- The readout planes make use of the "resistive bulk" Micromegas pads.
- The field cage is made with a solid layer of insulator which is laminated on a composite material minimising the dead space in the detector and maximising the tracking volume.

Each HA-TPC is made in a similar fashion to the original TPCs; an inner drift volume and outer field cage to provide the ground potential. The inner drift volume is separated into two halves by a cathode plane. Each half is readout by eight ERAM modules, each with 1152 pads. Figure 2.22 shows a cross section of an ERAM module (right) in comparison to the original "bulk Micromegas" design of the original TPCs (left). In the original design, there is nothing in the amplification gap between the mesh and the pads and so each hit is read out on one pad, limiting the spatial resolution. In the ERAM modules, there is a layer of resistive foil and an insulator between the pads and the mesh. The resistive layer now forms a 2D resistor-capacitor network which causes the

charge avalanche (which quenches quite quickly in the resistive layer) to be induced in the insulator layer and spread out over multiple pads. This improves spatial resolution and allows for the HA-TPCs to use fewer pads than the original TPCs. The quenching of the charge avalanche in the resistive foil also reduces the discharges (sparks) of the Micromegas modules and so protective diodes are no longer necessary in the circuitry, further reducing dead space and maximising tracking volume. Each HA-TPC uses the same gas mixture as the original TPCs and has an electric field strength of 275 Vm^{-1}.

A test of the ERAM modules at CERN in 2020 exposed the ERAM modules and a prototype of the HA-TPC to a charged particle beam. The results reported a spatial resolution of around 300 μm with a deposited energy resolution of between 9% and 11.2% [87]. Another beam test at DESY in 2021 exposed a prototype to an electron beam. The results showed a deposited energy resolution of 8.5% for horizontal tracks and between 7.5% and 9.6% for vertical or inclined tracks [88]. These results are all within the required resolution of 10%, with the higher resolution result from the CERN test coming from pions [87].

The bottom HA-TPC was installed in the ND280 detector on 8$^{\mathrm{th}}$ September 2023. The top HA-TPC was then installed in ND280 in early 2024.

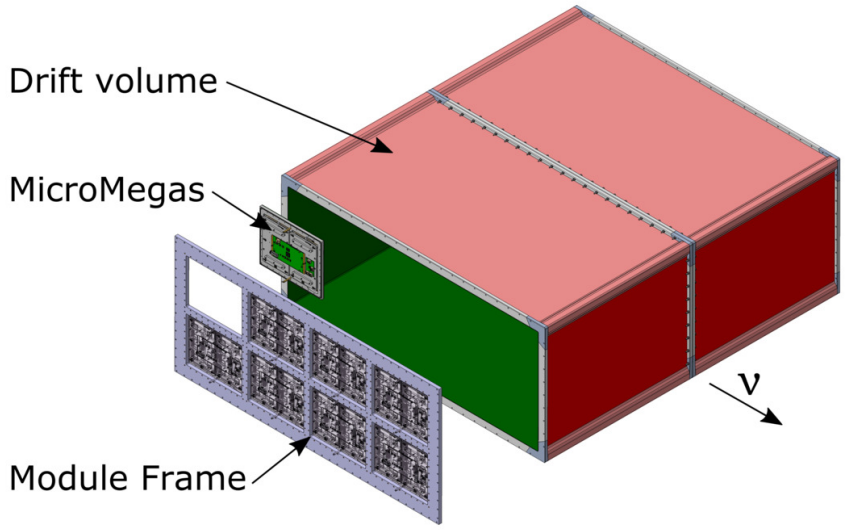

Figure 2.21: Schematic diagram of the HA-TPC showing eight ERAM modules on each side of the HA-TPC. Each side is divided by the cathode plane. Figure from Ref. [71].

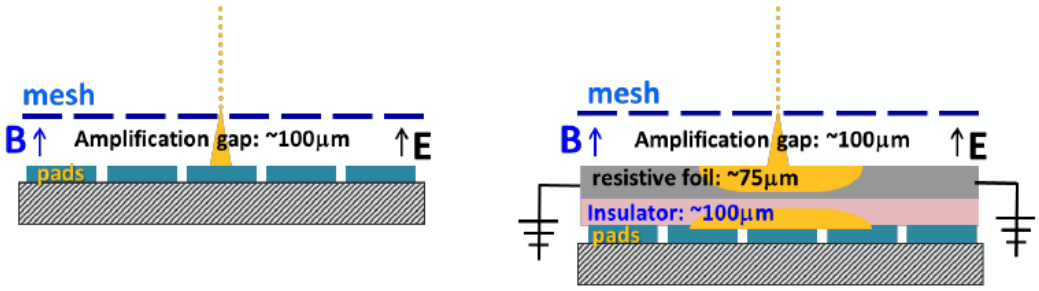

Figure 2.22: Schematic diagram of the (*right*) Encapsulated Resistive Anode Micromegas (ERAM). There is a layer of insulator between the pads and the mesh which forms a 2D RC circuit. This induces charge on neighbouring pads essentially spreading the charge across adjacent pads. Original "bulk Micromegas" design (*left*) uses a single pad for a drift charge, limiting spatial resolution. Figure from Ref. [71].

2.5.2 TOF planes

The TOF detector, composed of six TOF planes arranged to encapsulate the SFGD and HA-TPCs as shown in Figure 2.23, is designed so that the timing information of charged particles can be measured with high resolution [71]. In order to unambiguously determine the flight direction of charged particles, a timing resolution better than 500 ps is required [71]. However, in order to differentiate between muons and electrons at energies of $100 - 300$ MeV and protons and positrons at energies $1 - 2$ GeV, where $\mathrm{d}E/\mathrm{d}x$ measurements alone do not work, a time resolution of $100 - 200$ ps is required for particle identification. The design concept of the TOF detector is to use 10 mm cast plastic scintillator bars which are optimised for timing resolution. The design target time resolution was 150 ps across the complete 4π angular coverage. Due to the cage design of the TOF, it is also ideal for providing a cosmic trigger to the whole ND280 upgrade.

Each TOF plane is composed of 20 cast plastic scintillator bars. The bars each have a length of 120 cm with a width of 12 cm. This provides an active area of 120×240 cm^2. At each end of the scintillator bars is an array of eight silicon photomultiplier (SiPM) pixels which are arranged in pairs as shown in Figure 2.26. Each array of SiPMs is read as a single SiPM as the signal is summed before the final readout. Each SiPM has an active area of 6×6 mm^2, matching well with the 10 mm width of the scintillator bars in order to improve photodetection efficiency. The scintillator bars are EJ-200 from Eljen Technology [89]. This material is a general-purpose scintillator material which has a long attenuation length and fast timing properties. The model attenuation length is 380 cm, which is much longer than the bar lengths used in the TOF meaning the light is hardly attenuated before it is read out [89]. The peak wavelength emission is at 425 nm, which peaks in the violet region but has a component which extends to green wavelengths, a region with lower light attenuation and increased SiPM photodetection efficiency.

There are two main types of scintillator design: extruded plastic with WLS running through them, or cast scintillator with direct light readout. ND280 predominantly uses the former; however, the introduction of WLS introduces additional effects and uncertainties which can affect the timing resolution. For example, the amount of light collected depends on the trapping angle of the WLS itself and re-emission of the light within the WLS would broaden the time resolution [90]. Cast plastic scintillator with direct light readout can achieve better resolution with fewer scintillator bars, which means less space used inside the limited ND280 detector volume restricted by the magnet. The cast scintillator has less light loss due to multiple internal reflections and lower attenuation effects, providing up to an order of magnitude more photons detected [90].

A test using cosmic rays was conducted at CERN in 2021 [90] reported a time resolution for each end of the readout and for the weighted average of the two readout ends. The results, shown in Figure 2.25 show that the average time resolution across a whole scintillator bar is less than 140 ps, much less than the required resolution and a slight improvement on the design target.

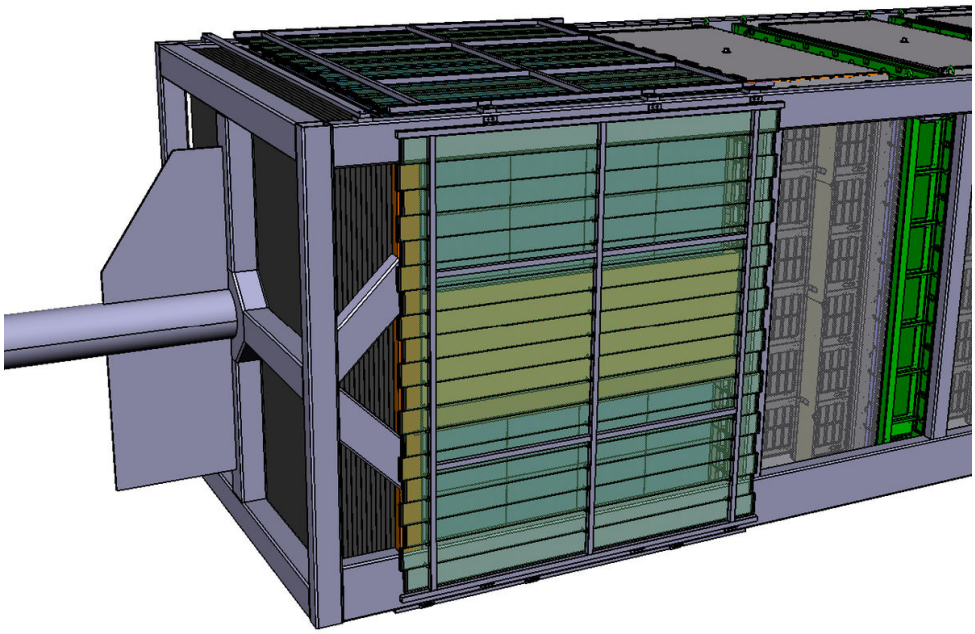

Figure 2.23: Schematic design of the TOF surrounding the SFGD and HA-TPCs. The TOF bars are staggered design due to frame holding SiPMs; this eliminates dead space and gaps. Figure from Ref. [71].

Figure 2.24: The TOF planes at CERN for testing with cosmic rays. Figure from Ref. [90].

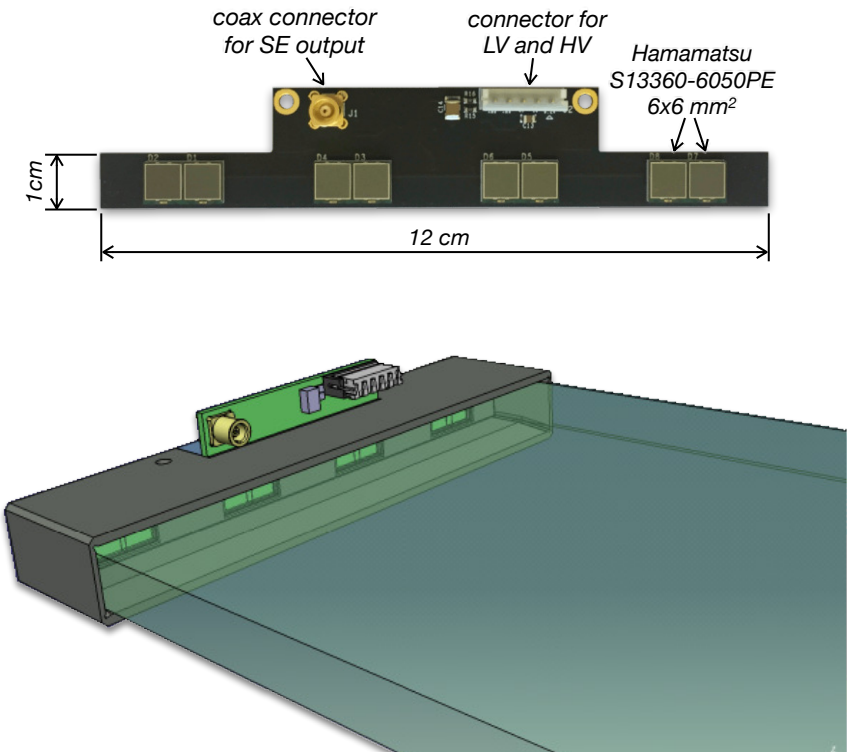

Figure 2.25: Schematic design of the SiPM connection for the end of the TOF bars. Figure from Ref. [90].

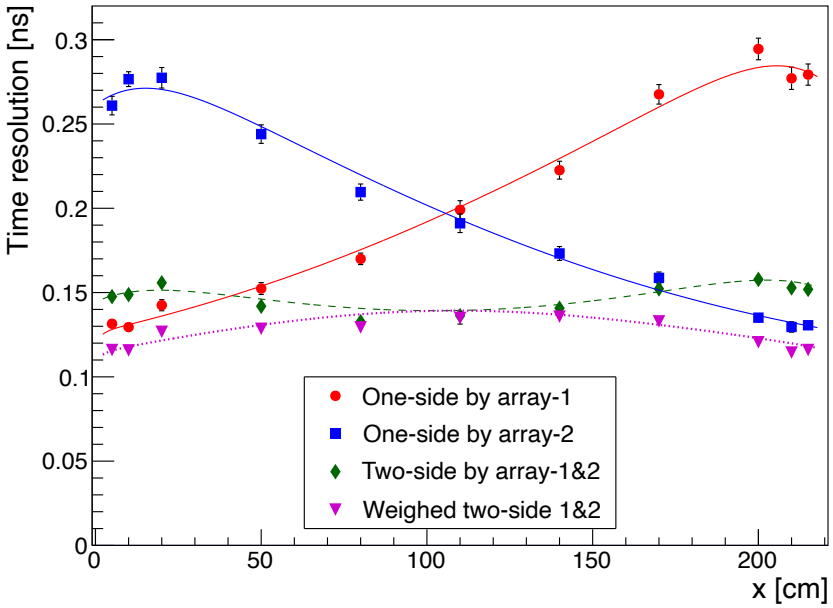

Figure 2.26: The time resolution across a single TOF bar. The reported time resolution was less than 140 ps. Figure from Ref. [90].

Chapter 3

The SFGD detector construction

This chapter describes the motivation for and the design of the SFGD. The steps performed during the assembly of the detector are then described. Finally, the SFGD prototypes and results are explained.

3.1 The motivation for the SFGD

The design of the SFGD was to improve the angular acceptance of particles that are created with a large transverse angle to the beamline and also to improve the acceptance of tracks going backward. The highly segmented design of the SFGD allows for improved spatial resolution as well as the ability to identify short tracks of low-energy hadrons that are created around the event vertex. Another benefit of the segmented design is the solution to a problem that is faced by the FGD. That is, particle tracks can no longer travel along a scintillating bar and so the track acceptance is increased. The improvements made possible by the SFGD will improve errors on the flux and cross-section measurements that are then used later in oscillation analysis as systematic error constraints and ND fits. Nuclear final-state interactions will also be able to be measured more accurately as a result of improved spatial resolution and reduced momentum threshold for tracks; leading to a reduction in the systematic error for nuclear models used in oscillation analysis [91]. The proton reconstruction and angular acceptance improvement can be clearly seen in Figure 3.1 which shows the reconstruction efficiency for muons and protons.

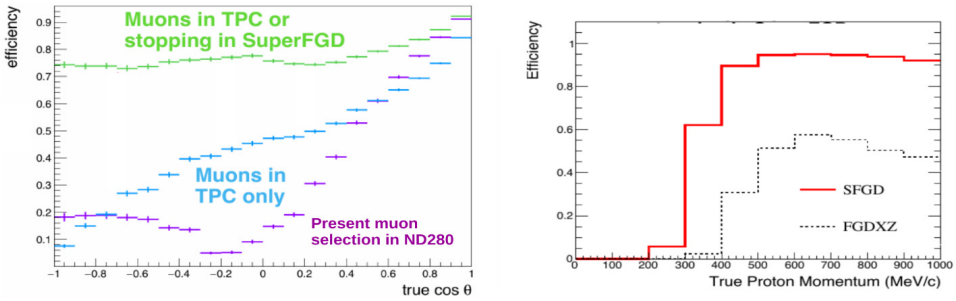

Figure 3.1: Monte Carlo Muon and proton reconstruction efficiency using the SFGD. (Left): muon reconstruction efficiency plotted against the cosine of the angle transverse to the beamline with $\cos\theta = 1$ being along the beamline. (Right): proton reconstruction efficiency plotted against true proton momentum. Also shown in the FGD comparison [92].

3.2 SFGD design overview

The SFGD is made up of almost two million $1 \times 1 \times 1\text{cm}^3$ cubes made from polystyrene scintillator. Each cube has a hole drilled in all three orthogonal directions with a WLS running through it. Thus, each SFGD cube is read out in all three dimensions, leading to a quasi-3D readout. The active volume has dimensions $192 \times 184 \times 56$ cm^3. The SFGD is read out on a single end of the WLS using MPPCs. On the opposite end of each WLS is an LED light injector system that is used to calibrate the MPPCs. This chapter explains, in detail, the assembly of the SFGD and the work which I contributed to during the assembly process. My contributions came after the SFGD cubes were already assembled in the SFGD box.

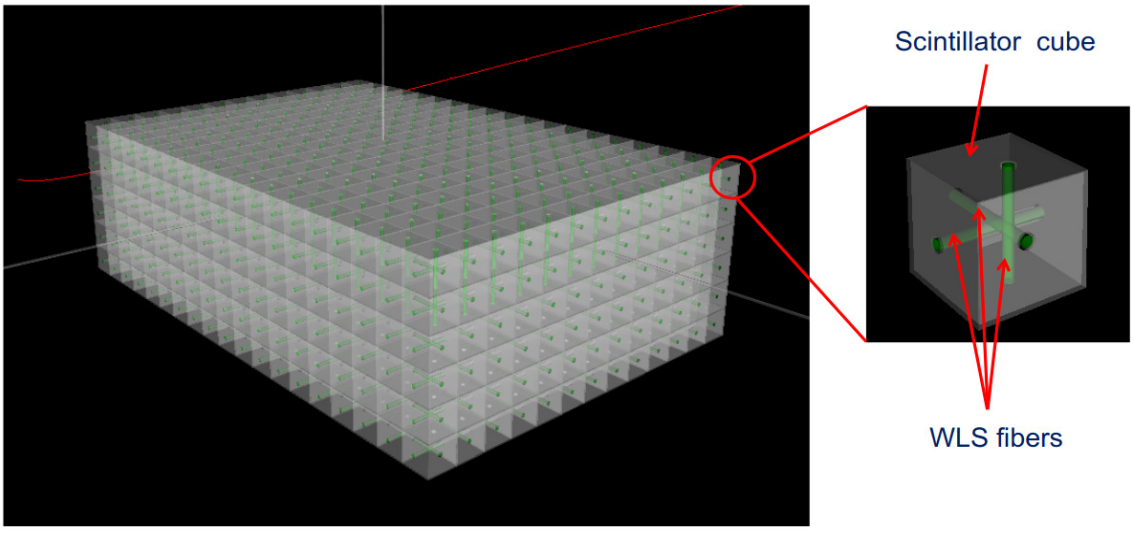

Figure 3.2: Schematic diagram of the SFGD showing isolated cubes and the WLS fibers that run through the three orthogonal axes of the cubes. Figure from Ref. [71].

3.3 SFGD cube assembly

The SFGD contains $1,978,368$ cubes made from extruded plastic scintillator each of dimensions $1 \times 1 \times 1\text{cm}^3$ [93, 71]. The cubes were made by UNIPLAST Co. in Russia by injection molding. Each cube is made of polystyrene doped with 1.5% of paraterphenyl (PTP) and 0.01% of POPOP [93, 71]. The cubes were chemically etched leaving a white polystyrene micropore deposit on the outer faces of the cubes with a thickness of $50 - 80$ μm. This etched layer was used to optically isolate each cube and avoid light leakage into adjacent cubes. There is a 1.5 mm diameter hole that is drilled through each face for a 1 mm WLS to be inserted through.

The cubes were prepared in 56 layers of 192×184 cubes. Each of these layers had fishing wire of diameter 1.3 mm through each hole in the plane. This was to ensure that the cube positions did not move too much while assembling the 56 layers together. All 56 layers were prepared in Russia and shipped to J-PARC in November 2022. The SFGD box was also shipped with the cubes. The layers were assembled within the box and once all layers were connected, metal welding rods were inserted through the 56 layers to reduce any skew of the cube layers. The SFGD box, which has holes in the sides to accommodate for the WLS fibres, was then completed around the 56 layers, ensuring that all fishing wires and welding rods were leaving the SFGD box holes. The SFGD box is described in more detail in Section 3.4.

3.4 Fibre insertion

The SFGD WLS are the Kuraray Y-11(200) fibres [94] which have a peak absorption at 430 nm and a peak emission at 476 nm, matching the emission from the SFGD scintillator. The general characteristics of this fibre is the long attenuation length and high light yield. The connector was glued to the end such that it could fit into the holes in the SFGD box and be flush to the MPPCs. The SFGD box holes are separated into blocks of 8×8 since each printed circuit board (PCB) contains an 8×8 grid of MPPCs.

Fibres were produced with two different lengths, one for the longer sides of the SFGD and one for the shorter side. The WLS insertion procedure was to begin with the sides. The fishing lines were taken out one by one in a checkerboard pattern in one 8×8 block at a time; this was to minimise cube movement within the SFGD which would make fibre insertion difficult and risk damaging the fibres outer coating. Before removing the fishing lines, a small pad of foam with the same 8×8 grid design was placed over the fishing lines and this created a buffer between the MPPC connector and the SFGD box. One fishing line was then removed and the corresponding WLS was inserted such that the end with the MPPC connector would then fit into the box hole. Figure 3.3 shows the small pad of foam placed over the fishing wires on the 8×8 block. Figure 3.4 shows the checkerboard pattern in which the fishing lines were removed and the WLSs were installed. Figure 3.5

shows a full installation for the 8×8 grids. The side the SFGD PCB is on switches partway down the SFGD with the first 12 being read out by the left-hand side and the other 11 being read out from the left (going upstream to downstream).

The vertical fibres are smaller and a similar procedure was followed but this time each welding rod was removed. The welding rods were originally inserted sporadically and the fibres were inserted in an 8×8 block where there were openings and then the welding rods were removed for the remaining fibres to be inserted. Figure 3.6 shows the foam over the welding roads which were inserted non-uniformly.

Each fibre, once inserted, was cut at the end without the MPPC connector such that 5 cm of the fibre exited the SFGD box. The fibres were hand-cut using nippers with a flat edge when closed. These cut fibres were then connected to a quality control (QC) test LED system which flashed all fibres directly. A corresponding QC MPPC PCB was placed on the other side of the fibres being flashed. This was to done for all fibres to detect if any fibres were broken or damaged during the insertion process. Figure 3.7 shows a QC test being conducted and a particular section of fibres being flashed with blue LEDs.

Once all fibres were QC tested, they were then hand-cut flush to the SFGD box ready for the LED calibration system to be installed. Figure 3.8 shows the WLSs after they were hand-cut flush to the SFGD box.

Figure 3.3: Fishing lines used to keep the SFGD cubes in place before wavelength shifting fibres were installed. A custom foam square was placed over all 64 fishing lines. This foam provided padding for the MPPC connector at the end of the wavelength shifting fibre.

Figure 3.4: Fishing lines holding the SFGD cubes in place were removed one at a time in a checkerboard pattern when inserting wavelength shifting fibres. The MPPC connector end of the fibres are shown sitting on the foam padding.

Figure 3.5: Fully installed horiztonal wavelength shifting fibres on the SFGD.

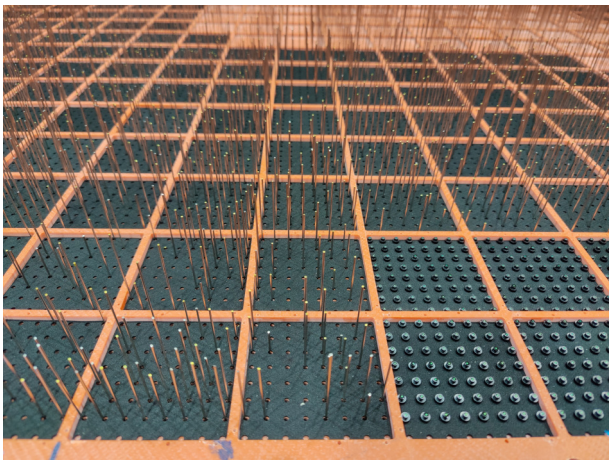

Figure 3.6: Metal welding rods were used to keep the SFGD cubes in place for vertical fibres. The welding rods were not inserting into every hole. The same foam padding was placed on top before any welding rods were removed and wavelength shifting fibres installed.

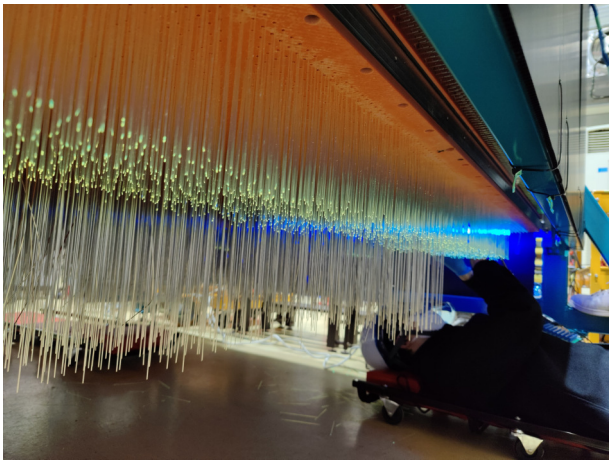

Figure 3.7: Vertical wavelength shifting fibres leaving the SFGD box. These fibres were cut to a length of 5 cm for a quality control test. This tested if any fibres were damaged during insertion. The right side of the image shows this test being performed with a blue LED array.

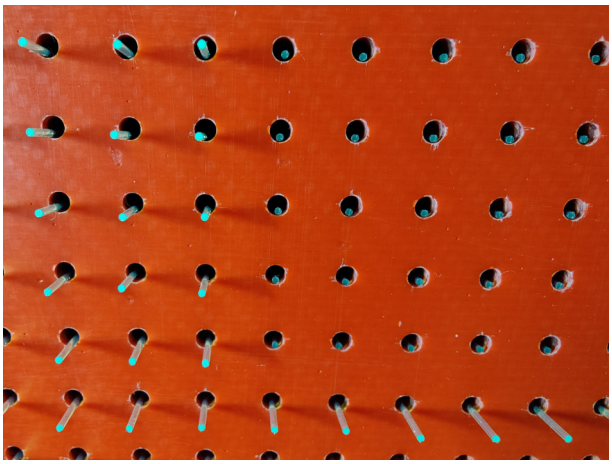

Figure 3.8: Horizontal wavelength shifting fibres cut flush to the SFGD box alongside fibres that have yet to be cut.

3.5 MPPC and PCB installation

The MPPCs used for the SFGD is the Hamamatsu S13360−1325PE [95] and is shown in Figure 3.9. These MPPCs have an active area of 1.3×1.3 mm^2 which matches the diameter of the WLSs. The pixel pitch is 25 μm which means per MPPC there are 2668 pixels. The MPPCs used have an order of magnitude lower dark noise rate (the rate that an MPPC undergoes an avalanche event without an actual signal event) and cross-talk probability than the MPPCs used in the original ND280 detectors. The gain of the MPPCs is given as 7×10^5 with a breakdown voltage of $V_{\text{br}} = 53 \pm 5$ V. The peak sensitivity

wavelength is 450 nm which matches the WLS peak emission well. There are a total of 55,888 MPPCs (channels) which are read out.

The MPPCs are arranged on PCBs which each have an 8×8 grid of MPPCs. The spacing between each MPPC is 10.3 mm and the PCB has an area of 83.8×83.8 mm^2. Each PCB has two bias voltage inputs, each for 32 MPPCs. The PCBs used is shown in Figure 3.10.

Once all fibres were QC tested, the MPPC PCBs were installed onto the SFGD box and screwed in place using two small screws. Figure 3.11 shows the first stages of the PCB installation. Figure 3.12 shows the top of the SFGD after the PCBs were fully installed. There are a total of 881 PCBs installed on the SFGD [96].

After the PCBs were installed, sheets of Viton were prepared with holes for the PCB connectors. These sheets were layed over the SFGD and held in place with RTV rubber glue. The Viton sheets act as a light barrier so any light that managed to get out of the box or LED injection system does not leave the SFGD. Figure 3.13 shows the light barrier placed over the downstream side of the SFGD.

The cabling procedure was performed so that there were no instances of cable directions clashing. To do this, there were two types of PCB in which the cable connector was placed in opposite directions. The ribbon cables used in the SFGD are shown in Figure 3.14.

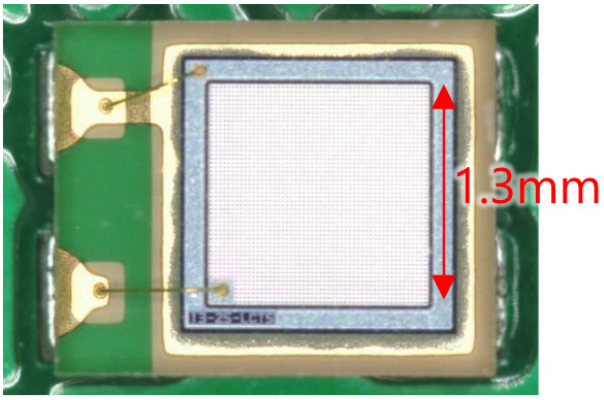

Figure 3.9: Hamamatsu S13360−1325PE MPPCs used on the SFGD. The active area is 1.3×1.3 mm^2. Figure from Ref. [59].

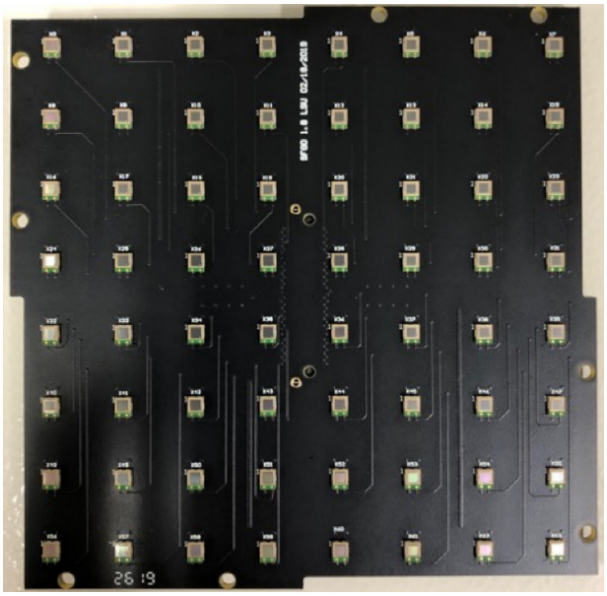

Figure 3.10: The SFGD MPPCs are arranged on an 8×8 grid on a PCB of area 83.8×83.8 mm^2.

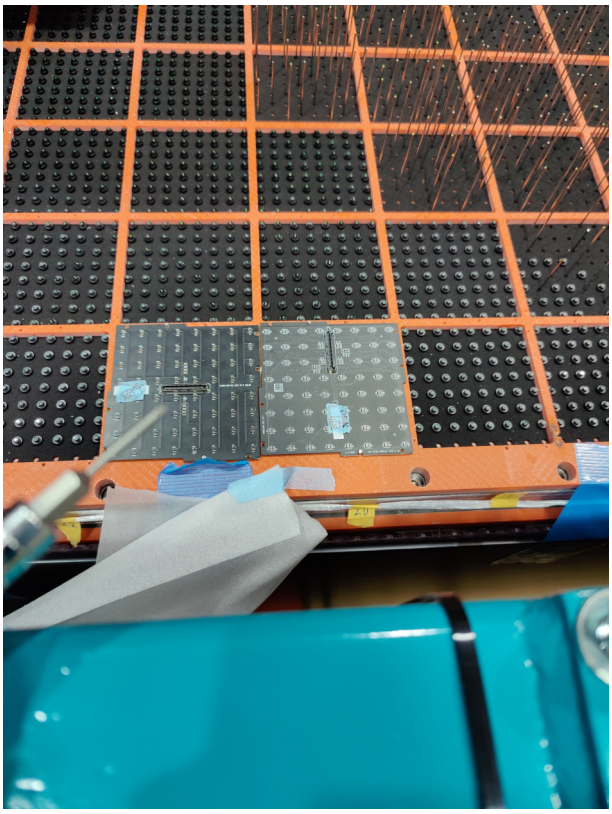

Figure 3.11: The PCBs were installed on the SFGD in specific orientations to ensure a clean cabling procedure. The PCBs are held in place with two small screws.

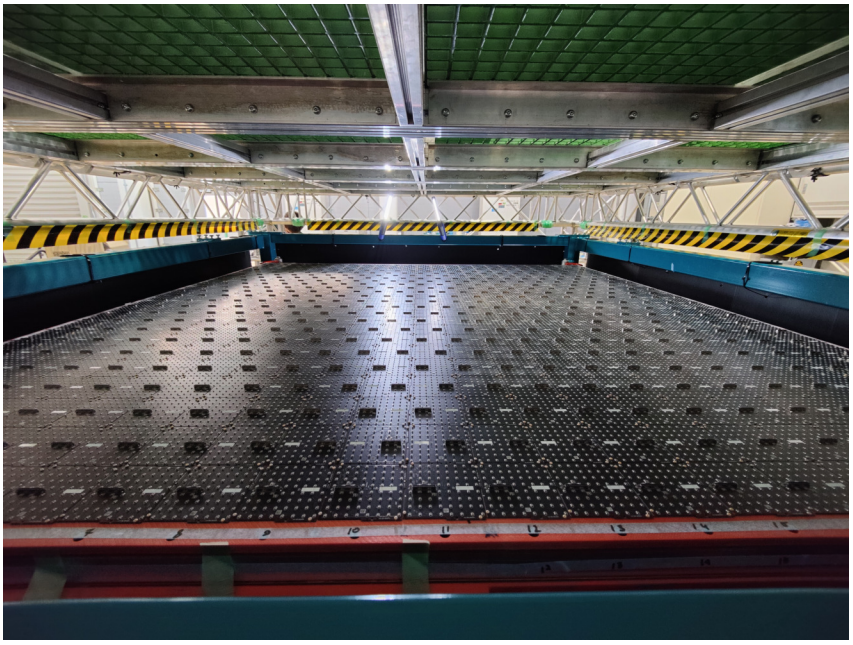

Figure 3.12: The top face of the SFGD after all PCBs were installed.

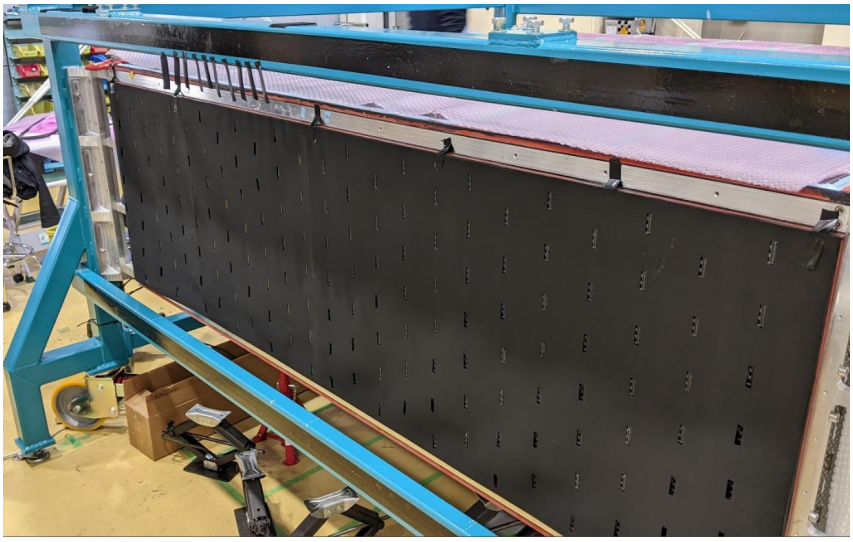

Figure 3.13: The upstream face of the SFGD after all PCBs were installed and the light barrier sheet was placed on top. The light barrier sheet avoids light leakage and has holes to connect cables to the PCBs.

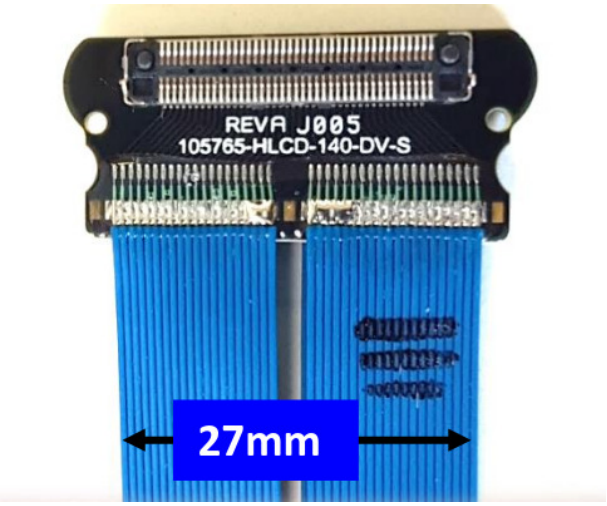

Figure 3.14: The ribbon cables used for the SFGD. The two sections can provide different bias voltages to each half of the PCBs. Figure from Ref. [97].

3.6 LED calibration system and installation

To calibrate the MPPCs, an LED light injection system was installed on the SFGD box opposite to the MPPC readout. The requirement for the LED system was at least a few photoelectrons such that the gain and pedestal value can be measured. The LED system used a light guide plate (LGP) which are designed with a main blue LED array at the end of the LGP module. There are holes (or "notches") along the module that scatter the LED light through; these notches match to where WLS fibres are in the SFGD box. Each notch is 3 mm in diameter in order to provide uniform light to the WLS end. The LED light passes through a 3 mm thick diffuser plate which makes the LED light emit more uniformly onto the fibre ends. Each LGP module was contained in a black acrylic container and was connected to a main LED driver which can provide the current to the modules and controls the LED brightness. Figure 3.15

47 LGP modules of dimensions $586.4 \times 81.1 \times 8.0$ mm^3 were installed on the sides and downstream end of the SFGD. Going from upstream to downstream, the left-hand side has 12 LGP modules and the right-hand side has 11, with the downstream having 24 modules. Each of these modules contain 56×8 notches to match with the MPPCs [98]. These modules also had six screwholes with which it was installed onto the SFGD box. There are 46 modules which cover the bottom of the SFGD. These modules have dimensions $999.5 \times 81.1 \times 8.0$ mm and contain 96×8 notches to match with the MPPCs. Due to the bottom of the SFGD being broader than the sides and downstream, the LGPs are installed as two columns of LGP modules. Each of the bottom LGPs contain 10 screw holes. All screw holes were equally spaced along the modules but were shown leak LED light. As a further measure to reduce light leakage, these screw holes were taped with black electrical tape and then a black caulk glue was pasted over them. This was also

done in the seams between each LGP module and above and below it.

The installation work began on March 7 and ended on March 13 2023. Figure 3.16 shows the LGP modules and the blue LED light being scattered through the notches. Figure 3.17 shows a snapshot of me during the installation of the LGPs.

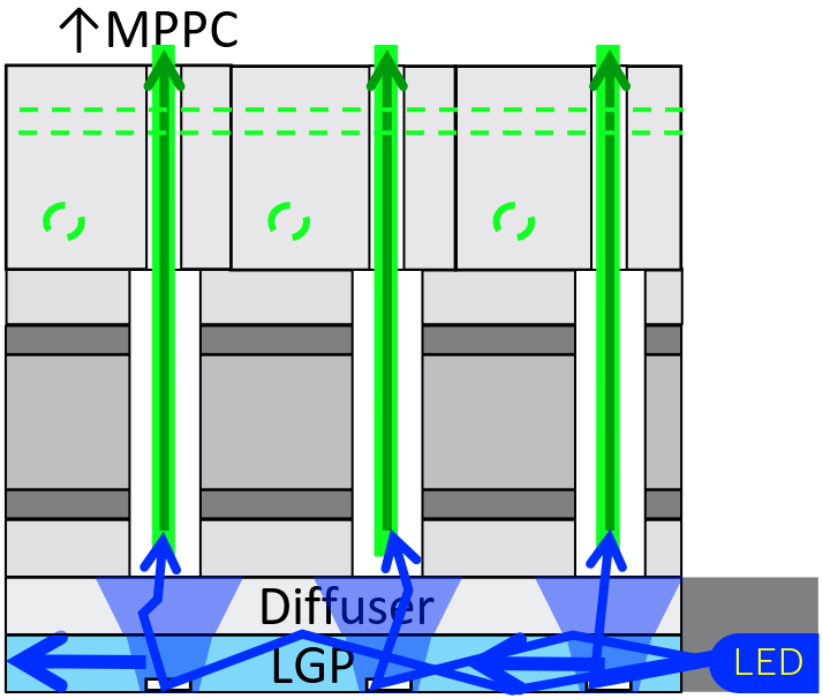

Figure 3.15: Schematic diagram of the LGP modules showing the blue LED light being scattered by the notches, sent through the diffuser plate and along the WLS. Figure from Y. Furui [98].

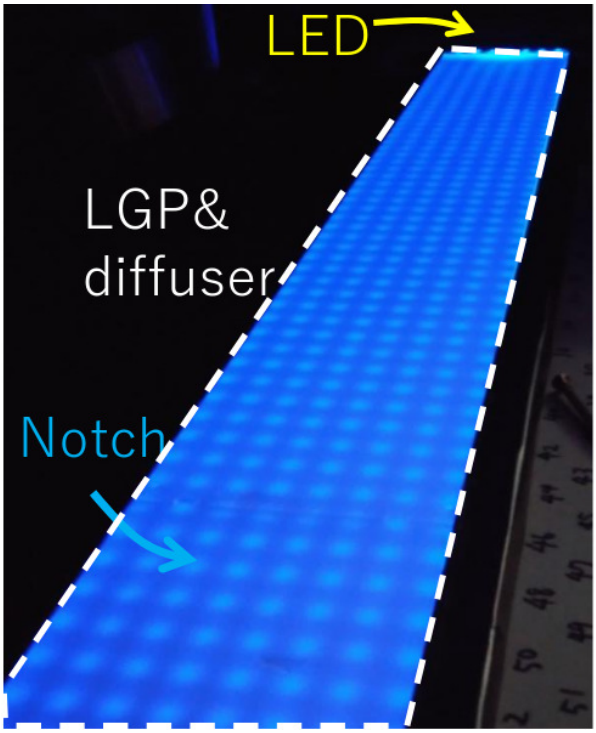

Figure 3.16: The LGP modules and diffuser plate showing the blue LED light being scattered through the notches. Figure from Y. Furui [98].

Figure 3.17: A picture of the author applying the caulk glue to the gaps between the SFGD modules.

3.7 SFGD electronics and data acquisition

The signal being read out of the SFGD MPPCs is often thought about in units of photoelectrons (p.e.), which is related to the output charge divided by the MPPC gain. The p.e. output is required to have a large dynamic range, meaning that it can be reliably read out for a signal as large as 1500 p.e. for stopping protons (which would leave a large energy deposit in the Bragg peak) but also retain a fine resolution for MIPs at around 2 p.e.. A hit detection threshold of 0.5 p.e. and a hit time resolution per cube of around 1 ns is also required [71]. As a result, the Cherenkov Imaging Telescope Integrated Read Out Chip (CITIROC) is used. The CITIROC is a 32 channel application-specific integrated circuit (ASIC) which are made by Weeroc in France [99]. The CITIROC design is based on existing, similar electronics used in the Baby-MIND detector [79]. The CITIROC is designed to have a hit detection threshold of down to 1/3 p.e. and a hit time resolution down to 100 ps, satisfying the requirements for the SFGD. The high voltage (HV) supplied to the MPPCs is adjustable in the CITIROC by using a channel-by-channel digital to analogue converter (DAC) which is connected to the ASIC input. This allows for the fine-tuning of the gains and non-uniformity which may arise over many CITIROCs.

Each CITIROC channel is split into two different signals: a high gain (HG) channel and low gain (LG) channel. Each channel has a specific preamplifier which can also be tuned to adjust the MPPC gains. There are also two separate shaping time constants (the HG channel is faster than the LG channel). An adjustable threshlold to trigger readout is also present and can be used to reduce dark noise rates. The Altera Arria 10 field-programmable gate array (FPGA) is used on the CITIROC to sample the readout as a desired rate or at a given trigger. The FPGA also provdes a timetable corresponding to a rising-edge and a falling-edge of the signal in 2.5 ns increments. The difference between these gives the time over threshold (TOT). The TOT can provide an approximation of the charge readout if HG or LG channels fail to readout (such is the case if two or more signals arrive during the CITIROC dead-time between readings). the FPGA is also responsible for the analogue-to-digital converter (ADC) which converts the analogue charge readout into a digitised unit of charge between $0 - 255$.

The ribbon cables which were connected to the back of each PCB allows the link to a front-end board (FEB). Each FEB contains 8 32-channel ASICs which means each FEB reads out 256 channels. There are a total of 222 FEBs. The FEBs are collected into groups of 14 and each group is placed in a metal crate on the sides of the SFGD box. Each crate also houses an extra board called the optical concentrator board (OCB). The OCB is responsible for aggregating the data from all the FEBs and also distributing trigger information to each FEB. It is also responsible for the monitoring of the FEBs and MPPCs by use of a slow control (SC) system. There are a total of 16 crates, with two crates only containing 13 FEBs. The OCB is also linked to the main clock board (MCB) which distributes beam trigger information to each OCB so that the MPPCs are readout during a beam spill. The MCB also provides a clock to the OCBs which is used to deter-

mine the timing of hits per channel.

The data acquisition (DAQ) is the final stage where all the data is collected by processes running on the dedicated DAQ computers. The DAQ is specific processes which aggregrate the raw data from the OCBs and package the information into files which are made each data-taking run. The DAQ use the Maximally Integrated Data Acquisition System (MIDAS) [100] which is also used in the rest of ND280. The MIDAS framework comes with an online database (ODB) which is a database of all the configuration settings for each subdetector. The ODB variables are dumped to a file at the beginning and end of every data-taking run, making it easy to go back and cross check the configuration settings. In the SFGD, there are lots of configurable settings; these settings have to be configured before the run begins. Figure 3.18 shows a schematic of the data flow and the configuration flow in the SFGD DAQ system.

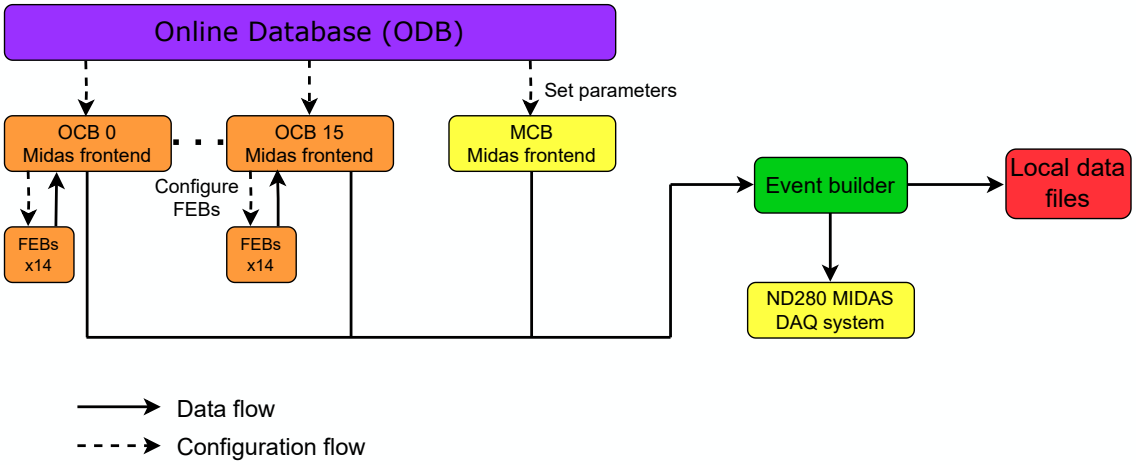

Figure 3.18: A schematic showing the data flow and configuration flow in the SFGD DAQ system. The dotted arrows indicate a configuration lead by the MIDAS ODB. The full arrows indicate the flow of data. Figure adapted from Ref. [101].

3.8 SFGD prototypes

Before the SFGD was constructed, there were a total of three prototypes constructed and tested. There was an initial prototype consisting of $5 \times 5 \times 5$ cubes [102]. The cubes for this prototype were manufactured by Uniplast Co. in Russia and the $1 \times 1 \times 1$ cm^3 cubes were cut from a bar of extruded scintillator instead of the injection molding used on the real SFGD. The composition of the cubes and the WLSs used were the same as the real SFGD. The prototype had 75 WLSs and used Hamamatsu 12571-025C MPPCs [102,

103]. This MPPC has an active area of 1×1 mm^2 and 1600 pixels. The electroncis used were similar to the Baby-MIND detector [79]. The prototype is shown in Figure 3.19 The prototype was placed in the T10 area of the CERN proto-synchrotron which supplies 6 GeV/c positively charged particles of mixed types to the prototype. The beam mostly consists of protons and positrons. The test found the time resolution for a single fibre to be 0.95 ns but this reduces to $0.65-0.71$ ns when two readout fibres are used.

A larger prototype, consisting of $24 \times 8 \times 48$ cubes was later constructed [104]. This prototype was constructed using the same cube manufacturing technique as the $5 \times 5 \times 5$ prototype and contained 1,728 readout channels. It also used the same WLSs as the real SFGD. There were three different Hamamatsu [103, 105] MPPCs used on the prototype: S13360-1325CS (type 1), S13081-050CS (type 2) and S12571-025C (type 3). There were 1152 of type 1, 384 of type 2 and 192 of type 3. Figure 3.20 shows a diagram of the prototype with the different areas read out by the three types of MPPCs. Type 1 and 2 had the same active area of 1.3×1.3 mm^3 while type 3 has 1×1 mm^3. The electronics used were based on the CITIROC ASICs used in the real SFGD. There was also a purpose-built LED light injection system to calibrate the MPPCs. The prototype was placed in T9 area of the CERN proto-synchrotron and was also placed in a 0.2 T magnetic field in order to mimic the environment in ND280. The beamline provided charged particles (positive and negative) in the momentum range of 0.4-8 GeV/c. The prototype results showed that the cube-to-cube optical cross talk is 2.94% per side of the cube; this was measured using the 8 cm and 24 cm WLSs. The time resolution for a single fibre was shown to be 1.14 ns. During the test, a study looking at protons stopping in the prototype was done and it was shown that the Bragg peak of the proton is visible and that the electronics were capable of capturing the large energy deposition (around 400 p.e.) at the peak. An example of a Bragg peak event display is shown in Figure 3.21. The prospects for particle identification by charge deposition was also investigated and it showed that muon, pion and proton hits were clearly distinguishable using the $\mathrm{d}E/\mathrm{d}x$ method. The resolution, using several layers, was shown to be up to 10% and is shown in Figure 3.22. Figure 3.23 shows the average energy deposition per unit length and per layer along the beam direction. A clear difference can be seen between protons and muons in both Figures.

The time resolution of the same prototype was studied in more detail in Ref. [106]. The study found that the time resolution of a single fibre was 0.97 ns. The improvement in time resolution likely came from an improved calibration procedure, the removal of cross-talk effects and a hit amplitude threshold of 20 p.e.. Figure 3.24 shows that the time resolution is dependent on the light yield, or the hit amplitude. This calculation was performed using the type 1 MPPCs, which are the ones used in the final SFGD. For signals with a p.e. values of 80 and 250 p.e., the time resolution was improved up to 0.89 ns. A function of the form

$$\sigma_t(A) = p_0/A^{p_1} + p_2$$

was fit to the data for a full range of $20-250$ p.e.. Here σ_t is the time resolution and p_1, p_1

and p_2 are free parameters. The p_2 parameter is responsible for the large amplitude limit to the time resolution and was found to be 0.87 $\pm$ 0.01 ns. This value is limited by the time digitisation step of the CITIROC electronics used in the prototype test beam. The digitisation step limit is 2.5 ns/$\sqrt{12}$ = 0.72 ns. The fit value being larger than the limit indicated that the full range of p.e. may not have been enough or that the functional form may not accurately describe the effects. It was also shown that using two fibre readouts for a single cube improves the time resolution to 0.68 ns, while averaging over two cubes with two fibres each brought this down to 0.47 ns. Figure 3.25 shows how using more than one cube increases the time resolution in average. This shows that in interactions which produce hits in multiple cubes, a much improved time resolution can be obtained.

The same prototype was also exposed to a neutron beam at Los Alamos National Laboratory in 2019 and 2020 [107]. The total neutron cross section on hydrocarbon was calculated and is shown in Figure 3.26.

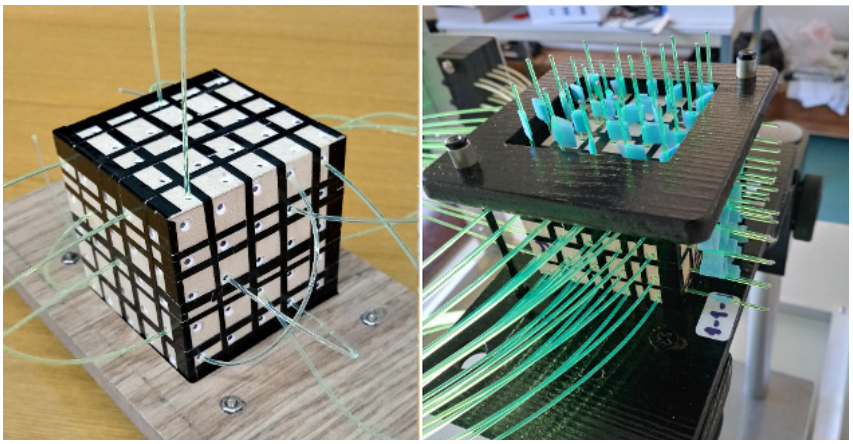

Figure 3.19: The SFGD $5 \times 5 \times 5$ prototype. This prototype was developed using the same SFGD scintillating cubes and WLS as the real SFGD but with a different cube production technique. It was placed in the T10 area of the CERN proto-synchrotron for a team beam. Figure from Ref. [102].

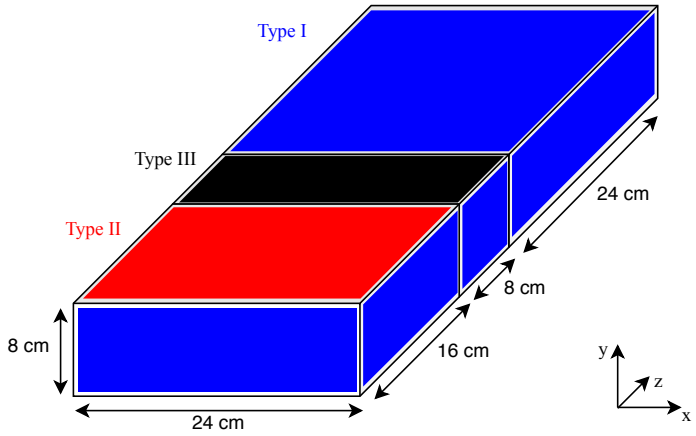

Figure 3.20: The SFGD 24×8×48 prototype showing the different areas of the detector being read out by different MPPC types. The MPPCs used are Hamamatsu S13360-1325CS (type 1), S13081-050CS (type 2) and S12571-025C (type 3). Figure from Ref. [104].

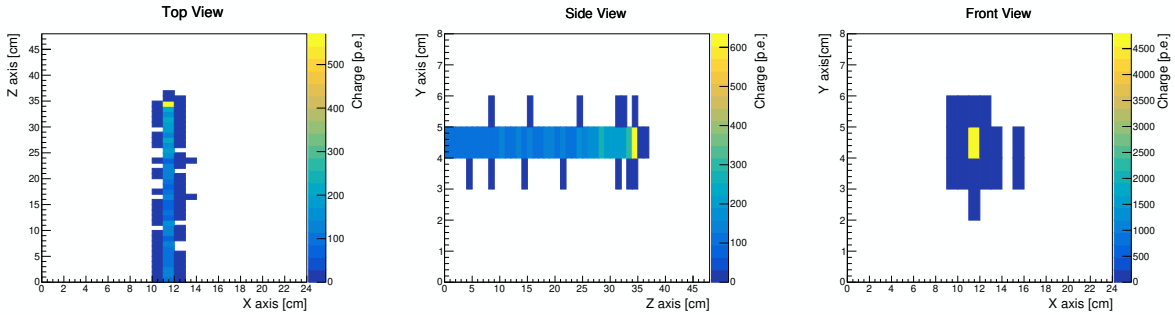

Figure 3.21: The Bragg peak of a 0.8 GeV/c proton stopping in the $24 \times 8 \times 48$ prototype. All three readout views are shown with the z-axis showin the charge deposition in p.e.. Figure from Ref. [104].

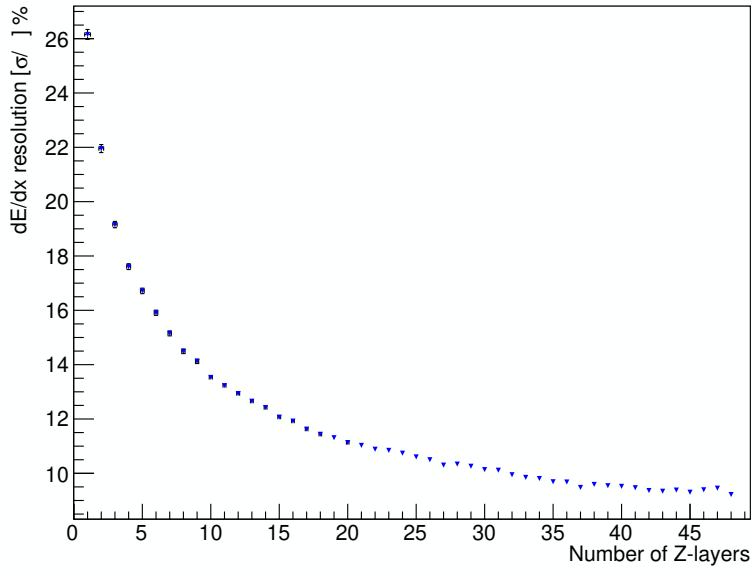

Figure 3.22: The $\mathrm{d}E/\mathrm{d}x$ resolution is plotted as a function of how many Z-layers of the SFGD prototype is used in the calculation. Using all 48 layers of the prototype produces a maximum resolution of 10%. Figure from Ref. [104].

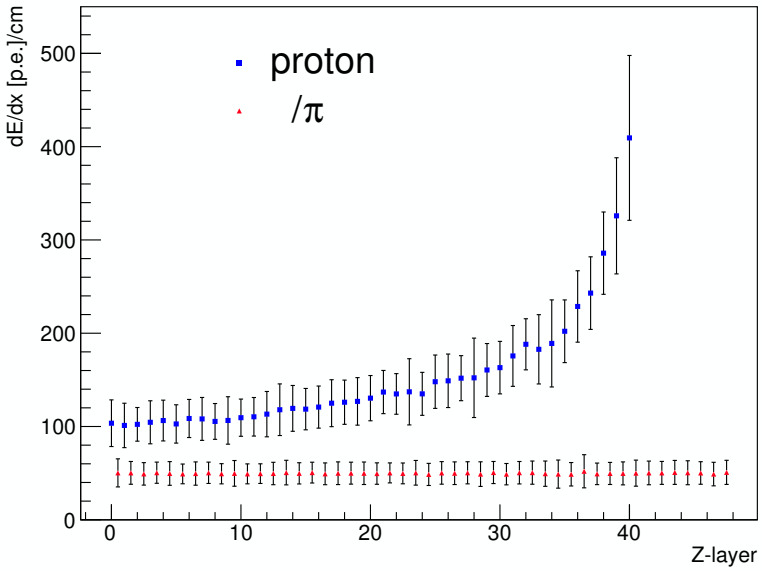

Figure 3.23: The $\mathrm{d}E/\mathrm{d}x$ for protons, muons and pions are plotted as a function of Z-layer for the SFGD prototype. The shape of the distribution for protons is clearly distinguishable from muons and pions, providing a powerful discriminant. Figure from Ref. [104].

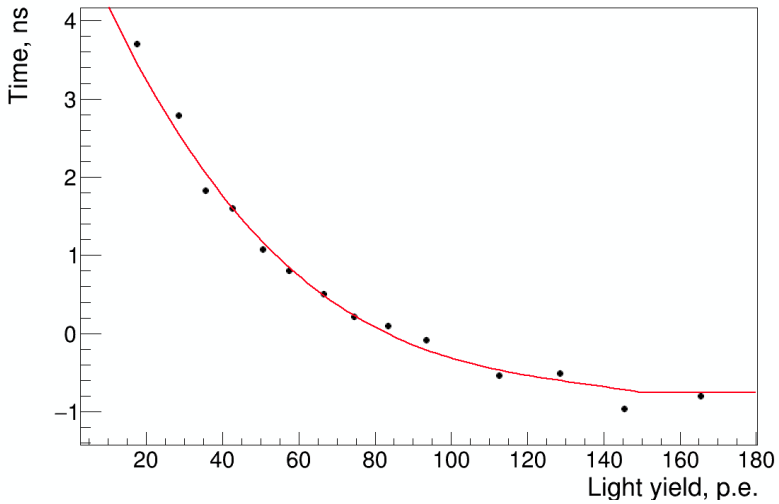

Figure 3.24: Timing resolution plotted as a function of recorded light yield for the SFGD prototype. Larger light yield signals produce an increased resolution. Figure from Ref. [106].

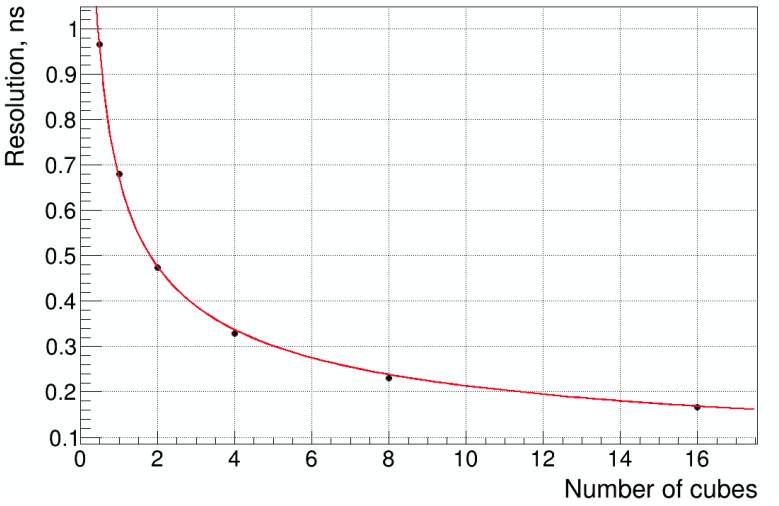

Figure 3.25: Timing resolution plotted as a function of cubes used for the calculation. As the number of cubes increases, the resolution improves. Figure from Ref. [106].

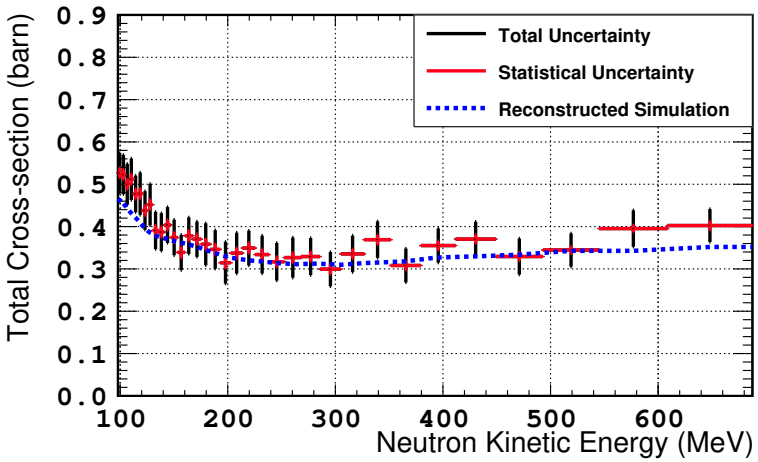

Figure 3.26: The total cross section for neutron collisions in the SFGD prototype. The prototype was exposed to a neutron beam at Los Alamos National Laboratory in 2019 and 2020 [107]. Figure from Ref. [107].

Chapter 4

The SFGD detector calibration and commissioning

This chapter explains the reason for calibrating detectors that utilise MPPCs. The LED calibration system and its use during calibration are then described. Several calibrations that were developed are then introduced. Finally, the current calibration routine during beam operation is explained.

4.1 SFGD Calibration

Before data taken with the SFGD can be used, a series of calibrations must be performed. The required calibrations can be roughly separated into two types: charge and time calibrations. Without charge calibrations, there is no certainty that the measured charge (and thus energy) for a given channel is measured on the same scale as another. Similarly, without time calibrations, the time at which a channel is digitised may be offset with respect to another. A series of calibration routines were developed by myself and colleagues which tackled these issues one by one. The time calibration is not touched upon in this thesis since the main effort of this work was on the charge calibration. In this section, the reasons for these calibrations are given in Subsection 4.1.1 and the individual calibrations are then described.

4.1.1 MPPCs and the need for calibration

An MPPC is a type of silicon photomultiplier (SiPM) which is a multi-pixel array of avalanche photodiodes (APDs). Each APD is a semiconductor device that converts light into an electronic signal by a "Geiger avalanche". The APD has a full valence band and an empty conduction band, separated by a band gap of energy E_g [108]. The APD is held at a reverse-bias, causing a depletion zone where there are fewer carriers. The bias voltage is just above the breakdown voltage of the device. This is called "Geiger mode". An avalanche occurs when a photon excites an electron-hole pair within the APD that is then accelerated by the electric field induced by the overvoltage, which is the difference between

the bias voltage and the breakdown voltage. The charge carrier is then accelerated and if its kinetic energy is enough to excite another electron-hole pair, it induces further charge carriers through impact ionisation with electrons (which are in the valance band) in the lattice structure. The charge carriers are now in a self-sustaining avalanche process which is quenched by a resistor in the circuit. This quenching process allows the avalanche process to stop and the APD to relax for the next avalanche process. The induced charge is dependent on the capacitance, C, and the overvoltage, ΔV.

$$Q = C(V_{\text{op}} - V_{\text{bd}}) = C\ \Delta V = Ne. \tag{4.1}$$

Here, V_{op} is the operating (bias) voltage, V_{bd} is the breakdown voltage of the APD, N is the total number of charge carriers and e is the elementary charge. The internal gain of an APD, is the total number of charge carriers in the avalanche process. The higher the gain, the larger the electronic signal that is produced.

The gain, often denoted as G, is dependent on ΔV. The operating voltage can be increased, making it easier to excite electron-hole pairs and instigate an avalanche process. However, if the operating voltage is too high, uncontrolled avalanches occur more often and damage to the device can also occur. The breakdown voltage of an APD is dependent on the temperature of the device itself. That is, $V_{\text{bd}} = V_{\text{bd}}(T)$. As the temperature increases, there are more phonon vibrations in the semiconductor lattice, which leads to more frequent scattering events with charge carriers. As a result, the charge carriers lose energy more quickly. Therefore, a higher voltage is required to induce the avalanche process, increasing V_{bd}. If V_{bd} increases, then from Equation 4.1, G will decrease.

Since the number of p.e., N_{pe}, is required in order to derive more physical quantities from the avalanche processes in particle detectors, the digitised output, given in HG ADC, must be converted by Equation 4.2,

$$N_{\text{p.e.}} = \frac{\text{ADC} - P}{G}. \tag{4.2}$$

Here P is the pedestal (where the zero p.e. events are). The SFGD CITIROC chips also have a LG and TOT channel, however, these values must first be converted to HG ADC to then use the Equation above. It is clear that N_{pe} is dependent on G, therefore G must be properly known for each APD in the recorded data. Because G is temperature dependent, this means that the gain must be recorded in regular intervals in accordance with any environmental changes, such as temperature. Since a specified dynamic range is required, the operating voltage must also be corrected when the environmental conditions change. This ensures that the APDs and therefore MPPCs respond similarly to light signals across different data runs.

The temperature also affects other properties of the MPPCs, such as the dark noise rate, which is the signal produced from non-photon-induced avalanches. The dark noise rate also increases with temperature because of the additional thermal energy the electrons

in the lattice have, contributing to spontaneous avalanches. Afterpulsing is when charge carriers get trapped in defects or impurities in the semiconductor. They thermally excite and are freed after a time delay, leading to a second signal not correlated with a photon. Afterpulsing decreases with temperature, but the increase in dark noise can mask these afterpulsing signals.

As a result of the tempurature dependence of the MPPC's intrinsic properties, various calibrations must be performed. These calibrations are below.

- Operating voltage (high voltage) trim: this is the adjustment of each MPPC's operating voltage in order to obtain the desired gain in units of p.e./ADC.
- HG gain calibration: the gain for the CITIROC's HG channel must be regularly recorded for each channel.
- Pedestal calibration: the pedestal must also be regularly found and recorded for each channel alongside the HG gain.
- LG to HG conversion: the LG channel must be converted to HG ADC in order to get the number of p.e. for that channel if the HG channel is saturated.
- TOT to HG conversion: the TOT is used as a proxy when both HG and LG channels do not digitise. This is then used to obtain a value for the p.e. for that channel.

In this work, only the high voltage trim, gain, pedestal calibration and LG to HG conversion are described. The TOT to HG conversion was performed by colleagues after me. Other charge calibrations, such as fibre attenuation calibrations, exist but were performed by colleagues after me.

4.1.2 LED calibration system

The LED calibration system, described in Section 3.6, is used to calibrate the MPPCs. The digitised output from the LED calibration system produces a "fingerplot". A fingerplot is a histogram of the HG ADC values. An example of a fingerplot is shown below in Figure 4.1; peaks corresponding to p.e. peaks can be seen. An oversight in the design of the LED system means that the SFGD channels around the screwholes in the LED LGP modules were oversaturated when illuminated by the nominal LED brightness. For these channels, a lower LED brightness is used. However, since the "screwhole channels" are only around the screwholes and the LED brightness can only be changed one LGP module at a time, both the nominal and the low LED brightness data must be taken for the whole SFGD whenever the LED calibration system is used.

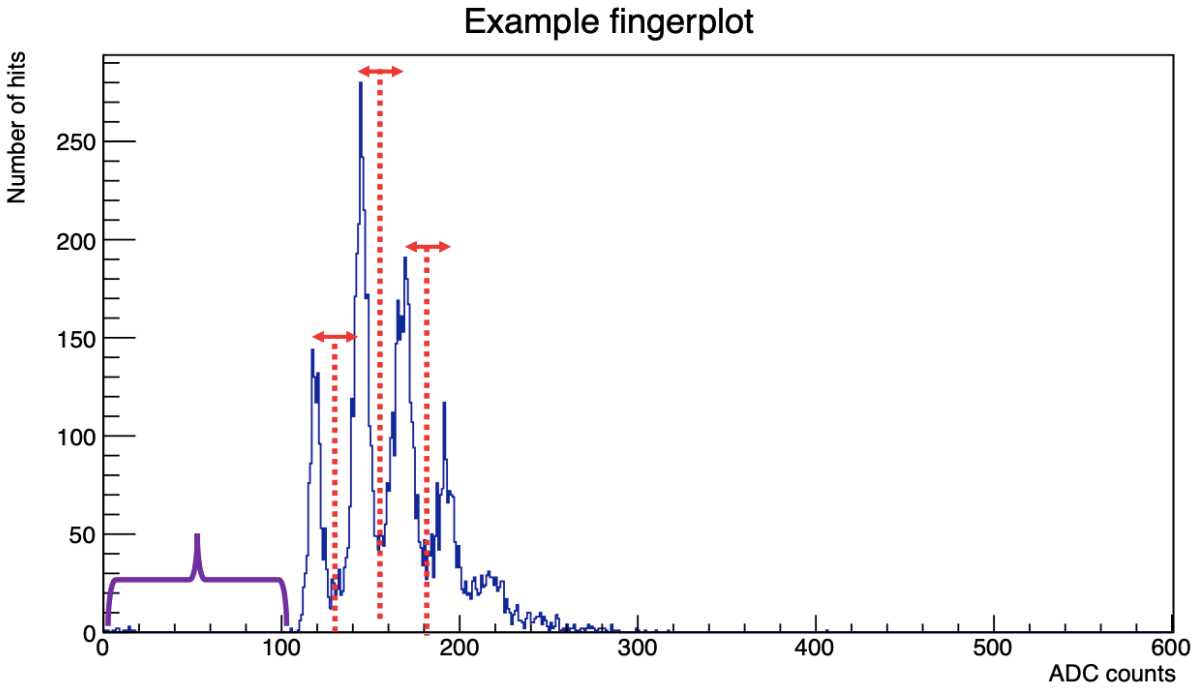

Figure 4.1: An example fingerplot for a SFGD channel. The read arrows indicate the distance between the photoelectron peaks; this is the gain. The purple bracket shows the offset from these photoelectron peaks from 0. The CITIROC chips are pedestal removed, therefore, the pedestal peak that would be seen in the purple region is not there.

4.1.3 Gain and pedestal calibrations

The gain corresponds to the distance between the fingerplot peaks in units of /ADC. The algorithm used to calculate this was originally written by a fellow colleague at Imperial College London, but was then altered by me to accommodate the SFGD DAQ output format. The algorithm itself is simple and is a peak-finding algorithm. If the peak-finding algorithm fails, the channel is assumed to be a screwhole channel and the low LED setting data is used for that channel. The gain value for each channel is stored in a format that can be uploaded to a calibration database. These values are then called "calibration constants".

Because the SFGD electronics are "pedestal-removed", the pedestal peak corresponding to the 0 p.e. peak is not visible. Instead, the HG DAC setting is change and fingerplots are obtained for differing HG DAC values. The number of the p.e. and ADC position of the peaks for each HG DAC setting fingerplot are plotted. Each HG DAC setting

plot is then fitted with a linear function and where the different HG DAC setting linear functions intersect is the pedestal value in ADC. This algorithm involves the peak-finding algorithm and then performs the linear fits and final interpolation. Figure 4.2 shows the pedestal algorithm used. The pedestal value is stored in a format that can be uploaded to a calibration database.

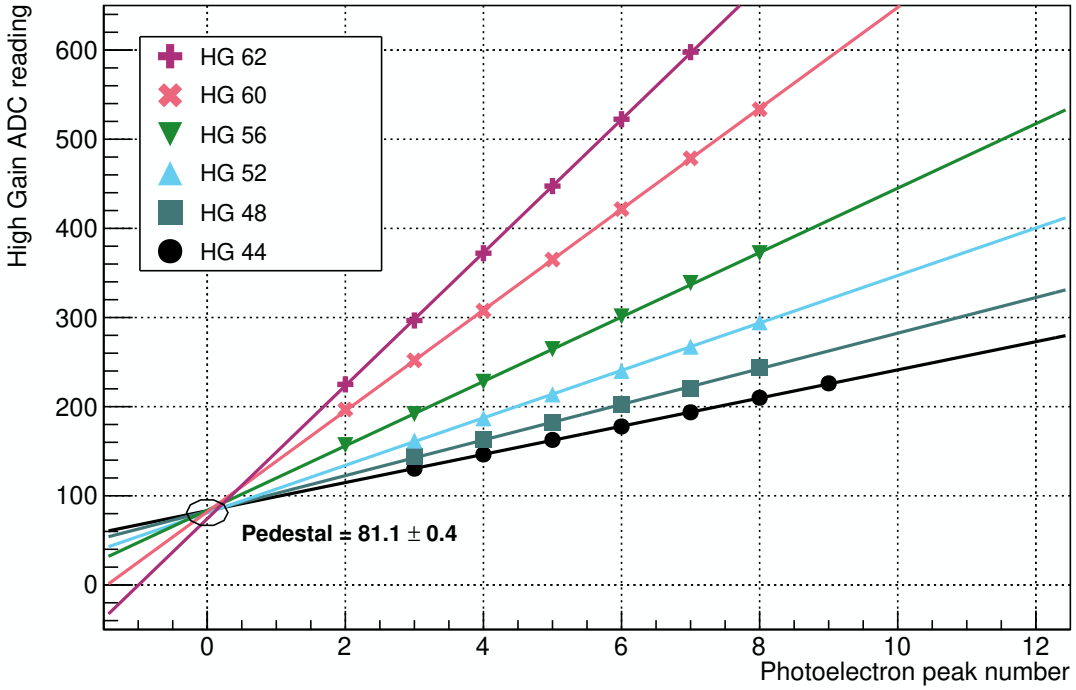

Figure 4.2: The CITIROC pre-amplifier setting for the HG channel, HG DAC, is varied and the fingerplot p.e. peaks are plotted against HG ADC value. The fitted lines from each HG DAC setting should intersect at 0 p.e. indicating the position of the pedestal. Figure from C. Lin.

4.1.4 High voltage trim

The high (operating) voltage, HV, must be adjusted regularly to adjust the gain to the desired value. The desired value for the SFGD was chosen to be 15 p.e./ADC; this provided the required dynamic range. HV is changed from the manufacturer's recommendation, V_m, between $V_m - 1.0$ to $V_m + 1.0$ in steps of 0.2 V. At each step, the LED light injection system is used and a fingerplot is obtained. The gain algorithm is used to get a value for that HV value for each channel. The gain values for all HV settings for all channels are plotted against HV. A linear function is fit through these points for each channel and interpolated to obtain the HV at the required gain. The linear regression algorithm is

$$S_x = \sum x \tag{4.3}$$

$$S_y = \sum y \tag{4.4}$$

$$S_{xx} = \sum x^2 \tag{4.5}$$

$$S_{xy} = \sum xy. \tag{4.6}$$

The following two quantities, SS_{xy} and SS_{xx}, are then calculated

$$SS_{xy} = S_{xy} - \frac{S_x S_y}{N} \tag{4.7}$$

$$SS_{xx} = S_{xx} - \frac{S_x S_x}{N} \tag{4.8}$$

where N is the total number of data points.

From these quantities, the gradient and the intercept of the fitted line can be calculated from

$$m = \frac{SS_{xy}}{SS_{xx}} \tag{4.9}$$

$$c = \frac{S_y - mS_x}{N}. \tag{4.10}$$

From this regression, the gain as a function of HV is obtained,

$$G(\mathrm{HV}) \tag{4.11}$$

where G is the gain. The HV value such that

$$G(\mathrm{HV} = \mathrm{HV}_T) = G_T \tag{4.12}$$

is desired. Here, HV_T is the target HV and G_T is the target gain. Figure 4.3 shows this for a single channel. The HV values are not stored in the calibration databases because they cannot be used to calibrate data after it has been taken. The distributions of the gain before and after a HV trim are shown in Figures 4.4 and 4.5.

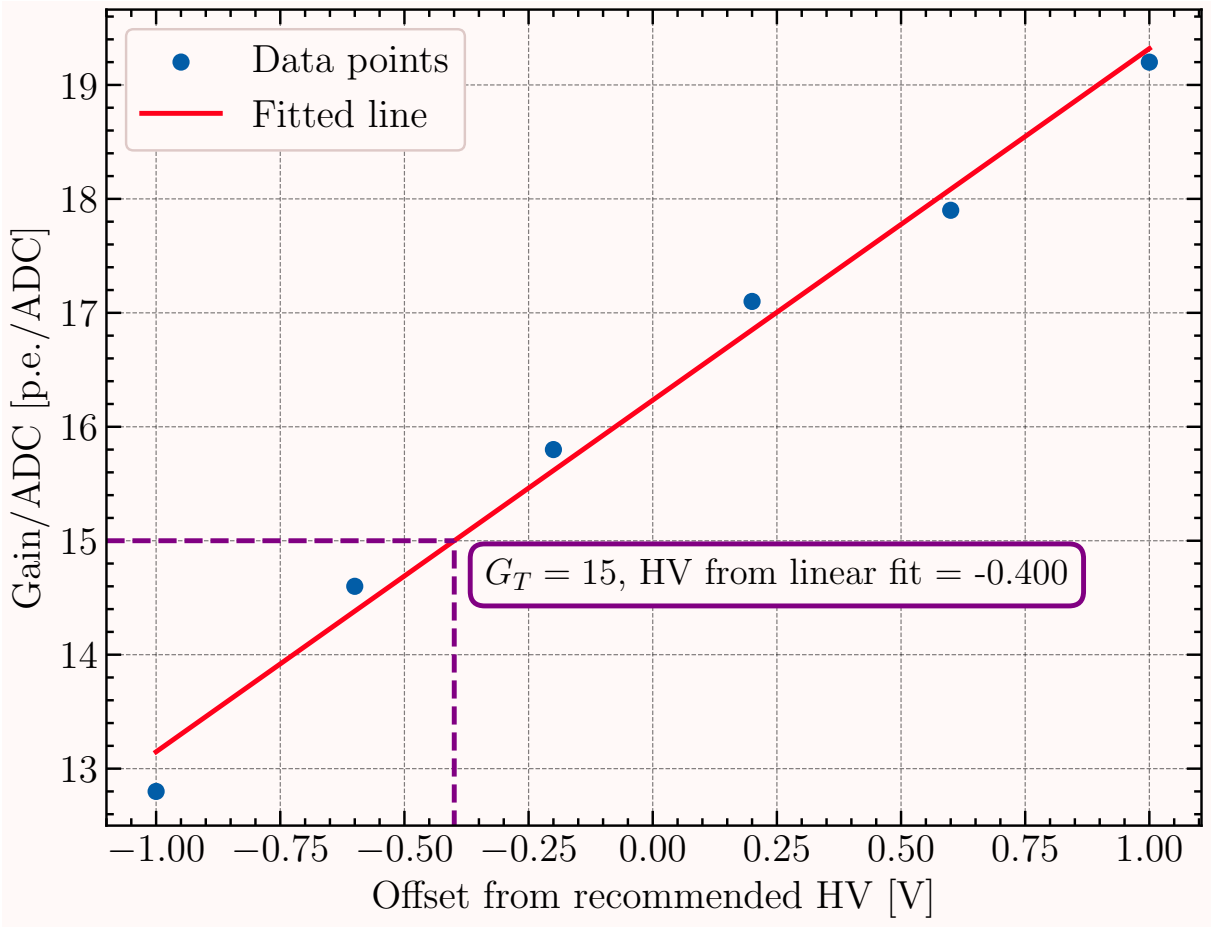

Figure 4.3: The HV trim method involves changing the operating voltage, referred to as the high voltage (HV), between two bounds and calculating the gain for each channel for each HV setting. The bounds are set at the manufacturer's recommended HV - 1.0 V and +1.0 V and stepped through in 0.2 V. The gain at each HV is plotted and a linear function is fit. The linear fit is interpolated at the desired gain value to obtain the required HV setting.

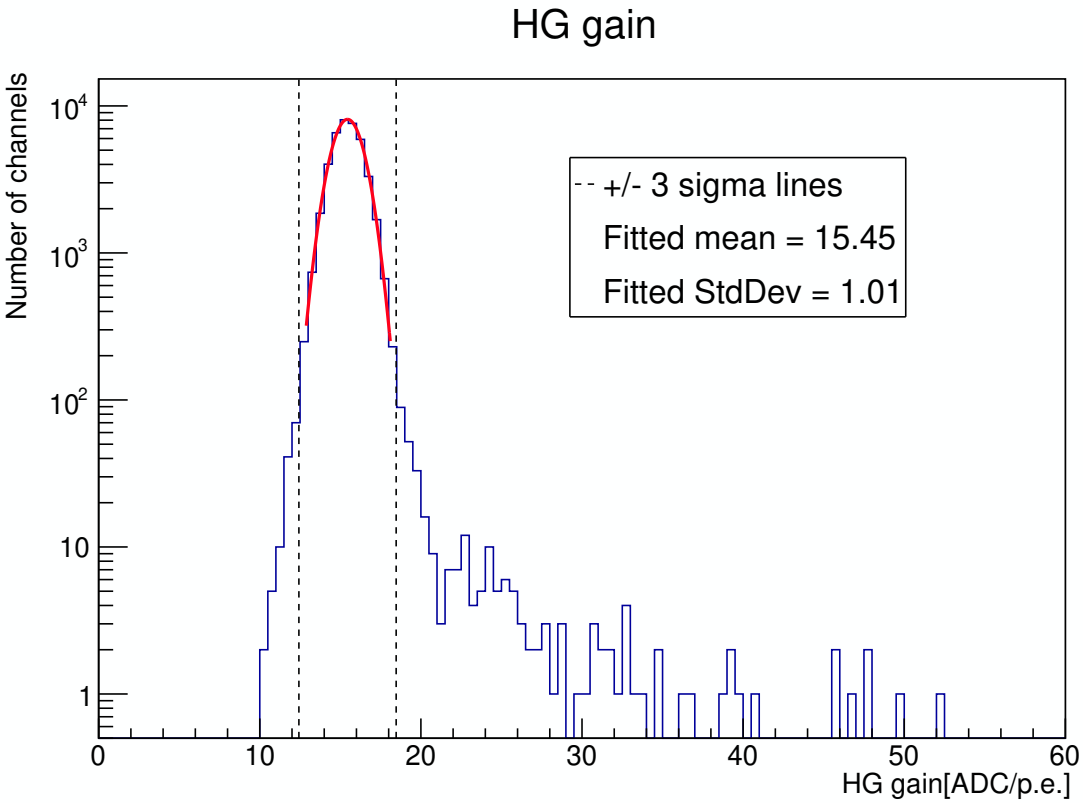

Figure 4.4: The distribution of the gain before the operating voltage, referred to as the high voltage, of each MPPC is calibrated. The width of the distribution is broad and the central value is slight off from the desired gain of 15 p.e./ADC.

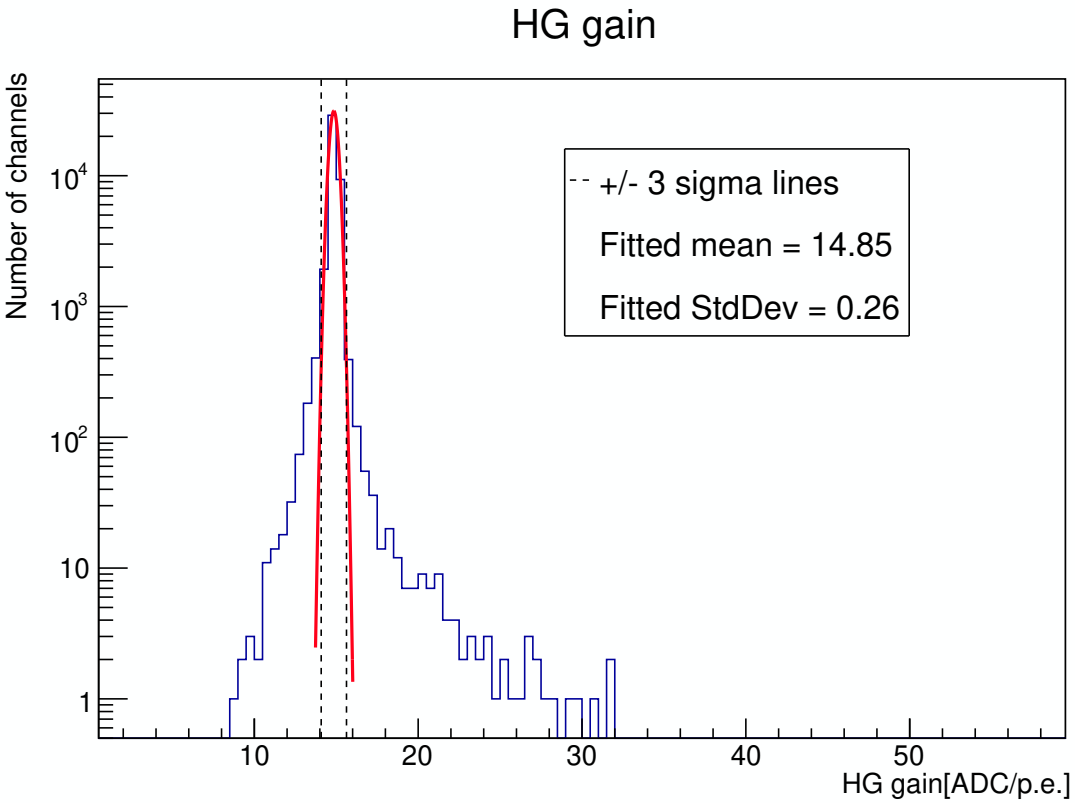

Figure 4.5: The distribution of the gain after the operating voltage, referred to as the high voltage, of each MPPC is calibrated. The width of the distribution is now much narrower with the central value more centered on 15 p.e./ADC.

4.1.5 LG to HG conversion

The LG channel in the SFGD is assumed to be linearly related to the HG channel. When the HG channel saturates, this becomes non-linear. A linear function can be fit to the LG ADC and HG ADC values until the linearity exceeds 1%. Figure 4.6 shows the relationship between the HG ADC and LG ADC. For each channel, Figure 4.6 is obtained and a linear function is fit. The linear function is

$$HG = p_0 LG + p_1 \tag{4.13}$$

where HG and LG are the HG ADC and LG ADC values respectively. p_0 and p_1 are the fit parameters determined for each channel. These parameters are stored in a format that can be uploaded to a calibration database. The LG to HG conversion requires a larger light signal that can be delivered by the LED calibration system. Therefore, cosmic ray data is used for this purpose. However, using cosmic ray data requires data to be taken for a long time in order to obtain enough statistics for all channels. Given the geometrical considerations of downward facing cosmic ray particles, this can take a long time.

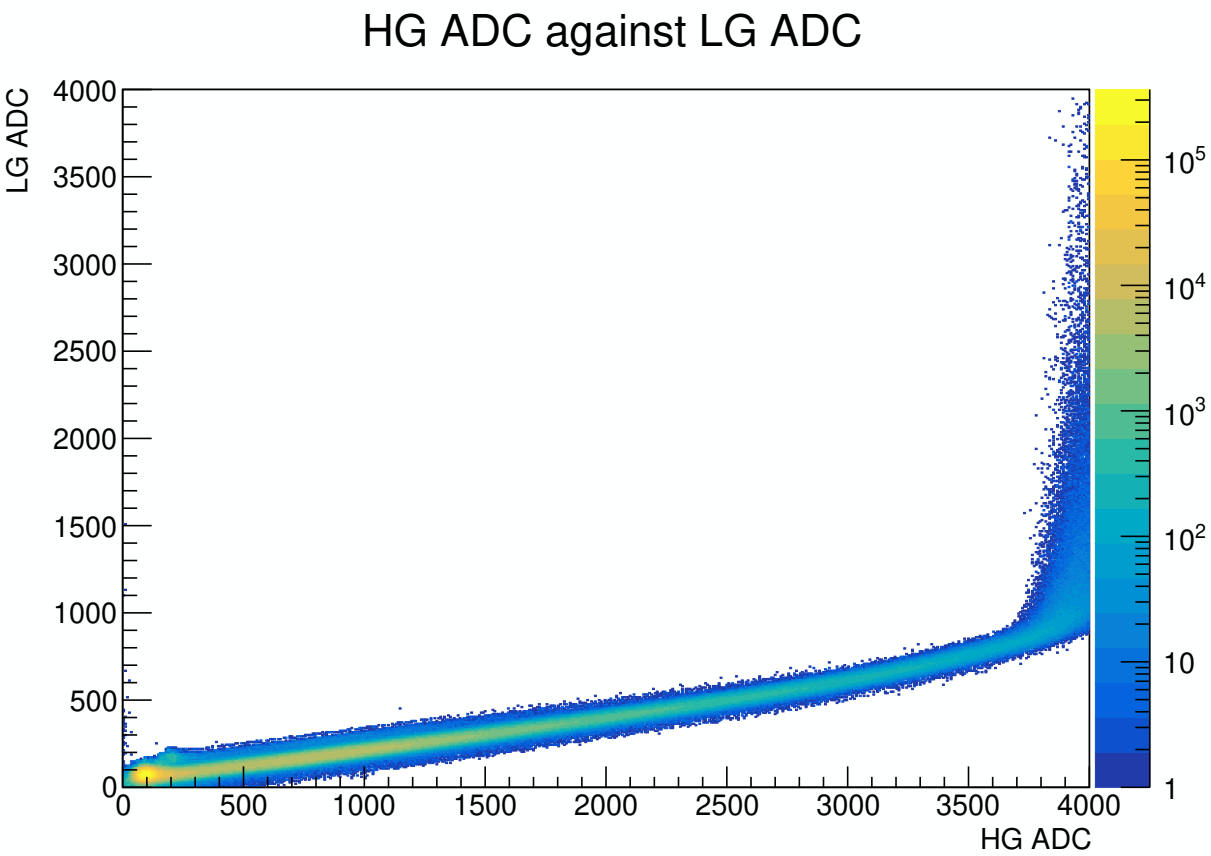

Figure 4.6: The LG ADC plotted against the HG ADC for a given MPPC. At high HG ADC, the CITIROC HG channel saturates while the LG ADC still provides usable data. A linear relationship is assumed and fitted until the linearity deviates by $> 1\%$.

4.1.6 Calibration routine during beam taking

During T2K beamtime and data taking, the ND280 detector is on 24 hours a day and the detectors are constantly taking data. Every week, the neutrino beamline shut down for either 12 hours or 24 hours, allowing for detector calibration and quick repairs if they are required. Between these maintenance days, the environmental temperature in the ND280 "pit" can vary drastically. Therefore, the MPPCs in the SFGD must be re-calibrated. I developed the maintenance-day calibration routine for the SFGD. The routine is outlined below.

1. The LED light injection system is used to obtain the current HG values for all channels. The gain values are plotted in a histogram. The gain distribution is then fit with a Gaussian function. If the central value of the Gaussian function is far from the desired value of 15, or the Gaussian width is too wide, a high voltage trim is required.

2. A high voltage trim, described in Section 4.1.4, is performed.

3. With the new high voltage settings applied to the MPPCs, the new gain distribution is then obtained.

4. These new gain values are saved to be uploaded to the calibration databases.

5. The HG DAC values are varied in the CITIROC electronics, stepping through a set of pre-agreed values. For each value, the LED calibration system is used and the data, both nominal and low LED brightness, are taken.

6. The pedestal algorithm, described in Section 4.1.3, is performed on the data. The pedestal values are saved to be uploaded to the calibration databases.

Chapter 5

ND280 Software

This chapter introduces the official ND280 software that is used for data processing in T2K. The code design used to implement the ability to process SFGD data in the ND280 software suite is then explained. Then, MySQL calibration database tables that are used to calibrate the SFGD are explained, and the design of the tables used is described. Finally, software written to visualise events within the SFGD and monitor the detector during operation is shown.

5.1 The ND280 software framework

The calibration routines developed must be implemented in the official ND280 software [109] before they can be used in general data processing. The software contains various "packages" that each perform a particular task or contain important and useful classes for use by other packages. The original software structure is shown in Figure 5.1. There are meta-packages, each suited to a different purpose, that contain respective packages. The meta-packages are:

- Base: contains base packages and is the low-level framework.
- Calibration: contains low-level data processing and calibration routines.
- Reconstruction: contains reconstruction algorithms.
- Analysis: contains tools for physics analysis.
- Simulation: contains tools for simulation of Monte Carlo samples based on the ND280 detector.
- Monitor: contains the software used for the online and offline monitoring of detectors.

Of importance in this work are the packages in the Base, Calibration and Monitor meta-packges. This section outlines the work done to implement the SFGD calibration routines

in the software. This was initially a difficult task, since, when I began this effort, I was the only person who attempted to integrate the SFGD calibration routines into the ND280 software. At the time, the input format of the data was also not solidified. As a result, until the detector was built and the DAQ system was finalised, the software was kept as "boilerplate" as possible to be easily adaptable.

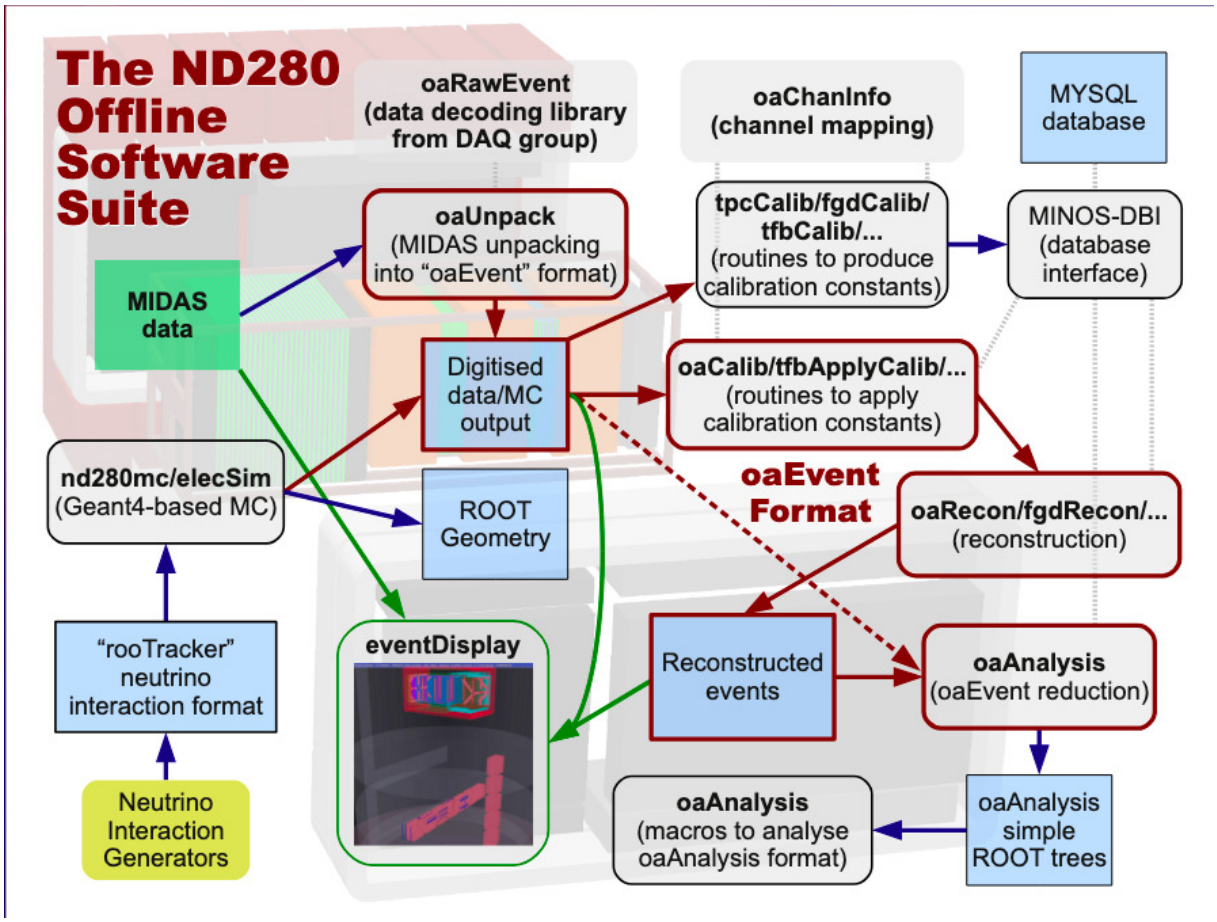

Figure 5.1: Original ND280 software structure before the ND280 upgrade detector packages were added. Figure taken from [110].

5.1.1 General overview

The general workflow from raw MIDAS [100] format to usable calibrated data was necessary for the SFGD to be used in the main data processing pipelines.

A simplified version of the calibration pipeline using the ND280 software is as follows:

- Midas → TDigit
- TDigit → THit ("cali" level)

- THit → SfgReco ("reco" level)
- SfgReco → eventAnalysis ("ana" level).

Each term is defined in the following subsections. The terms "cali", "reco" and "ana" correspond to calibration, reconstruction and analysis.

5.1.2 Implementation of SFGD in software

In the ND280 software, the raw data from Midas is converted into different C++ class structures for easier use and storage. The first step of this is to convert Midas data banks into "TDigits". TDigits are a C++ class structure in the `oaEvent` package. TDigits contains all of the raw information necessary for later processing. It is essentially a re-design of the raw data format, keeping only necessary information. In the case of the SFGD, the TDigit class was designed to contain:

- High Gain ADC (`int`);
- Low Gain ADC (`int`);
- Rising Edge TDC (`int`);
- Falling Edge TDC (`int`);
- Boolean for checking that the ADC and TDC counts are matched (`bool`).

Here, the C++ data type is given by the brackets. The above TSFGDigit inherits from the general TDigit class which also contains a TChannelId. The TChannelId is a long int that is unique across ND280 and denotes a single electronic channel. The Midas-to-TDigit conversion occurs in the `eventUnpack` package in the ND280 software. This is called automatically when running the main calibration executable `RunEventCalib.exe`. The CITIROC HG channel digitisation time is long enough for signals to overlap. In this case, many time stamps are recorded for a single amplitude readout. Only the largest amplitude is recorded. Each TDigit requires an ADC and TDC value; all TDigits in this digitisation time are given the same ADC value but have different TDC values. It was decided that the largest TOT signal was likely the largest amplitude hit. The Boolean value in the TDigit contains this information. Thus, ideally analyses should use TDigits where this boolean is true and the amplitude signal is correctly matched to the time signal.

5.1.3 TDigits to THits

THits are a different C++ class structure in the `oaEvent` package. THits are designed to hold only the calibrated data information. THits are created when running the `RunEventCalib.exe` executable; this is the main calibration routine used by T2K in data processing. Calibration constants must be applied to the TDigits to produce THits. The THits contain:

- Charge (in photoelectrons, p.e.);
- Time (in ns);
- The original TDigit it once was.

The calibration constants are obtained from the aforementioned calibration routines in Section 4.1. The charge calibration routines are in the `sfgExtractCalib` package and the time calibration routines are in the `sfgExtractTimeCalib` package. The calibration constants for each channel are stored in a MySQL calibration constant database. The `RunEventCalib.exe` executable automatically connects to the database and will find the most appropriate set of constants for the given data run and apply them, producing THits.

5.1.4 Calibration Constant Databases

The calibrations applied in general data processing are simply the application of calibration constants to raw data in order to shift or scale values. The databases contain tables for each calibration for each subdetector. The structure of the database, the SFGD-specific database tables and how it is accessed within the ND280 software will be outlined below.

Database Overview

The calibration databases are actually two separate databases: `nd280calib` and `testnd280calib`. The test database is used for testing new constants such as when one improves an algorithm. The main database, `nd280calib`, is used in general data processing. Inside the databases are tables. Each table corresponds to a specific calibration and is required to have a name that ends in "TABLE". It is convention to begin the table name with the subdetector in question. So, a good example would be `SFG_HG_TABLE` for the HG calibration constants. There are two tables per calibration constant set because one table contains the constants and the other table (the "validity table") contains the ranges in time for the validity of the constants. The associated validity table must have the same name as the constant table, but end with "VLD". The two tables are connected through the first column of the tables called the "sequence number". The sequence number of a specific set of constants will match to that in the validity table, thus providing the time for which the constants are valid. The time of a data file is automatically retrieved in `RunEventCalib` and used when retrieving constants from the database.

SFGD Tables

Initially, there were no tables in database for the SFGD. Throughout the course of the SFGD commissioning, I added tables to improve the general calibation routine for SFGD data. Currently, the tables available are as follows:

- HG table;
- Pedestal table;
- HG/LG table;
- TOT table;
- Bad channels table;
- Cable length table;

The HG table corresponds to the HG channel gain. This is given in Equation 4.2. The pedestal table is also the pedestal value given in Equation 4.2. The HG/LG table is conversion from LG channel ADC to HG channel ADC. The TOT table is the conversion from TOT to HG channel ADC. The bad channels table is a list of all channels that are classes as bad from a data quality perspective. This can be for reasons such as broken hardware that affects the readout of a channel. This table allows analyses to ignore these channels in processing. The cable length table contains the length of the electronics cables for each channel. Due to the geometry of the detector and its positioning within ND280, not all the cables are the same length. This results in a time difference between different channels. Each table has its respective validity table and is currently being used by `RunEventCalib`. The `sfgApplyCalib` package is used to explicitly apply the calibration constants and only communicates to `sfgExtractCalib` through the calibration databases.

Accessing And Modifying The Database

The general routines for accessing the database, uploading calibration constants and retrieving constants were already in the ND280 software in the `oaOfflineDatabase` package. Once calibration constants are prepared in the correct format, uploading to the database is straightforward. The steps to making SFGD-specific tables are outlined below.
The creation of a new table is done through `.sql` files detailing the structure. The constant table and validity table are made at the same time. The validity table structure is not modified, but the name of the table must match a constant table. The structure of the HG table is

```
CREATE TABLE SFG_HG_TABLE(
SEQNO integer not null, ROW_COUNTER integer not null,
CHANNEL integer,
HG float,
HGErr float,
primary key(SEQNO, ROW_COUNTER ));
```

The associated validity table structure is

```
CREATE TABLE SFG_HG_TABLEVLD (
SEQNO integer not null primary key,
TIMESTART datetime not null,
TIMEEND datetime not null,
EPOCH tinyint(4),
REALITY tinyint(4),
DETECTORMASK tinyint(4),
SIMMASK tinyint(4),
TASK integer,
AGGREGATENO integer,
CREATIONDATE datetime not null,
INSERTDATE datetime not null,
key TIMESTART (TIMESTART),
key TIMEEND (TIMEEND));
```

The validity table structure is identical for all tables. The structure of the pedestal table is below.

```
CREATE TABLE SFG_PED_TABLE(
SEQNO integer not null, ROW_COUNTER integer not null,
CHANNEL integer,
Ped float,
PeddErr float,
primary key(SEQNO, ROW_COUNTER ));
```

The structure of the LG-to-HG conversion table is below

```
CREATE TABLE SFG_PED_TABLE(
SEQNO integer not null, ROW_COUNTER integer not null,
CHANNEL integer,
p0 float,
P0Err float,
p1 float,
P1Err float,
primary key(SEQNO, ROW_COUNTER ));
```

Here, p_0 and p_1 correspond to the constants required in Equation 4.13.

Accessing from the ND280 software

To extract the calibration constants from the database and apply them to data with the ND280 software, routines to access and retrieve constants were required in the `oaCalibTables` package. Here, the structure of one class I wrote in order to do this is described; all other classes follow the same structure.

The name of the class which would access a calibration table is required to have the same name but with a "T" affixed to the beginning. For example, the accessor class for the HG table is called `TSfg_HG_Table`. The ND280 software will automatically remove the "T". There are a number of class methods required for it to work properly.

1. The `Fill` method: This method is needed to fill a `TResultSetHandle` class with the row information from the tables. An example is given in the case of the HG calibration table.

```
virtual void Fill(ND::TResultInputStream& ris){
        UInt_t id; // Channel ID from table
    ris >> id >> fHG >> fHGErr;
    fChannel_Id = TSFGChannelId(id);
};
```

2. The `GetIndex` method: This method is needed to build a lookup table which the ND280 software can read to obtain a row based on the TSFGChannelId.

```
virtual UInt_t GetIndex(UInt_t defindex) const {return fChannel_Id.AsUInt();}
```

3. The `MakeTableRow` method: This is required to make a specific class that corresponds to a table row to read in. This looks like this.

```
virtual ND::TTableRow* MakeTableRow() const {
    return new TSfg_HG_Table;
};
```

4. Finally, correct class member variables and appropriate "getter" functions are required to match.

With all this complete, the ND280 software can read the calibration database tables.

Bad channels

Channels which are broken or otherwise unusable are referred to as "bad channels". Bad channels are defined by the SFGD group and are stored in a table called `BAD_CHANNELS_TABLE`. Bad channels from all ND280 subdetectors are stored in this same table. Unlike other calibration constant tables, this table is read in `oaChanInfo` (which is normally called by `eventUnpack` during the unpacking procedure to construct the TSFGChannelID and TSFGGeomId classes). This table is also used in calibration to stop bad TDigits from being made into THits. The SFGD calibrator class `TSFGChannelCalibrator` calls the `oaChanInfo` which in turn checks if a TDigit originates from a bad channel.

5.1.5 Online event display

The online event display is a staple in T2K and is known for providing ND280 DAQ shifters with live event displays. It is also used to produce official event display figures for conferences. The SFGD detector geometry was produced years before I entered the collaboration. However, the raw data being taken by the SFGD was not shown in the online event display. I implemented the channel map lookup table that is used to map the electronic channels to geometric channels in the online event display graphics. It was necessary to use the SFGD TDigit data format to obtain the hit information (unlike other subdetectors which uses the raw MIDAS data). A hard-coded threshold on the ToT was produced by brute force and is used to reduce noise shown in the display for each event. Figure 5.2 shows an example of an event display with the SFGD shown by the pink box.

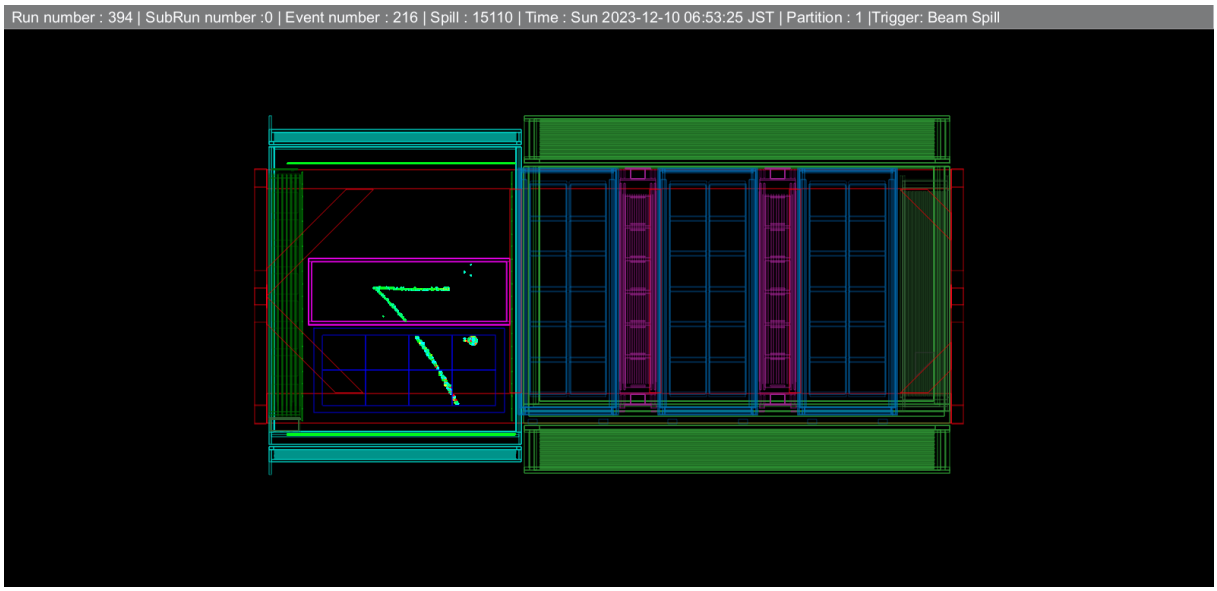

Figure 5.2: An event display showing a neutrino event in the SFGD (pink box) with the neutrino beam direction going from left to right.

5.1.6 Online monitoring software

When taking data, the safe and stable running of detectors is paramount. In order to monitor the status of the detectors and the quality of the data being taken, the online monitoring (OM) software is used. Using a similar method as in the online event display, I wrote the first implementation of the OM for the SFGD. The OM used the SFGD TDigit data format to extract the HG ADC, LG ADC, hit rising and falling times, and a boolean indicating matched ADC and TDC values. The following monitoring plots were created by myself.

- Hit occupancy.

- HG ADC hit map.
- LG ADC hit map.
- HG ADC spectra.
- LG ADC spectra.
- Rising time hit map.
- Falling time hit map.

Additional monitoring plots, such as FEB-summarised hit occupancy and gain monitoring, were added by myself and colleagues. Figures 5.3, 5.4, and 5.5 show the hit occupancy, HG ADC spectra and HG ADC hit occupancy respectively. The hit occupancy is especially important as it highlights "hot channels" which digitise more than other channels. This can be an indication of a bad configuration for that particular MPPC. It can also quickly highlight dead channels. The HG ADC spectra, when used with the LED calibration system, show channels which may have an incorrect configuration leading to a fingerplot peak in the low HG ADC region. This is referred to as a "low baseline peak". This is a problem when using the gain and pedestal calibration algorithms as it can confuse or bias the peak-finding algorithms. The HG and LG hit occupancy plots highlight errors in configurations for channels that can lead to digitising the HG or LG channels too frequently or infrequently.

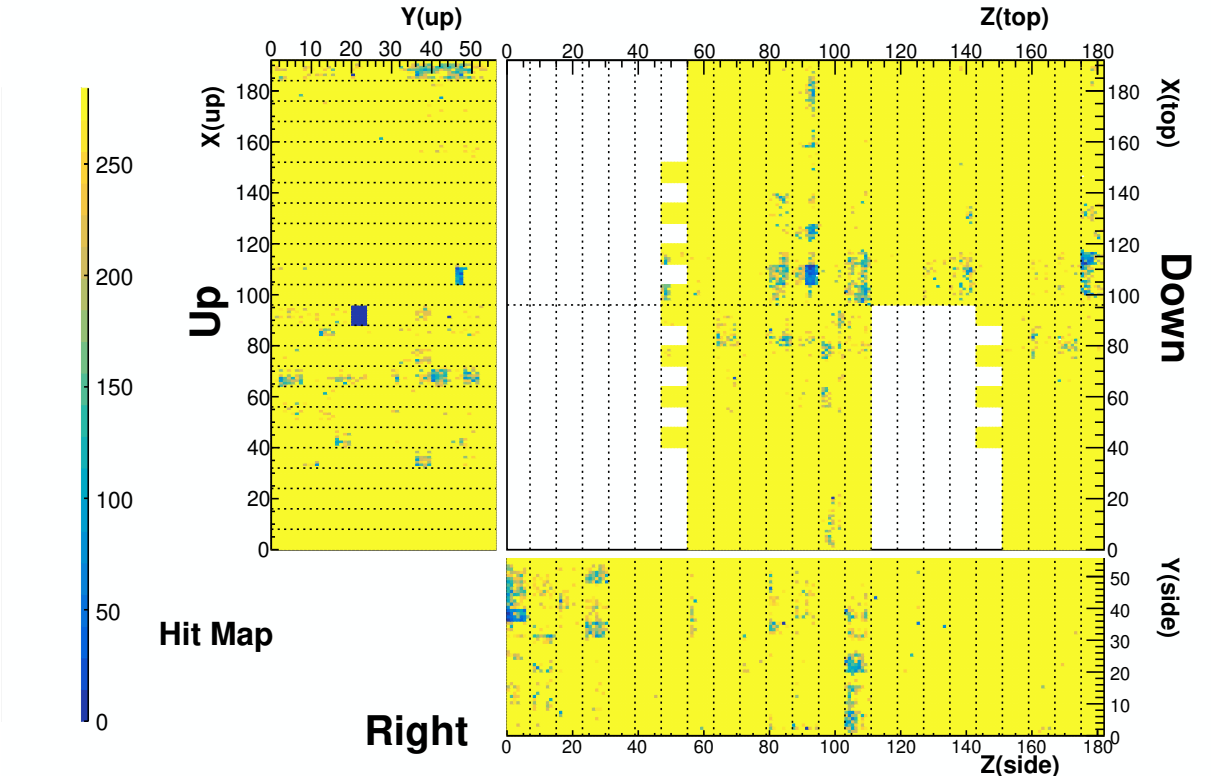

Figure 5.3: An online monitoring hit occupancy plot. The plot is filled with 1 for every TDigit unpacked in the raw data. This Figure is from before the SFGD had all of the electronics installed and so white gaps are visible. Dead channels also appear in this way. A blue square on the left indicates an MPPC-PCB that has a configuration problem and is not sending data. This is referred to as a "cold channel".

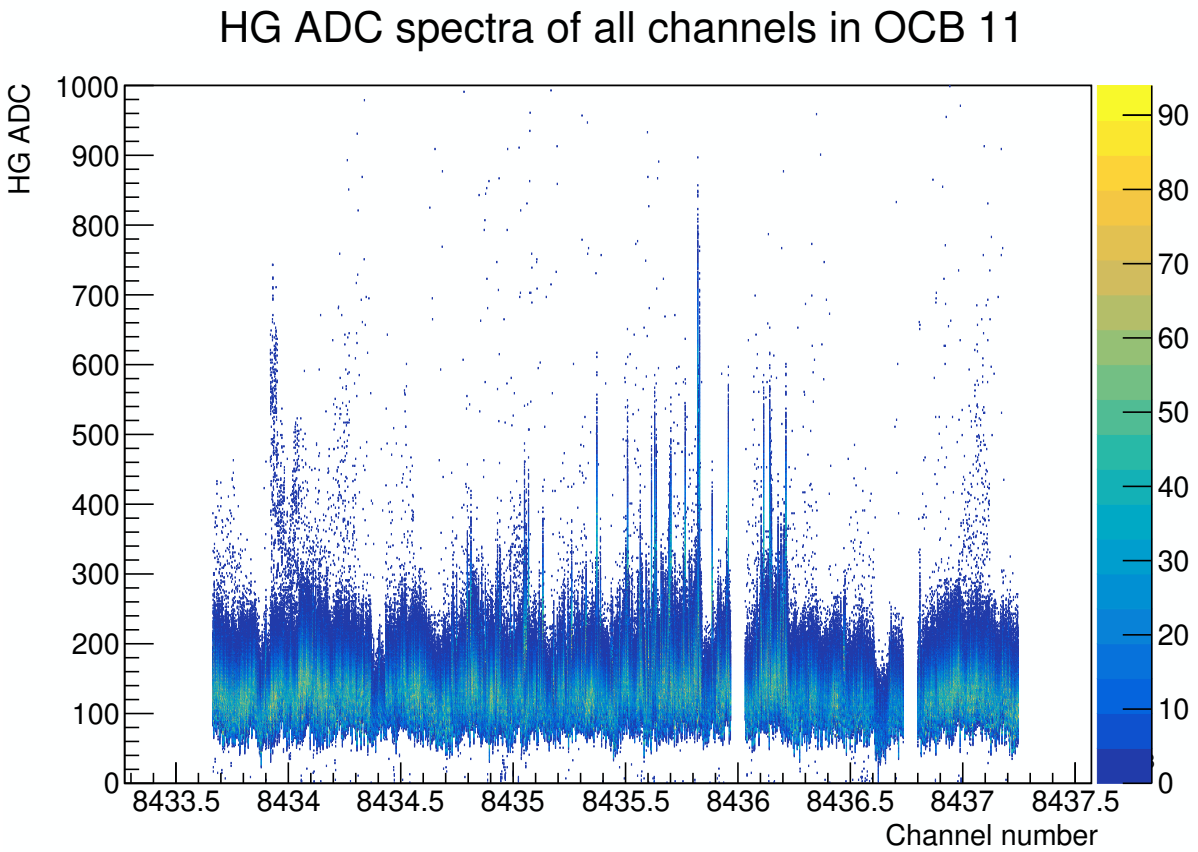

Figure 5.4: An online monitoring HG ADC spectra plot for OCB 11. The HG ADC is plotted against the global channel ID. White gaps can be seen indicating missing channels. Some channels have entries below the average horizontal HG ADC value, indicating a "low baseline" channel.

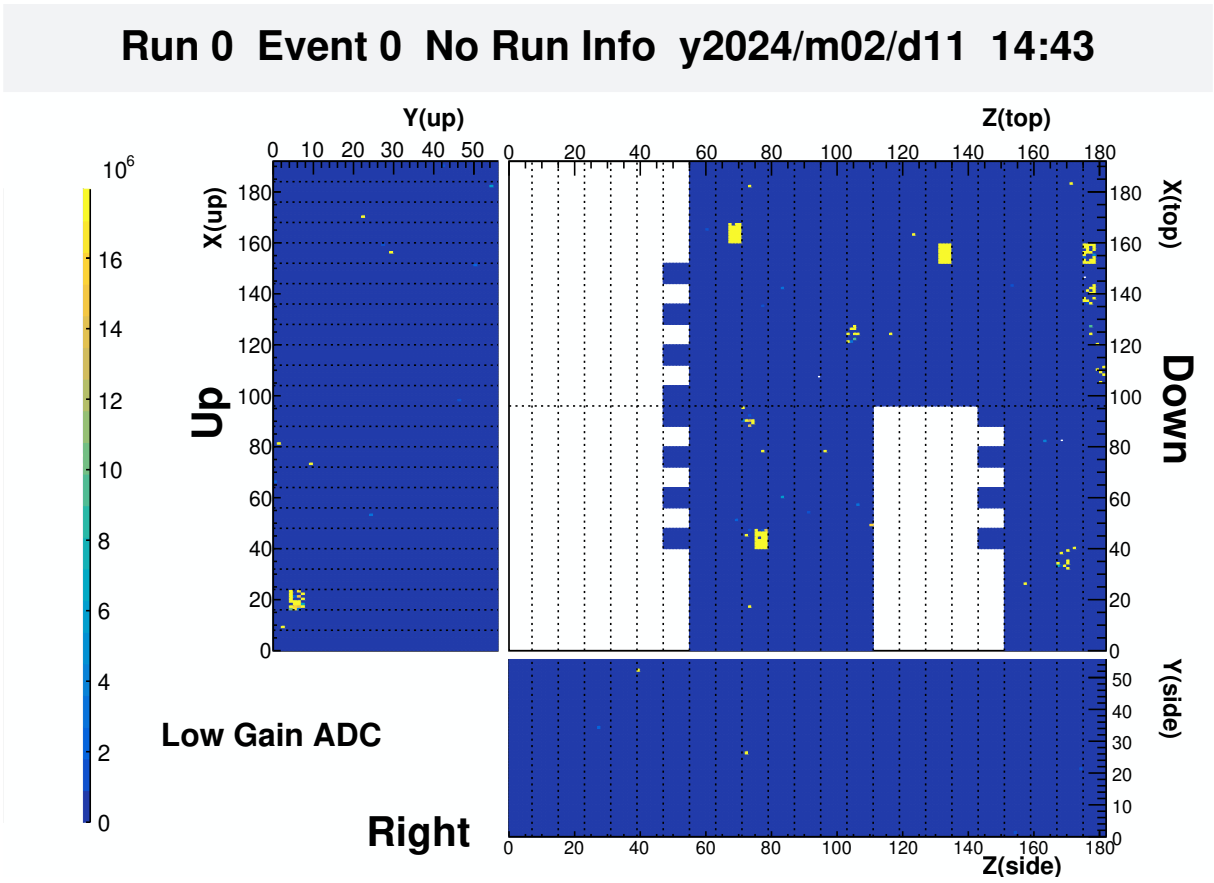

Figure 5.5: An online monitoring LG hit occupancy plot. The plot is filled with 1 for every LG ADC value unpacked in the raw data. This Figure is from before the SFGD had all of the electronics installed and so white gaps are visible. Dead channels also appear in this way. Blocks of yellow indicate MPPC-PCBs that are digitising the LG channel too often, causing "hot channels" makes those channels unusable in data processing.

Part III

Investigating Neutrino-Nucleus Interactions Within a Relativistic Mean Field Framework

Chapter 6

Electron-nucleon elastic scattering

This chapter introduces the theoretical framework for electron-nucleon scattering. The derivation of the differential cross section is performed in full and important aspects, such as form factors, lepton and handron tensors, and currents are introduced.

Studying electron–proton scattering provides a strong foundation for understanding neutrino scattering, as the two processes share a theoretical connection rooted in the symmetry principles of the Standard Model. In electron–proton scattering, the electromagnetic interaction is mediated by photons, which couple to the isoscalar and isovector currents, quantities that are both highly constrained and precisely measured. In contrast, neutrino scattering proceeds via the weak interaction, mediated by the massive W and Z bosons, and involves both vector and axial-vector currents. Crucially, the electromagnetic isovector current and the weak vector current are related through isospin symmetry, a component of electroweak symmetry, making the vector contributions in the two processes fundamentally connected. Because electron scattering experiments provide abundant and high-precision data, they serve as a valuable source of constraints on the vector current in neutrino scattering. This makes electron scattering data an extremely useful tool for studying weak interactions via neutrino scattering.

The scattering cross section is a quantity that tells us the probability of a reaction to occur with a given set of kinematics for the particles involved. It is defined as the transition probability per particle per unit time divided by the incoming current of particles. This is shown mathematically in Equation 6.1,

$$d\sigma = \frac{|S_{fi}|^2}{\Phi_{\text{inc}} T}\, dN_f. \tag{6.1}$$

where T is the normalisation time for the reaction to occur and S_{fi} is the S-matrix element for the transition from state $i \to f$. dN_f are the number of final accessible states for the interaction. Φ_{inc} is the incoming particle flux and is given in Equation 6.2,

$$\Phi_{\text{inc}} = \frac{1}{V} \frac{\sqrt{(K_i \cdot P)^2 - m_i^2 M^2}}{E_i E}. \tag{6.2}$$

Here, K_i and P are the initial electron and nucleon four momenta respectively, m_i and M are the initial electron and nucleon masses respectively, and E_i and E are the initial electron and nucleon energies respectively. The volume is given by V. The number of final states, dN_f is given by

$$dN_f = V\frac{d\mathbf{p_f}}{(2\pi)^3}, \tag{6.3}$$

where p_f is the momentum of the final state particle. Elastic scattering is a process in which only kinetic energy is transferred between the particles involved in the process. By the definition of "elastic", there are no new particles created.

6.1 Feynman rules in position space

The Feynman rules in position space is given by the following rules [111, 112, 113]:

1. At each vertex, there is a contribution of $i\int d^4X\bar{\mathcal{L}}$. Where X is the spacetime coordinate of the vertex and $\bar{\mathcal{L}}$ is the Lagrangian without the fields.

2. For a boson propagating from X to Y with four momentum P^μ, the rules depend on the boson itself.

   - W boson: $D_W(X-Y) = \int \frac{d^4P}{(2\pi)^4}\frac{-ig_{\mu\nu}}{P^2-M_W^2}e^{iP\cdot(X-Y)}$, where $g_{\mu\nu}$ is the metric tensor and M_W is the W boson mass.
   - Photon, γ:
   $$D_\gamma(X-Y) = \int \frac{d^4P}{(2\pi)^4}\frac{-ig_{\mu\nu}}{P^2}e^{iP\cdot(X-Y)} \tag{6.4}$$
   - Pion:
   $$D_\pi(X-Y) = \int \frac{d^4P}{(2\pi)^4}\frac{i}{P^2-M_\pi^2}e^{iP\cdot(X-Y)} \tag{6.5}$$
   - Nucleon:
   $$D_N(X-Y) = \int \frac{d^4P}{(2\pi)^4}\frac{i(\not{P}+M)}{P^2-M_N^2}e^{iP\cdot(X-Y)} \tag{6.6}$$

3. Each external particle with four momentum $P^\mu = (E, \mathbf{p})$, the corresponding Dirac spinor is:

   - Incoming fermion:
   $$\Psi(X) = \sqrt{\frac{M}{VE}}\,\mathcal{U}(\mathbf{p}, s)e^{-iP\cdot X} \tag{6.7}$$

- Outgoing fermion:

$$\bar{\Psi}(X) = \sqrt{\frac{M}{VE}}\,\bar{\mathcal{U}}(\mathbf{p}, s)e^{iP\cdot X} \tag{6.8}$$

Here, $\mathcal{U}(\mathbf{p}, s)$ is a Dirac plane wave for a given momentum $\bar{p}$ and spin s.

6.2 Lagrangian and reduced Lagrangian

Using the Feynman rules in position space, each vertex requires the Lagrangian but without the fields (reduced Lagrangian, $\bar{\mathcal{L}}$ from here on). For elastic scattering between a photon and an electron, the Lagrangian is given by

$$\mathcal{L}_{\gamma ee} = e\bar{\Psi}_e\gamma^\mu\Psi_e A_\mu \tag{6.9}$$

where A_μ is the four potential of the electromagnetic field, e is the elementary charge of the electron and $\overset{(-)}{\Psi}_e$ are the incoming (outgoing) electron. Therefore, the corresponding reduced Lagrangian is simply

$$\bar{\mathcal{L}}_{\gamma ee} = e\gamma^\mu \tag{6.10}$$

If one were to consider a photon scattering off a nucleon, the corresponding Lagrangian is given by

$$\mathcal{L}_{\gamma NN} = -e\bar{\Psi}_p\gamma^\mu\Psi_p A_\mu, \tag{6.11}$$

with the reduced Lagrangian being simply

$$\bar{\mathcal{L}}_{\gamma NN} = -e\gamma^\mu. \tag{6.12}$$

where now the photon couples to the proton only since the neutron is electrically neutral. To account for neutrons inside a nucleon, the gamma matrix operator, γ^μ can be replaced with a generic operator, $\hat{\Gamma}^\mu_N$, where N can be the neutron or proton. This is called the hadron current operator. This reduced Lagrangian is

$$\bar{\mathcal{L}}_{\gamma NN} = -e\big(\hat{\Gamma}^\mu_p + \hat{\Gamma}^\mu_n\big) \tag{6.13}$$

with the proton and neutron operator given by

$$\hat{\Gamma}^\mu_{p/n}(Q^2) = F_1^{p/n}(Q^2)\gamma^\mu + i\frac{F_2^{p/n}(Q^2)}{2M}\sigma^{\mu\alpha}Q_\alpha. \tag{6.14}$$

Here, Q^2 is the square of the four momentum transfer $(P_N - P)$, M is the mass of the nucleon in question and $\sigma^{\mu\alpha}$ is given by [114]

$$\frac{i}{2}(\gamma^\mu\gamma^\alpha - \gamma^\alpha\gamma^\mu). \tag{6.15}$$

Here, $F_1^{p/n}$ and $F_2^{p/n}$ are referred to as the Dirac and Pauli form factors respectively. At $Q^2 = 0$, the Dirac and Pauli form factors taken on the values

$$\begin{aligned} F_1^p &= 1, \quad F_1^n = 0 \ ; \\ F_2^p &= \kappa_p, \quad F_2^n = \kappa_n. \end{aligned} \tag{6.16}$$

Here, the Dirac form factor represents the charges of the proton and neutron and the Pauli form factor represents the anomalous magnetic moment, κ, of the proton and neutron. The form factors can be recast into the electric and magnetic Sachs form factors by

$$\begin{aligned} G_E^{p/n} &= F_1^{p/n} - \tau F_2^{p/n} \\ G_M^{p/n} &= F_1^{p/n} + F_2^{p/n}, \end{aligned} \tag{6.17}$$

where $\tau = \frac{Q^2}{4M^2}$. The Sachs form factors are related to the spatial charge G_E and Fourier transform of the spatial magnetisation distribution, G_M.

6.3 Calculating the scattering matrix element

Using the Feynman rules defined in Section 6.1 and the reduced Lagrangians defined in Section 6.2, one can calculate the scattering matrix element, S_{fi}, for the interaction.

$$\begin{aligned} S_{fi} = i \int d^4X \ i \int d^4Y \ \int \frac{d^4Q}{(2\pi)^4} \\ &\times e\bar{\Psi}_{e'}(X)\gamma^\mu \Psi_e(X) \\ &\times \frac{-ig_{\mu\nu}}{Q^2} e^{iQ\cdot(X-Y)} \\ &\times -e\bar{\Psi}_{p'}(Y)\hat{\Gamma}^\nu[(P_N - P)^2]\Psi_p(Y). \end{aligned} \tag{6.18}$$

This equation can be broken down into the leptonic part, the bosonic part and the hadronic part, given respectively by the second, third and last line of Equation 6.18.

Leptonic vertex

Focusing on the leptonic vertex, one can substitute for the Dirac spinors given in Equations 6.7 and 6.8,

$$e\bar{\Psi}_{e'}(X)\gamma^\mu \Psi_e(X) \tag{6.19}$$

becomes

$$e\sqrt{\frac{m_f}{VE_f}}\sqrt{\frac{m_i}{VE_i}}\,\bar{\mathcal{U}}(\mathbf{k_f}, s_f)\gamma^\mu \mathcal{U}(\mathbf{k_i}, s_i)e^{iK_f\cdot X}e^{-iK_i\cdot X}. \tag{6.20}$$

This can be further simplified using the definition of the leptonic current in Equation 6.21.

$$j^{\mu} = \bar{\mathcal{U}}(\mathbf{k_f}, s_f)\gamma^{\mu}\mathcal{U}(\mathbf{k_i}, s_i). \tag{6.21}$$

Using the leptonic current, the leptonic vertex simplifies to

$$e\sqrt{\frac{m_f}{VE_f}}\sqrt{\frac{m_i}{VE_i}}j^{\mu}e^{i(K_f-K_i)\cdot X} \tag{6.22}$$

Hadronic vertex

The hadronic vertex, like the leptonic vertex, can be simplified using the definition of the hadronic current and substituting for the Dirac spinors. The hadronic current is given by Equation 6.23.

$$J^{\nu} = \bar{\mathcal{U}}(\mathbf{p_N}, s_N)\Gamma^{\nu}(Q^2)\mathcal{U}(\mathbf{p_i}, s). \tag{6.23}$$

The simplified result is

$$-e\sqrt{\frac{M}{VE_N}}\sqrt{\frac{M}{VE}}J^{\nu}e^{i(P_N-P)\cdot Y} \tag{6.24}$$

Calculation

Performing the d^4X integral first using the definition of the four-dimensional Dirac delta function in Equation A.17 and denoting pre factors as A, the expression for S_{fi} becomes

$$S_{fi} = A\int \frac{d^4Q}{(2\pi)^4} \int d^4Y e^{i(P_N-P-Q)\cdot Y}(2\pi)^4\delta^4(Q - K_i + K_f)j^{\mu}J^{\nu}. \tag{6.25}$$

The Dirac delta $\delta^4(Q - K_i + K_f)$ now provides the relation $Q = K_i - K_f$. Performing the integral over Q, it becomes

$$S_{fi} = A\int d^4Y e^{i(P_N+K_f-K_i-P)\cdot Y}j^{\mu}J^{\nu}. \tag{6.26}$$

Now, performing the final integral over Y, and adding back in the pre-factors, the final expression for the elastic scattering matrix element is

$$\boxed{S_{fi} = -i\sqrt{\frac{M}{VE_N}}\sqrt{\frac{M}{VE}}\sqrt{\frac{m_f}{VE_f}}\sqrt{\frac{m_i}{VE_i}}(2\pi)^4\delta^4(K_f + P_N - K_i - P)\frac{ej_{\mu}eJ^{\mu}}{Q^2}} \tag{6.27}$$

6.3.1 Calculating the cross section

Once the scattering matrix element is obtained, we require the modulus squared of the element for the cross section with a sum over the final states and an average over the initial states. In the case of elastic electron scattering, this reduces to an average and sum over two helicity states of the electron and proton.

$$\overline{\sum}|S_{fi}|^2 = \overline{\sum} S_{fi}^* S_{fi} \tag{6.28}$$

where * denotes the complex conjugate. When using four vectors, a new index is required when multiplying an object by itself. That is to say that the modulus square term will include terms such as

$$\frac{1}{2}\sum_{s_i}\sum_{s_f}(j_\mu)^* j_\nu \overset{\text{def}}{=} L'_{\mu\nu}, \tag{6.29}$$

and

$$\frac{1}{2}\sum_{s}\sum_{s_N}(J^\mu)^* J^\nu \overset{\text{def}}{=} H^{\mu\nu}, \tag{6.30}$$

where $L'_{\mu\nu}$ and $H^{\mu\nu}$ are defined as the lepton and hadron tensor respectively and the factor of a half comes from the average and there are summations over both spin states. These tensors contain the physics for the associated vertex and due to the nature of elastic scattering being a $2 \to 2$ interaction exchanging only one boson, these two vertices can be factorised and separated. The explicit derivation of the expression for the tensors are given in Section B.1 and B.2 for the lepton and hadron tensors respectively.
Performing the average sum and square, we get

$$\overline{\sum}(S_{fi})^*(S_{fi}) = \frac{m_f m_i}{E_i E_f}\frac{M^2}{E E_N}\frac{e^4}{Q^4}\frac{1}{V^4}\Big[(2\pi)^4\delta^4(K_f + P_N - K_i - P)\Big]^2 L'_{\mu\nu}H^{\mu\nu}. \tag{6.31}$$

It is often convention to absorb the lepton masses into the definition of the lepton tensor. That is.

$$L_{\mu\nu} \overset{\text{def}}{=} m_i m_f L'_{\mu\nu}. \tag{6.32}$$

Using the identity in Equation A.18, the final expression for the squared matrix element is

$$\overline{\sum}(S_{fi})^*(S_{fi}) = \frac{m_f m_i}{E_i E_f}\frac{M^2}{E E_N}\frac{e^4}{Q^4}\frac{T}{V^3}(2\pi)^4\delta^4(K_f + P_N - K_i - P)L_{\mu\nu}H^{\mu\nu}. \tag{6.33}$$

Finally, putting this expression for the squared matrix element into Equation 6.1 and using Equation 6.3, the expression for the cross section becomes

$$d^6\sigma = \frac{m_f m_i}{E_i E_f}\frac{M^2}{E E_N}\frac{e^4}{Q^4}\frac{1}{V\Phi_{\text{inc}}}(2\pi)^4\delta^4(K_f + P_N - K_i - P)L_{\mu\nu}H^{\mu\nu}\frac{d^3\mathbf{k_f}}{(2\pi)^3}\frac{d^3\mathbf{p_N}}{(2\pi)^3}. \quad (6.34)$$

It is important to note that the above equation for the six-fold differential cross section is Lorentz invariant and so is correct in all frames of reference. The constant terms in the beginning can be grouped as K and then one obtains a general equation for the differential cross section for such a given interaction.

$$d^6\sigma = K(2\pi)^4\delta(K_f + P_N - K_i - P)L_{\mu\nu}H^{\mu\nu}\frac{d^3\mathbf{k_f}}{(2\pi)^3}\frac{d^3\mathbf{p_N}}{(2\pi)^3}, \quad (6.35)$$

where $K = \frac{M^2}{E_f E_N}\frac{1}{\sqrt{(K_i\cdot P)^2 - m_i^2 M^2}}\frac{(4\pi\alpha)^2}{Q^4}$.

Once the general six-fold differential cross section is obtained, it can be integrated over a desired set of variables using the Dirac delta function and leave the tripled differential cross section in either the lepton or nucleon variables. Integrating over the nucleon variables (i.e. performing experimental measurements of leptons) leaves

$$\frac{d^3\sigma}{d\mathbf{k_f}} = \frac{K}{(2\pi)^2}\delta(E_f + E_N - E_i - E)L_{\mu\nu}H^{\mu\nu}. \quad (6.36)$$

This can be further simplified as

$$\frac{\mathrm{d}^3\sigma}{\mathrm{d}k_f\mathrm{d}\Omega_f} = k_f^2\int \mathrm{d}\Omega_N \ \frac{\mathrm{d}^5\sigma}{\mathrm{d}\mathbf{k_f}\mathrm{d}\Omega_N}. \quad (6.37)$$

The remaining Dirac delta in Equation 6.36 can be used to integrate over the remaining variables. However, in this case the variables are not independent and so a more careful treatment needs to be performed using the identity given in Equation A.19.

Chapter 7

Neutrino-nucleon elastic scattering

In order to calculate the neutrino-nucleon scattering cross section, minimal changes to the electromagnetic interaction framework introduced in the Section 6 are required. The key changes come from the electroweak interaction being a $V - A$ (vector - axial) interaction due to the chiral nature of the Lagrangian, and the use of a weak propagator instead of a photon [112]. In this chapter, the changes required to the Lagrangian, lepton tensor and hadron tensor are explained. The neutrino-nucleon differential cross section is then calculated. The form factors introduced in this framework are then explained.

7.1 Weak boson Lagrangian

The Lagrangian for a W boson-neutrino-lepton vertex is given by [113, 115]

$$\mathcal{L}_{W\nu_l l} = \frac{-g}{2\sqrt{2}}\Big[\bar{\Psi}_l\gamma^\mu(1-\gamma^5)\Psi_{\nu_l}W^-_\mu + \bar{\Psi}_{\nu_l}\gamma^\mu(1-\gamma^5)\Psi_l W^+_\mu\Big]. \tag{7.1}$$

Here, g is the weak coupling constant. Ψ_l and Ψ_ν are the Dirac spinors for the lepton and neutrino respectively. The W^+_μ field creates a W^- boson or annihilates a W^+ boson. Conversely, the W^- field creates a W^+ boson or annihilates a W^- boson.
The Lagrangian for a W boson-nucleon-nucleon vertex is

$$\mathcal{L}_{WNN} = \frac{-g\cos(\theta_c)}{2\sqrt{2}}\Big[\bar{\Psi}_p\gamma^\mu(1-\gamma^5)\Psi_n W^+_\mu + \bar{\Psi}_n\gamma^\mu(1-\gamma^5)\Psi_p W^-_\mu\Big]. \tag{7.2}$$

Here, the Cabibbo mixing angle, $\cos(\theta_c)$ is included to account for the quark flavour change when a proton changes to a neutron or vice versa in the weak interaction. The Dirac spinors have the same definition as above but for protons and neutrons respectively. Similar to what is done in the electron scattering case, the nucleon vertex can be re-expressed with a vector operator; however, now an axial vector component is included. In general, the hadronic current can be expressed as $J^\mu = a_V\gamma^\mu + a_A\gamma^\mu\gamma^5$ where for the electromagnetic case in electron scattering, $a_V = 1$ and $a_A = 0$ [115]. For the electroweak

case in neutrino scattering, $a_A = \mp 1$ with -1 for neutrinos and $+1$ for antineutrinos. The weak hadronic current is then expressed as $J^\mu_{\text{weak}} = J^\mu_V - J^\mu_A$. Thus, in Equation 7.2, the operator $\gamma^\mu(1-\gamma^5)$ is replaced with the difference of two operators, the vector and axial vector operators, $\hat{\Gamma}^\mu_V(Q^2) - \hat{\Gamma}^\mu_A(Q^2)$. Q^2 is defined in the same way as the electron-scattering case. This leads to

$$\mathcal{L}_{WNN} = \frac{-g\cos(\theta_c)}{2\sqrt{2}}\Big[\bar{\Psi}_p(\hat{\Gamma}^\mu_V - \hat{\Gamma}^\mu_A)\Psi_n W^+_\mu + \bar{\Psi}_n(\hat{\Gamma}^\mu_V - \hat{\Gamma}^\mu_A)\Psi_p W^-_\mu\Big]. \tag{7.3}$$

7.1.1 Neutral current interactions

Though not the focus of this thesis, neutrinos can also undergo a NC interaction through the exchange of a Z boson. The general formalism is similar to that of CC interactions, with the leptonic and hadronic tensors taking the same structure but with modified coupling constants and isospin combinations in the weak current. In the NC case, the species of the hadron, and so isospin, is unchanged. The coupling constant for the cross section is also modified by a factor of $\sin^2(\theta_W)$, where θ_W is the Weinberg angle.

7.2 Connection between weak and electromagnetic form factors

The vector and axial-vector operators, in a manner similar to Equation 6.14, can be expressed in terms of the form factors [114].

$$\begin{aligned}\hat{\Gamma}^\mu_V(Q^2) &= F_1^V(Q^2)\gamma^\mu + i\frac{F_2^V(Q^2)}{2M}\sigma^{\mu\alpha}Q_\alpha \\ \hat{\Gamma}^\mu_A(Q^2) &= G_A(Q^2)\gamma^\mu\gamma^5 + F_p(Q^2)Q^\mu\gamma^5.\end{aligned} \tag{7.4}$$

Here, $G_A(Q^2)$ is known as the axial-vector form factor. $F_p(Q^2)$ is known as a pseudoscalar axial form factor. This parameterisation of the nucleon current operator is known as the CC2 formalism [114].

In electromagnetic interactions, such as electron scattering, the Dirac and Pauli form factors, $F_1^{p/n}$ and $F_2^{p/n}$, are used to describe the electromagnetic current. The current itself contains an isoscalar and isovector contribution, $J^\mu_{\text{EM}} = J^\mu_{(0)} + J^\mu_{(1)}$, where (0) and (1) are the respective isoscalar and isovector contributions. This is described in more detail in Appendix C. The Dirac and Pauli form factors can be linearly combined to form isoscalar and isovector form factors. The isoscalar contribution has $I = 0$ and is proportional to the identity operation in isospin space. Therefore, it is given by $F_i^{(0)} = F_i^p + F_i^n$. The isovector contribution has $I = 1$ and involves a change of sign between operating on protons to neutrons. This is given by $F_i^{(1)} = F_i^p - F_i^n$.

In weak CC interactions, the weak vector form factors describe the vector contribution to the weak current. The conserved vector current hypothesis, described in Appendix C, provides a direct connection between the weak vector form factors and the electromagnetic isovector form factors. Therefore,

$$F_i^V(Q^2) = F_i^{(1)}(Q^2) = F_i^p(Q^2) - F_i^n(Q^2). \tag{7.5}$$

This enabled the weak vector form factors to be well constrained by electron scattering data and taken on a dipole parameterisation. At higher values of Q^2, deviations from this dipole form have been observed and corrections can be applied [116].

The weak CC interaction also contains contributions from the axial-vector and pseudoscalar currents and is described by the axial-vector and pseudoscalar form factors, $G_A(Q^2)$ and $F_p(Q^2)$. The axial-vector current, unlike the vector current, is not conserved in reality. It is conserved only in the limit that quarks and pions are massless. However, the divergence of the axial-vector current is proportional to the pion field. This leads to the partially conserved axial current hypothesis and, alongside pion pole dominance, allows for the pseudoscalar form factor to be related to the axial-vector form factor by

$$F_p(Q^2) \approx \frac{4M^2}{m_\pi^2 + Q^2} G_A(Q^2). \tag{7.6}$$

The Q^2 scaling and parameterisation of the axial-vector form factor is less known and is the largest contributor to the uncertainty in CCQE neutrino-nucleus interactions. It is often given a "dipole" parameterisation:

$$G_A(Q^2) = \frac{g_A}{(1 + Q^2/M_A^2)^2}, \tag{7.7}$$

where g_A is the axial vector coupling constant given by 1.2695 ± 0.0029 from β-decay measurements [117]. M_A is the least constrained parameter but from the 1970s onward, direct measurements of M_A using light nuclei reported values of M_A in the range of [0.80, 1.07] GeV/c^2 [118, 119, 120, 121, 122, 123]. More recently, the MINERvA experiment reported a measurement of M_A using muon antineutrinos interacting on hydrogen in the plastic scintillator detector [124]. A fit to the "z-expansion" parameterisation for $G_A(Q^2)$ is also shown [125]. In 2023, lattice-QCD (LQCD) calculations reported that better control over the Q^2 dependence, and therefore reduced uncertainties, can be obtained. However, this comes at the expense of requiring a lot of computation time [126]. Experimental and theoretical advances all point to the conclusion that the dipole parameterisation, or value of M_A, is inconsistent with data.

7.3 Weak lepton tensor

The lepton tensor is similar to that in the electromagnetic case in Equation B.24. However, because of the weak current that involves an additional component of the axial vector,

there is an additional term. The weak lepton tensor is given below.

$$L_{\mu\nu} \stackrel{def}{=} m_i m_f L'_{\mu\nu} = \frac{1}{2}\Big[K_{i,\mu}K_{f,\nu} + K_{i,\nu}K_{f,\mu} - g_{\mu\nu}(K_i \cdot K_f - m_i m_f) + i a_A \epsilon_{\mu\nu\alpha\beta} K_i^{\alpha} K_f^{\beta}\Big]. \quad (7.8)$$

The additional term involves the fully antisymmetric levi-civita tensor ϵ. Here a_A is known as neutrino helicity and is defined the same as in Section 7.1. This additional term means that the lepton tensor is different for neutrinos and antineutrinos.

7.4 Weak hadron tensor

After substituting the weak hadron current operator of Equation 7.4 and Equation 7.3 into the general equation for the hadron tensor given in Equation 6.23, the weak hadron is given as

$$\begin{aligned} H^{\mu\nu} = &- W_1(Q^2) g^{\mu\nu} + W_2(Q^2)\frac{P^{\mu}P^{\nu}}{M^2} + iW_3(Q^2)\epsilon^{\mu\nu\alpha\beta}\frac{P_{\alpha}P_{\beta}}{2M^2} \\ &+ W_4(Q^2)\frac{Q^{\mu}Q^{\nu}}{M^2} + W_5(Q^2)\frac{P^{\mu}Q^{\nu} + Q^{\mu}P^{\nu}}{2M^2}. \end{aligned} \quad (7.9)$$

Here, the hadron tensor is given in terms of give structure functions. The structure functions can be expressed in terms of the form factors.

$$\begin{aligned} &\bullet\ W_1(Q^2) = \tau\big[(F_1^V + F_2^V)^2 + G_A^2\big] + G_A^2 \\ &\bullet\ W_2(Q^2) = (F_1^V)^2 + \tau(F_2^V)^2 + G_A^2 \\ &\bullet\ W_3(Q^2) = 2G_A(F_1^V + F_2^V) \\ &\bullet\ W_4(Q^2) = \frac{(F_2^V)^2}{4}(\tau - 1) - \frac{F_1^V F_2^V}{2} - MF_P G_A + \tau M^2 F_P^2 \\ &\bullet\ W_5(Q^2) = W_2(Q^2). \end{aligned} \quad (7.10)$$

Here, $\tau = \frac{|Q|^2}{4M^2}$. The above structure functions are functions of Q^2 as are the form factors, however it is left out of the above equation for brevity.

7.5 Cross section

The final change required for the neutrino-nucleon cross section is to replace the electromagnetic coupling constant to the electroweak charged current coupling constant. In the limit where the four momentum transfer, $|Q|^2/M_W^2 \ll 1$, that is, the energy transfer in the interaction is much less than the W boson mass scale, the coupling constant is

$$\frac{\alpha^2}{4\pi} \rightarrow \frac{G_F^2 \cos^2(\theta_c)}{2}, \quad (7.11)$$

where $G_F \approx 1.17 \times 10^{-5}$ GeV^{-2} is the Fermi coupling constant and $\cos(\theta_c) \approx 0.974$ is the Cabibbo quark mixing angle.

The general equation for the neutrino-nucleon cross section is

$$d^6\sigma = K(2\pi)^4\delta^4(K_f + P_N - K_i - P)L_{\mu\nu}H^{\mu\nu}\frac{d^3\mathbf{k_f}}{(2\pi)^3}\frac{d^3\mathbf{p_N}}{(2\pi)^3}, \tag{7.12}$$

where $K = \frac{M^2}{E_f E_N}\frac{1}{\sqrt{(K_i\cdot P)^2 - m_i^2 M^2}}\frac{G_F^2\cos^2(\theta_c)}{2}$. In the case of neutrinos, the mass can be neglected. Therefore, $m_i \approx 0$ and this reduces the above K constant to be

$$K = \frac{M^2}{E_f E_N}\frac{1}{|K_i \cdot P|}\frac{G_F^2\cos^2(\theta_c)}{2}. \tag{7.13}$$

Chapter 8

From nucleon to nucleus scattering

Interacting with a nucleus rather than a nucleon introduces complexity into the scattering problem because the nucleon is bound within the nucleus with other nucleons. Therefore, new effects must be taken into account in both the initial and final states. Further, the nucleus itself must be modelled. In this section, the initial and final states, along with their respective nuclear effects, are explained. The impact of the nuclear effects are also shown. Nuclear models are briefly shown and some CCQE neutrino-nucleus scattering models are introduced.

8.1 Initial state and nuclear models

Changes in the initial state are required to change from nucleon scattering to nucleus scattering because the nucleon is no longer free.

8.1.1 The impulse approximation

Quite obviously, the first point is with which nucleon in the nucleus to interact. A common approximation made to approach this question is called the impulse approximation (IA) [127]. The IA assumes an interaction on a single nucleon and then sums this contribution across all nucleons in the nucleus. The other nucleons not present in the interaction are referred to as spectator nucleons. Mathematically, this converts it from a many-body problem to a single-body problem. Considering an initial nucleus A, residual nucleus $A-1$ and scattered nucleon N,

$$J^{\mu}_{\text{hadron}} = \langle N, A-1 | \, \mathcal{O}^{\mu}_{\text{many body}} \, | A \rangle \, , \tag{8.1}$$

under the IA becomes

$$J^{\mu}_{\text{hadron, IA}} = \int \mathrm{d}^3\mathbf{p} \bar{\Psi}_f(\mathbf{p_N}, \mathbf{q}+\mathbf{p}) \mathcal{O}^{\mu}_{\text{one body}} \Psi_i(\mathbf{p}). \tag{8.2}$$

Here, $\mathbf{p}$ is the three-momentum of the initial nucleon, $\mathbf{p_N}$ is the three-momentum of the scattered nucleon and $\mathbf{q}$ is the three-momentum transfer. Ψ_f and Ψ_i are the final- and

initial-state wavefunctions. The integral over the initial nucleon momentum enables the summation over the nucleons in the nucleus. The one-body CCQE operator is the same as defined in Equation 7.4 with electroweak form factors.

Under the IA, the cross section is then the incoherent sum over all the active nucleons (nucleons which take part in the interaction) in the nucleus. This is shown below where S_{fi} is the scattering matrix element defined in previous sections.

$$\sigma_{\mathrm{QE}} \propto \sum_{\text{active nucleons}} |S_{fi}|^2 = \sum_{\text{active nucleons}} K(2\pi)^4 \delta(K_f + P_N - K_i - P) L_{\mu\nu} H^{\mu\nu} \frac{\mathrm{d}^3\mathbf{k_f}}{(2\pi)^3} \frac{\mathrm{d}^3\mathbf{p_N}}{(2\pi)^3}. \tag{8.3}$$

The right side of Equation 8.3 is the same as defined in the single nucleon scattering case.

8.1.2 Initial-state wavefunctions and nuclear shells

The nucleon that undergoes the interaction is within the nucleus and therefore bound by a nuclear potential. There are many choices for the description of the initial state wavefunctions and whether to include nuclear potentials. All approaches to this using a wave equation leads to the concept of nuclear shells—nucleons within the nucleus occupy nuclear shells in a fashion similar to electron shells. The different shells have different ground-state energies which can be thought of as the binding energy of that nucleon. The simplest case would be to use the Schrodinger equation and neglect the nuclear potential. The solutions to this would yield wavefunctions for each energy eigenvalue. However, this description is both non-relativistic and neglects the nuclear potential. A more sophisticated approach would be to use the Dirac equation, thereby retaining spin and relativistic information. Using nuclear potentials, including that of the Coulomb field, would then produce initial-state wavefunctions that are relativistic, retain spin information, include couplings to the nuclear potential and include correct differences due to Coulomb effects for protons.

The initial-state wavefunctions will likely be solved in position space or momentum space. In position space, it provides information about where the nucleon is likely to be for a given nuclear shell. In momentum space, however, it provides information about the likely initial nucleon momentum. This initial momentum is referred to as "Fermi momentum" and can directly bias neutrino energy reconstruction based on Equation 1.32.

8.1.3 Nuclear correlations

Nucleon wavefunctions within the nucleus can overlap with another nearby nucleon. When this happens, the overlap integral between the two wavefunctions is large. Physically, this manifests itself as a binary system of two nucleons with high relative momentum [128].

The binary system itself has low momentum and is therefore still bound within the nucleus. If a lepton interacts with one of the correlated nucleons as is removed from the nucleus, the other correlated nucleon now has a high momentum and is also ejected from the nucleus. This lepton-nucleus interaction, despite if the interaction is CCQE, two final-state nucleons are ejected. This is referred to as short-ranged correlations (SRC). The first and second ejected nucleon are referred to as the primary and SRC (or secondary) nucleon respectively.

To a first-order approximation, the momentum of the SRC nucleon is equal and opposite to the initial momentum of the primary nucleon. This results in a back-to-back ejection in the centre-of-mass frame of the SRC nucleons. The presence of SRCs affects the shell structure of the nucleus, reducing the expected shell occupancies by around 20% [128].

8.2 Final state

The description of the final state becomes more complicated in the nucleus scattering case. In this section, the main nuclear effects are introduced along with different ways to theoretically model them.

8.2.1 Final-state interactions

In the lepton-nucleon scattering case, the scattered nucleon is completely free and therefore no further consideration is required. In the lepton-nucleus scattering case, the scattered nucleon is ejected from the nucleus and therefore must traverse the nuclear medium before leaving. The journey of the nucleon through the nucleus is theoretically complex to model. The momentum of the scattered nucleon is no longer known while it is traversing the nuclear medium and only the "asymptotic momentum", the momentum far away from the nucleus is originated, is known. There are also many re-interactions that can take place, some producing extra particles which can then be re-absorbed or ejected themselves. These re-interactions are referred to as final-state interactions (FSI) and there are two main types of FSI:

- Elastic FSI: a process where only kinetic energy is transferred, meaning that the initial and final quantum states are the same (e.g. the same particle).
- Inelastic FSI: a process where the initial and final quantum states are different. This could be due to e.g. a change in the type or number of particles between the initial and final states, or leaving the final nucleus in an excited state.

Beginning first with elastic FSI, mathematically this occurs because the dispersion relation of the scattered nucleon gets altered by the presence of the nuclear potential. Therefore, the final-state wavefunction must be a solution of the wave equation with this potential taken into account. This further branches into two approximations: the plane-wave impulse approximation (PWIA) and the distorted-wave impulse approximation (DWIA).

PWIA

The simplest solution to this is to ignore the potential altogether. In this approximation, the final-state wavefunction represents a free plane wave. Mathematically, this produces a simpler calculation, but fails to capture any elastic FSI in the final-state wavefunction. The Fourier transform of a plane wave being a Dirac delta function is fundamentally what makes this approach computationally simpler. In this case, the integrals in the cross section are trivial, and the momentum inside the nucleus is the same as the asymptotic momentum.

DWIA

Including the nuclear potential into the final-state wavefunction requires the wave equation to include the nuclear potential. The final-state wavefunction represents a "distorted wave". In the DWIA, the momentum inside the nucleus cannot be known, and only the asymptotic momentum can be known. This can be visualised below in Figure 8.1. This approach is often computed in a partial-wave expansion, meaning the calculation is summed over many angular momentum quantum number contributions. This involves solving for the initial-state wavefunction for each quantum-number contribution. Therefore, this approach is more computationally expensive but captures elastic FSI depending on the nuclear potential chosen.

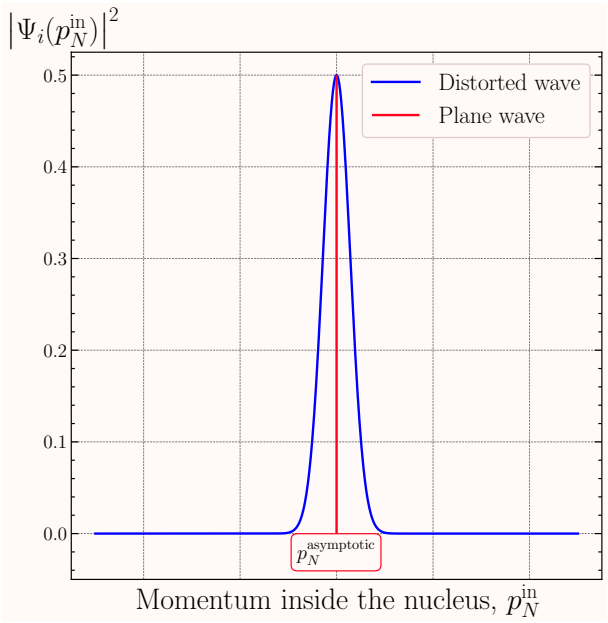

Figure 8.1: A plane wave approach in lepton-nucleus scattering theory results in the asymptotic momentum matching the momentum of the particle as it traverses the nuclear medium. A distorted wave approach breaks this equivalence. In this visualisation, the distorted wave momentum distribution is no longer a Dirac delta and is smeared. The y-axis is written in arbitrary units.

8.2.2 Pauli blocking and the Pauli exclusion principle

The Pauli exclusion principle states that no two spin-1/2 particles can occupy the same quantum state [129]. In lepton-nucleus scattering, this becomes important when not enough momentum is transferred to the scattered nucleon and it cannot leave the nuclear system. If this happens, the nucleon must try to occupy a nuclear state which is already occupied by a spectator nucleon. This is forbidden by the Pauli exclusion principle and so this interaction does not happen. In lepton-nucleus scattering, this is referred to as "Pauli blocking". This can be visualised below in Figure 8.2.

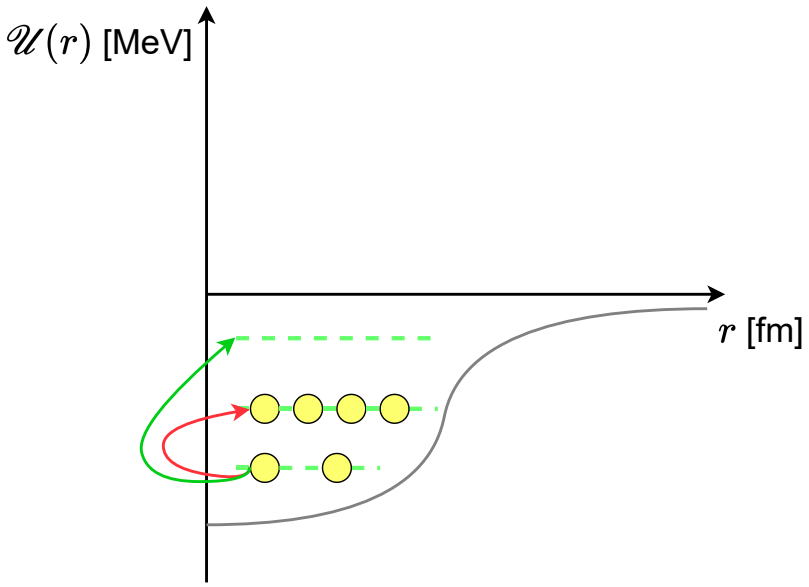

Figure 8.2: A nucleon (yellow sphere) in a nuclear state can only occupy empty states (given by the green transition arrow). Due to the Pauli exclusion principle, a nucleon cannot occupy a state that is already occupied by another spin-1/2 particle (given by the red transition arrow). Here the black line indicates an arbitrary nuclear potential as a function of radial distance from the centre of the nucleus. The potential depth, $\mathcal{U}(r)$ is of arbitrary scale.

Mathematically, this can be described by considering two wavefunctions, each describing two particles in a system, $\psi(x_1, x_2) = \psi_\alpha(x_1)\psi_\beta(x_2)$ and $\psi'(x_1, x_2) = \psi_\beta(x_1)\psi_\alpha(x_2)$. Here, ψ_α and ψ_β are the wavefunctions of two identical particles. The two are indistinguishable so the eigenvalue solutions to that quantum system for two identical particles is the same. However, on exchanging the two particles, it can be written as:

$$\psi'(x_1, x_2) = \psi(x_2, x_1). \tag{8.4}$$

Fermions are described as having antisymmetric wavefunctions. This means that under

exchange of two particles in the wavefunction, a negative sign is introduced.

$$\psi(x_1, x_2) = -\psi(x_2, x_1). \tag{8.5}$$

This antisymmetric nature must be taken into account in the final averaged wavefunction. Therefore, if two fermions are in the same potential, the resulting wavefunction is

$$\begin{aligned}\chi(x_1, x_2) &= \frac{1}{\sqrt{2}}\Big(\psi(x_1, x_2) - \psi'(x_1, x_2)\Big) \\ &= \frac{1}{\sqrt{2}}\Big(\psi(x_1, x_2) - \psi(x_2, x_1)\Big) \\ &= \frac{1}{\sqrt{2}}\Big(\psi_\alpha(x_1)\psi_\beta(x_2) - \psi_\alpha(x_2)\psi_\beta(x_1)\Big).\end{aligned} \tag{8.6}$$

If the two fermions occupy the same state, that is $x_1 = x_2 = x$, then

$$\begin{aligned}\psi(x_1 = x, x_2 = x) &= \psi_\alpha(x)\psi_\beta(x), \\ \psi'(x_1 = x, x_2 = x) &= \psi_\beta(x)\psi_\alpha(x),\end{aligned} \tag{8.7}$$

and so the overall wavefunction $\chi(x_1 = x, x_2 = x) = 0$. The probability of the two fermions being in the same place (the same state) is 0.

The result is that, at zero temperature, fermions occupy all the available states from the lowest energy level up to a point called the Fermi energy. This also gives rise to the "Fermi momentum" as described in Section 8.1.2. All states above the Fermi energy are free and this is illustrated below in Figure 8.3. This is often described as the "Fermi sea" of states. At temperatures above 0 K, the fermions will receive some thermal energy and excite slightly above the Fermi energy.

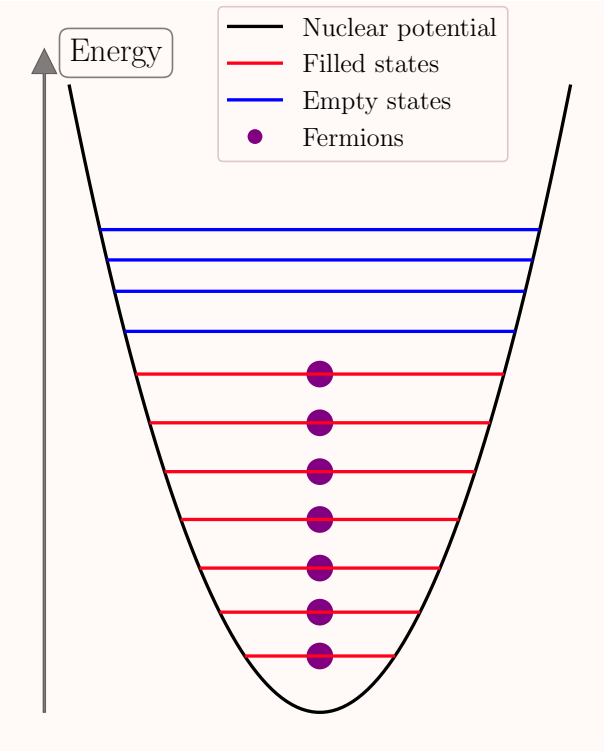

Figure 8.3: Nuclear potential is purely for illustrative purposes and is arbitrary

A more sophisticated approach shows that fermions that have all the same quantum numbers of a system cannot occupy the same state. This means that two fermions with spin up and spin down can occupy two distinct states in the space where quantum numbers form a basis.

8.3 Nuclear models and quasi-elastic scattering

A nuclear model is required to model quasi-elastic lepton-nucleus scattering. As metioned previously, that requires choosing how to model the initial state. In this section, following closely Ref. [130], the details of some nuclear models and how to obtain the lepton-nucleus scattering cross section are explained. Electron-nucleus inclusive cross-section data comparisons are shown to benchmark these models.

8.3.1 Global relativistic Fermi gas

The simplest model is known as a global Fermi gas model. This description arises from treating the nucleus as an infinite gas of non-interacting identical fermions in thermodynamic equilibrium. These particles are in an infinite potential well within the nucleus.

The number of particles per energy level is given by the following Fermi-Dirac function

$$f(p,T) = \frac{1}{1+\exp\left(\frac{\sqrt{p^2+M^2}-\sqrt{p_F^2+M^2}}{k_B T}\right)}. \tag{8.8}$$

Here, p_F is the Fermi momentum given by $(3\rho\pi^2)^{1/3}$ where ρ is the nuclear density which is constant at a given temperature. $k_B \approx 8.617 \times 10^{-5}$ eV K^{-1} is the Boltzmann constant. T is the temperature of the system. As $T \to 0$, the above density function approaches a Heaviside step function

$$\begin{aligned} f(p, T \to 0) &\to \Theta(p_F - p) \\ \Theta(p - p_F) &= \begin{cases} 1 & p < p_F \\ 0 & p > p_F. \end{cases} \end{aligned} \tag{8.9}$$

At non-zero temperatures, $T > 0$, the density function tends to a Fermi-Dirac function. In this case, Pauli blocking is implemented in the same way using a step function. The effect of temperature on the density function, $f(p,T)$, is shown in Figure 8.4.

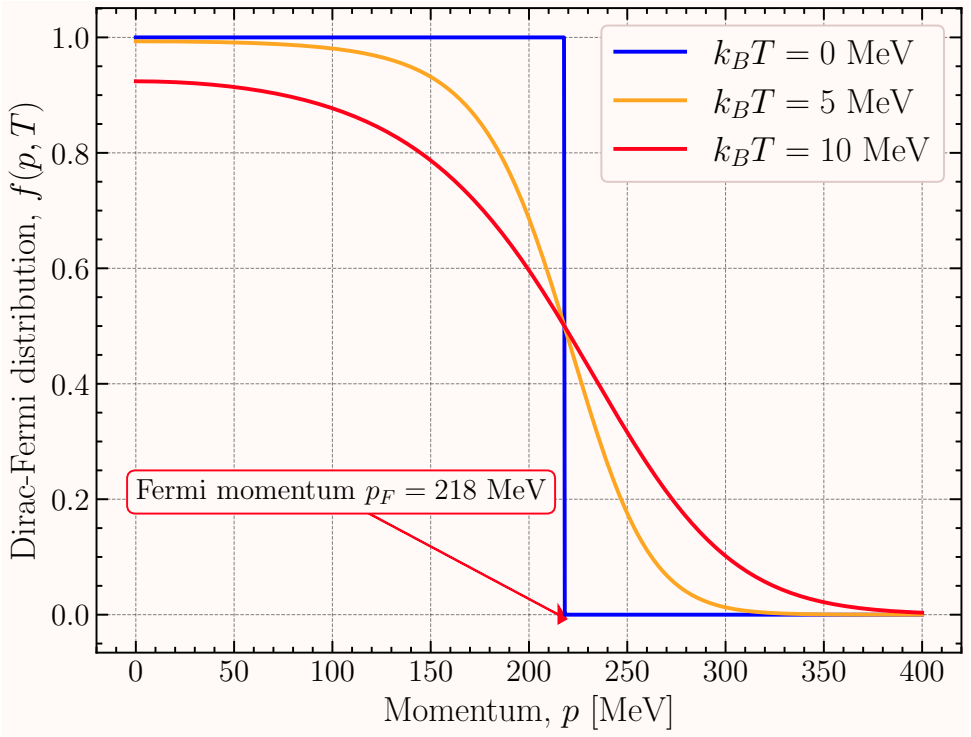

Figure 8.4: Density function for the Fermi gas model shown for different temperatures. As the temperature tends to 0 K, the density function tends to a Heaviside step function. In this example, the Fermi momentum for carbon is chosen to be 218 MeV. k_B is set to 1.

The total number of particles in the system is given as a sum over all the quantum numbers of the density function.

$$N = \sum_{\alpha} f(p, T) \tag{8.10}$$

In this system, the quantum numbers are the momentum and spin of the particles. It is easier to write it as an integral over the momenta of the particles and a sum over the spins.

$$N = \frac{V}{(2\pi)^3} \int \mathrm{d}\mathbf{p} \sum_{s} f(p, T) = 2\frac{V}{(2\pi)^3} \int \mathrm{d}\mathbf{p} f(p, T). \tag{8.11}$$

Here, $s = \pm\frac{1}{2}$ is the spin of the particle and V is the volume of the system. The summation over the particle spins introduces a simple factor of 2.

A momentum density distribution, $n(p)$, can be defined as the probability of finding a particle within the nucleus with momentum p. By definition,

$$\int \mathrm{d}\mathbf{p}\ n(p) = N \tag{8.12}$$

where the density function is a function of the magnitude of the momentum only. Comparing this with Equation 8.11, an expression for the volume is obtained.

$$V(T) = \frac{(2\pi)^3}{2} \frac{N}{\int \mathrm{d}\mathbf{p} f(p, T)}, \tag{8.13}$$

and so the momentum density can be expressed as

$$n(p, T) = N \frac{f(p, T)}{\int \mathrm{d}\mathbf{p} f(p, T)}. \tag{8.14}$$

The momentum density is often shown including a phase space factor of p^2 to account for the spherical symmetry. Both descriptions of the momentum density are shown below in Figure 8.5.

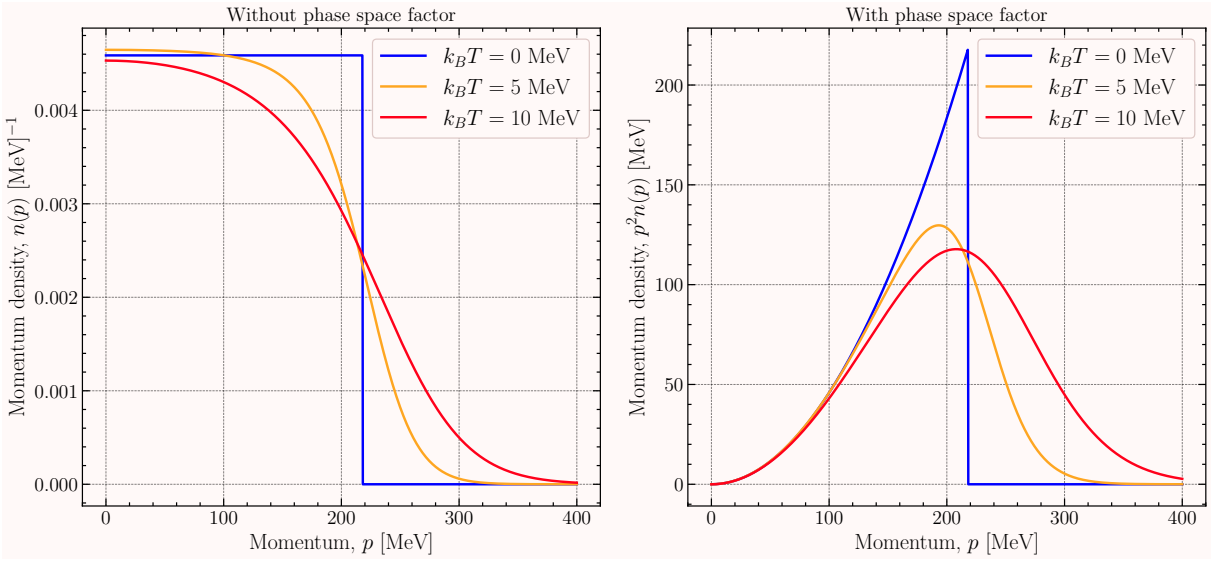

Figure 8.5: Momentum density of a Fermi gas model shown with and without the phase space factor of p^2. The density is normalised such that integral of $n(p)dp = 1$. The y-axis scale is arbitrary. k_B is set to 1.

With this nuclear model and its description of the initial-state nucleons, it is now trivial to get the lepton-nucleus cross section. As per the IA, the lepton-nucleon cross section can be average over the number of active nucleons. At $T = 0$ K, the total differential cross section is

$$\frac{\mathrm{d}^6\sigma}{\mathrm{d}\mathbf{k_f}\mathrm{d}\mathbf{p_N}} = \frac{N}{(4/3)\pi p_F^3}\int \mathrm{d}E\ \delta(E - \sqrt{p^2+M^2}\ )\int \mathrm{d}^3\mathbf{p}\ \Theta(p_F - p)\Theta(p_N - p_F) \times \frac{K}{(2\pi)^2}\delta^4(K_f + P_N - K_i - P)L_{\mu\nu}H^{\mu\nu}. \tag{8.15}$$

This differential cross section uses plane waves for the final state, hence it is a PWIA model. Equation 8.15 can be broken down into physically motivated sections:

- $\frac{K}{(2\pi)^2}\delta^4(K_f + P_N - K_i - P)L_{\mu\nu}H^{\mu\nu}$ is the elastic lepton-nucleon cross section from Equation 6.35.
- The two integrals are averages over the energy and momentum of the nucleons within the nucleus.
- $\Theta(p_F - p)$ is the momentum density distribution and is a step function at zero temperature.
- $\Theta(p_N - p_F)$ is the implementation of Pauli blocking such that all states above the Fermi energy are free.

- The prefactor $\frac{N}{(4/3)\pi p_F^3}$ is a normalisation factor and normalises to the number of nucleons.
- $\delta(E - \sqrt{p^2 + M^2}\ )$ ensures that the scattered particle is on-shell.

If $T > 0$ K, then the step function $\Theta(p_F - p)$ is replaced by a Fermi-Dirac function as shown in Figure 8.4. The inclusive cross section, given in Equation 6.37, is shown against electron-nucleus scattering data in Figure 8.6. An important point of the global Fermi gas model is that the binding energy of the initial nucleon is not included. It is true that the nuclear model does predict a potential well in which protons and neutrons have a slightly different well depth due to the Coulomb force. The Fermi energy for protons and neutrons is approximately 8 MeV deep and this is approximately the binding energy per nucleon. However, this information is not taken into account in Equation 8.15 and must be added. This results in a horizontal shift of the differential cross-section distributions by the value of the binding energy. This is also shown in Figure 8.6.

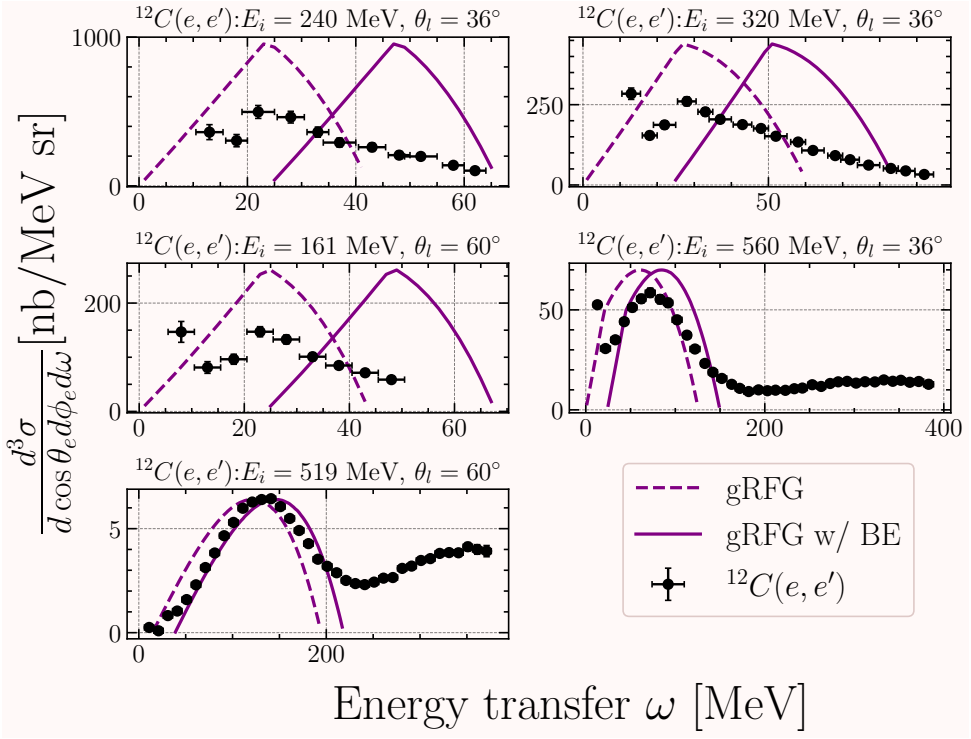

Figure 8.6: The global relativistic Fermi gas model from Ref [130] compared to electron-nucleus scattering data from Ref. [131] carbon. The solid line shows the model including a binding energy shift that is not present in the model.

8.3.2 Local Fermi gas

A local Fermi gas model is similar to the global Fermi gas model, but with the difference that the Fermi momentum is now radially dependent.

$$p_F = \left(3\pi^2\rho(r)\right)^{1/3}. \tag{8.16}$$

Here, $\rho(r)$ is the nuclear density given by $\rho(r) = \frac{N(r)}{V(r)}$. The nuclear density is normalised such that

$$\int \mathrm{d}\mathbf{r}\ \rho(r) = 4\pi \int \mathrm{d}r\ r^2\rho(r) = N. \tag{8.17}$$

This means that the nuclear density per nucleon can be used as a probability density function. The nuclear density is taken from theoretical models or from electron-nucleus scattering data. The approach from Ref. [132] is given as

$$\rho(r) = \rho_0\left[1 + a_{n,p}\left(\frac{r}{R_{n,p}}\right)^2\right]e^{-\left(\frac{r}{R_{n,p}}\right)^2} \tag{8.18}$$

with the values of $R_{p/n}$ and $a_{p/n}$ being given in Table 8.1.

Nucleus	R_p [fm]	R_n [fm]	a_p	a_n
^{12}C	1.692	1.692	1.082	1.082
^{16}O	1.833	1.815	1.544	1.529

Table 8.1: The parameters are split by proton (p) and neutron (n). For carbon, the proton and neutron parameters are the same. For oxygen, the proton and neutron parameters differ slightly.

Figure 8.7 and 8.8 show the nuclear density as a function of position in the nucleus, r, for carbon and oxygen respectively.

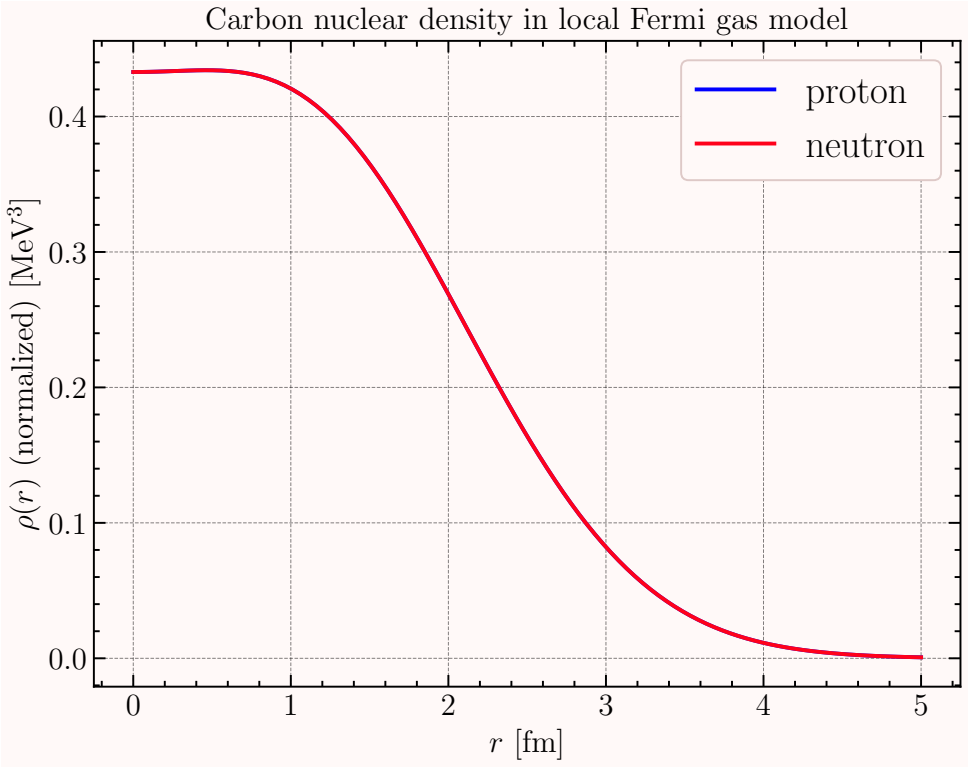

Figure 8.7: Nuclear density as a function of position in nucleus for carbon. The curves for protons and neutrons overlap. The curves are normalised such that the areas are unity.

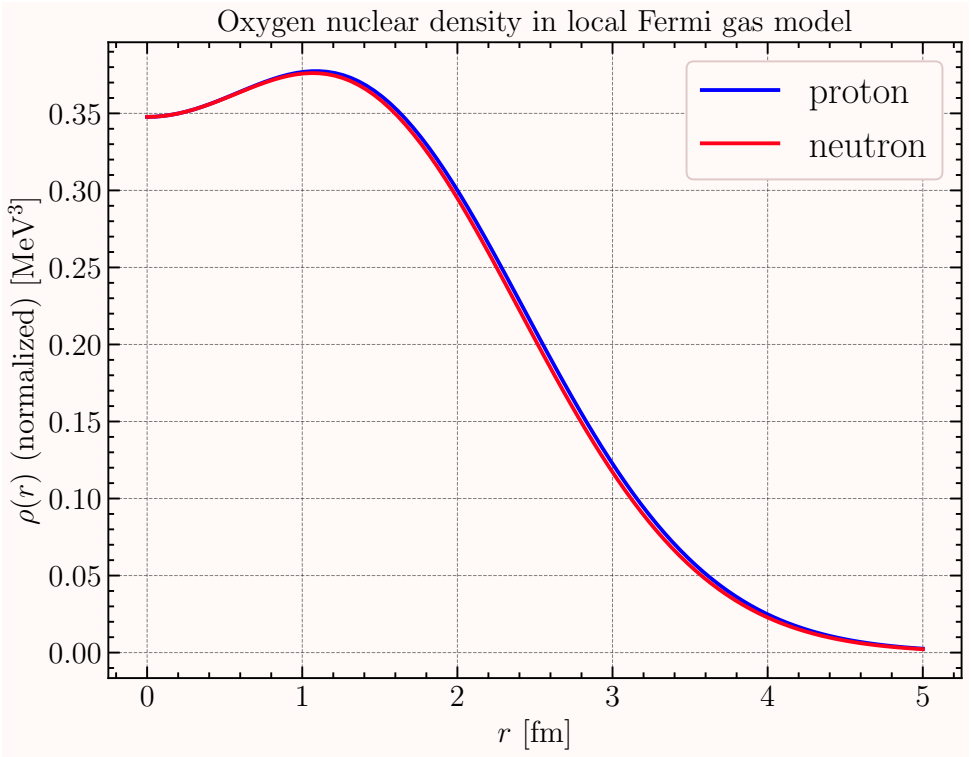

Figure 8.8: Nuclear density as a function of position in nucleus for oxygen. The curves for protons and neutrons differ mostly in the low r region. The curves are normalised such that their areas are unity.

The momentum density is given such that $\int \mathrm{d}\mathbf{p}\ n(p) = N$. The momentum density is given as

$$n(p) = \int \mathrm{d}\mathbf{r}\ \frac{\rho(r)}{N}\left[N\frac{\Theta(p_F(r)-p)}{(4/3)\pi p_F^3(r)}\right], \tag{8.19}$$

where the factor $\Theta(p_F(r)-p)$ accounts for local Pauli blocking in this phenomenological model [130]. The Fermi momentum is given in Equation 8.16 and, after converting the three-dimensional integral to $4\pi\int r^2\mathrm{d}r$, it becomes

$$n(p) = \frac{1}{\pi^2}\int \mathrm{d}r\ r^2\Theta\big(p_F(r)-p\big). \tag{8.20}$$

The momentum densities are shown below in Figure 8.9 and 8.10.

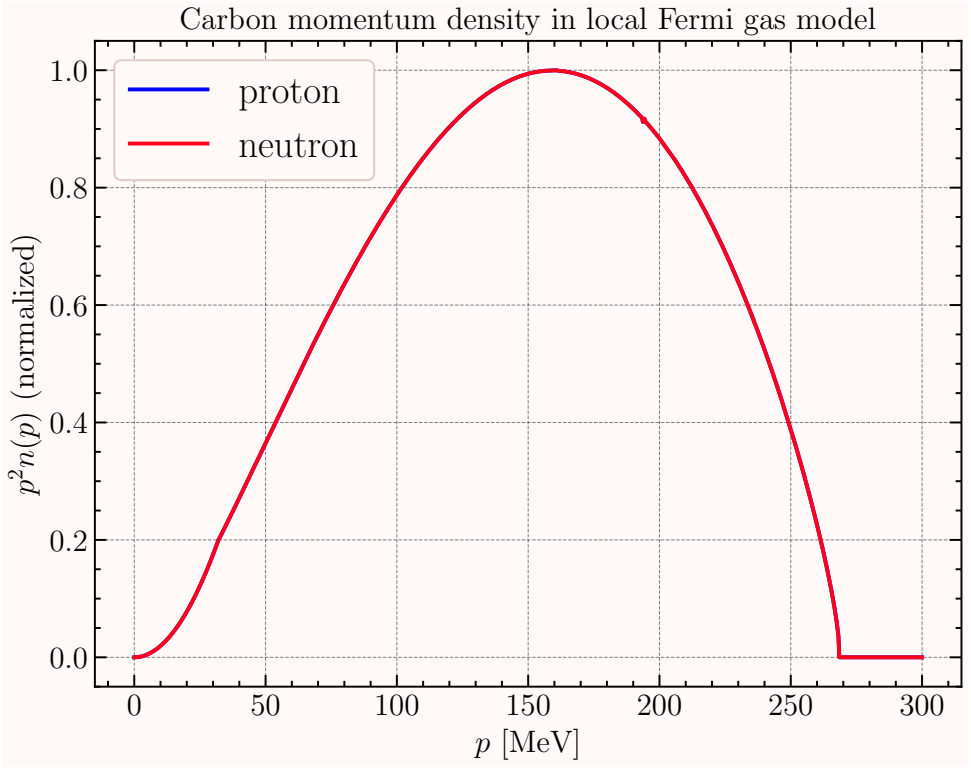

Figure 8.9: Momentum density for carbon as a function of initial nucleon momentum. The curves are normalised to the peak of the distribution.

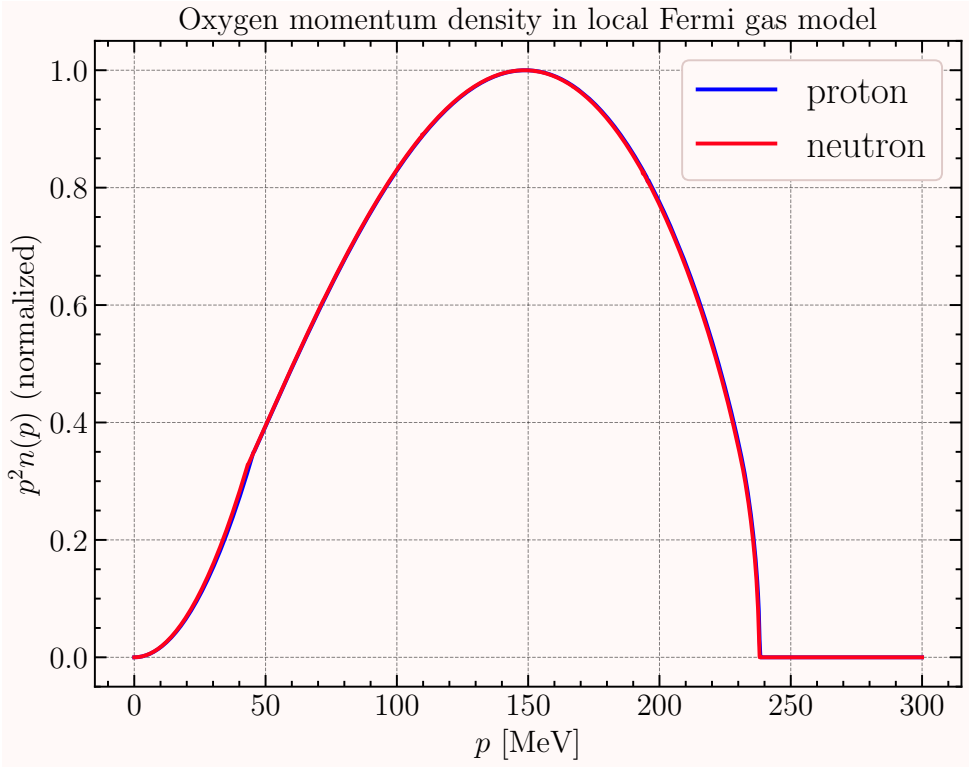

Figure 8.10: Momentum density for oxygen as a function of initial nucleon momentum. The curves are normalised to the peak of the distribution.

The differential cross section for the local Fermi gas is given as

$$\frac{\mathrm{d}^5\sigma}{\mathrm{d}\mathbf{k}_\mathrm{f}\mathrm{d}\Omega_\mathrm{N}} = \int \mathrm{d}\mathbf{r}\ \frac{\rho(r)}{N}\frac{p_N^2}{f_\mathrm{rec}}\Theta\big(p_N - p_F(r)\big)\left[N\frac{\Theta\big(p_F(r)-p\big)}{(4/3)\pi p_F^3(r)}\right]\ \frac{K}{(2\pi)^2}L_{\mu\nu}H^{\mu\nu}. \tag{8.21}$$

Here, the recoil factor, f_rec is given as

$$f_\mathrm{rec} = \left|1 + \frac{k_f - k_i\cos(\theta_f)}{E_N}\frac{E_f}{k_f}\right|. \tag{8.22}$$

The inclusive cross section, given in Equation 6.37, is shown against electron-nucleus scattering data in Figure 8.11.

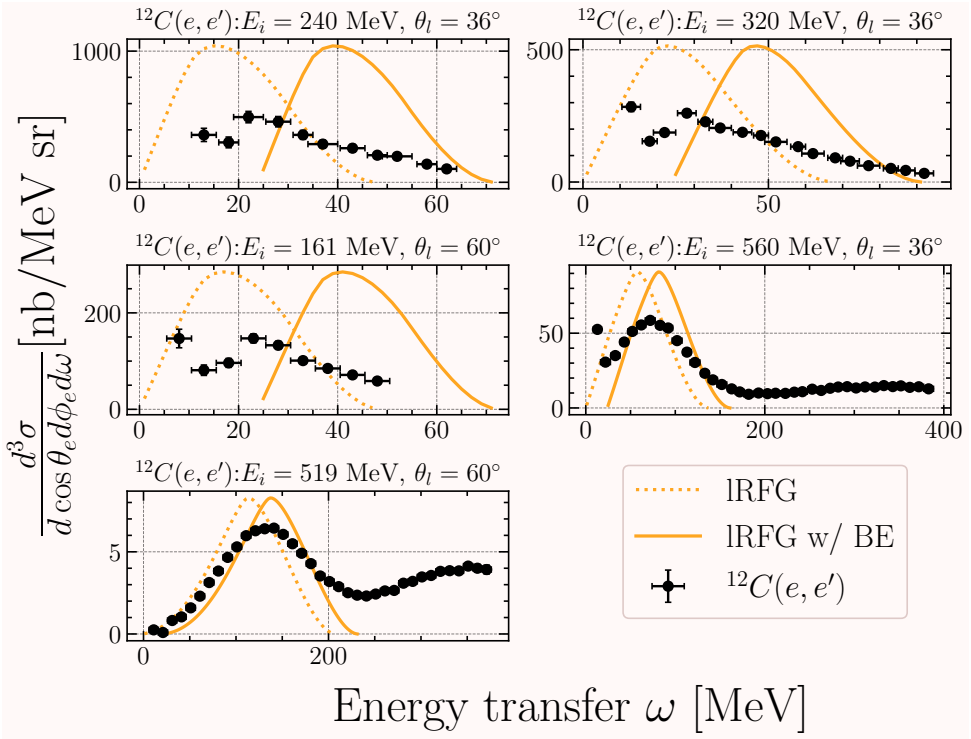

Figure 8.11: The local relativistic Fermi gas model from Ref [130] compared to electron-nucleus scattering data from Ref. [131] carbon. The solid line shows the model including a binding energy shift that is not present in the model.

8.3.3 Spectral function

We now introduce a different semi-phenomenological nuclear model which is based on a nuclear "spectral function". A spectral function is any function that describes the energy and momentum of nucleons within a nucleus. Indeed, both the global and local Fermi gas models can be described with a relatively simple spectral function. The approach in [133], known here as the Benhar spectral function (SF), uses fits to $(e, e'p)$ scattering data. This produces a realistic description of the initial nuclear state containing information about the spectroscopic factors (nuclear shell occupancies) and nuclear shell peak positions and widths. For larger nuclei, e.g. ^{40}Ar, there is little experimental data, both $(e, e'p)$ and inclusive, with which to fit to. Because of this, and because larger nuclei have more complex nuclear structures, there are more uncertainties associated with them. The approach used by Benhar *et. al.* shows that the strength in the nuclear shells is redistributed with respect to an independent-particle shell model (IPSM). The nuclear shells themselves do not have full nucleon occupancy (as in the IPSM), but a reduced occupancy of roughly 80%. The remaining approximately 20% of the nucleons were found to exist in the region that is attributed to SRC interactions [128].

The missing energy, E_m, of the system is defined as the energy that is passed to the

residual nuclear system. The residual nucleus can be in an excited or group state. This quantity is inherently dependent on the nuclear model used. In this model, it is defined as

$$E_m = \omega - T_N, \tag{8.23}$$

where T_N is the scattered nucleon kinetic energy and ω is the time component of the momentum transfer, often called the energy transfer. This definition neglects nuclear recoil, T_B. In neutrino detectors, nuclear recoil is not normally reconstructed. Including this recoil, the definition becomes

$$E_m = \omega - T_N - T_B. \tag{8.24}$$

The missing momentum, p_m, is defined as

$$\mathbf{p_m} = \mathbf{q} - \mathbf{p_N}. \tag{8.25}$$

The Benhar SF is defined using the E_m and p_m of a nuclear system. It was constructed from two parts: the mean-field (MF) contribution and the SRC tail of the missing-energy and momentum distributions.

$$S(E_m, p_m) = S_{\mathrm{MF}}(E_m, p_m) + S_{\mathrm{SRC}}(E_m, p_m). \tag{8.26}$$

The two-dimensional SF is shown in Figure 8.12 and the missing energy and momentum projections are given in Figures 8.13 and 8.14. The missing energy distribution shows two clear peaks. The peaks come from the shells the initial nucleon occupies. The broader shell at higher E_m is the $1s_{1/2}$ shell and the narrower, taller peak at lower E_m is the $1p_{3/2}$ shell. The missing momentum distribution, however, shows a single peak with a longer tail at higher p_m.

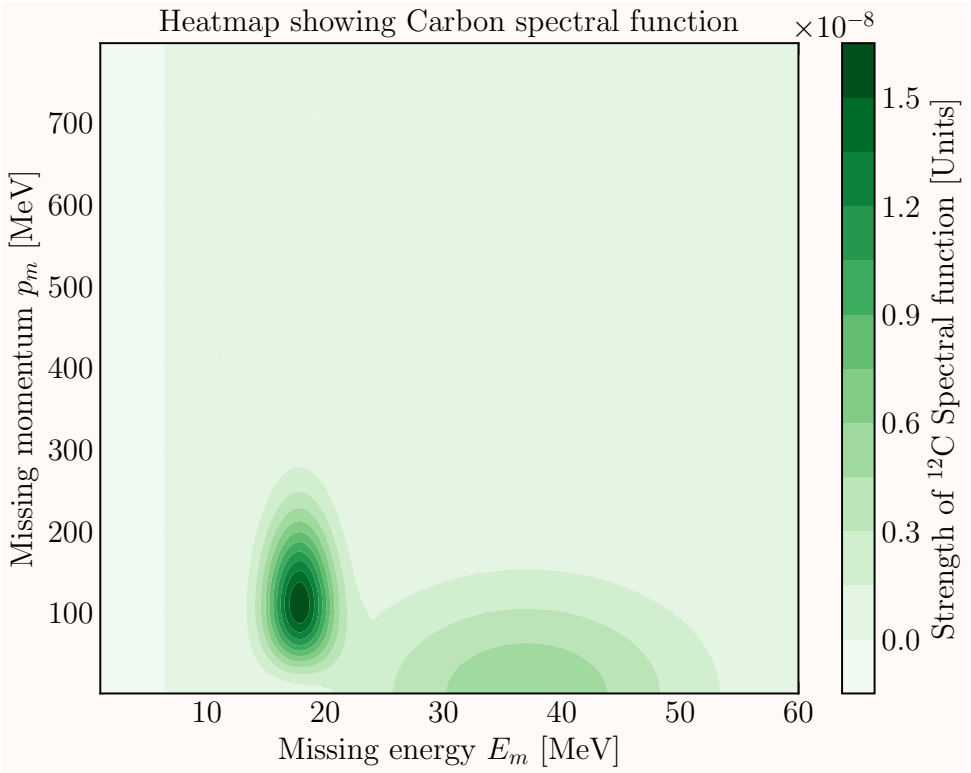

Figure 8.12: The Benhar SF for carbon as a function of missing energy and momentum. The z-axis shows the strength of the spectral function $S(E_m, p_m)$.

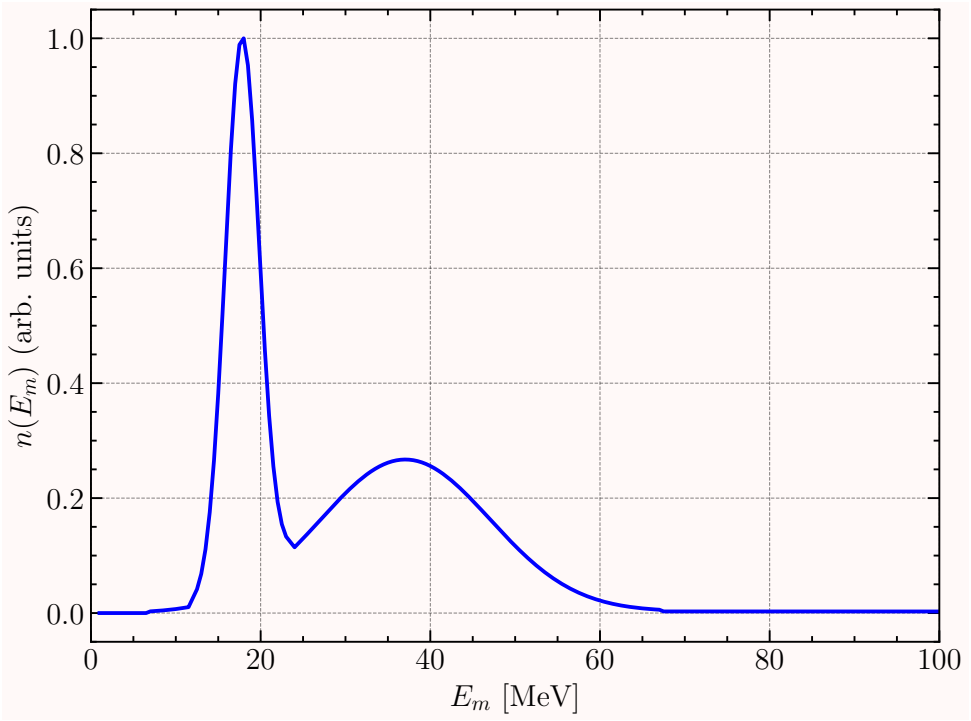

Figure 8.13: The Benhar SF missing energy projection for carbon. The distribution is normalised to the peak. A clear two peak structure resulting from the two occupied nuclear shells is visible.

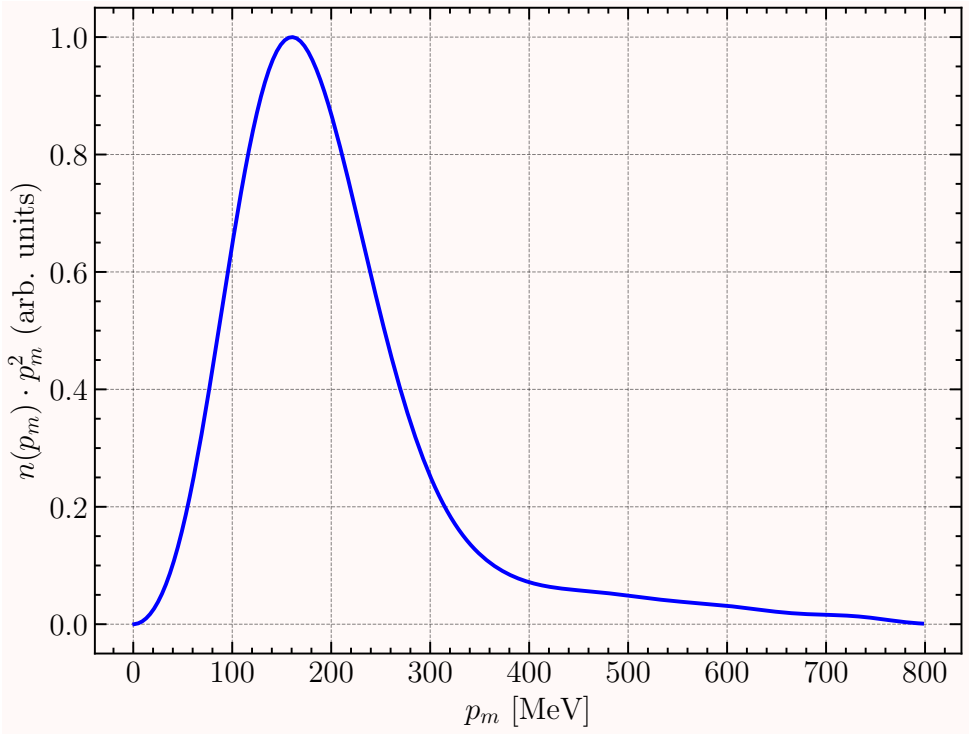

Figure 8.14: The Benhar SF missing momentum projection for carbon. The distribution is normalised to the peak.

Starting from Equation 7.12, the same average over energy and momentum is done.

$$\frac{\mathrm{d}^6\sigma}{\mathrm{d}\mathbf{k}_\mathrm{f}\,\mathrm{d}\mathbf{p}_\mathrm{N}} = \int \mathrm{d}\mathbf{p} \int \mathrm{d}E\; S(E,\mathbf{p})\; \frac{K}{(2\pi)^2}\; \delta^4(P_N + K_f - P - K_i). \tag{8.27}$$

Here, we can define a momentum density associated with the SF.

$$n(\mathbf{p}) = \int \mathrm{d}E\; S(E,\mathbf{p}). \tag{8.28}$$

It can be seen now that $S(E,\mathbf{p})$ is analogous to

$$\delta(E - \sqrt{M^2 + p^2}\;)\frac{N}{(4/3)\pi p_F^3}\Theta(p_F - p), \tag{8.29}$$

which is essentially a probability density function for finding a nucleon with a given energy and momentum. Therefore,

$$\int \mathrm{d}E \int \mathrm{d}\mathbf{p}\; S(E,\mathbf{p}) = N \tag{8.30}$$

which gives the total number of nucleons in the nucleus. The SF is defined in the rest frame of the target nucleus, therefore the Fermi motion is isotropic, allowing the SF to be expressed as

$$S(E,\mathbf{p}) = S(E,p). \tag{8.31}$$

The SF is a realistic description of the initial state nucleon energy and momentum distribution. However, in Equation 8.27, there is no Pauli blocking term included. This is included using a LFG-style Pauli blocking mechanism given by

$$\left.\frac{\mathrm{d}^6\sigma}{\mathrm{d}\mathbf{k}_\mathrm{f}\,\mathrm{d}\mathbf{p}_\mathrm{N}}\right|_\mathrm{PB} = \frac{\mathrm{d}^6\sigma}{\mathrm{d}\mathbf{k}_\mathrm{f}\,\mathrm{d}\mathbf{p}_\mathrm{N}}\left[1 - \frac{1}{N}\int \mathrm{d}\mathbf{r}\rho(r)\Theta(p_F(r) - p_\mathrm{N})\right] \tag{8.32}$$

where $p_F(r)$ is the Fermi momentum given for the LFG case. The Pauli blocking term is

$$\frac{1}{N}\int \mathrm{d}\mathbf{r}\rho(r)\Theta(p_F(r) - p_\mathrm{N}). \tag{8.33}$$

As p_N surpasses the Fermi momentum the term becomes zero. This term is shown for carbon and oxygen below.

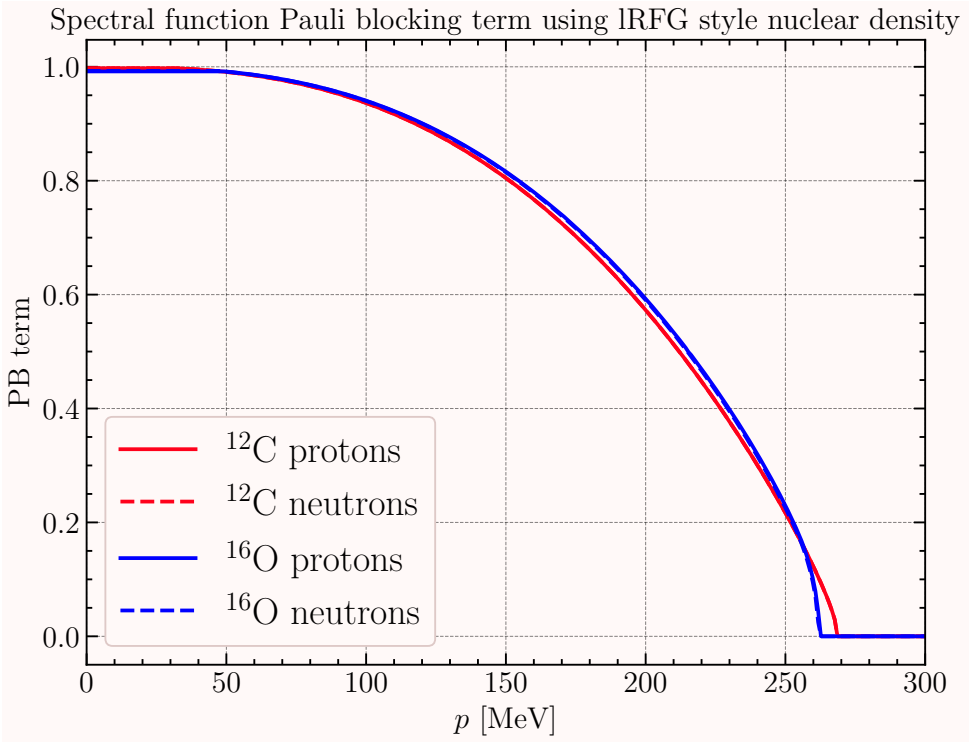

Figure 8.15: Pauli blocking term used in the SF approach. The nuclear density for the LFG given in Section 8.3.2 is used.

The inclusive cross section is shown against electron-nucleus scattering data in Figure 8.16

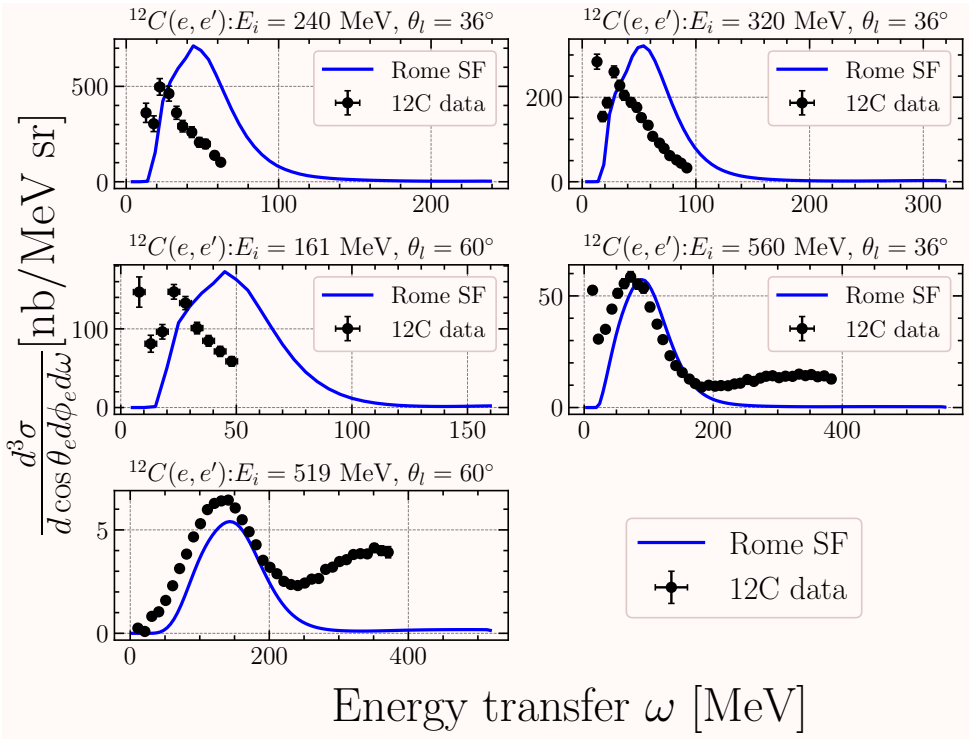

Figure 8.16: The spectral function model from Ref [130] compared to electron-nucleus scattering data from Ref. [131] carbon.

Drawbacks to the spectral function approach

The differential cross section given in Equation 8.27 is factorised into a "spectral-function" term, $S(E, \mathbf{p})$, and the free lepton-nucleon cross section. This calculates an incorrect value for the ratio of ν_μ to ν_e cross sections for the CCQE process in the forward lepton scattering region of phase space [134]. Additionally, as can be seen in Figure 8.16, at low values of ω, the SF model peak does not match inclusive electron scattering data. This is because at low ω, the distortions from the nuclear potential are large. However, the SF model is based on the PWIA and neglects these contributions.

Chapter 9

Relativistic mean field theory

This section outlines another theory used to describe the initial nuclear bound state, the interaction vertex and the post-scatter nuclear state. This approach differs from the Fermi gas and SF nuclear model because it solves the Dirac equation in the presence of nuclear potentials.

The study of neutrino-nucleus interactions requires an understanding of the structure of nuclei themselves. This is particularly challenging due to the gauge field nature of the nucleus; the nucleus is a turbulent environment with lots of forces at play. At the energy scales we are interested in the context of neutrino interactions, QCD is too strong and therefore perturbative methods cannot be employed. In addition to this, the nucleon-nucleon potential is spin-dependent, short-ranged and has a repulsive core. Many different approximate methods have been developed in the history of studying atomic nuclei; each has short-falls and good points. When considering very low energy interactions, one can consider using the Schrodinger equation to describe the nucleons and incident particle. However, in our context, the particles are of too high an energy to use the Schrodinger equation. The goal is to formulate a hadronic description of the nucleus that is consistent with quantum mechanics, special relativity, causality and symmetries of the strong Lagrangian.

Once an adequate description of the ground state nucleus is obtained, it is necessary to describe the interaction vertex operator and also describe the propagation of the scattered state. These three components are crucial in obtaining the hadronic current for a given interaction. From the hadronic current, the hadronic tensor can be obtained, which when contracted with the corresponding leptonic tensor, describes the interaction cross section (with additional pre-factors).

9.1 Relativistic mean field description of the nuclear bound state

The need for a hadronic description of the nucleus lead to the development of the "Relativistic mean field" (RMF) description of nuclei. RMF theory is a phenomenological description and describes nucleons as point-like Dirac spinors. RMF theory naturally outputs the bound state wavefunctions and the bound state potentials that are required in the hadron current. This section follows the approaches given in Refs. [135, 136, 137] The Dirac spinors are represented as

$$\Psi = \begin{pmatrix} \Psi^+ \\ \Psi^- \end{pmatrix}, \tag{9.1}$$

where the plus and minus signs indicate the positive and negative energy solutions. They interact through the exchange of point-like particles called "mesons". This description was originally developed by Walecka [138] and used a simple phenomenological σ scalar meson and a ω vector meson. Since then, extensions have been developed to include a ρ isovector meson and Coulomb contributions, along with the non-linear self-coupling of the σ meson.

This model has freedoms in: the number of mesons within the theory; the masses of such mesons; the coupling constants of such mesons; and the quantum numbers of such mesons. The simplest meson is the pion (π meson), with quantum numbers $J = 0$, $T = 1$, and $P = -1$. The pion does not conserve parity and so to include such a meson in the theory, it would have to also contain another meson with negative parity, forcing one to consider the interaction via a pair of mesons. This would complicate the model significantly and so instead different force mediating mesons are used.

The σ meson has quantum numbers $J = 0$, $T = 0$ and $P = 1$. The corresponding scalar field $\sigma(x)$ generates the attractive force required in the nucleus. The ω meson has quantum numbers $J = 1$, $T = 0$ and $P = -1$ and the corresponding vector field $\omega^\mu(x)$ generates the repulsive force. The Coulomb force is mediated by the time-like component of the vector potential $A^\mu(x)$. Finally, the ρ meson has quantum numbers $J = 1$, $T = 1$ and $P = -1$ and has a corresponding isovector field $\rho\,^\mu(x)$.

The "mean-field" aspect of RMF theory comes after forming a Lagrangian with the nucleon and meson fields in the model. To illustrate this, forming a Lagrangian with a single scalar meson field, we get

$$\mathcal{L} = \bar{\Psi}(i\gamma_\mu\partial^\mu - M)\Psi + \frac{1}{2}\Big(\partial_\mu\sigma(x)\partial^\mu\sigma(x) - m_\sigma^2\sigma^2(x)\Big) - g_\sigma\bar{\Psi}\sigma(x)\Psi, \tag{9.2}$$

where the nucleon field operators are given by Ψ and the mass of the corresponding nucleons is M. The meson mass is given by m_σ and the coupling constant for the meson field is g_σ. As it stands, the meson field operators have quantum fluctuations included as

$\sigma(x)$. RMF theory removes such fluctuations and takes the meson field operators as the expectation value of the field. This results in using classical fields to describe the meson fields. The nucleon field operators can be expanded in terms of single particle states with the density source terms for the fields becoming summations over the single particle states. This would produce both positive and negative energy solutions, but since mesons and nucleons are composite particles, the negative energy solutions (and so the vacuum polarisation effects) are not taken into account.

$$\sigma(x) \;\rightarrow\; \langle\sigma(x)\rangle \;\overset{\text{def}}{=}\; \sigma. \tag{9.3}$$

A further approximation is required before RMF theory is usable. That is, the summation over the single particle states, to obtain the meson field densities, are taken to only be a sum over occupied states. This assumes states are filled up to some Fermi level and nothing is filled above this level. This is called the no-sea approximation.

9.2 Full RMF Lagrangian

Now we have seen the RMF approximations applied to a simple single scalar meson theory, we can now introduce the full RMF Lagrangian and begin to formulate the equations for the nucleon and meson fields.

$$\begin{aligned}\mathcal{L} = \bar{\Psi}(i\gamma_\mu\partial^\mu - M)\Psi + \frac{1}{2}\Big(\partial_\mu\sigma(x)\partial^\mu\sigma(x) - m_\sigma^2\sigma^2(x)\Big) - U(\sigma) - g_\sigma\bar{\Psi}\sigma\Psi \\ - \frac{1}{4}\Omega_{\mu\nu}\Omega^{\mu\nu} + \frac{1}{2}m_\omega^2\omega_\mu\omega^\mu - g_\omega\bar{\Psi}\gamma_\mu\omega^\mu\Psi \\ - \frac{1}{4}\mathbf{R}_{\mu\nu}\mathbf{R}^{\mu\nu} + \frac{1}{2}m_\rho^2\boldsymbol{\rho}_\mu\boldsymbol{\rho}^\mu - g_\rho\bar{\Psi}\gamma_\mu\boldsymbol{\tau}\boldsymbol{\rho}^\mu\Psi \\ - \frac{1}{4}F_{\mu\nu}F^{\mu\nu} - e\Big(\frac{1+\tau_3}{2}\Big)\;\bar{\Psi}\gamma_\mu A^\mu\Psi.\end{aligned} \tag{9.4}$$

Here, $U(\sigma) = \frac{1}{3}g_2\sigma^3 + \frac{1}{4}g_3\sigma^4$ and mediates the non-linear self-coupling of the σ meson. The σ meson is a phenomenological meson, meaning it is not a real particle, therefore it can only be introduced into a Lagrangian with a non-linear coupling. The field tensors for the meson fields are defined as:

$$\begin{aligned}\Omega^{\mu\nu} &= \partial^\mu\omega^\nu - \partial^\nu\omega^\mu \\ \mathbf{R}^{\mu\nu} &= \partial^\mu\boldsymbol{\rho}^\nu - \partial^\nu\boldsymbol{\rho}^\mu \\ F^{\mu\nu} &= \partial^\mu A^\nu - \partial^\nu A^\mu.\end{aligned} \tag{9.5}$$

Such a Lagrangian has six free parameters: g_σ, g_2, g_3, g_ω, g_ρ and m_σ. Because the σ meson is a phenomenological meson, m_σ is a free parameter.

The mean field approach allows us to treat the meson fields as classical and so when the Euler-Lagrange equation is applied, classical Klein-Gordan fields are obtained. For nucleons, this produces the Dirac equation.

9.2.1 Meson field equations

Using the σ meson as an explicit example, the corresponding Lagrangian is

$$\mathcal{L} \supset \frac{1}{2}\Big(\partial_\mu\sigma(x)\partial^\mu\sigma(x) - m_\sigma^2\sigma^2(x)\Big) - \frac{1}{3}g_2\sigma^3 - \frac{1}{4}g_3 - g_\sigma\bar{\Psi}\sigma\Psi. \tag{9.6}$$

Here $\supset$ indicates that we are only considering the terms pertaining to the σ meson. When performing the Euler-Lagrange equation,

$$\partial_\mu\Big(\frac{\partial\mathcal{L}}{\partial(\partial_\mu q)}\Big) - \frac{\partial\mathcal{L}}{\partial q} = 0, \tag{9.7}$$

we see that we get

$$\begin{aligned}\frac{\partial\mathcal{L}}{\partial(\partial_\mu q)} &= \partial^\mu\sigma \\ \frac{\partial\mathcal{L}}{\partial\sigma} &= -m_\sigma^2 - g_2\sigma^2 - g_3\sigma^3 - g_\sigma\sum_i^{\text{occ}}\bar{\Psi}\Psi\end{aligned} \tag{9.8}$$

where there is a sum over the occupied states only due to the no-sea approximation. This summation becomes the density of states ρ_σ. This leads to a final equation of

$$\Big[\partial_\mu\partial^\mu + m_\sigma^2\Big]\sigma = -g_2\sigma^2 - g_3\sigma^3 - g_\sigma\rho_\sigma. \tag{9.9}$$

Likewise, for the other meson fields, the Klein-Gordan equations become

$$\begin{aligned}\Big[\partial_\mu\partial^\mu + m_\omega^2\Big]\omega^\mu &= g_\omega\rho_\omega^\mu \\ \Big[\partial_\mu\partial^\mu + m_\rho^2\Big]\rho^{\ \mu} &= g_\rho\rho_\rho^{\ \mu} \\ \Big[\partial_\mu\partial^\mu\Big]A^\mu &= ej_c^\mu.\end{aligned} \tag{9.10}$$

The densities for each meson field is given by

$$
\begin{aligned}
\rho_\sigma &= \sum_i^{\text{occ}} n_i \bar{\Psi}\Psi \\
\rho_\omega^\mu &= \sum_i^{\text{occ}} n_i \bar{\Psi}\gamma^\mu\Psi \\
\boldsymbol{\rho}_\rho{}^\mu &= \sum_i^{\text{occ}} n_i \bar{\Psi}\gamma^\mu\boldsymbol{\tau}\Psi \\
\rho_c^\mu &= \sum_i^{\text{occ}} n_i \bar{\Psi}\Big(\frac{1+\tau_3}{2}\Big)\gamma^\mu\Psi.
\end{aligned}
\tag{9.11}
$$

Here, n_i is the occupation number (which accounts for nucleon pairing), which for the occupied states we are restricting the summation to, is equal to 1 and so can be omitted.

9.2.2 Nucleon field equation

The nucleon field equation results in the relativistic Dirac equation and is given below.

$$
\Big[\gamma_\mu\big(i\partial^\mu + g_\omega\omega^\mu + g_\rho\boldsymbol{\tau}\cdot\boldsymbol{\rho}^\mu - e\frac{1+\tau_3}{2}\,A^\mu\big) - M + g_\sigma\sigma\Big]\Psi_i = 0. \tag{9.12}
$$

Here, the index i is over the nucleons in the occupied states. That is, the equation is satisfied for each nucleon.

9.2.3 Stationary state solutions

We want to describe the stationary states as this corresponds to the nuclear ground states. In doing so, all time derivatives and all space-like four vector components vanish. Allowing the time components and derivatives to vanish, the single particle wavefunction can separate as

$$
\Psi_i(\boldsymbol{r}, t) \to \Psi_i(\boldsymbol{r})e^{-iE_i t}. \tag{9.13}
$$

Here E_i is the ground state energy of the i_{th} nucleon. It is assumed that nucleon single particle states do not mix isospin, and so only the third component of the isospin vector is retained. Also, the following RMF equations will be solved for spherically symmetric nuclei. It is perhaps a hint of fate that many of the nuclei that particle detectors are constructed from (^{12}C, ^{16}O and ^{40}Ar) happen to be spherically symmetric (or almost, in the case of ^{40}Ar). Finally, it is assumed that the interaction on such nuclei happens with a single nucleon within the nucleus (the IA). As a result, one only needs to solve the RMF stationary state equations for single particle nucleon wavefunctions. However, to be consistent, one would need to also describe the incident particle as a Dirac particle.

With this in mind, the meson field Klein-Gordan equations simplify to

$$\begin{aligned}
\big[-\nabla^2 + m_\sigma^2\big]\sigma(r) &= -g_\sigma\rho_\sigma - g_2\sigma^2(r) - g_3\sigma^3(r) \\
\big[-\nabla^2 + m_\omega^2\big]\omega^0(r) &= g_\omega\rho_\omega^0 \\
\big[-\nabla^2 + m_\rho^2\big]\rho_3^0(r) &= g_\rho\rho_3^0 \\
-\nabla^2 A^0(r) &= e\rho_c^0.
\end{aligned} \tag{9.14}$$

For brevity we will group the vector and isovector potentials together and define generalised scalar and vector potentials, $S(r)$ and $V(r)$, with corresponding coupling constants g_S and g_V.

$$\begin{aligned}
S(r) &= g_\sigma\sigma(r) \\
V^0(r) &= g_\omega\omega^0(r) + g_\rho\tau_3\rho_3^0(r) + e\frac{1+\tau_3}{2}A^0(r)
\end{aligned} \tag{9.15}$$

The baryon field Dirac equation then becomes

$$\Big[i\gamma_\mu\partial^\mu - g_V\gamma^0V^0(r) - \big(M - g_SS(r)\big)\Big]\Psi_i(\mathbf{r})e^{-iE_it} = 0, \tag{9.16}$$

which can be further simplified if we introduce Dirac matrices.

$$\begin{aligned}
\gamma^0 \equiv \beta &= \begin{pmatrix} 1 & 0 \\ 0 & -1 \end{pmatrix} \\
\gamma_i &= \begin{pmatrix} 0 & \sigma_i \\ -\sigma_i & 0 \end{pmatrix} \\
\alpha_i &= \begin{pmatrix} 0 & \sigma_i \\ \sigma_i & 0 \end{pmatrix}.
\end{aligned} \tag{9.17}$$

Here σ_i are the Pauli spin matrices [113]. It follows that $\gamma_i = \beta\alpha_i$. Using these expressions, it is quick to show that the derivative term of Equation 9.16 becomes

$$\begin{aligned}
\gamma_\mu\partial^\mu &= \gamma_0\partial_t + \beta\alpha_i\partial_i \\
&= \beta\partial_t + \beta\ \boldsymbol{\alpha}\cdot\boldsymbol{\nabla}.
\end{aligned} \tag{9.18}$$

Which, when acting on our baryon wavefunction, becomes

$$\begin{aligned}
i\big(\beta\partial_t + \beta\ \boldsymbol{\alpha}\cdot\boldsymbol{\nabla}\big)\Psi(\mathbf{r})e^{-iE_it} &= i\big(-iE_i\beta\Psi(\mathbf{r})e^{-iE_it} + \beta\boldsymbol{\alpha}\cdot\boldsymbol{\nabla}\Psi(\mathbf{r})e^{-iE_it}\big) \\
&= \big(E_i\beta + i\beta\boldsymbol{\alpha}\cdot\boldsymbol{\nabla}\big)\Psi(\mathbf{r})e^{-iE_it}.
\end{aligned} \tag{9.19}$$

And so Equation 9.16 becomes

$$\begin{aligned}\Big[i\beta\boldsymbol{\alpha}\cdot\boldsymbol{\nabla}-g_V\beta V^0(r)-\big(M-g_SS(r)\big)\Big]\Psi(\mathbf{r})&=-\beta E\Psi(\mathbf{r})\\ \Big[-i\boldsymbol{\alpha}\cdot\boldsymbol{\nabla}+g_VV^0(r)+\beta\big(M-g_SS(r)\big)\Big]\Psi(\mathbf{r})&=E\Psi(\mathbf{r}).\end{aligned}\tag{9.20}$$

This is in the form $\hat{H}\Psi(\mathbf{r})=E\Psi(\mathbf{r})$ where $\hat{H}$ is the Dirac Hamiltonian. The solution to this equation has both positive and negative energy solutions and so the field operator can be expanded in such solutions. Previously we have mentioned that we neglect the negative energy solutions in the no-sea approximation and so we can expand the single particle wavefunctions as

$$\Psi(\mathbf{r})=\sum_q A_q\mathcal{U}_q,\tag{9.21}$$

where q are the set of quantum numbers corresponding to the state. It can be explicitly expressed as $q=\{n,l,j,m,t\}$. $\mathcal{U}_q$ are the positive energy solutions and A_q are the baryon creation operators. We seek solutions for $\mathcal{U}_q$ in the form of the following ansatz.

$$\mathcal{U}_q(\mathbf{r})=\begin{pmatrix} i\frac{G_{n\kappa t}(r)}{r}\Phi_{\kappa m}\\ -\frac{F_{n\kappa t}(r)}{r}\Phi_{-\kappa m}\end{pmatrix}\zeta_t.\tag{9.22}$$

There are two wavefunctions, $G(r)$ and $F(r)$ where I have omitted the quantum numbers for brevity. These correspond to the upper and lower spinor component wavefunctions. Φ contains the angular dependence and are spherical spinors. ζ is the isospin projection operator where $t=1/2$ is for protons and $t=-1/2$ is for neutrons. In the ansatz, it appears that we have lots the quantum numbers l,j in place of κ. This comes from our introduction of spherical spinors.

The reason for introducing spherical spinors comes from combining spherical harmonics, which are eigenfunctions of the angular momentum operators L^2 and L_z, with two-component spinors χ_s which are eigenfunctions of the spin operators S^2 and S_z. Such combinations are spherical spinors and they are, by construction, eigenfunctions of the total angular momentum operators J^2 and J_z. We can explicitly write them as

$$\begin{aligned}\Phi_{jlm}(\theta,\phi)&=\sum_s CY_{lm}(\theta,\phi)\chi_s\\ \chi_{\frac{1}{2}}&=\begin{pmatrix}1\\0\end{pmatrix}\\ \chi_{-\frac{1}{2}}&=\begin{pmatrix}0\\1\end{pmatrix},\end{aligned}\tag{9.23}$$

where C are the corresponding Clebsch-Gordan coefficients which depend on appropriate quantum numbers. Here, to be explicit, θ and ϕ are the polar and azimuthal angle

corresponding to a spherical coordinate system. Spherical spinors are also eigenfunctions of $\sigma \cdot \mathbf{L}$ and so also eigenfunctions of the following $\hat{K}$ operator

$$\hat{K} = -1 - \sigma \cdot \mathbf{L}, \tag{9.24}$$

such that

$$\hat{K}\Phi_{jlm}(\theta, \phi) = \kappa\Phi_{jlm}(\theta, \phi). \tag{9.25}$$

κ is a quantum number introduced to conveniently express l and j at the same time.

$$\begin{cases} \kappa = -l - 1 & \text{for } j = l + 1/2 \\ \kappa = l & \text{for } j = l - 1/2 \end{cases} \tag{9.26}$$

which can be reversed to show

$$\begin{cases} l = -\kappa - 1 & \text{for } \kappa < 0 \\ l = \kappa & \text{for } \kappa > 0 \\ j = |\kappa| - \frac{1}{2}. \end{cases} \tag{9.27}$$

Since κ can express l and j, we can rewrite the spinors as $\Phi_{\kappa m}(\theta, \phi)$. It is important to discuss the behaviour of spherical spinors under the operation of the parity operator, $\sigma \cdot \hat{r}$, and $\sigma \cdot \mathbf{p}$.

The parity operator transforms $\mathbf{r} \to -\mathbf{r}$. However, in a spherical coordinate system, it also transforms the angles such that $\theta \to \pi - \theta$ and $\phi \to \phi + \pi$. Under such operations, by construction it follows that they are eigenfunctions with eigenvalues $(-1)^l$. The two spinors $\Phi_{\kappa m}(\theta, \phi)$ and $\Phi_{-\kappa m}(\theta, \phi)$ corresponding to the same value of j but differ in l by one have opposite parity.

$$(\boldsymbol{\sigma} \cdot \hat{r})\Phi_{\kappa m}(\theta, \phi) = -\Phi_{-\kappa m}(\theta, \phi). \tag{9.28}$$

To investigate how spherical spinors behave under the operation of $\boldsymbol{\sigma} \cdot \mathbf{p}$, we make use of the following identity and relation.

$$\begin{aligned} &(\boldsymbol{\sigma} \cdot \mathbf{A})(\boldsymbol{\sigma} \cdot \mathbf{B}) = \mathbf{A} \cdot \mathbf{B} + i\sigma \cdot (\mathbf{A} \times \mathbf{B}) \\ &(\boldsymbol{\sigma} \cdot \hat{r})(\boldsymbol{\sigma} \cdot \hat{r}) = \mathbb{I}. \end{aligned} \tag{9.29}$$

Letting $\mathbf{A} = \hat{r}$ and $\mathbf{B} = \mathbf{p}$, we obtain

$$(\boldsymbol{\sigma} \cdot \hat{r})(\boldsymbol{\sigma} \cdot \mathbf{p}) = (\hat{r} \cdot \mathbf{p}) + i\frac{\boldsymbol{\sigma} \cdot (\mathbf{r} \times \mathbf{p})}{r}, \tag{9.30}$$

which can be further simplified using the above identity relation to

$$(\boldsymbol{\sigma} \cdot \mathbf{p}) = -i(\boldsymbol{\sigma} \cdot \hat{r})\Big[i(\hat{r} \cdot \mathbf{p}) - \frac{\boldsymbol{\sigma} \cdot \mathbf{L}}{r}\Big]. \tag{9.31}$$

We recall that we use the ansatz $\frac{iG(r)}{r}\Phi_{\kappa m}(\theta,\phi)$ which has been simplified for the following demonstration of the operator upon such a solution.

$$(\boldsymbol{\sigma}\cdot\mathbf{p})\frac{iG(r)}{r}\Phi_{\kappa m}(\theta,\phi) = -i(\boldsymbol{\sigma}\cdot\hat{r})\Big[\nabla_r - \frac{\boldsymbol{\sigma}\cdot\mathbf{L}}{r}\Big]\frac{iG(r)}{r}\Phi_{\kappa m}(\theta,\phi). \tag{9.32}$$

After some algebra, it results in the following expression.

$$(\boldsymbol{\sigma}\cdot\mathbf{p})\frac{iG(r)}{r}\Phi_{\kappa m}(\theta,\phi) = \Big[-\frac{\partial G}{\partial r}\frac{1}{r} - \kappa\frac{G(r)}{r^2}\Big]\Phi_{-\kappa m}. \tag{9.33}$$

We are now armed with the tools to simplify the nucleon wavefunction Dirac equation given in Equation 9.20. After some algebra and extensive use of the previously derived relations, we reach a final set of equations.

$$\begin{aligned}
&\frac{\partial F_{n\kappa t}(r)}{\partial r} - \frac{F_{n\kappa t}(r)}{r}\kappa + \big[E_{n\kappa t} - g_V V^0(r) - M + g_S S(r)\big]G_{n\kappa t}(r) = 0\\
&\frac{\partial G_{n\kappa t}(r)}{\partial r} + \frac{G_{n\kappa t}(r)}{r}\kappa - \big[E_{n\kappa t} - g_V V^0(r) + M + g_S S(r)\big]F_{n\kappa t}(r) = 0.
\end{aligned} \tag{9.34}$$

And so it shows that the spherical nuclear ground state is described by coupled one dimensional differential equations.

In our current approximations, the meson field equations, which are still considered classical, reduce to

$$\begin{aligned}
&\frac{\partial^2 S(r)}{\partial r^2} + \frac{2}{r}\frac{\partial S(r)}{\partial r} - m_S^2 S(r) = -g_S\rho_S(r)\\
&\frac{\partial^2 V^0(r)}{\partial r^2} + \frac{2}{r}\frac{\partial V^0(r)}{\partial r} - m_V^2 V^0(r) = -g_V\rho_B(r),
\end{aligned} \tag{9.35}$$

where our meson field densities now become

$$\begin{aligned}
\rho_S(r) &= \sum_i^{\text{occ}} n_i\bar{\Psi}\Psi = \sum_i^{\text{occ}}\bar{\mathcal{U}_q}\mathcal{U}_q\\
&= \sum_i^{\text{occ}}\frac{(2j+1)}{4\pi r^2}\big(|G(r)|^2 - |F(r)|^2\big).
\end{aligned} \tag{9.36}$$

We have made use of the following spherical spinor relation $\sum_{m=-j}^{j}\Phi^\dagger_{\kappa m}\Phi_{\kappa' m} = \frac{(2j+1)}{4\pi}\delta_{\kappa\kappa'}$. Note that the sources are spherically symmetric; this is another result of the no-sea approximation. We also have the baryon density, which I will only show for the case of the vector field but there are corresponding equations for the isovector and Coulomb fields.

$$\begin{aligned}\rho_B(r) &= \sum_i^{\text{occ}} n_i \bar{\Psi}\gamma^0\Psi = \sum_i^{\text{occ}} \bar{\mathcal{U}}_q\gamma^0\mathcal{U}_q \\ &= \sum_i^{\text{occ}} \frac{(2j+1)}{4\pi r^2}\big(|G(r)|^2 + |F(r)|^2\big).\end{aligned} \tag{9.37}$$

9.2.4 Numerical solutions to stationary ground state equations

We have now derived the stationary nuclear ground-state solutions in the RMF regime using the impulse and no-sea approximation considering only spherically symmetric nuclei. The final equations can be solved in a Dirac-Hartree iterative approximation. The algorithm for this is as follows:

1. Propose a guess for the initial potentials $S(r)$ and $V^0(r)$. A suitable guess uses a Woods-Saxon potential.
2. Solve the Dirac equations (Equation 9.34) to obtain the upper and lower spinor component wavefunctions $G(r)$ and $F(r)$.
3. From these wavefunctions, calculate the meson field densities $\rho_S(r)$ and $\rho_B(r)$ using Equations 9.36 and 9.37.
4. Solve the meson field Klein-Gordan equations (Equation 9.35) to obtain new expressions for the potentials.
5. Substitute these new potentials back into Step 1 and repeat until convergence.

The convergence requirement is enforced by comparing the change in energy eigenvalue E to a convergence requirement input. That is, the change in the energy eigenvalues between the current iteration and the previous must be less than the convergence requirement input by the user, for all nucleons.

9.2.5 Solutions for the stationary ground states for different nuclei

A software from Ref. [135] called `TIMORA` is used to perform the above numerical solutions and obtain the energy eigenvalues, wavefunctions and nuclear potentials for carbon, oxygen and argon. The Coulomb potential is absorbed into the vector potential. The scalar and vector potentials for carbon are given in Figure 9.1 and the wavefunction for the nuclear bound states are given in Figure 9.2. The scalar and vector potentials for oxygen are given in Figure 9.3 and the wavefunction for the nuclear bound states are given in Figure 9.4. The scalar and vector potentials for argon are given in Figure 9.5 and the

wavefunction for the nuclear bound states are given in Figure 9.6. The parameters used in the solutions shown are from the "NLSH" parameter set [139]. The parameters are given in Table 9.1.

m_σ	g_σ	g_ρ	g_ω	g_2	g_3
526.059	10.444	4.3830	12.945	−6.9099	−15.8337

Table 9.1: Parameters for the RMF model are chosen to match the NLSH set. All values are in MeV/c [139].

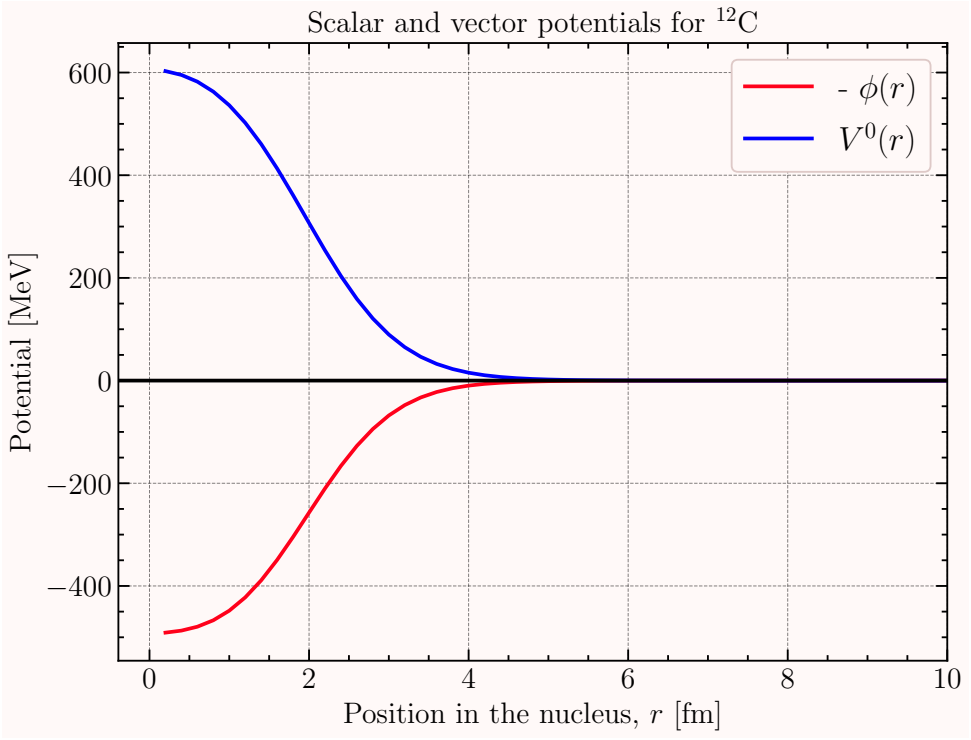

Figure 9.1: RMF scalar and vector potentials for carbon outputted by the `TIMORA` code.

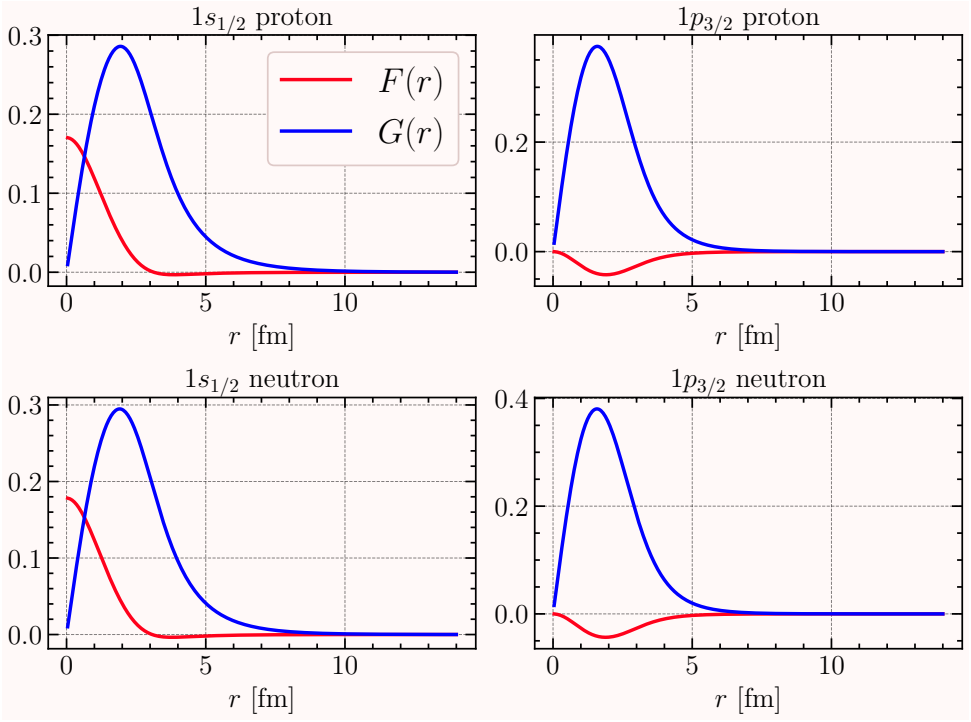

Figure 9.2: RMF wavefunction components $G(r)$ and $F(r)$ for carbon outputted by the `TIMORA` code.

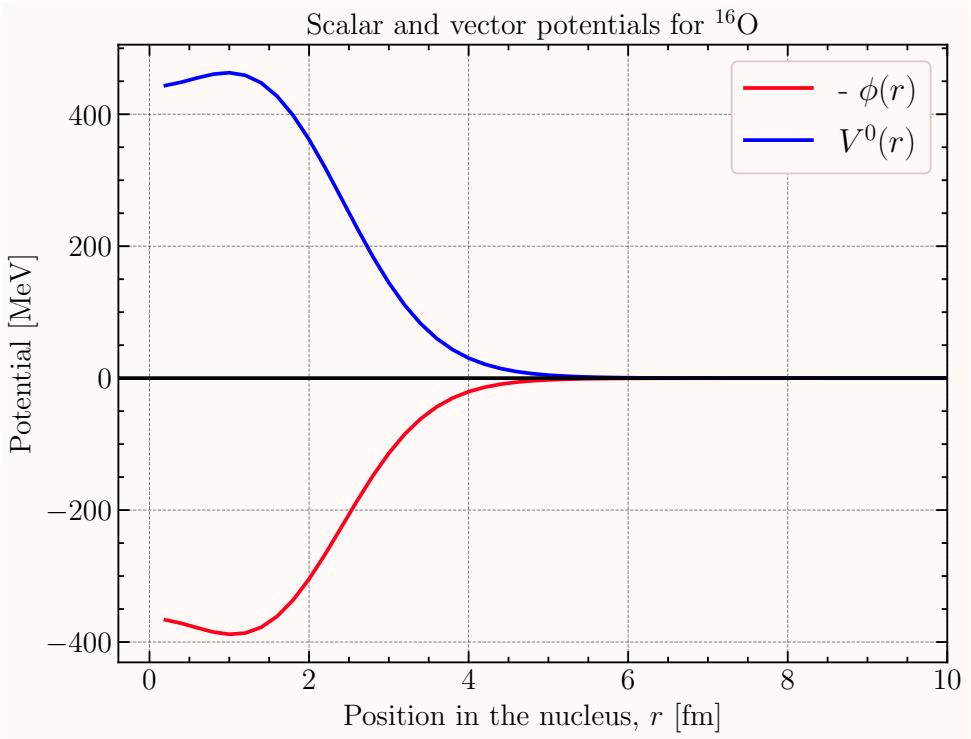

Figure 9.3: RMF scalar and vector potentials for oxygen outputted by the `TIMORA` code.

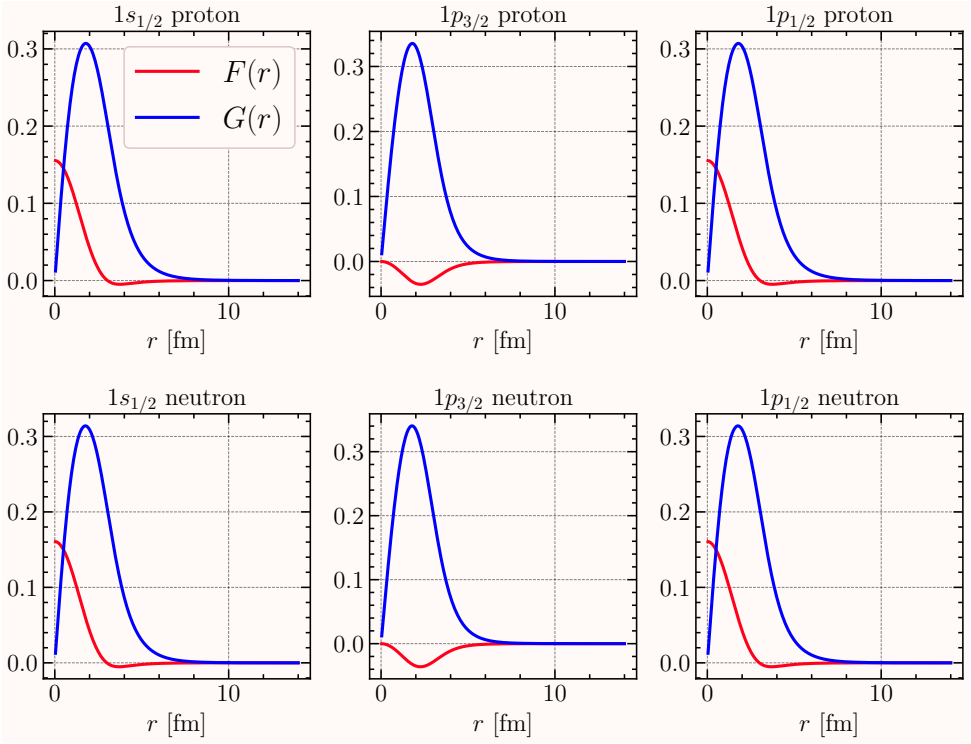

Figure 9.4: RMF wavefunction components $G(r)$ and $F(r)$ for oxygen outputted by the `TIMORA` code.

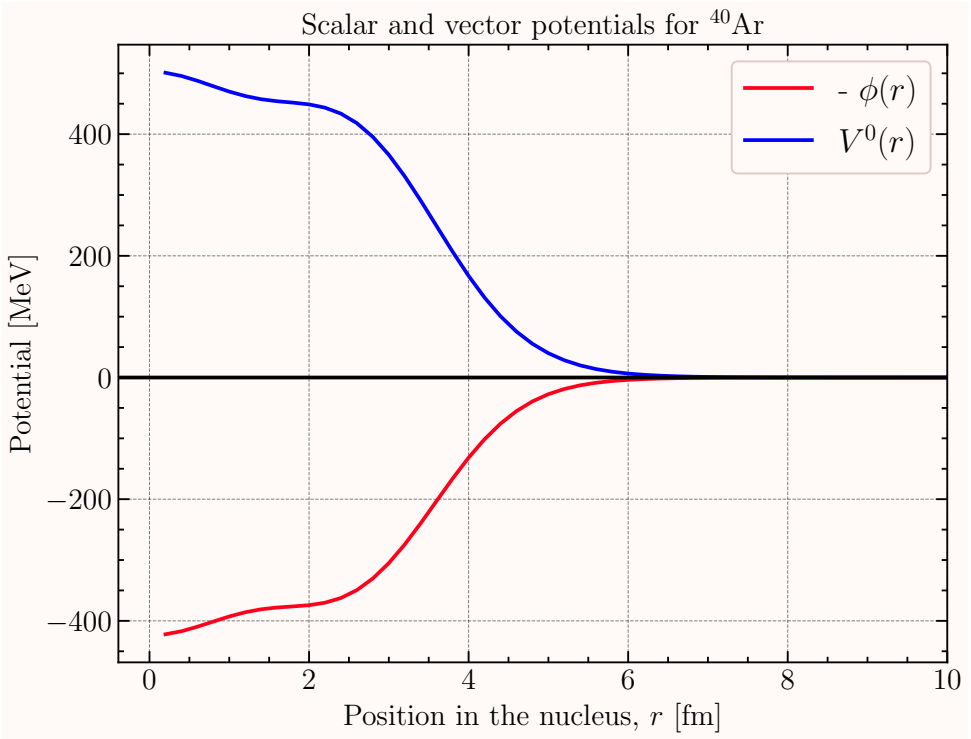

Figure 9.5: RMF scalar and vector potentials for argon outputted by the `TIMORA` code.

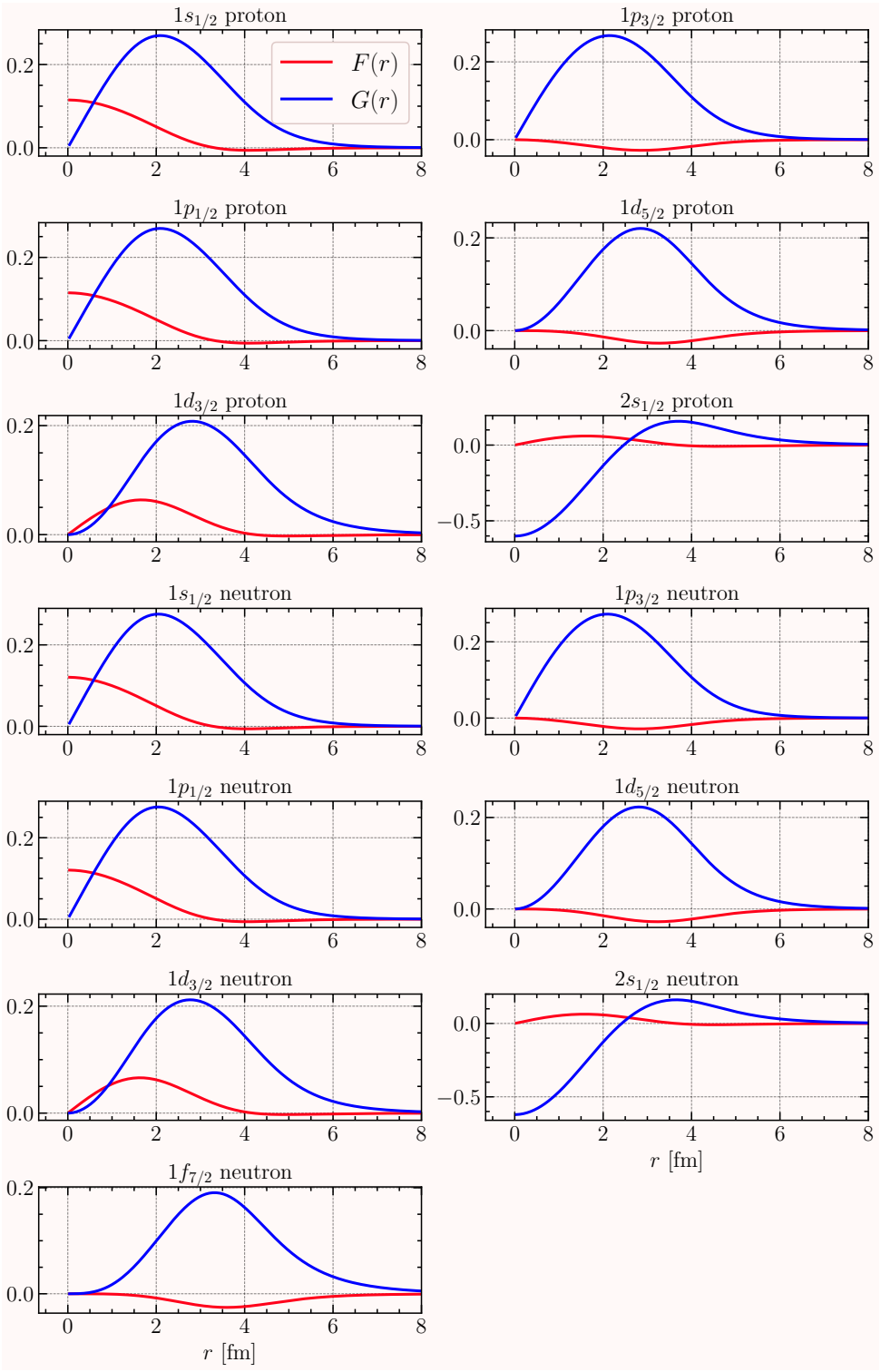

Figure 9.6: RMF wavefunction components $G(r)$ and $F(r)$ for argon outputted by the `TIMORA` code.

Chapter 10

Relativistic mean field theory with distorted waves – a model combining the best of both worlds

This section explains a lepton-nucleus scattering model, developed mostly by Universidad Complutense de Madrid and the University of Seville, that is used for the rest of this work. This section is mostly paraphrased from the preprint [140] which I wrote on the implementation into the NEUT event generator (see Section 11 for details). However, additional details describing the electron scattering model are explained.

The model is described in the first-order Born approximation, meaning there is only a single boson exchanged in the interaction [141, 142]. The Born approximation allows for the separation of the lepton and hadron parts of the interaction into lepton and hadron tensors as described in previous chapters. The IA is also used, meaning there is a sum over the contributions from all nuclear shells for a given nucleus. In this model, the treatment of the scattered nucleon can include interactions with the nuclear potential as it traverses the nuclear medium. This makes it possible to model elastic FSI as described in Section 8.2.1.

Taking the kinematic definitions shown in Figure 10.1, the incident neutrino is assumed to be along the z-axis, $\hat{\mathbf{z}}$, with four momentum $K^\mu = (E_\nu, \mathbf{k})$. The interaction on a single nucleon with four momentum $P_A^\mu = (M_A, \mathbf{0})$ produces a lepton and hadron in the final state; this is often called a "one-particle one-hole" (1p1h) final state. The lepton part of the interaction is contained within a plane, called the scattering plane, and has four momentum $K_l^\mu = (E_l, \mathbf{k_l})$. The polar angle θ_l is defined as the angle between the vector $\mathbf{k_l}$ and $\hat{\mathbf{z}}$ within the scattering plane. A rotation of the scattering plane around $\hat{\mathbf{z}}$ is denoted by the azimuthal angle ϕ_l. The hadron part of the interaction can also be contained within a plane, called the reaction plane, and has four momentum $P_N^\mu = (E_N, \mathbf{p_N})$. The polar angle θ_N is defined between the vector $\mathbf{p_N}$ and $\hat{\mathbf{z}}$ in the reaction plane. The azimuthal angle between the reaction plane and the scattering plane is defined as ϕ_N. The momentum

transfer Q^μ is defined as

$$Q^\mu = K^\mu - K_l^\mu = (\omega, \mathbf{q}). \tag{10.1}$$

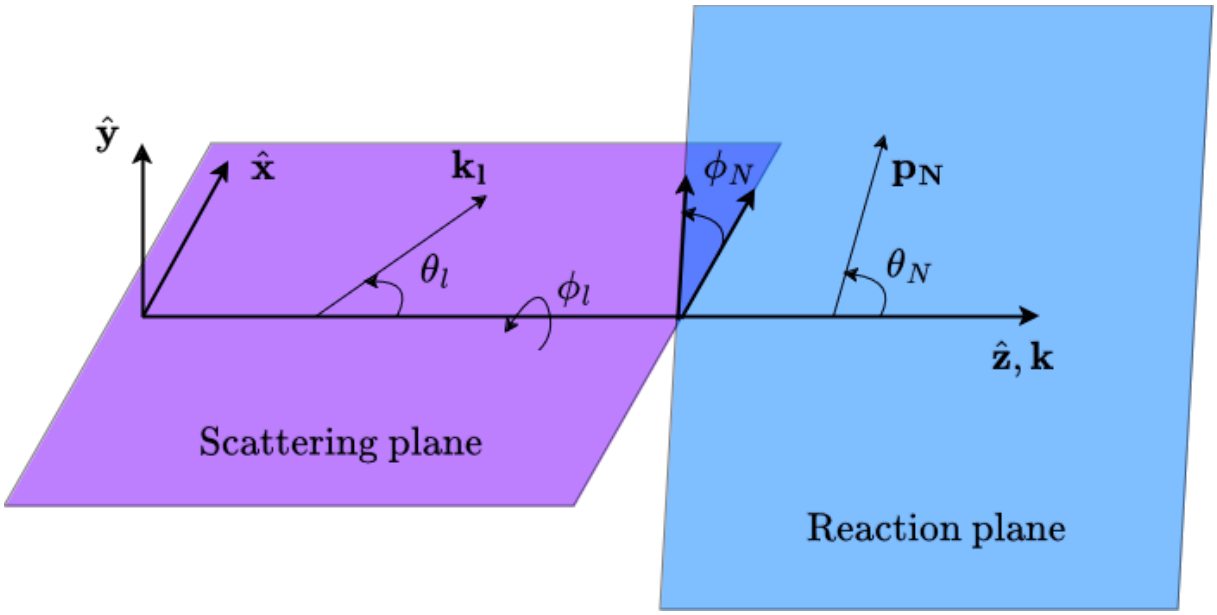

Figure 10.1: Schematic showing the coordinates and kinematic vectors used in this model. The scattering plane and reaction plane are explicitly separated and are chosen to contain the scattered lepton and nucleon respectively. The incident particle direction is always considered to be along the z-axis, $\hat{\mathbf{z}}$.

For a given neutrino energy, the full neutrino-nucleus interaction is described by six independent variables; the laboratory variables $(k_l, \theta_l, \phi_l, p_N, \theta_N, \phi_N)$ are used. With these independent variables, the fully exclusive cross section is given by

$$\frac{d^6\sigma}{dk_l' d\Omega_k dp_N d\Omega_N} = \frac{G_F^2 \cos^2(\theta_c) k_l^2 p_N^2}{64\pi^5} \frac{W_B}{E_B f_{\text{rec}}} \times L_{\mu\nu} \sum_\kappa \rho_\kappa(E_m) H_\kappa^{\mu\nu}. \tag{10.2}$$

Here, the cross section depends on the invariant mass of the residual nucleus, W_B, and the energy, E_B. The recoil factor, f_{rec}, is defined as

$$f_{\text{rec}} = \left| 1 - \frac{\mathbf{p_m} \cdot \hat{\mathbf{z}}}{E_B} \right|. \tag{10.3}$$

The lepton tensor is defined like Equation 7.8 as

$$L_{\mu\nu} = \frac{2}{E_\nu E_l} \left[K_\mu K_{l;\,\nu} + K_\nu K_{l;\,\mu} - g_{\mu\nu} K^\lambda K_{l;\,\lambda} - ih\epsilon_{\mu\nu\alpha\beta} K^\alpha K_l^\beta \right],$$

where $g_{\mu\nu}$ is the metric tensor (Minkowski metric), $\epsilon_{\mu\nu\alpha\beta}$ is the four-dimensional Levi-Civita tensor and h is the helicity of the neutrino state, defined as $h = -1$ for neutrinos and $h = +1$ for antineutrinos.
$\rho_\kappa(E_m)$ is the missing energy density for each shell κ. In the IPSM, it is given by a Dirac delta centred at the binding energy of each shell E_b^κ, i.e.:

$$\rho_\kappa(E_m) = \delta(E_m - E_b^\kappa)\,. \tag{10.4}$$

The hadron tensor is more complex and encodes nuclear effects experienced by the scattered nucleon as it leaves the nuclear medium. It is defined through hadron currents of single-particle RMF solutions as

$$H_\kappa^{\mu\nu} = \frac{1}{2j+1}\sum_{m_j,s}[J^\mu_{\kappa,m_j,s}]^*[J^\nu_{\kappa,m_j,s}], \tag{10.5}$$

where the sum is over the quantum numbers m_j and s, which denote the third component of the total angular momentum of the hole state and spin of the scattered nucleon state, respectively. The quantum number j is the total angular momentum of the shell and $2j+1$ gives the total occupancy available to the shell. The hadron current is defined by the four dimensional spinors of the bound nucleon state and the scattered nucleon state, along with the transition operator defining the interaction:

$$J^\mu_{\kappa,m_j,s} = \int \mathrm{d}\mathbf{p}\,\bar{\psi}_s(\mathbf{p}+\mathbf{q},\mathbf{p_N})\,\Gamma^\mu\,\Psi_\kappa^{m_j}(\mathbf{p}). \tag{10.6}$$

Here, ψ is the scattered nucleon distorted wavefunction and Ψ is the bound nucleon wavefunction. The transition operator, Γ^μ, is that of the CCQE operator in the CC2 formalism [114] and is defined as

$$\Gamma^\mu = F_1\gamma^\mu + \frac{iF_2}{2M_N}\sigma^{\mu\nu}Q_\nu + G_A\gamma^\mu\gamma^5 + \frac{G_P}{2M_N}Q^\mu\gamma^5, \tag{10.7}$$

where F_1, F_2, G_A and G_P are the vector, axial-vector and pseudoscalar form factors. This is the same definition as in Section 7.2. The axial-vector form factor is described using a dipole formalism with a value of $M_A^{\mathrm{QE}} = 1.0$ GeV/c^2 .

10.1 Initial state modelling

The initial state is modelled with RMF theory explained in Chapter 9. The parameters used for the initial state are given in Table 9.1

10.2 Final state modelling

The final state is modelled in the RDWIA similar to that of Ref. [143]; the scattered nucleon wavefunction is the solution to the Dirac equation in the presence of a relativistic

nuclear potential. The distorted wave is expanded in the spherical harmonic basis (also called a partial-wave expansion), similar to Chapter 9.

$$\Psi_{\mathrm{DW}}(\mathbf{r},\mathbf{p},m_s) = 4\pi\sqrt{\frac{E+M}{2EV}}\sum_{\kappa=-\infty}^{\infty}\sum_{m_j=-j}^{+j} e^{-i\delta_\kappa} i^l \left\langle l, m_l, \frac{1}{2}, m_s \middle| j, m_j \right\rangle \left[Y_{l,m_l}(\Omega_{\mathbf{p}})\right]^\dagger \Psi_{\kappa,m_j}(\mathbf{r}). \tag{10.8}$$

Here, δ_κ denote phase shifts, $m_l = m_j - m_s$ and $\Psi_{\kappa,m_j}(\mathbf{r})$ is the solution to the Dirac equation in the presence of a central potential as described in Equation 9.22. The difference now, is that the central potential is the nuclear potential we want to use to describe the nuclear medium which the scattered particle traverses through. The choice of this potential alters the wavefunctions and has different predictions for the scattered state particle. If there is no potential, then it collapses back to the RPWIA.

10.2.1 Nuclear potentials

This model proposed in this work is computed in five different nuclear potential models. These potentials are the relativistic plane wave impulse approximation (RPWIA), i.e. without a nuclear potential, but more interestingly, the pure RMF, energy-dependent RMF (ED-RMF) and the energy-dependent A-independent (EDAI) relativistic optical potential (ROP) and the real only EDAI ROP. The ROPs used are that of Cooper *et. al.* [144]. Each potential is introduced and their respective qualities are briefly explained.

Pure RMF

The pure RMF potential is the same real potential as the bound-state potential found in Chapter 9. This is an obvious first choice of potential and has the advantage of introducing consistency between the initial and final states; the initial nucleon and scattered nucleons are both solutions to the Dirac equation. As a result, the wavefunctions are orthogonal and naturally introduces Pauli blocking [145, 134]. However, an important drawback of the RMF potential is its inherent energy-independent nature. As a result, at larger scattered nucleon energies, the RMF potential is too strong and predicts a large reduction in the CCQE peak and an increased cross section in the high ω tail in (e,e') inclusive electron scattering data [146].

The ROP

RMF potential is purely real and therefore can only describe the elastic propagation of a nucleon in the nuclear medium. Inelastic interactions, which can result in a significant amount of energy transfer, are not included in real potentials. As the energy of the interaction increases, the inelastic contribution increases and it also opens up more channels. A complex component of the nuclear potential may be included which can describe the flux lost due to inelastic interactions. Such potentials, referred to as ROPs, have been

extracted from proton-nucleus scattering data [144] and are widely used in the field [147, 148, 149, 150]. However, in an experimental setting, in the case where the final-state nucleon is not detected, the strength lost to inelastic FSI should not be removed. On top of this nuclear potential lacking the consistency between the initial and final states, this makes using this potential difficult in experimental settings. The predictions from the ROP correspond to a scenario where the struck nucleon exists the nucleus without losing energy, except for that lost to elastic interactions. This is equivalent to only events with a nucleon passing through the nucleus without interacting are retained. In the case of CCQE, that means a final state lepton and a single nucleon. Therefore, the EDAI potential provides a lower bound for the CCQE cross section when compared to semi-inclusive neutrino-nucleus scattering samples.

The rROP

Retaining only the real component of the ROP means that the reduction of strength due to inelastic interactions is retained while the empirical energy-dependence of the real potential is maintained. Because of this, the elastic propagation of the nucleon is described well. At high T_N, this matches predictions from the ED-RMF potential but differs at lower T_N differences arise from the lack of consistence and orthogonality between the initial and final states [146, 145]. In this model, for interactions on ^{12}C, proton-^{12}C elastic scattering data is used for the fit and is referred to as the EDAIC model. The same is true for ^{16}O. However, for ^{40}Ar, an optical potential is not available; therefore the potential for the isobaric ^{40}Ca is used and denoted as EDAICa. The Coulomb potential is different for calcium and so this is corrected for.

ED-RMF

To make the RMF potential energy dependent, an empirical approach developed in Ref. [145] modifies the original RMF potential with a blending function that is dependent on the scattered nucleon kinetic energy, T_N. The parameters in this approach are taken from the SuSAv2 scaling parameters [151, 152], which are tuned to (e, e') inclusive electron scattering data. This results in the EDRMF potential getting attenuated at large nucleon energies, in a similar fashion to the real part of phenomenological optical potentials and more consistent with dispersion relationships [146]. The scaling function is given as

$$f_b(T_N) = L(T_N) + F(T_N), \tag{10.9}$$

with $L(T_N)$ and $F(T_N)$ being given by

$$\begin{aligned} L(T_N) &= \frac{0.85}{(T_N/200)^2 + 3.5} + 0.29, \\ F(T_N) &= \frac{0.48}{\exp\{[(T_N - 90)/23]\} + 1}. \end{aligned} \tag{10.10}$$

The blending function is used in the fashion $V_{\text{ED-RMF}}(T_N) = f_b(T_N)V_{\text{RMF}}(T_N)$. The blending function is shown in Figure 10.2. At low T_N, the value of $f_b(T_N) \to 1$, meaning

$V_{\text{ED-RMF}}(T_N) = V_{\text{RMF}}(T_N)$ and the initial and final states are consistent and orthogonal. The blending function is then quickly suppressed and stabilises at around 200 MeV where it tends to asymptote at 0.3. The ED-RMF potential is shown alongside the pure RMF, EDAI and energy-dependent A-dependent (EDAD) complex optical potential in Figure 10.3. Here the RMF, ED-RMF, EDAI and EDAD nuclear potentials are shown for ^{12}C. It is clear that at low T_N the ED-RMF and RMF potential match well, while at larger T_N, the strength of the potential is suppressed to match that of the optical potentials. At $T_N = 1500$ MeV, the ED-RMF potential now drops below the optical potentials; however, it should be noted that this region is outside of the range the optical potentials were fit to, and so should be used with caution. The ED-RMF potential is a real potential so there is no flux lost to the inelastic channel. The results obtained with this approach match well to those obtained when using only the real part of an energy-dependent optical potential [146] or within a relativistic Green function approach [153].

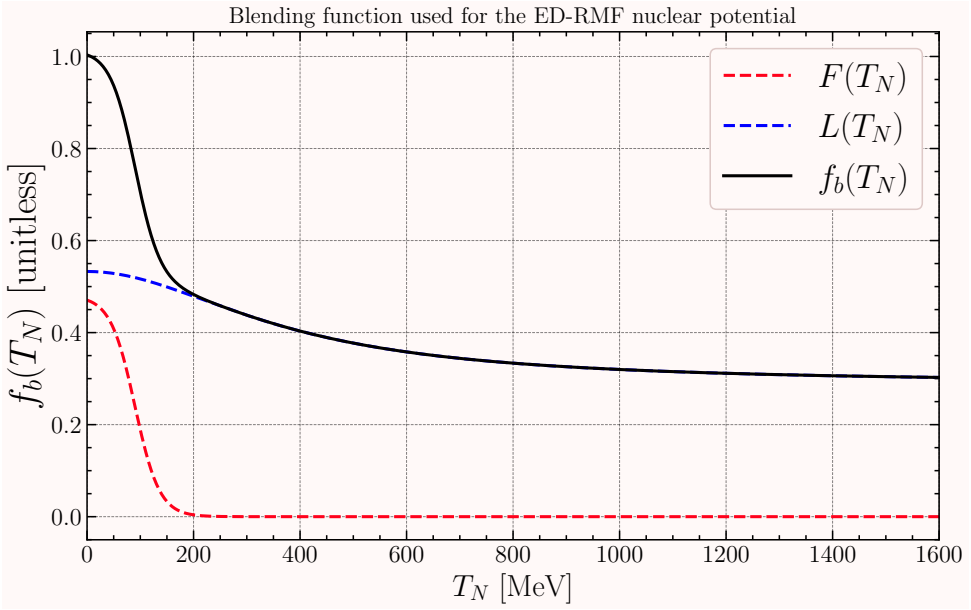

Figure 10.2: Empirical blending function used in the ED-RMF approach. The functions are determined using SuSAv2 scaling parameters that are fit to (e, e') inclusive electron scattering data.

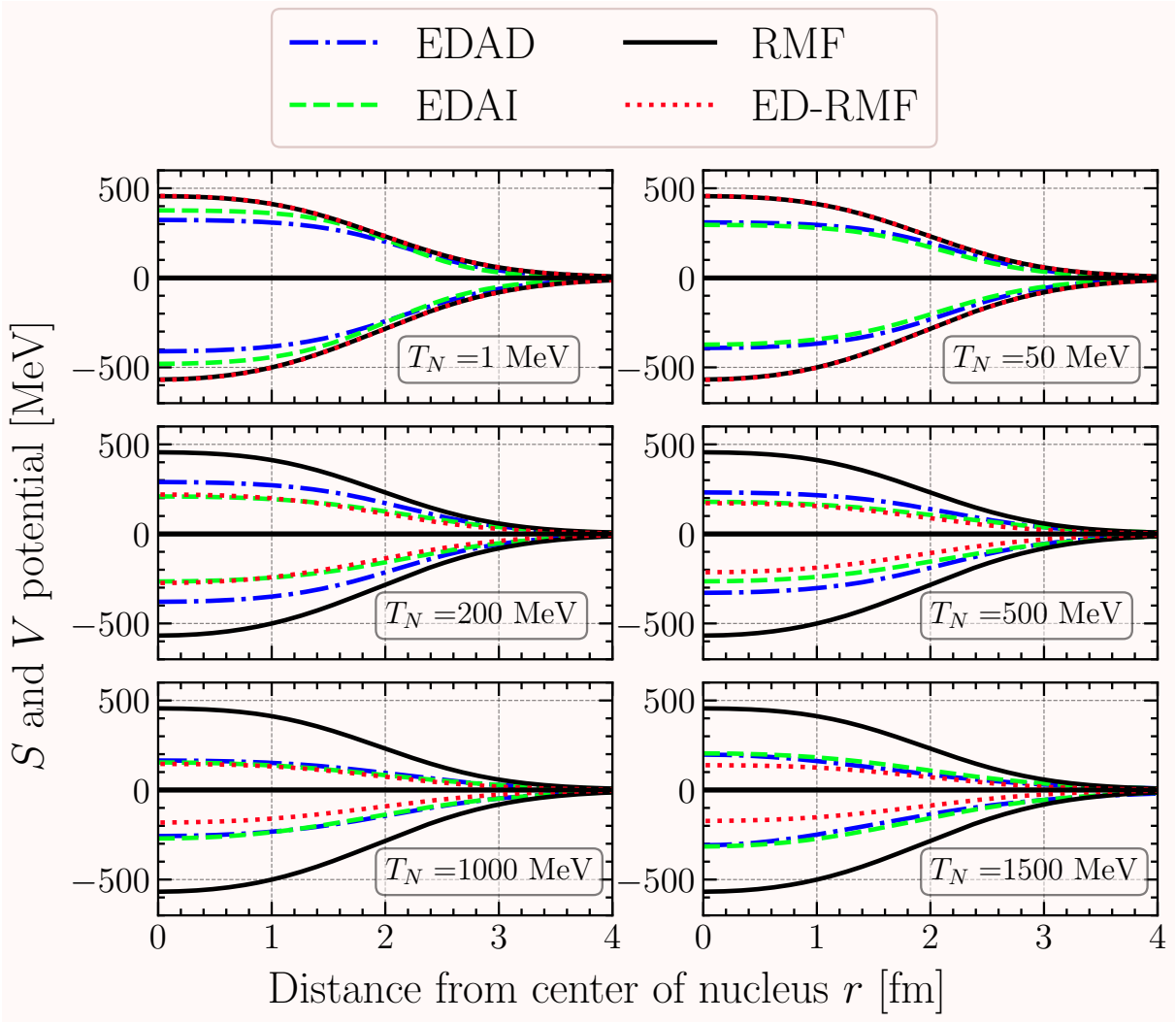

Figure 10.3: Pure RMF, energy-dependent RMF (ED-RMF), energy-dependent A-independent (EDAI) and energy-dependent A-dependent (EDAD) nuclear scalar and vector potentials shown as a function of radial distance to the centre of the nucleus. Each panel increases with scattered nucleon kinetic energy.

10.3 Beyond the independent-particle shell model

Due to the presence of nuclear correlations, such as SRC, the energy and momentum distributions of the nucleons are not fully described within the IPSM. IPSM models have been shown to overestimate data indicating that shell occupancies in nature are lower compared to IPSM predictions [154, 155, 156, 157, 158, 159, 160, 161, 162, 147, 148, 163]. This indicates that the mathematical structures which describe the nuclear shells in the E_m profile are not Dirac delta functions. To obtain a more realistic model, contributions from nuclear correlations need to be included. This is done in the spectral function ap-

proach as explained in Section 8.3.3. In the spectral function approach, the shell-model contributions are smeared and depleted when compared to IPSM predictions. The spectral function approach also explicitly includes SRC contributions which appear at higher energy [133].

Drawbacks of the spectral function approach, explained in Section 8.3.3, mean that it is not an approach that can be used universally. However, it is possible to build a representation of a realistic spectral function, where the shell-model contribution is described by the sum of momentum distributions computed within the RMF approach with an additional term describing the high-energy high-momentum tail where SRC contributions arise [164].

The model introduced in this section achieves this by using Gaussian functions to model the missing energy densities, replicating the Rome SF [165, 166]. Gaussian functions were chosen because of their simplicity to model and sum together for different shells. This is described in more detail in Section 10.4. The central values of the Gaussian functions were chosen to be the RMF eigenvalues described in Chapter 9, or experimental values where they are available. The widths of the Gaussian functions for ^{12}C and ^{16}O are described in Refs. [164, 167]. For ^{40}Ar, the Gaussian widths come from Ref. [149]. The approach described in Refs. [164, 167, 168, 169] is used to introduce an additional $s_{1/2}$ shell in order to capture the SRC contributions [170, 128]. This shell is referred to as the "background shell" and is described in Section 10.4.4. The occupancies of the shells, which translates to an overall normalisation scale to the Gaussian functions, are chosen to model the Rome SF and assume an 80% occupancy in the nuclear shells with the remaining 20% in the background shell. As shown in Ref. [164], this approach to modelling the missing energy density results in matching the Rome SF to within a few percent.

The final missing energy density is given as a sum over the densities of each shell:

$$\rho(E_m) = \sum_{\kappa} \rho_{\kappa}(E_m), \tag{10.11}$$

with $\int dE_m \rho(E_m)$ giving the total number of protons or neutrons.

10.4 Modelling of missing energy profile

10.4.1 Carbon missing energy density

Nucleons in Carbon occupy the $1s_{1/2}$ and $1p_{3/2}$ shells. For these shells, the missing energy density is given as

$$\rho_{\kappa}(E_m) = \frac{N_{\kappa}}{\sqrt{2\pi}\sigma^{\kappa}} e^{-\frac{(E_m - E_m^{\kappa})^2}{2(\sigma^{\kappa})^2}}, \tag{10.12}$$

where N_{κ} is the occupancy of the shell κ. The central values and widths of these Gaussian functions, E_m^{κ}, σ^{κ}, are given below in Table 10.1 and Table 10.2. The normalised missing

energy distribution for protons is shown in Figure 10.4.

Shell	Occupancy	E_m^κ[MeV]	σ^κ[MeV]
$1s_{1/2}$	1.9/2	40.5	10.0
$1p_{3/2}$	3.3/4	14.46	2.0

Table 10.1: Central values and widths of Gaussian functions used to model the proton shells in ^{12}C.

Shell	Occupancy	E_m^κ[MeV]	σ^κ[MeV]
$1s_{1/2}$	1.9/2	44.37	10.0
$1p_{3/2}$	3.3/4	17.81	2.0

Table 10.2: Central values and widths of Gaussian functions used to model the neutron shells in ^{12}C.

10.4.2 Oxygen missing energy density

Nucleons in Oxygen occupy the $1s_{1/2}$, $1p_{3/2}$ and $1p_{1/2}$ shells. The central values and widths of the Gaussian functions are given below in Table 10.3 and Table 10.4. The normalised missing energy density is shown in Figure 10.5.

Shell	Occupancy	E_m^κ[MeV]	σ^κ[MeV]
$1s_{1/2}$	1.62/2	37.70	15.0
$1p_{3/2}$	3.47/4	18.27	1.0
$1p_{1/2}$	1.51/2	11.49	1.0

Table 10.3: Central values and widths of Gaussian functions used to model the proton shells in ^{16}O.

Shell	Occupancy	E_m^κ[MeV]	σ^κ[MeV]
$1s_{1/2}$	1.62/2	42.24	15.0
$1p_{3/2}$	3.47/4	22.36	1.0
$1p_{1/2}$	1.51/2	15.49	1.0

Table 10.4: Central values and widths of Gaussian functions used to model the neutron shells in ^{16}O.

10.4.3 Argon missing energy density

Nucleons in Argon occupy the $1s_{1/2}$, $1p_{3/2}$, $1p_{1/2}$, $1d_{5/2}$, $1d_{3/2}$ and $2s_{1/2}$ shells. The central values and widths of the Gaussian functions are given below in Table 10.5 and Table 10.6. The normalised missing energy density is shown in Figure 10.6.

Shell	Occupancy	E_m^κ[MeV]	σ^κ[MeV]
$1s_{1/2}$	2.0/2	47.42	8.0
$1p_{3/2}$	3.8/4	32.31	8.0
$1p_{1/2}$	1.9/2	27.72	8.0
$1d_{5/2}$	4.8/6	17.14	4.0
$1d_{3/2}$	1.7/4	10.02	2.0
$2s_{1/2}$	1.7/2	9.89	2.0

Table 10.5: Central values and widths of Gaussian functions used to model the proton shells in ^{40}Ar.

Shell	Occupancy	E_m^κ[MeV]	σ^κ[MeV]
$1s_{1/2}$	2.0/2	54.56	15.0
$1p_{3/2}$	3.8/4	38.74	8.0
$1p_{1/2}$	1.9/2	34.20	8.0
$1d_{5/2}$	4.8/6	23.09	4.0
$1d_{3/2}$	3.3/4	15.95	2.0
$2s_{1/2}$	1.7/2	16.11	2.0
$1f_{7/2}$	1.6/8	8.27	2.0

Table 10.6: Central values and widths of Gaussian functions used to model the neutron shells in ^{40}Ar.

The normalised missing energy profile is shown in Figure 10.6

10.4.4 Background shell modelling

The additional $1s_{1/2}$ shell is modelled differently for different E_m regions.

$\underline{E_m < 26 \text{ MeV}}$:

$$\rho(E_m) = 0 \tag{10.13}$$

$\underline{26 < E_m < 100 \text{ MeV}}$:

$$\rho(E_m) = \frac{ae^{-100b}}{e^{-(E_m - c)/w} + 1} \tag{10.14}$$

$\underline{E_m > 100 \text{ MeV}}$:

$$\rho(E_m) = ae^{-bE_m} \tag{10.15}$$

The parameters for oxygen are described in Table 10.7. The same functional form is used for carbon and argon, but it is rescaled using the background shell occupancies given in Table 10.8 to ensure the correct number of nucleons.

Parameter	Value
a	0.03113 MeV^{-1}
b	0.0112371 MeV^{-1}
c	40 MeV
ω	5 MeV

Table 10.7: Parameters used to model the background $1s_{1/2}$ shell.

Nucleus	p	n
^{12}C	0.8	0.8
^{16}O	1.4	1.4
^{40}Ar	2.1	2.9

Table 10.8: Proton (p) and neutron (n) occupancies of the background $1s_{1/2}$ shell

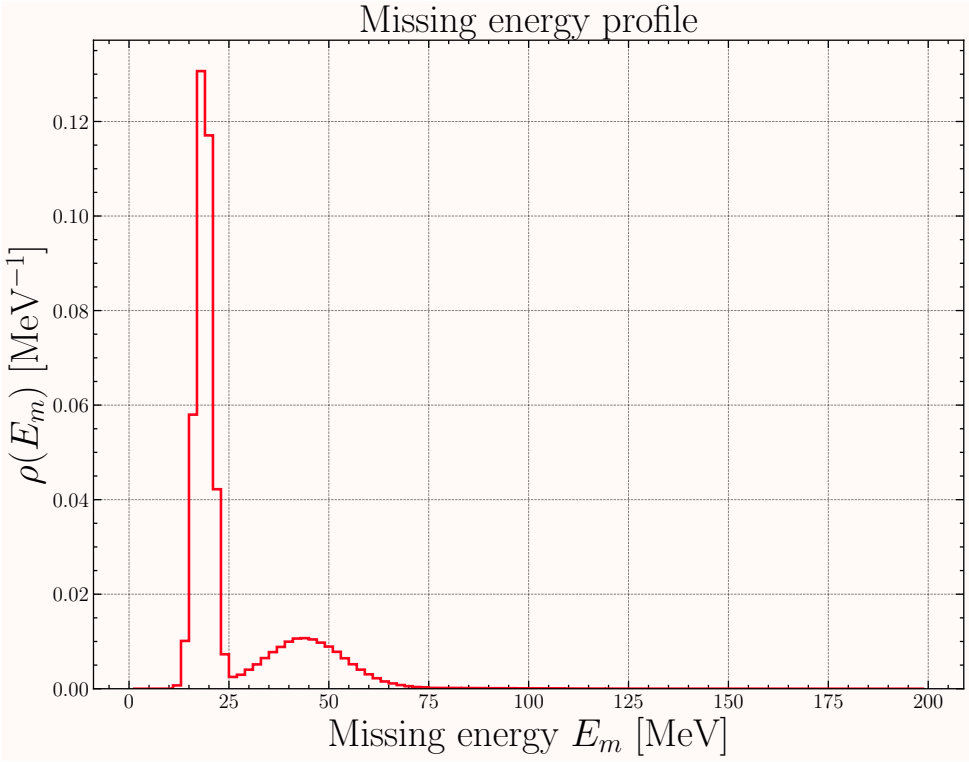

Figure 10.4: Missing energy profile for ^{12}C. The two $1p_{3/2}$ and $1s_{1/2}$ shells are clearly seen as the large, narrow peak and broad lower peak respectively.

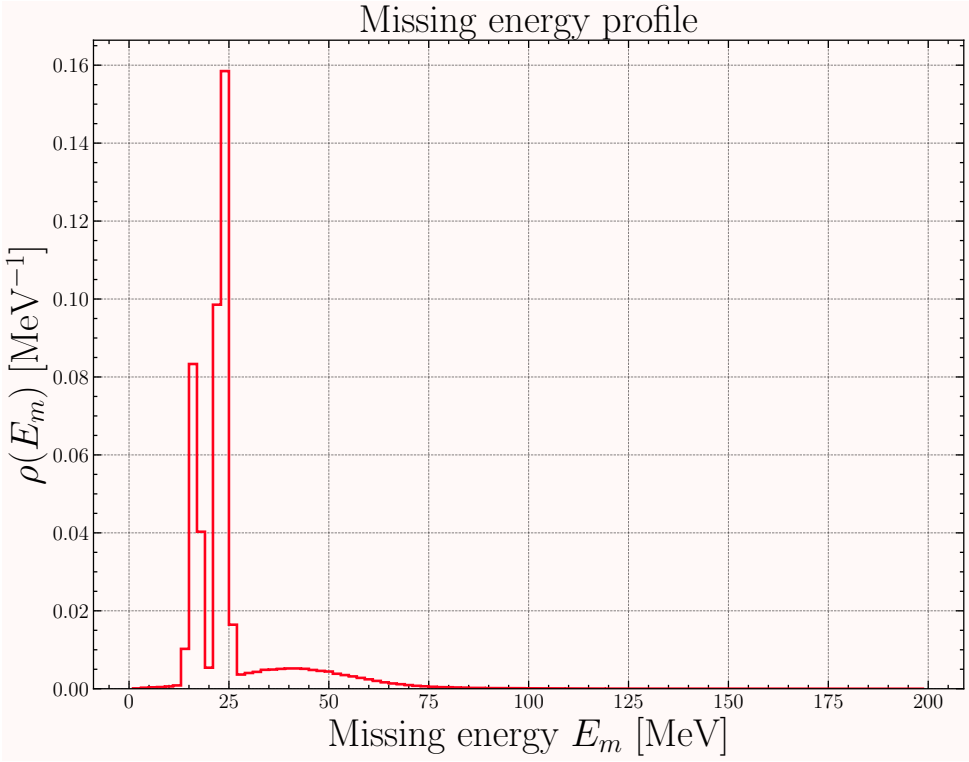

Figure 10.5: Missing energy profile for ^{16}O. The two $1p_{3/2}$ and $1p_{1/2}$ shells are clearly seen as the large, narrow peaks and the $1s_{1/2}$ is the broad lower peak respectively.

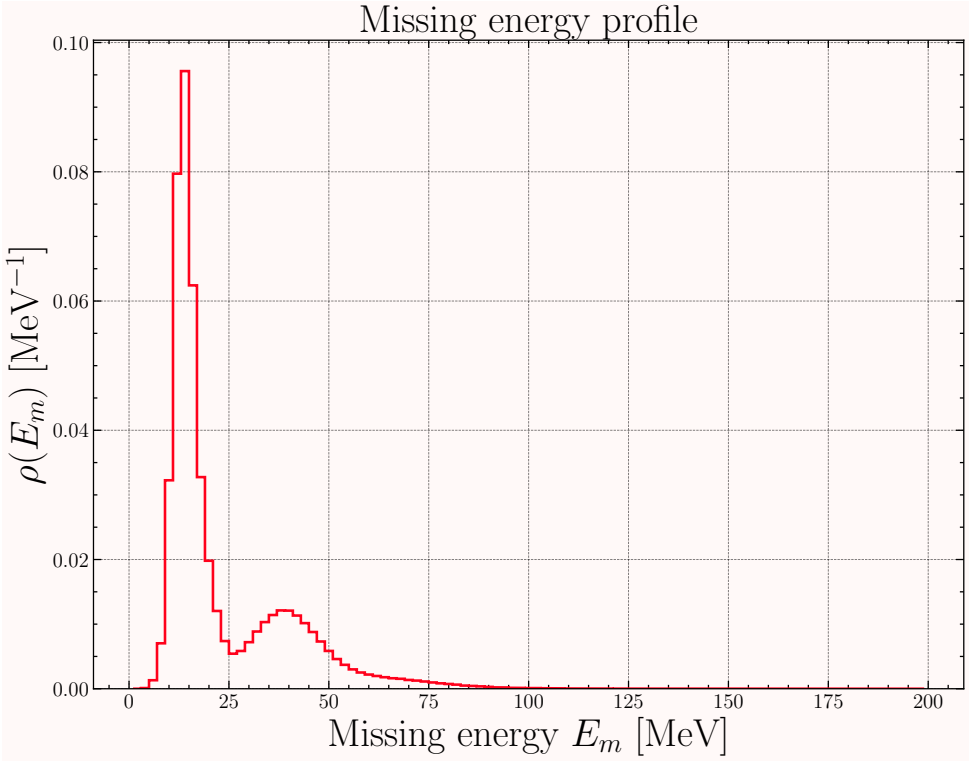

Figure 10.6: Missing energy profile for ^{40}Ar. The two $1p_{3/2}$ and $1p_{1/2}$ shells are clearly seen as the large, narrow peaks and the $1s_{1/2}$ is the broad lower peak respectively.

Chapter 11

Implementation into the NEUT event generator

Neutrino event generators (EGs) are pieces of software which simulate neutrino interactions on various nuclei. Some EGs are capable of including detector geometry such that an accurate simulation of neutrino interactions within a detector can be produced. EGs contain interaction channels from CCQE to DIS and are capable of containing specialised reaction channels. Quite often, the available channels differ between EGs. Also, the implementation of different interaction models can differ between EGs. This creates a challenge for experiments wanting to model neutrino-nucleus interactions. Often, multiple EGs are used in an experiment to get an average. There are many EGs available for neutrino interactions (some of which include electron scattering). The T2K experiment has used NEUT [171] historically. This work also focuses on NEUT as I implemented the model described in Chapter 10 into NEUT. Other EGs include NuWro [172], GENIE [173], Achilles [174] and GiBUU [175]. It is important to note that the model that I implemented in NEUT is currently not available in any of the other EGs. This chapter details the implementation into the NEUT EG.

11.1 The NEUT event generator

NEUT works to simulate neutrino events according to a neutrino flux such that neutrino experiments can be simulated. A flux file can be passed directly to NEUT. A monochromatic beam can also be simulated. Within NEUT, an event rate is produced from the flux shape and the shape of the total cross section of the interaction channels chosen to simulate. The shape of this event rate distribution is used to draw neutrino energies for event simulation. This ensures that neutrino energies are drawn with respect to the given flux shape and total cross section, improving the efficiency of event production.

The NEUT generator is based on the assumption that the initial interaction vertex can be separated entirely from the FSI that the final-state particles experience. It does this by simulating the initial interaction via standard rejection-sampling Monte Carlo methods.

This produces an event which should be distributed by the underlying interaction model and the information of all the particles (the particle stack) is saved. The final-state particle momentum information is then used in a separate algorithm, the NEUT intra-nuclear cascade ("cascade" from now on), which dictates whether a particular final-state particle undergoes FSI. The NEUT cascade is semi-classical, meaning it treats the particles like billiard balls that scatter into each other, changing the momentum and producing new final-state particles.

The NEUT cascade is based on a particle's mean free path within the nuclear medium and simulates interactions between pions, kaons, etas, omegas, protons and neutrons [171]. From the point a particle is inserted into the cascade, its position is tracked and stepped by a fixed step size of 0.2 fm until it leaves the nucleus. At every step, whether a particle has interacted or not is decided based on its mean free path. Regardless of the nuclear model used in the initial interaction vertex, the cascade uses a Woods-Saxon nucleon density function with a local Fermi gas to calculate interaction positions and kinematics [171]. The cascade can be separated into two types of interactions: meson and nucleon interactions. For nucleon interactions, or nucleon re-scattering, the Bertini model, which takes into account elastic scattering, one and two pion production, is used [176]. Meson interactions in the cascade are based on Ref. [177]. Despite containing elastic nucleon re-scattering, the NEUT cascade always outputs both particles after the re-scatter, meaning the final state of the cascade is always an inelastic FSI contribution. An elastic FSI contribution, as described in previous chapters, is not implemented in NEUT.

NEUT event generation can be separated into the following steps:

1. The total cross section as a function of neutrino energy is loaded for the given flux or monochromatic beam setting.
2. A given channel is chosen to produce an event based on the probability, P, of a channel's cross section with respect to the total cross section for a target [171]
$$P = \sigma_T^i(E_\nu)/\sigma_T^{\text{tot}}(E_\nu) \tag{11.1}$$
where T is the target nucleus or nucleon and i is a given channel. For a single channel, this step is simplified and all other channels are multiplied by 0.
3. The initial interaction vertex for the chosen channel is simulated and the accepted event particle stack is saved.
4. The final-state nucleons and mesons are passed into the NEUT cascade where nucleon re-scattering and pion absorption FSI are simulated.

11.2 Implementation into NEUT

The implementation of such a fundamentally different model into NEUT was quite a challenge. The model without any modifications was too slow to be used practically in

EGs. Therefore, the decision was made to produce precomputed tables for the hadron tensor. The calculation for the distorted wave spinor is the bottleneck of the model due to the partial wave expansion method. Therefore, having precomputed hadron tensor tables removes this expensive calculation and allows for the contraction of the lepton and hadron tensor directly. This made the model fast enough to be usable in EGs. Initially, however, the method used produced an event approximately every two seconds; this is still too slow for large-scale MC productions. The model was improved by changing the independent variables in which the fully exclusive cross section is calculated; speeding the model up to an event approximately every 0.01 s. This section details the implementation details, such as the hadron tensor tables, their structure and the algorithm and its improvements.

11.2.1 Hadron tensor tables

The precomputed hadron tensor tables were produced for each neutrino helicity state, each nuclei and each final-state nuclear potential. The tables in this implementation were all produced with the dipole parameterisation for the axial form factor with the axial mass parameter, $M_A^{\mathrm{QE}} = 1$ GeV. Currently, there are tables for ^{12}C, ^{16}O and ^{40}Ar implemented since these nuclei are mostly used in neutrino experiments.

The hadron tables are given as a seven-column text file with the hadron tensor being a function of:

- scattered nucleon kinetic energy, T_N;
- scattered nucleon polar angle, θ_N;
- third component of the missing momentum, p_m^z;
- and missing energy, E_m.

The other three columns comprise the tensor index (0 to 10, with the other 6 being removed through symmetry arguments), real component and the imaginary component of the tensor. The tables are calculated in the reference frame such that the momentum transfer in the interaction is parallel to the incident beam, i.e. $\mathbf{q}$ is parallel to $\hat{\mathbf{z}}$. The kinematics for an event is initially thrown in the laboratory frame where the target nucleus is at rest. Therefore, the reference frames need to be switched when the hadron tensor table values need to be retrieved, after which they are switched back to the laboratory frame. The required rotations are described in Section 11.2.2

The tables are encoded such that only integers are stored for the above four bulleted variables. The integers describe steps in a given step size between a pre-defined minimum and maximum value. This was done to save memory when saving the tables to a text file as they are saved as integers rather than floats or doubles.

The hadronic tensors are precomputed for the aforementioned variables within a certain range. This range was chosen for two reasons:

1. The T2K experiment flux tails off to a negligible value while 5% of the DUNE flux is missed at the upper limit (see Fig. 2 in Ref. [164]).

2. Calculating the hadronic current takes time and, for larger values of T_N, the computation time increases.

The ranges of variables used in the tables are given in Table 11.1. The units for T_N is MeV, θ_N is degrees and p_m^z is MeV.

Variable	Min	Max	Step
T_N	1	1101	10
θ_N	0	180	2.0
p_m^z	-800	800	20.0

Table 11.1: Ranges of variables used in the hadronic tensor tables. Units are in MeV apart from nucleon angle which is in degrees.

It is important to note that the variable T_N changes quite rapidly below around 10 MeV. As a result, between 0 and 10 MeV, there is a separate table with a dedicated 1 MeV T_N step. All other variables are the same in this separate "low T_N" table. The E_m variable is closely related to properties of individual nuclei and so the step size between nuclei changes.

Carbon

The E_m range is shell dependent and neutrino helicity dependent. All following values in Table 11.2 are given in MeV.

Neutrino helicity	Shell	Min	Max	Step
Neutrino	$1p_{3/2}$	17.8075	17.8075	1
Neutrino	$1s_{1/2}$	20	110	15
Antineutrino	$1p_{3/2}$	14.46	14.46	1
Antineutrino	$1s_{1/2}$	20	110	15
Both	Background	20	300	40

Table 11.2: Missing energy steps, in MeV, for ^{12}C is different depending on the shell and neutrino helicity.

Oxygen

For ^{16}O, the E_m range is also shell dependent and neutrino helicity dependent. All following values in Table 11.3 are given in MeV.

Neutrino helicity	Shell	Min	Max	Step
Neutrino	$1p_{1/2}$	15.4871	15.4871	1
Neutrino	$1p_{3/2}$	22.3652	22.3652	1
Neutrino	$1s_{1/2}$	20	110	15
Antineutrino	$1p_{1/2}$	11.488	11.488	1
Antineutrino	$1p_{3/2}$	18.27	18.27	1
Antineutrino	$1s_{1/2}$	20	110	15
Both	Background	20	300	40

Table 11.3: Missing energy steps in MeV for ^{16}O is different depending on the shell and neutrino helicity.

Argon

For ^{40}Ar, the same is true and all values given in Table 11.4 are in MeV.

Neutrino helicity	Shell	Min	Max	Step
Neutrino	$2p_{1/2}$	9.857	9.857	1
Neutrino	$1d_{3/2}$	10.023	10.023	1
Neutrino	$1d_{5/2}$	10	40	10
Neutrino	$1p_{1/2}$	10	100	15
Neutrino	$1p_{3/2}$	10	100	15
Neutrino	$1s_{1/2}$	20	110	15
Antineutrino	$1f_{7/2}$	8.27	8.27	1
Antineutrino	$2s_{1/2}$	16.11	16.11	1
Antineutrino	$1d_{3/2}$	15.95	15.95	1
Antineutrino	$1d_{5/2}$	10	40	5
Antineutrino	$1p_{1/2}$	10	100	15
Antineutrino	$1p_{3/2}$	10	100	15
Antineutrino	$1s_{1/2}$	20	110	15
Both	Background	20	300	40

Table 11.4: Missing energy steps in MeV for ^{40}Ar is different depending on the shell and neutrino helicity.

11.2.2 Reference frame rotations

To go from the laboratory frame in which the events are initially thrown, to the frame in which the hadron tensor tables are evaluated, three rotations are required. The reference frames which the transformations go through are defined in terms of the kinematics outlined in Section 10.

- $\{x, y, z\}_L$: The reference frame where the target nucleus is at rest, neutrino momentum, $\mathbf{k}$, is along $\hat{\mathbf{z}}$ and $\mathbf{k}_l$ is in an arbitrary direction.

- $\{x, y, z\}_{L0}$: The reference frame where the target nucleus is at rest, $\mathbf{k}$ is along $\hat{\mathbf{z}}$ and, $\mathbf{k}$ and $\mathbf{k}_l$ define the scattering plane, $\mathbf{k}_l$ has no second component.
- $\{x, y, z\}$: The reference frame where the target nucleus is at rest and $\mathbf{q}$ is along $\hat{\mathbf{z}}$.
- $\{1, 2, 3\}$: The reference frame where the scattered nucleon kinematics define the reaction plane. $\mathbf{p}_N$ has no second component.

The rotations required are

- $\{x, y, z\}_L \rightarrow \{x, y, z\}_{L0}$: A rotation by ϕ_l angle clock wise along the z-axis.

$$\begin{pmatrix} x \\ y \\ z \end{pmatrix}_{L0} = \begin{pmatrix} \cos(\phi_l) & -\sin(\phi_l) & 0 \\ \sin(\phi_l) & \cos(\phi_l) & 0 \\ 0 & 0 & 1 \end{pmatrix} \begin{pmatrix} x \\ y \\ z \end{pmatrix}_{L}. \tag{11.2}$$

- $\{x, y, z\}_{L0} \rightarrow \{x, y, z\}$: A counter clockwise rotation of θ_{kq}, along the y axis. θ_{kq} is defined by $\cos(\theta_{kq}) = \mathbf{q} \cdot \mathbf{k}/(k \cdot q)$, where k and q are the magnitude of the vectors in the $\{x, y, z\}_{L0}$ frame. Because $\mathbf{k}$ is defined to be along $\hat{\mathbf{z}}$, it only has one component.

$$\begin{pmatrix} x \\ y \\ z \end{pmatrix} = \begin{pmatrix} \cos(\theta_{kq}) & 0 & \sin(\theta_{kq}) \\ 0 & 1 & 0 \\ -\sin(\theta_{kq}) & 0 & \cos(\theta_{kq}) \end{pmatrix} \begin{pmatrix} x \\ y \\ z \end{pmatrix}_{L0}. \tag{11.3}$$

- $\{x, y, z\} \rightarrow \{1, 2, 3\}$: A rotation of angle ϕ_N^{xyz} along the z axis so that $\mathbf{p}_N$ has no y component. ϕ_N^{xyz} is defined by $\cos(\phi_N^{xyz}) = \mathbf{p}_N^{xyz}[1]/(p_N \sin(\theta_N^{xyz}))$ and $\sin(\theta_N^{xyz}) = \sqrt{1 - (\mathbf{p}_N^{xyz}[3]/p_N)^2}$. Here $[X]$ denotes the X component of the three vector in the reference frame.

$$\begin{pmatrix} 1 \\ 2 \\ 3 \end{pmatrix} = \begin{pmatrix} \cos(\phi_N^{xyz}) & -\sin(\phi_N^{xyz}) & 0 \\ \sin(\phi_N^{xyz}) & \cos(\phi_N^{xyz}) & 0 \\ 0 & 0 & 1 \end{pmatrix} \begin{pmatrix} x \\ y \\ z \end{pmatrix}_{x,y,z}. \tag{11.4}$$

Once in the $\{1, 2, 3\}$ reference frame, the hadron tensor tables can be interpolated as described in Section 11.2.3. The hadron tensor components are then transformed back into the laboratory frame when calculating the differential cross section given in Equation 10.2.

11.2.3 Table interpolation

The hadron tensor tables are interpolated using a four-dimensional bilinear interpolation. To estimate the value of a complex function $f(x, y, z, w)$ at an arbitrary point (p_x, p_y, p_z, p_w), the algorithm iteratively applies the linear interpolation formula across the four dimensions. For a single dimension, the linear interpolation between two points x_0 and x_1 is given by:

$$f_{\text{interp}}(p_x) = \frac{x_1 - p_x}{x_1 - x_0} f(x_0) + \frac{p_x - x_0}{x_1 - x_0} f(x_1).$$

Extending this to four dimensions, the interpolated value $f_{\text{interpolated}}$ is calculated by first performing the interpolation over the x-dimension:

$$f_x(y,z,w) = \frac{x_1 - p_x}{x_1 - x_0} f(x_0,y,z,w) + \frac{p_x - x_0}{x_1 - x_0} f(x_1,y,z,w).$$

This result is then interpolated along the y-dimension:

$$f_{xy}(z,w) = \frac{y_1 - p_y}{y_1 - y_0} f_x(y_0,z,w) + \frac{p_y - y_0}{y_1 - y_0} f_x(y_1,z,w).$$

Next, interpolation proceeds in the z-dimension:

$$f_{xyz}(w) = \frac{z_1 - p_z}{z_1 - z_0} f_{xy}(z_0,w) + \frac{p_z - z_0}{z_1 - z_0} f_{xy}(z_1,w).$$

Finally, interpolation along the w-dimension yields the fully interpolated value:

$$f_{\text{interpolated}} = \frac{w_1 - p_w}{w_1 - w_0} f_{xyz}(w_0) + \frac{p_w - w_0}{w_1 - w_0} f_{xyz}(w_1).$$

In the implementation, the algorithm calculates the bounds $[x_0, x_1], [y_0, y_1], [z_0, z_1], [w_0, w_1]$ from the input values and extracts the corresponding function values from a four-dimensional array. This algorithm is applied to each hadron tensor index.

11.2.4 ϕ_l dependence

The differential cross section given in Equation 10.2 has no dependence on the angle ϕ_l. This angle is shown in Figure 10.1 and is the angle around $\hat{\mathbf{z}}$ in the laboratory frame. The fact that the differential cross section does not depend on this angle is not surprising as it denotes a symmetry around $\hat{\mathbf{z}}$ and that there is no special orientation of the scattering or reaction planes. As a result, the angle is integrated over and produces a factor of 2π; this factor is added in directly into the code. In the model itself, ϕ_l can be fixed to any arbitrary angle and it does not affect any final kinematic distributions. However, if the model is used to produce geometry information, then ϕ_l should be sampled on the interval $[0,\ 2\pi]$.

11.2.5 Missing energy profile

The E_m profile, described in Section 10.4, is modelled such that the centres and widths of the Gaussian distributions used to model the nuclear shells can be changed. The normalisations of the shells can also be varied. This is made possible by ensuring that the E_m density function in Equation 10.2, $\rho(E_m)$, is independent of the hadron tensor and is implemented analytically. Therefore, NEUT users can change the nuclear shell properties in the E_m profile. However, for nuclei such as ^{12}C and ^{16}O, the centres, widths and normalisations of the nuclear shells are well known and constrained by inclusive electron scattering data. Users changing these profiles in NEUT must be wary of breaking model

agreement with the inclusive electron scattering data. For heavier nuclei, such as ^{40}Ar and ^{40}Ca, the uncertainties on the shell parameters are significantly larger [169, 178]. The varying of these shell parameters allows the systematic uncertainties associated with them to be studied.

11.2.6 Initial algorithm and improvements

The initial algorithm sampled the independent variables $(k_l, \theta_l, \phi_l, p_N, \theta_N, \phi_N)$. The ranges for the variables were initially pre-defined as:

- k_l: $[0,\ \sqrt{(E_\nu^{\max})^2 - m_l^2}]$ where $E_\nu^{\max}$ is the maximum neutrino energy that the neutrino flux extends to and m_l is the scattered lepton mass.
- θ_l: $[0,\ \pi]$.
- ϕ_l: $[0,\ 2\pi]$.
- p_N: $[0,\ \sqrt{(E_N^{\max})^2 - M_N^2)}]$ where $E_N^{\max} = E_\nu - m_l + M_A - (M_A - M_N - 299)$.
- θ_N: $[0,\ \pi]$.
- ϕ_N: $[0,\ 2\pi]$.

The initial algorithm was as follows.

1. Uniformly sample the six independent variables to describe the scattered state system given an incident neutrino energy.
2. Calculate E_m, p_m, Q^2 and ω.
3. Reject any events that have such values outside of theoretically allowed bounds for these quantities.
4. Transform to the reference frame of the hadron tensor tables.
5. Interpolate tensor values and transform back to laboratory frame.
6. Calculate the six-fold differential cross-section.
7. Accept or reject event based on random sample of the six-fold differential cross section where the ceiling is an input.

The rejection sampling method, stated in step (6), involved sampling the six-fold differential cross section on the interval $[0,\ \mathrm{d}^6\sigma^{\max}]$ where $\mathrm{d}^6\sigma^{\max}$ is the maximum six-fold differential cross section across the neutrino energy range $[0,\ E_\nu^{\max}]$.

In the above algorithm, the boundary check on E_m, which is dependent on the sampled p_N value, was found to be the point which caused the most rejected events. The E_m distribution is very peaked meaning a general rejection sampling method would be inefficient

at reproducing it. As a result, the original algorithm was changed such that E_m is sampled directly from the true distribution, defined by the parameterisation in Section 10.4, using it as a probability density function. This required an additional weighting of the rejection sampling ceiling by a factor of $\frac{1}{\rho(E_m)}$. Also, since the independent variables $(k_l, \theta_l, \phi_l, E_m, \theta_N, \phi_N)$ are sampled, an additional Jacobian, shown in Equation 11.5, was required.

$$\frac{d^6\sigma}{d\mathbf{k_l} dp_N d\Omega_N} = \left|\frac{\partial p_N}{\partial E_m}\right|^{-1} \frac{d^6\sigma}{d\mathbf{k_l} dE_m d\Omega_N}. \tag{11.5}$$

The Jacobian used in the implementation neglects nuclear recoil and is given by

$$\left|\frac{\partial p_N}{\partial E_m}\right| = \frac{E_N}{p_N}. \tag{11.6}$$

The details of the Jacobian derivation are given in Section 11.2.10. Additionally, because the neutrino energy is fixed per event, k_l needs only to be sampled from $[0,\ E_\nu]$ for per event. Further improvements came from tabulating the maximum six-fold differential cross section as a function of neutrino energy and using this as an input to the model. By doing this, the rejection sampling ceiling is optimised per event. A simple linear interpolation algorithm is used to interpolate the maximum six-fold differential cross section for intermediary neutrino energies.

11.2.7 Final algorithm

The final algorithm incorporating these improvements is given as

1. Uniformly sample the five independent variables to describe the scattered state system given an incident neutrino energy.
2. Sample E_m from missing energy density.
3. Calculate p_N, p_m, Q^2 and ω.
4. Reject any events that have such values outside of theoretically allowed bounds.
5. Transform to the reference frame of the hadron tensor tables.
6. Interpolate tensor values and transform back to laboratory frame.
7. Calculate the six-fold differential cross-section.
8. Accept or reject event based on random throw of the six-fold differential cross-section. The ceiling is an input.

11.2.8 Total cross section

The NEUT EG can be used with a single monochromatic neutrino energy or a neutrino flux. For NEUT to sample neutrinos from a given neutrino flux efficiently, it calculates the "event rate" distribution from the flux multiplied by the total cross section of a given model. The shape of this event rate distribution is used by NEUT to sample neutrino energies. As a result, the total cross section as a function of neutrino energy is required as a model input. This input is required for all neutrino flavours, nuclei and final-state potentials. The total cross section is calculated by systematically stepping through incident neutrino energy in a user-defined step size and calculating the six-fold differential cross-section of accepted events and summing the six-fold differential cross-section, which is then divided by the total number of events thrown for that given neutrino energy. This value is then multiplied by the total averaged six dimensional phase space to obtain a total cross section for that neutrino energy. Figure 11.1 shows the total cross section for ν_μ scattering on ^{12}C. Other total cross section tables are given in Appendix D.

11.2.9 Maximum differential cross section

The maximum six-fold differential cross section, used as a ceiling for the rejection sampling algorithm, is different for each neutrino species, helicity and final-state potential. The ceiling value is calculated by systematically stepping through incident neutrino energy in a user-defined step size and retaining the maximum six-fold differential cross section of all accepted events for that neutrino energy. This input can drastically affect the model performance and accuracy. There are three cases to consider: the ceiling is too low; the ceiling is too high, or the ceiling is optimised.

The ceiling is too low

As shown below in Figure 11.2, in the case where the ceiling is too low, the true distribution can be cut out and the efficiency can be improved significantly at this cost. This results in a final kinematic distribution that does not correctly follow the cross section predicted by the model.

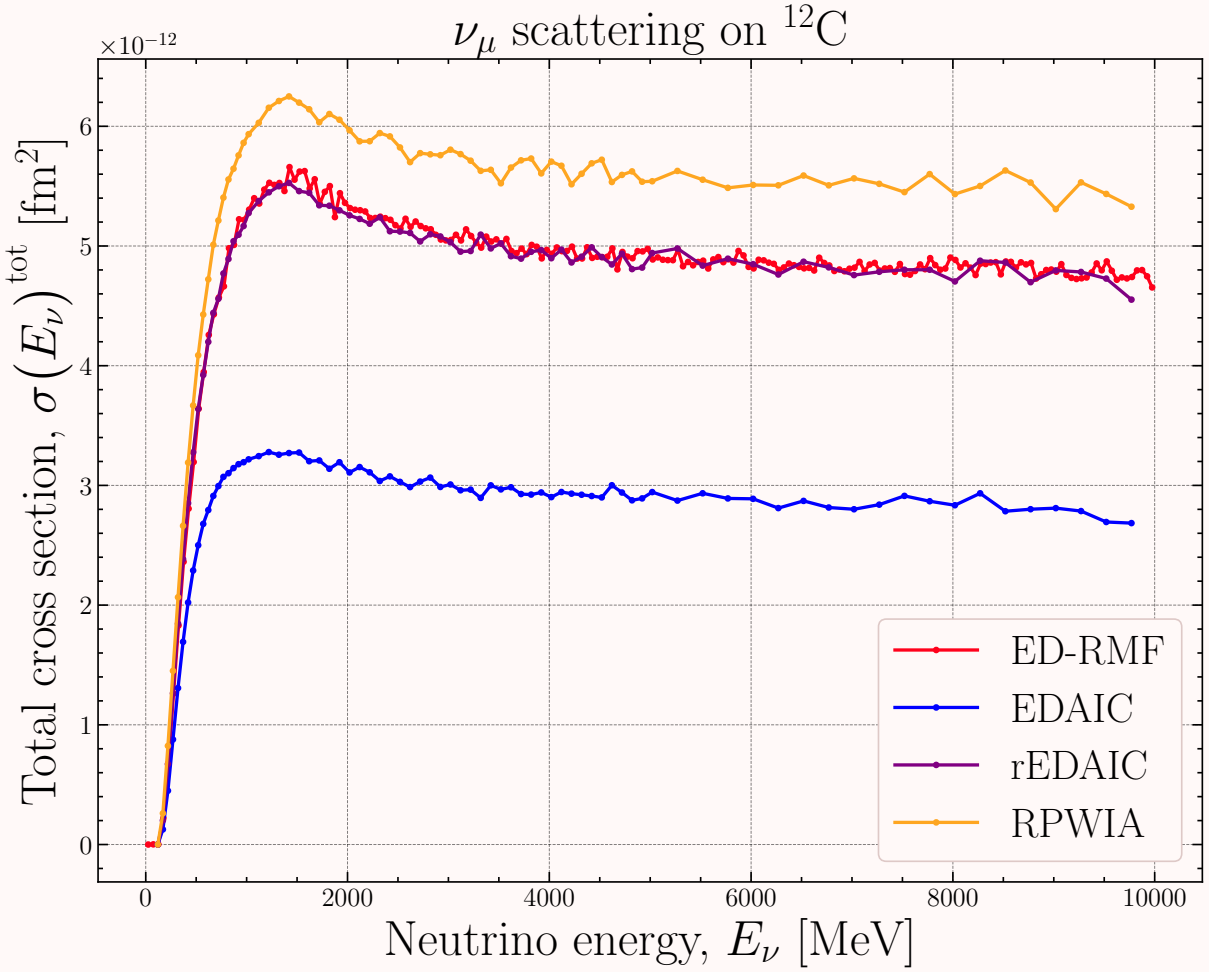

Figure 11.1: Total differential cross section as a function of neutrino energy for ν_μ on ^{12}C. The models shown are EDRMF, EDAIC (ROP), rEDAIC (real only ROP) and RPWIA.

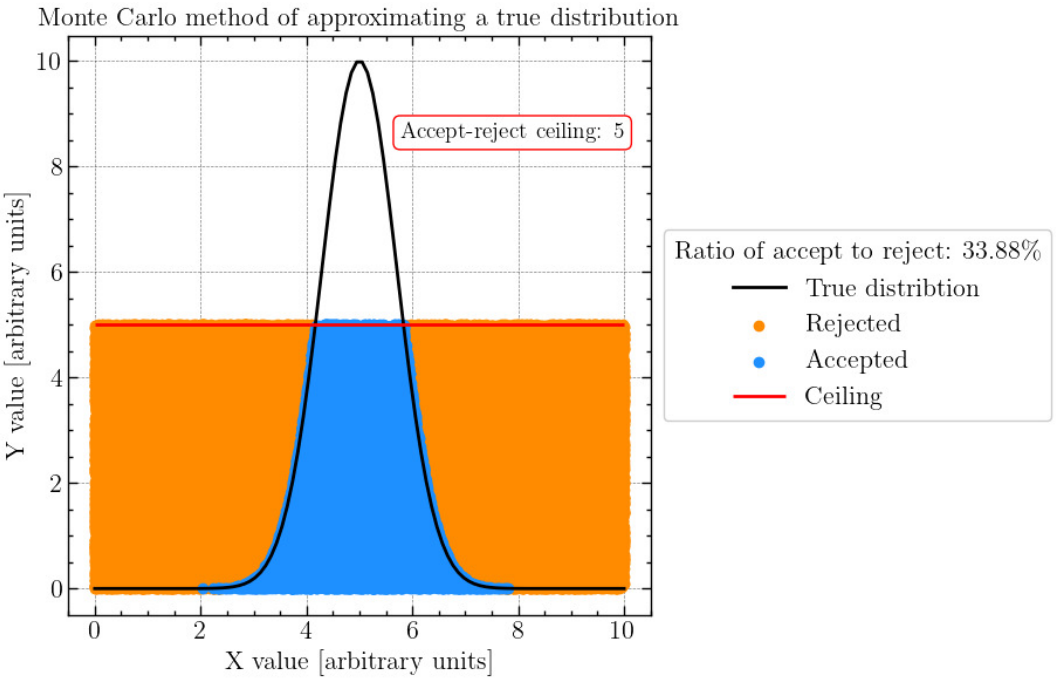

Figure 11.2: Visualisation of rejection sampling when the ceiling (red) is too low causing some of the true distribution to be missed.

The ceiling is too high

As shown below in Figure 11.3, in the case where the ceiling is too high, the true distribution can be fully encapsulated at the cost of efficiency. The number of points outside the true distribution (reject events) increases significantly if the ceiling value succeeds that of the true distribution maximum.

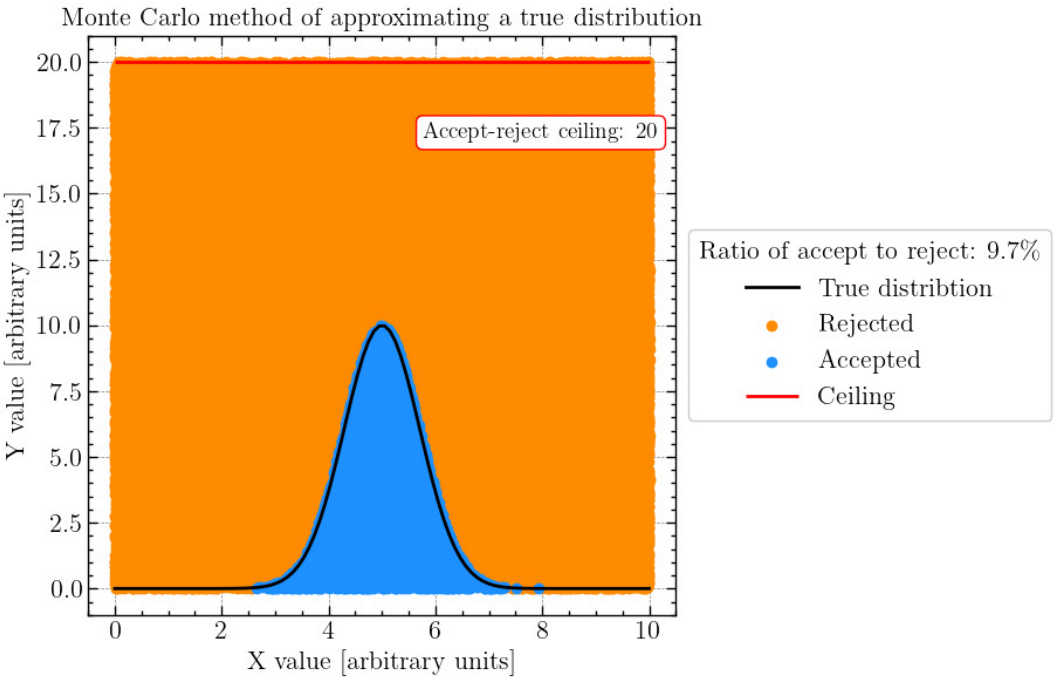

Figure 11.3: Visualisation of rejection sampling when the ceiling (red) is too high. All of the true distribution is captured, however, the proportion of rejected points increases causing the overall efficiency of the rejection sampling algorithm to decrease.

Optimised ceiling

Below, Figure 11.4 shows an example of a perfectly optimised ceiling for a rejection sampling method.

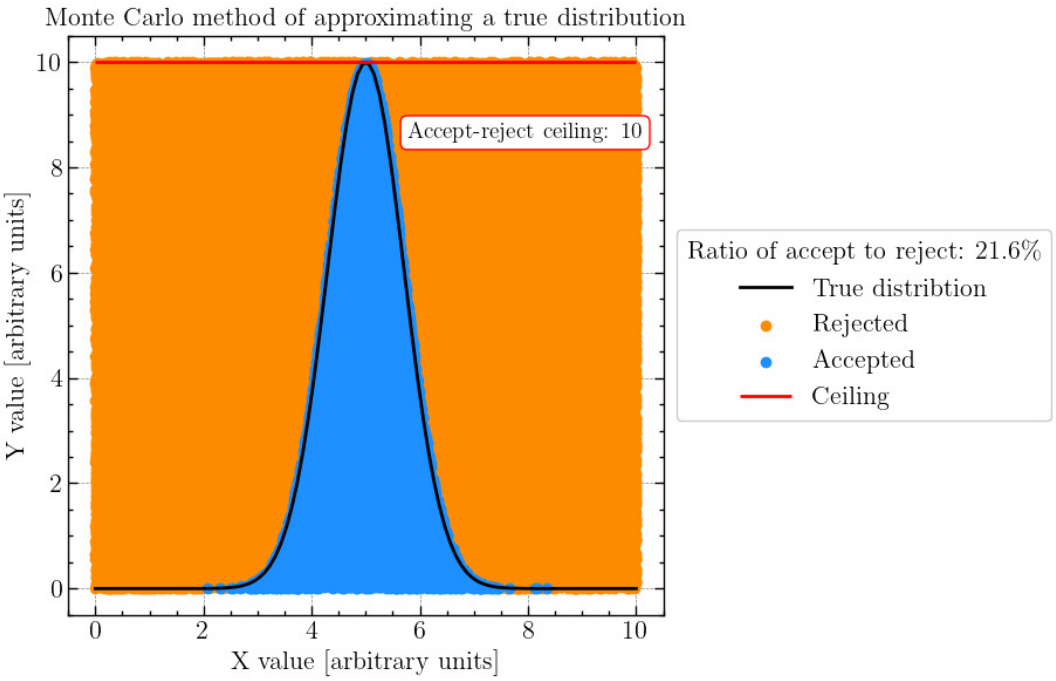

Figure 11.4: Visualisation of rejection sampling when the ceiling (red) is optimised. All of the true distribution is captured and the number of rejected points is minimised.

Figure 11.5 shows the maximum six-fold differential cross section for ν_μ scattering on ^{12}C. Other maximum six-fold differential cross section tables are given in Appendix D.

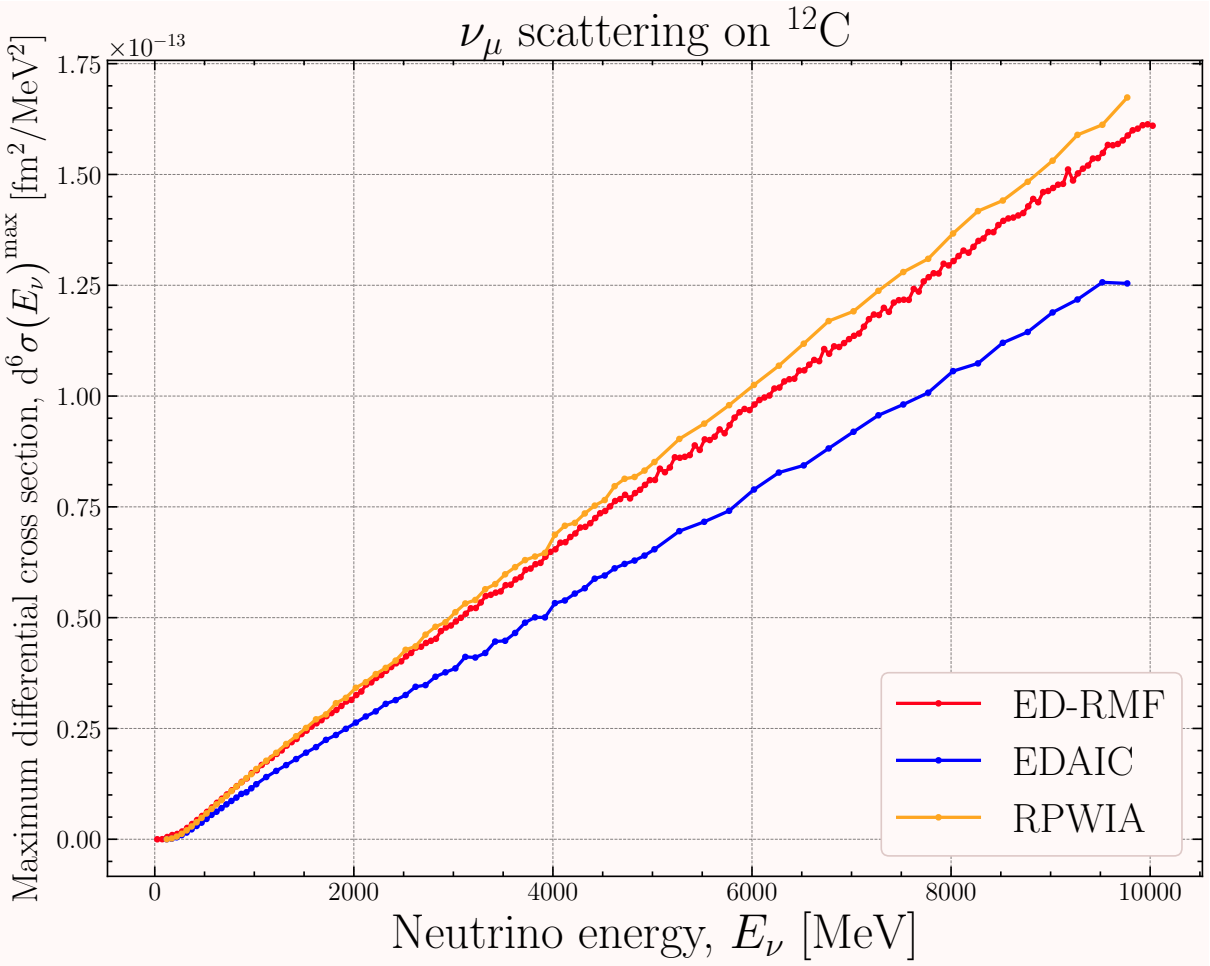

Figure 11.5: Total differential cross section as a function of neutrino energy for ν_μ on ^{12}C. The models shown are EDRMF, EDAIC (ROP), rEDAIC (real only ROP) and RPWIA.

11.2.10 Jacobian

Without nuclear recoil

The Jacobian required is given as

$$\left|\frac{\partial p_N}{\partial E_m}\right|. \tag{11.7}$$

This can be expressed approximately by considering the definition of E_m within the system.

$$p_N^2 = E_N^2 - M_N^2, \tag{11.8}$$

where E_N can be expressed as $T_N + M_N$. The missing energy is given as

$$E_m = \omega - T_N - T_B, \tag{11.9}$$

where T_B is the energy of the residual nucleus and ω is the energy transfer given by $E_\nu - E_l$. Using this, we can express E_m as follows.

$$E_m = \omega - E_N + M_N - T_B. \tag{11.10}$$

This can be substituted into Eq. 11.8 to yield

$$p_N^2 = (\omega - E_m + M_N - T_B)^2 - M_N^2. \tag{11.11}$$

Performing the required differentiation in Eq. 11.6,

$$2p_N \frac{\partial p_N}{\partial E_m} = -2(\omega - E_m + M_N - T_B) = -2E_N. \tag{11.12}$$

Finally, the required Jacobian is

$$\left| \frac{\partial p_N}{\partial E_m} \right| = \frac{E_N}{p_N}. \tag{11.13}$$

With nuclear recoil

To obtain the Jacobian given in 11.7, we make use of the relation

$$\frac{\partial E_m}{\partial p_N} = \frac{\partial E_m}{\partial E_B}\frac{\mathrm{d}E_B}{\mathrm{d}p_N} + \frac{\partial E_m}{\partial E_N}\frac{\mathrm{d}E_N}{\mathrm{d}p_N}. \tag{11.14}$$

where E_B is the recoil energy. The recoil energy and other useful relations are given below in Eq. 11.15

$$\begin{aligned}
&E_B^2 = M_B^2 + p_B^2, \\
&p_B^2 = q^2 + p_N^2 - 2qp_N\cos(\theta_{qN}), \\
&M_B = E_m - E_N + M_A, \\
&E_N = M_A + \omega - \\
&\sqrt{q^2 + p_N^2 - 2qp_N\cos(\theta_{qN}) + (E_m - M_N + M_A)^2}.
\end{aligned} \tag{11.15}$$

Here, the subscript "B" refers to the residual nucleus, q is the magnitude of the momentum transfer and θ_{qN} is the angle between the momentum transfer and the scattered nucleon. The first term in Eq. 11.14 is

$$\frac{\partial E_m}{\partial E_B}\frac{\mathrm{d}E_B}{\mathrm{d}p_N} = \frac{E_B}{M_B}\left(\frac{p_N - q\cos(\theta_{qN})}{E_B}\right), \tag{11.16}$$

and the second term is

$$\frac{\partial E_m}{\partial E_N}\frac{\mathrm{d}E_N}{\mathrm{d}p_N} = \frac{E_B}{M_B}\left(\frac{p_N}{E_N}\right). \tag{11.17}$$

The final Jacobian is then given as the inverse of the above

$$\begin{aligned}\left|\frac{\partial p_N}{\partial E_m}\right| &= \left|\frac{\partial E_m}{\partial p_N}\right|^{-1} \\ &= \frac{M_B}{E_B}\left|\frac{p_N}{E_N} + \frac{p_N - q\cos(\theta_{qN})}{E_B}\right|^{-1}\end{aligned} \tag{11.18}$$

This Jacobian is not used in the current implementation but will be incorporated in the next model iteration.

The effect of including of nuclear recoil

Although the Jacobian that neglects nuclear recoil, J_0 was used in the initial model implementation, the effect of including the nuclear recoil, J was approximated and it was found to be of the order of a percent.

The Jacobians, J_0 and J, are written below

$$\begin{aligned}J_0 &= \frac{E_N}{p_N} \\ J &= \frac{M_B}{E_B}\left|\frac{p_N}{E_N} + \frac{p_N - q\cos(\theta_{qN})}{E_B}\right|^{-1}.\end{aligned} \tag{11.19}$$

For interactions on ^{12}C, the residual nucleus, B, is either ^{11}C or ^{11}B. Therefore, $\frac{M_B}{E_B} \approx 1$. Let us define the quantity δ to be

$$\delta \stackrel{\text{def}}{=} \frac{p_N - q\cos(\theta_{qN})}{E_B} \approx \frac{p_N - q\cos(\theta_{qN})}{M_B}. \tag{11.20}$$

Then, looking at the ratio J/J_0,

$$\frac{J}{J_0} = \frac{1}{\frac{p_N}{E_N} + \delta}\frac{p_N}{E_N} = \left(1 + \frac{E_N}{p_N}\delta\right)^{-1} \approx 1 - \delta\frac{E_N}{p_N}. \tag{11.21}$$

Therefore, the relative change with respect to J_0 is given as

$$\frac{J - J_0}{J_0} \approx -\frac{E_N}{p_N}\delta. \tag{11.22}$$

This can now be approximated using rough typical values. Taking $M_B \approx 11$ GeV and $p_N \approx 0.5 - 0.8$ GeV/c, one can test some values of δ to quantify the relative difference by including nuclear recoil. For a CCQE interaction on a stationary target nucleon, p_N is often aligned with q, which means $p_N - q\cos(\theta_{qN}) \approx \mathcal{O}(10$ MeV).

Taking $p_N - q\cos(\theta_{qN}) = 20,\ 50$ and 300 MeV, the relative differences are approximately 1%, 0.4% and 4.6% respectively. For larger nuclei, such as ^{16}O and ^{40}Ar, these relative differences decrease further because of the suppressing $1/M_B$ term.

11.2.11 Background shell modelling

As described in Section 10.4, an additional $s_{1/2}$ shell is used to describe the additional strength seen at high E_m in the spectral function which corresponds to SRC (see Section 8.3.3). An important implementation detail is the hadron tensor table corresponding to the background shell is the same for neutrino and antineutrino interactions. However, since the hadron current, given in Equation 10.6, also depends on the initial state wavefunctions, which are affected by the Coulomb interaction, the contribution from the Coulomb interaction is neglected. A neutron initial state and a proton final state is assumed. This makes sure the Coulomb contribution is present for neutrino interactions. The same configuration is used for antineutrinos, meaning that the Coulomb contribution is included where it should not be.

11.2.12 Adding SRC

The initial model implementation, though including the background contribution from SRCs, only produced a 1p1h final state, neglecting the ejection of an additional SRC nucleon. Other CCQE models, such as the spectral function, has a check on E_m and p_m per event in NEUT. If an event falls above either of these checks, the event is classified as an SRC event and an additional nucleon is ejected in the model. The momentum for this SRC nucleon is the opposite of the initial struck nucleon. However, because the RMF-based model uses RMF wavefunctions to describe the initial state, the initial struck nucleon momentum is not known and cannot be known. In order to tackle this, the RPWIA approach is used for the SRC nucleon. The RPWIA approach introduces an equivalence between the initial struck nucleon and p_m, therefore, the momentum of the SRC nucleon is given as p_m.

In NEUT, the check for whether an event is classed as SRC is a check on E_m only. The value of the E_m check is configurable in the NEUT6 `toml` configuration file. The SRC nucleon type is defined probabilistically by another configurable parameter in the `toml` configuration file. The default setting is that the chance of the SRC nucleon being the same as the initial struck nucleon is 95% and the opposite 5%. In electron scattering, this is clear, but in neutrino scattering, due to the process being electroweak, it results in final states which have two of the same nucleon type.

11.2.13 Position in nucleus for cascade

The NEUT cascade takes information from events that pass the rejection sampling algorithm. The final-state particle is placed into the cascade at a radius which is defined by each model. If a model does not define a radius value, then NEUT samples randomly from a sphere defined by the maximum radial distance for a given nucleus. The current implementation does not set a radius value and so NEUT performs this random sampling.

11.2.14 Systematic uncertainties within the model

The model contains several adjustable parameters that can be varied to study systematic uncertainties. The parameters are summarised in Table 11.5 alongside the suggested boundaries of such parameters.

Table 11.5: Model parameters that can be varied to assess systematic uncertainties.

Parameter	**Description**	**Associated Uncertainty Study**	**Notes**
$E_m^{12C/16O}$	Shell positions for carbon or oxygen	Removal energy for carbon oxygen	Shell positions in carbon and oxygen are highly constrained by inclusive (e, e') data.
$\sigma^{12C/16O}$	Gaussian shell widths for carbon or oxygen	Width of the carbon or oxygen nuclear shells	Widths are constrained by inclusive (e, e') data and should match recent SF calculations.
$N^{12C/16O}$	Shell occupancies for carbon or oxygen	Overall shell occupancy (normalisation)	Occupancies are constrained by inclusive (e, e') data.
E_m^{40Ar}	Shell positions for argon	Removal energy for carbon	Shell positions in argon are less constrained by inclusive data and have more freedom.
σ^{40Ar}	Gaussian shell widths for argon	Width of the argon nuclear shells	Widths are less constrained by inclusive data and have more freedom.
N^{40Ar}	Shell occupancies for argon	Overall shell occupancy (normalisation)	Occupancies are less constrained by inclusive data and have more freedom.
$\text{SRC}^{p/n}$	Fraction of SRC nucleons that are the same or different to the correlated nucleon	Fraction of SRC nucleons that are the same or different to the correlated nucleon	SRC implementation is based on the SF implementation and so should be consistent with the values used for that model.

11.3 Implementation of electron scattering model into NEUT

I also implemented an electron scattering version of the same RMF-based model described in Section 10. The electron scattering model simulates the electromagnetic (EM) interaction only. This model has some key differences to the neutrino scattering model. This section describes these implementation differences.

11.3.1 Total and maximum six-fold differential cross section

The electron scattering implementation does not have a Q^2 cut like other implementations in NEUT [179]. This cut is there to avoid the divergence of the differential cross section as the scattered electron angle, θ_e tends to 0. Instead the inputs, the total cross section and maximum six-fold differential cross section are precomputed as a function of incident electron energy and θ_e and have a θ_e cut-off directly. However, electron scattering data is usually at a specific θ_e or a small angle range so this is not an issue for the user.

11.3.2 Background shell modelling

The electron scattering model has an additional background shell tensor table in order to correctly include the Coulomb contributions.

11.3.3 Reference frame rotations

Unlike the neutrino scattering model, there are only two rotations. This is because the scattering plane is forced to coincide with the xz-plane for every event. This assumes ϕ_l is 0 for all events. The two rotations are

- $\{x, y, z\}_L \rightarrow \{x, y, z\}$,
- $\{x, y, z\} \rightarrow \{1, 2, 3\}$,

and are described in Section 11.2.2

Chapter 12

Validation of model in NEUT

This chapter details the steps taken in order to validate the implemented model against the original model outside of NEUT. The approach involves plotting the normalised differential cross sections for the scattered lepton energy, E_l, square of momentum exchange, Q^2, missing energy, E_m, scattered nucleon momentum, p_N, cosine of lepton polar scattering angle, $\cos(\theta_l)$ and the missing momentum, p_m. The electron scattering model validations are then shown.

12.1 NEUT implementation validation

In order to validate whether the model was implemented correctly in NEUT, comparisons to the original model for specific monochromatic neutrino energies were made. Only the normalised single differential cross sections are compared. The normalisation of the differential cross sections enables the comparison of the shape of the distributions. To convert from events in a histogram bin to a differential cross section is a simple scaling given by

$$\left.\frac{\mathrm{d}\sigma}{\mathrm{d}X}\right|_{\text{bin } i} = \left.\frac{N}{\Delta}\right|_{\text{bin } i} \times \frac{\sigma_{\text{total}}}{N_{\text{total}}}, \tag{12.1}$$

where N is evaluated at bin i and is the number of events within that bin, Δ evaluated at bin i is the width of the bin and σ_{total} and N_{total} are the total cross section for the model and channel and the total number of events respectively.

Therefore, when comparing an equal number of events in the NEUT generation and the original model, all other values should be equivalent and so only the shape of the distribution is important, rather than the absolute scale. To only look at the shape, the differential cross section is normalised by

$$\left.\left(\frac{\mathrm{d}\sigma}{\mathrm{d}X}\right)^{\text{norm}}\right|_{\text{bin } i} = \left.\frac{\mathrm{d}\sigma}{\mathrm{d}X}\right|_{\text{bin } i} \times \frac{N_{\text{total}}}{\Delta_{\text{bin } i}}. \tag{12.2}$$

This forms a probability distribution where the integral of the distribution is unity.

The NEUT implementation has four neutrino modes and can be used when interaction with ^{12}C, ^{16}O and only two neutrino modes for ^{40}Ar. There are a total of ten channels to validate and these are shown in Table 12.1

Nucleus	Channel
^{12}C	ν_μ / $\bar{\nu}_\mu$ / ν_e / $\bar{\nu}_e$
^{16}O	ν_μ / $\bar{\nu}_\mu$ / ν_e / $\bar{\nu}_e$
^{40}Ar	ν_μ / ν_e

Table 12.1: Table showing the available neutrino channels for the model. Only the hadron tensor tables for neutrinos have been produced for Argon.

This section shows the validations for the ED-RMF final-state potential, for all neutrino flavours, helicities and available nuclei. Other final-state potential validations are shown in Appendix E. The full list of validations are shown in Table 12.2.

Nucleus	Potential	Channel	Notes
^{12}C	ED-RMF, RPWIA, EDAI, rEDAI	ν_μ, $\bar{\nu}_\mu$, ν_e, $\bar{\nu}_e$	Normalised differential cross section at $E_\nu = 250$ MeV
^{16}O	ED-RMF, RPWIA, EDAI, rEDAI	ν_μ, $\bar{\nu}_\mu$, ν_e, $\bar{\nu}_e$	Normalised differential cross section at $E_\nu = 250$ MeV
^{40}Ar	ED-RMF, RPWIA, EDAI, rEDAI	ν_μ, $\bar{\nu}_\mu$, ν_e, $\bar{\nu}_e$	Not shown in this thesis

Table 12.2: All validations performed for the neutrino model.

12.1.1 Monochromatic neutrino energies

1×10^6 events were generated at an incident neutrino energy of 250 MeV using both the NEUT implementation and the original model code.

Normalised single differential cross section on Carbon

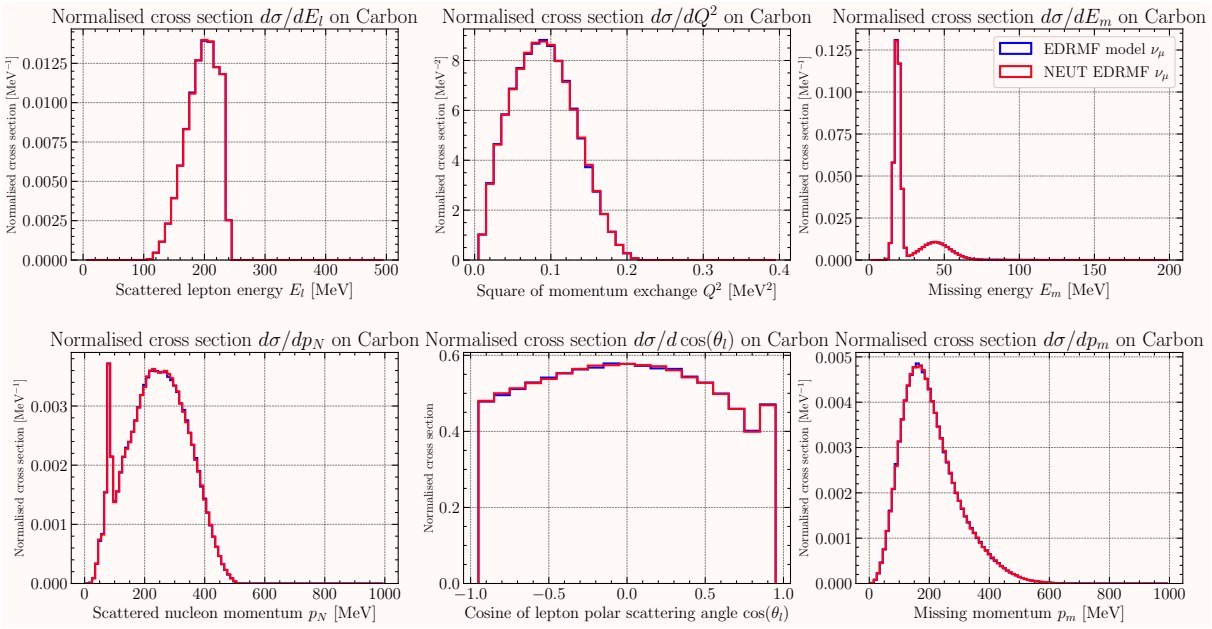

Figure 12.1: ED-RMF model with ν_μ on carbon.

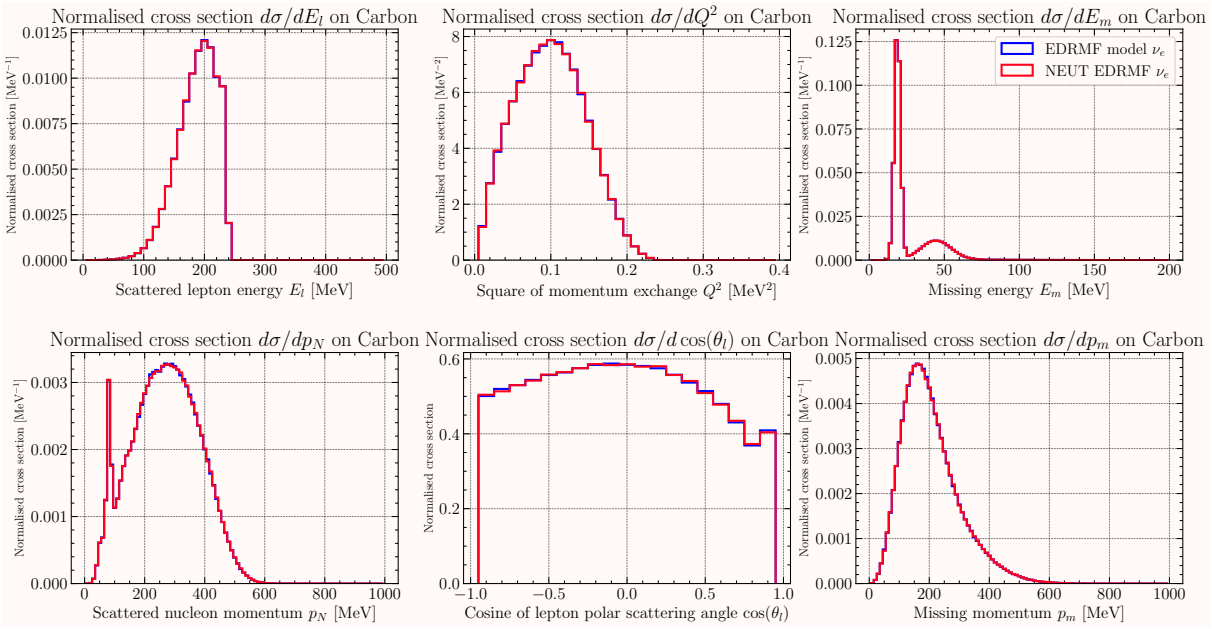

Figure 12.2: ED-RMF model with ν_e on carbon.

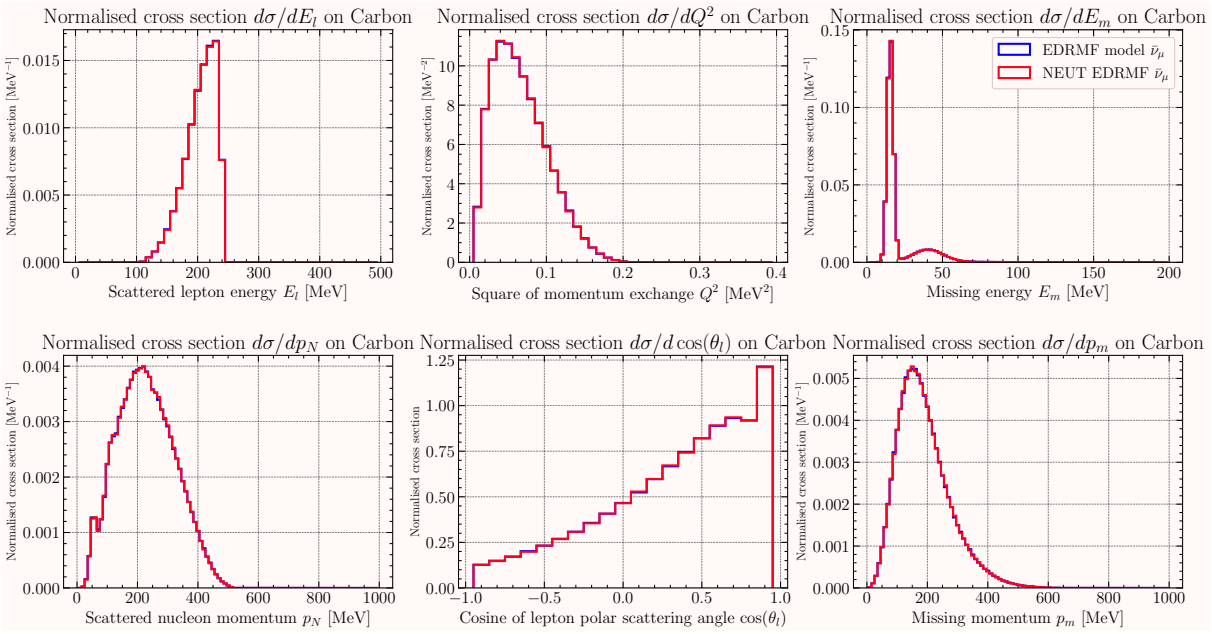

Figure 12.3: ED-RMF model with $\bar{\nu}_\mu$ on carbon.

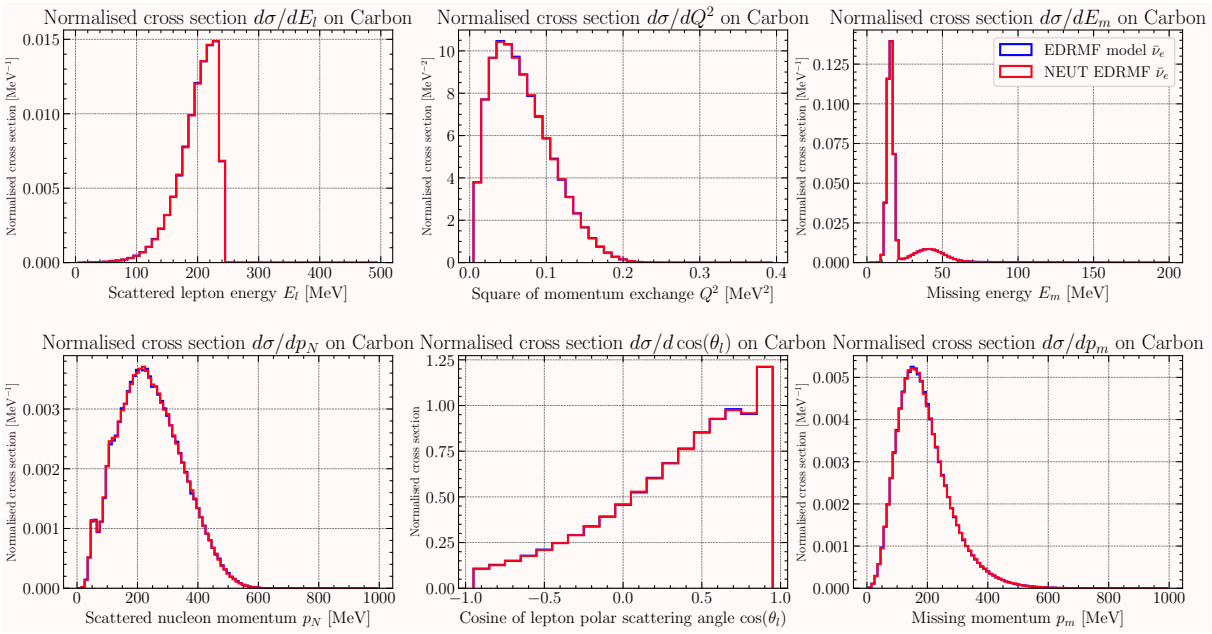

Figure 12.4: ED-RMF model with $\bar{\nu}_e$ on carbon.

Normalised single differential cross section on Oxygen

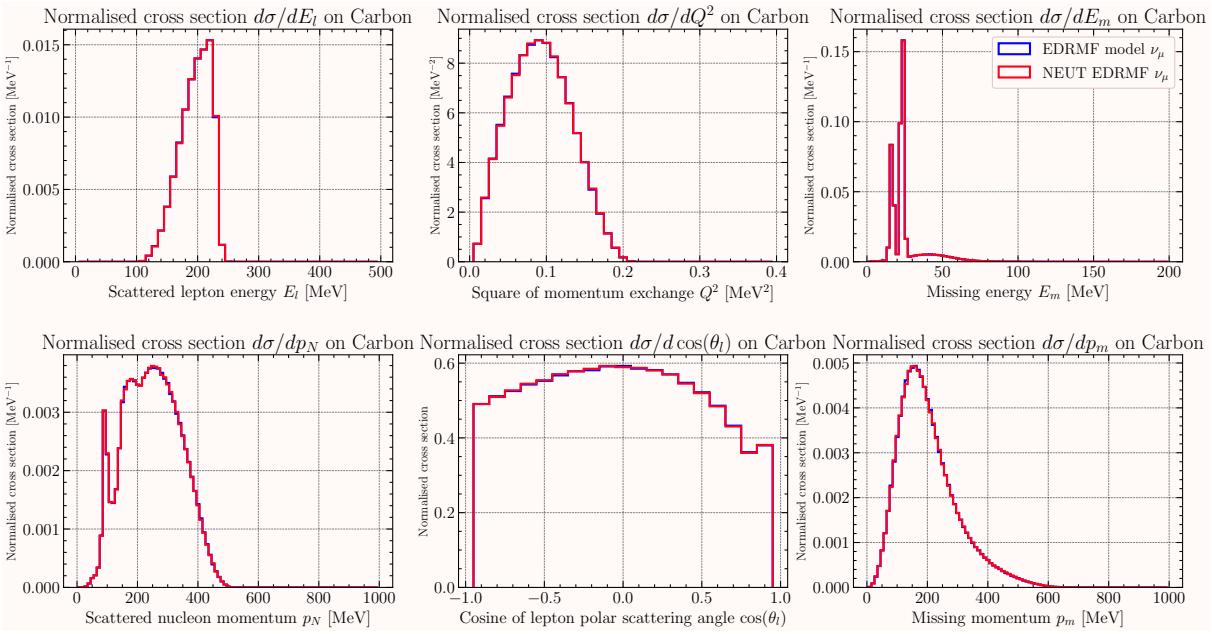

Figure 12.5: ED-RMF model with ν_μ on oxygen.

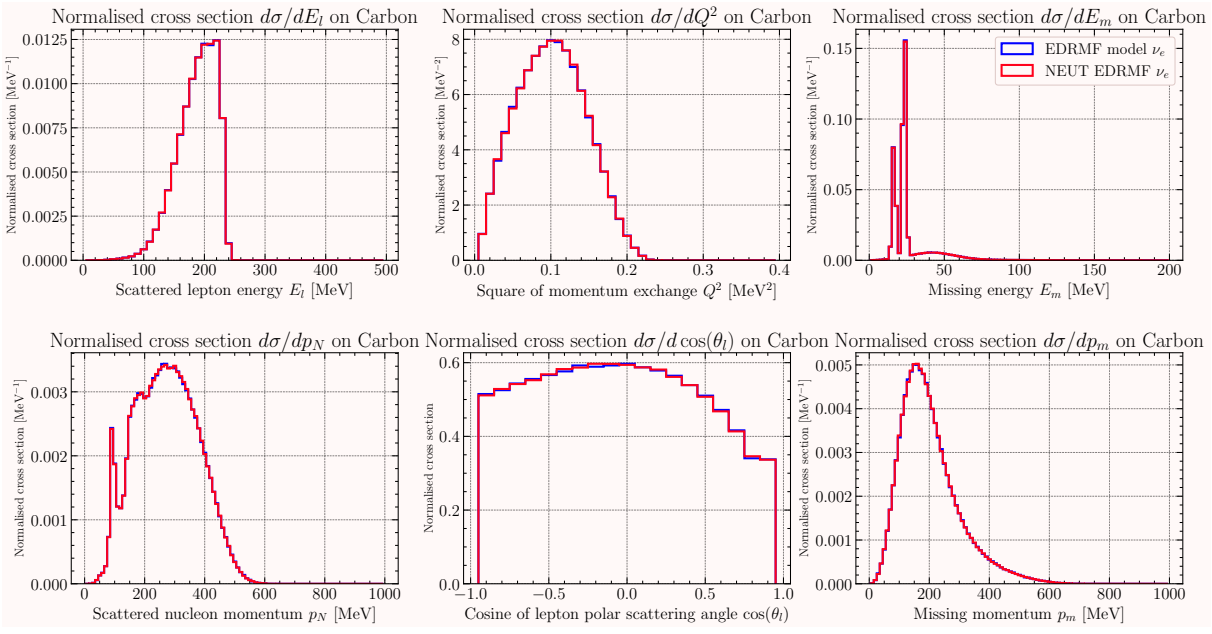

Figure 12.6: ED-RMF model with ν_e on oxygen.

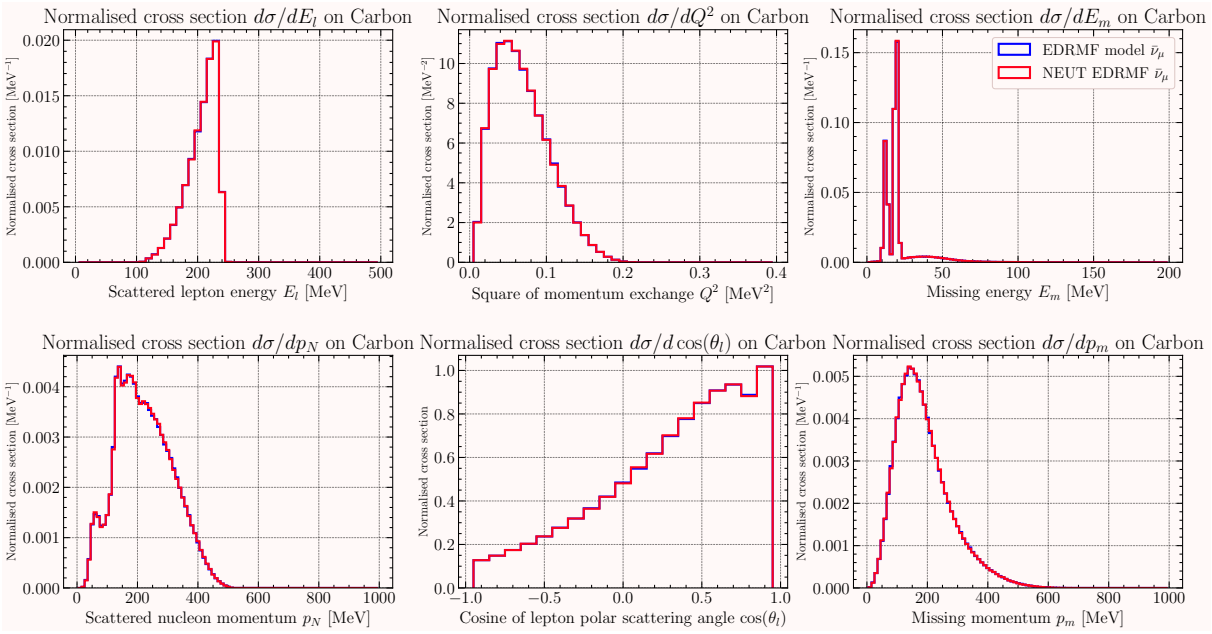

Figure 12.7: ED-RMF model with $\bar{\nu}_\mu$ on oxygen.

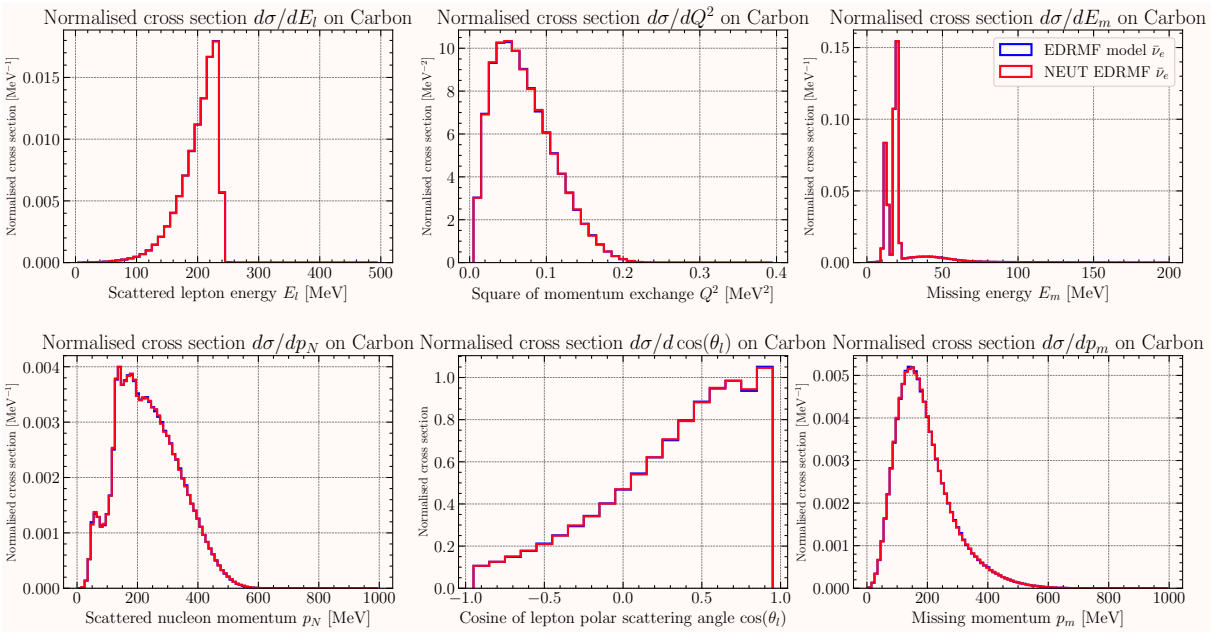

Figure 12.8: ED-RMF model with $\bar{\nu}_e$ on oxygen.

12.1.2 Electron scattering validation

For electron scattering validation, a range of incident electron energies, E_e, and scattered electron angles, θ_e, were chosen and compared with the original model code. The chosen

kinematics are given in Table 12.3. The comparison between the original model code and the NEUT implementation is shown in Figure 12.9.

E_e [MeV]	θ_e [deg]
240	36
320	36
560	36
161	60
519	60

Table 12.3: Selected kinematics for validation the ED-RMF electron scattering implementation in NEUT.

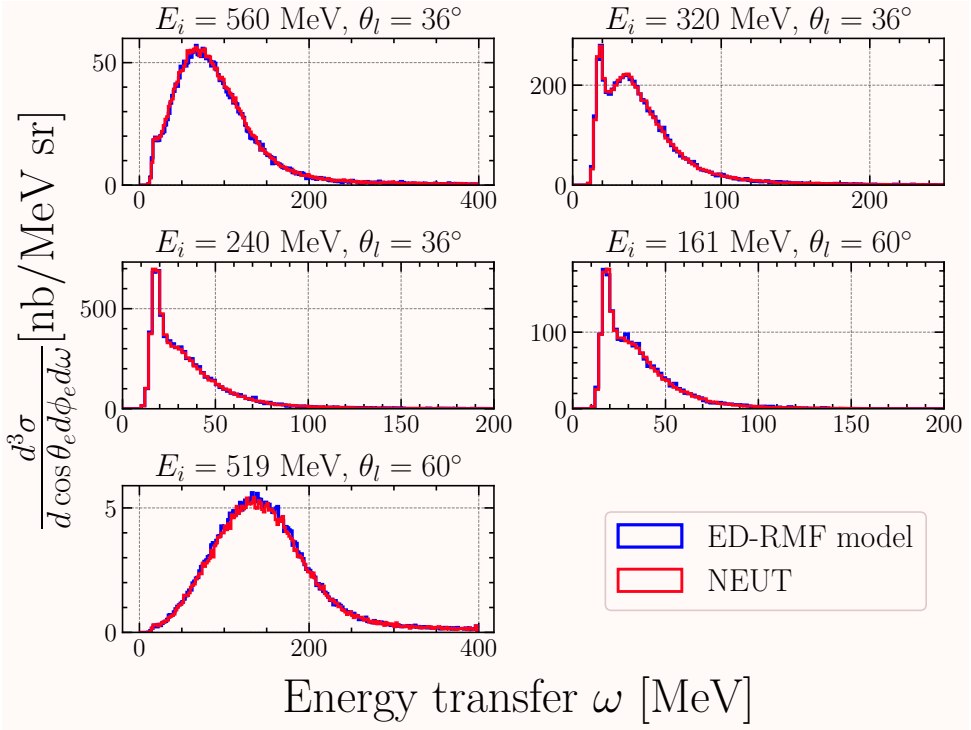

Figure 12.9: Validation of the ED-RMF electron scattering model in NEUT (red) against the original model (blue) for five different inclusive electron scattering configurations.

Chapter 13

Comparison with other NEUT CCQE models: how is it different?

This chapter details the baseline differences between the RMF-based model and other NEUT CCQE models. The differential cross section is shown for the scattered lepton energy, E_l, cosine of the lepton polar scattering angle, $\cos(\theta_l)$, missing energy, E_m, scattered nucleon momentum, p_N, and transverse kinematic imbalance (TKI) variables. The differential cross sections are also shown to highlight differences between the differential nuclear potentials for the RMF-based model. These comparisons are shown for a monocrhomatic neutrino energy and the T2K ν_μ neutrino flux.

13.1 Transverse Kinematic Imbalance (TKI) variables

With the RMF-based CCQE model implemented and validated in NEUT, it is informative to compare the predictions of the model with other CCQE models. This chapter will show the different NEUT CCQE models' differences and similarities for monochromatic neutrino energies and with a T2K flux. The other NEUT models used are the Rome spectral function (SF) implementation [51] and the Nieves *et. al.* lRFG-based model (N1p1h) presented in Ref. [180]. 1 million ν_μ CCQE events are generated on ^{12}C with all CCQE models and then the differential cross sections are compared. Of the different comparisons, transverse kinematic imbalance (TKI) variables, which are sensitive to the initial-state nuclear modelling and FSI effects [181], are also shown. The definitions of these TKI variables are given in Equation 13.1 and are shown in Figure 13.1

$$\begin{aligned}
\delta p_T &= |\mathbf{p}_T^{\,l} \; + \; \mathbf{p}_T^{\,p}|, \\
\delta\alpha_T &= \arccos\Big(\frac{-\mathbf{p_T}^{l} \; \cdot \; \delta\mathbf{p_T}}{p_T^l \delta p_T^l}\Big), \\
\delta\phi_T &= \arccos\Big(\frac{-\mathbf{p_T}^{l} \; \cdot \; \mathbf{p_T}^{p}}{p_T^l p_T^p}\Big).
\end{aligned} \tag{13.1}$$

Here, p^l and p^p represent the lepton and leading proton momentum (proton with the largest momentum), respectively, and T indicates the plane transverse to the direction of the neutrino beam. The δp_T variable is a measure of the transverse momentum balance between the scattered lepton and nucleon. In the case of a free nucleon, this value is 0; in the absence of FSI, it describes the Fermi motion of the initial nucleon. Therefore, without FSI, δp_T gives a measure of the Fermi momentum independent of neutrino energy. As a result, it is a powerful discriminator between different nuclear models [181, 182].

The $\delta\alpha_T$ variable gives a measure of the angle between the scattered nucleon momentum and momentum transfer vectors. In the case where there is no FSI, the distribution of $\delta\alpha_T$ is flat due to the isotropic nature of the Fermi momentum. However, FSI can cause an acceleration (deceleration) that pushes the distribution to 0 (180) degrees. The final variable, $\delta\phi_T$, measures the deflection between the scattered nucleon momentum and momentum transfer vectors in the transverse plane. In the absence of FSI, this variable should also be 0.

In Ref. [182], it is shown that $\delta\alpha_T$ can be split into three equal-sized regions of low, intermediate and high FSI respectively. In these regions, the shape of the δp_T distribution changes and the bulk of the interaction (CCQE in this case) can be separated from the tail. This highlights that the tail of the δp_T distribution provides an indication on the amount of FSI experienced by the scattered nucleon.

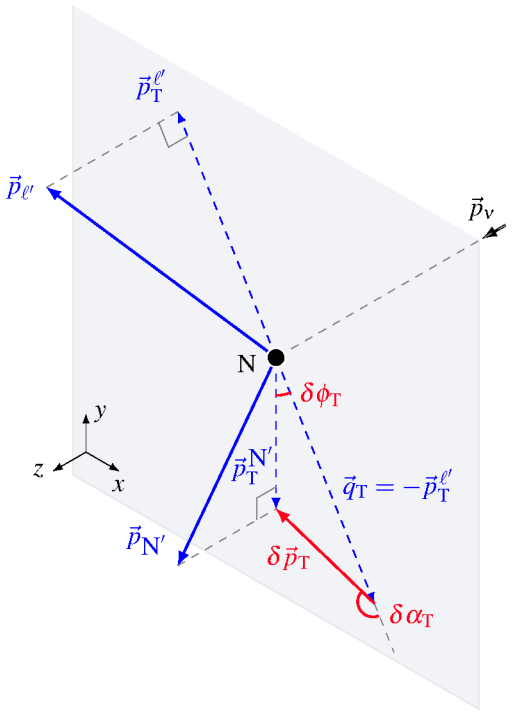

Figure 13.1: Graphical representation of the transverse kinematic imbalance (TKI) variables. Figure from Ref. [181].

13.2 Monochromatic neutrino energy 250 MeV

13.2.1 Comparison of ED-RMF to other NEUT CCQE models

In this section, the SF and N1p1h models are compared to the ED-RMF model. The SF and N1p1h NEUT samples are produced with Pauli blocking (PB). The SF and N1p1h samples are produced with $M_A^{QE} = 1.21$ GeV. For the ED-RMF samples, PB is not turned on in NEUT; this is due to the ED-RMF model having PB naturally implemented due to the orthogonality of the initial- and final-state wavefunctions at low scattered nucleon kinetic energy.

Figure 13.2 shows the differential cross sections for the scattered lepton energy E_l and angle $\cos(\theta_l)$, scattered nucleon momentum p_N, missing energy E_m and TKI variables δp_T, $\delta\alpha_T$ and $\delta\phi_T$. In turn, the E_l differential cross section shows that the peak of the distribution for the ED-RMF model is at higher energies than the SF and the N1p1h models. The overall normalisation at this neutrino energy is also varied between all three models. The N1p1h model has a more Gaussian-type shape in comparison to the SF and ED-RMF models, which are both based on a similar nuclear model.

The $\cos(\theta_l)$ differential cross section shows a stark difference in scattered lepton angle between the SF and the other models, with the SF model having more scattered leptons at forward angles. Despite the overall normalisation being different due to the differing total cross sections, the N1p1h and ED-RMF distribution shape is not that different between $-1 < \cos(\theta_l) < 0$. The TKI variable δp_T shows the SF and ED-RMF models having similar peak positions. However, the ED-RMF model has a longer tail indicating the elastic FSI is having the expected effect on the final-state kinematics. The $\delta\alpha_T$ distributions show varied behaviour from all models. The SF and ED-RMF models both increase with the ED-RMF model having the largest difference overall, again highlighting the effects of the elastic FSI. $\delta\phi_T$ shows a similar shape between the SF and N1p1h models, which is different to the ED-RMF model that shows a shallower drop.

The E_m distribution shows clearly the initial-state nuclear modelling. The SF and ED-RMF models have a similar shape showing the large $1p_{1/2}$ nuclear shell followed by a broader $1s_{1/2}$ shell and an SRC tail. Despite the ED-RMF model following the description in Ref [167], the positions and width of these shell have slight differences. Finally, the p_N shows the ED-RMF model having a shifted peak in comparison to the SF and N1p1h models.

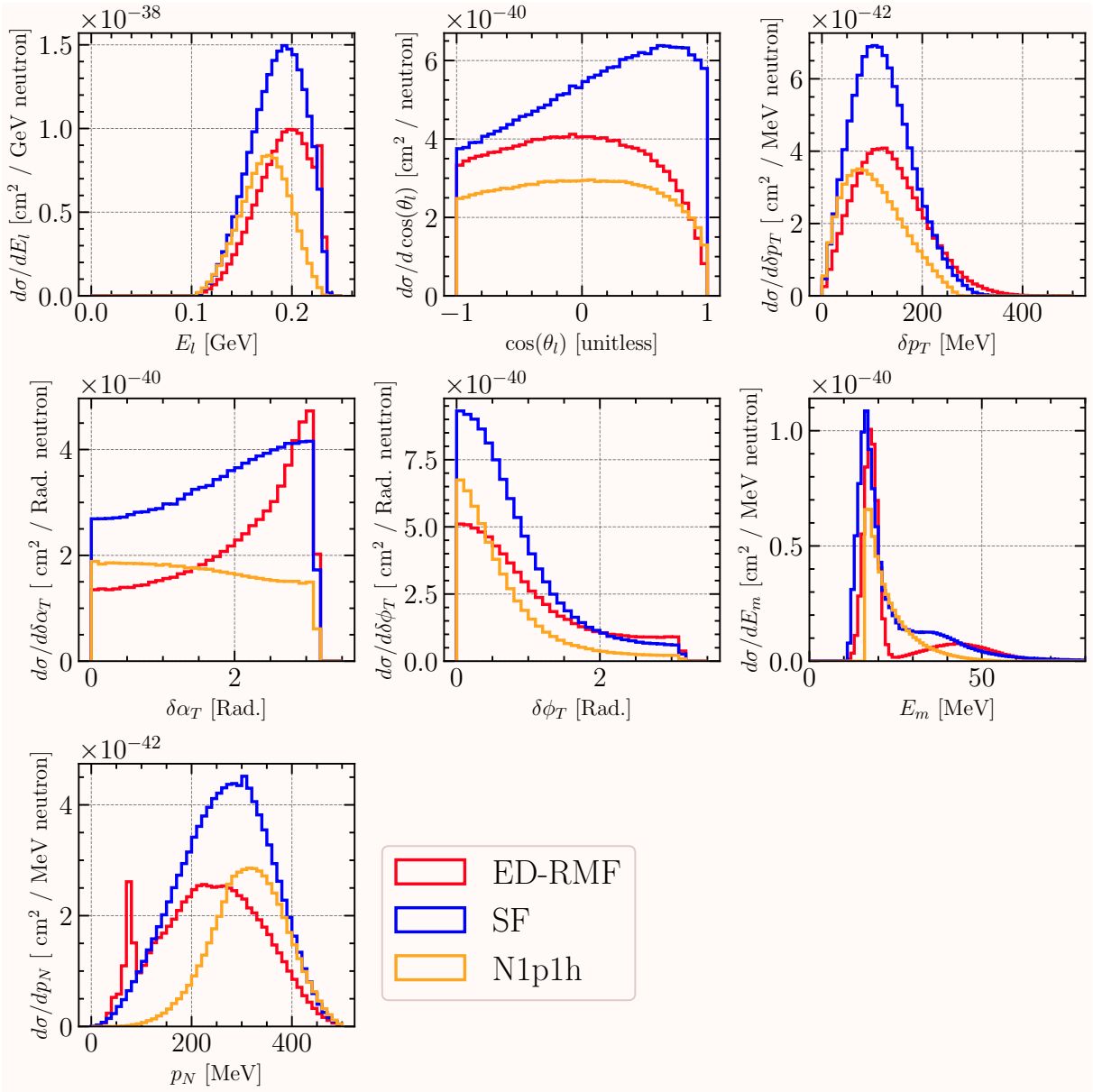

Figure 13.2: NEUT samples for the ED-RMF (red), SF (blue) and N1p1h (orange) CCQE models produced using a monochromatic neutrino energy of 250 MeV. The scattered lepton energy E_l and angle $\cos(\theta_l)$, scattered nucleon momentum p_N, missing energy E_m and TKI variables δp_T, $\delta\alpha_T$ and $\delta\phi_T$ are shown.

13.2.2 Comparison of RDWIA models

Figure 13.3 shows the differential cross sections for the same variables for the ED-RMF, RPWIA, EDAIC and rEDAIC models. The E_l distribution shows that the ED-RMF and rEDAIC models are similar in normalisation and shape. The EDAIC model shows a similar shape to RPWIA but with a drastically reduced total cross section due to the

imaginary component in the potential. The RPWIA model has the largest normalisation due to the plane wave nature of the model. The $\cos(\theta_l)$ distribution shows a slightly differing shape between the ED-RMF and rEDAIC models. The RPWIA model shows more scattered leptons at forward angles, similar to that of the SF model. The δp_T distributions show very similar shapes. Figure 13.4 shows the same differential cross section but normalised to unit area for all models. It is clear that the ED-RMF and rEDAIC models are identical in shape, and the RPWIA and EDAIC models also have identical shape. This is not surprising since the initial-state modelling is identical and the ED-RMF and rEDAIC models both have elastic FSI only. $\delta\alpha_T$ shows a larger increase for the ED-RMF and rEDAIC models with the ED-RMF model having a larger strength at high values of $\delta\alpha_T$. E_m shows the expected identical shapes of the E_m profile. This is because the model draws from a pre-defined E_m profile that is identical for all nuclear potentials. The difference is due purely to the different total cross section. p_N shows the RPWIA model having a peak that is shifted to higher values of p_N. The elastic FSI present in the ED-RMF and rEDAIC models reduce the total cross section and shift the peak back to lower values of p_N. Interestingly, the rEDAIC model shows a broader distribution than the ED-RMF model.

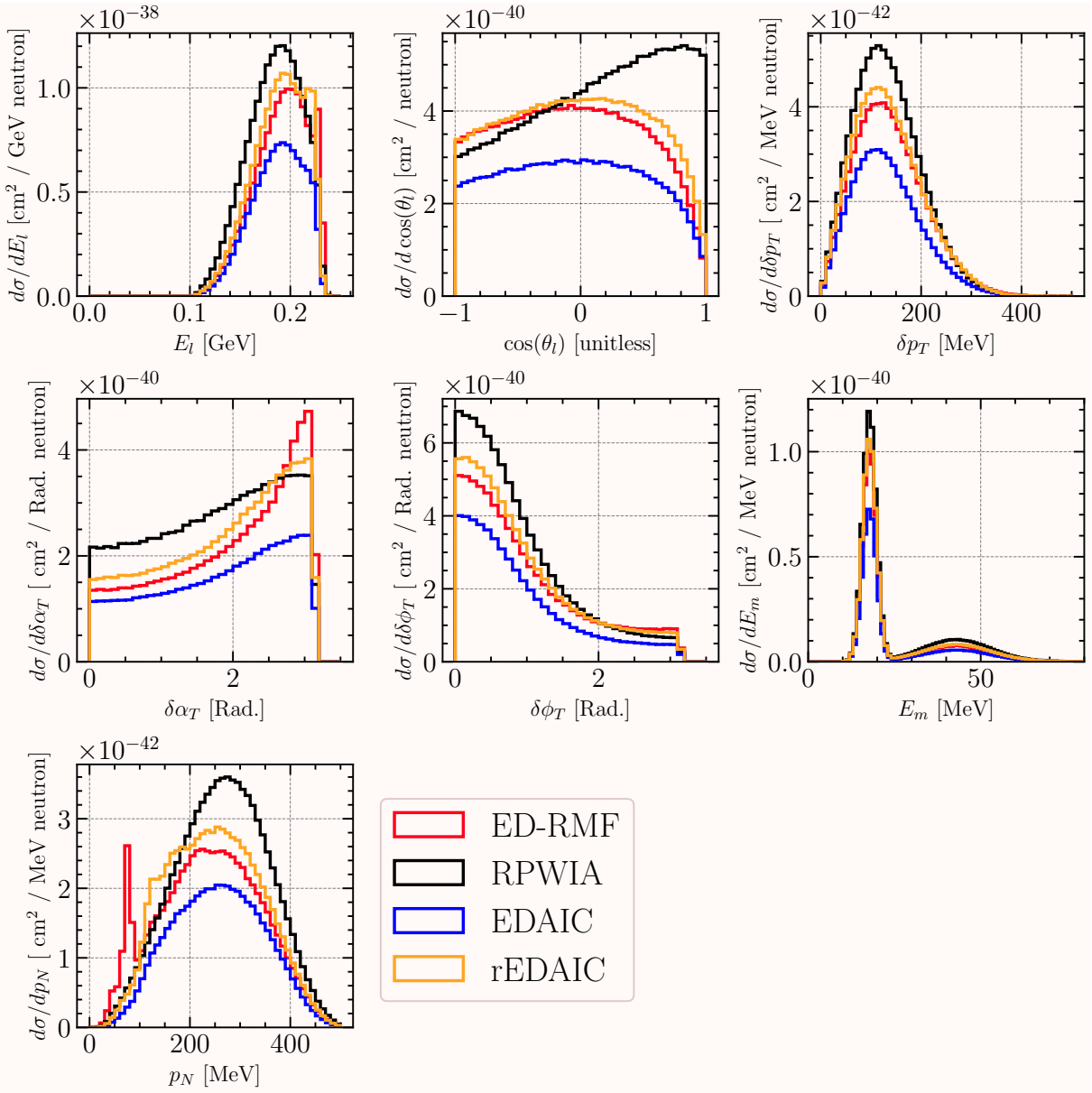

Figure 13.3: NEUT samples for the ED-RMF (red), RPWIA (black), EDAIC (blue) and rEDAIC (orange) models produced using a monochromatic neutrino energy of 250 MeV. The scattered lepton energy E_l and angle $\cos(\theta_l)$, scattered nucleon momentum p_N, missing energy E_m and TKI variables δp_T, $\delta\alpha_T$ and $\delta\phi_T$ are shown.

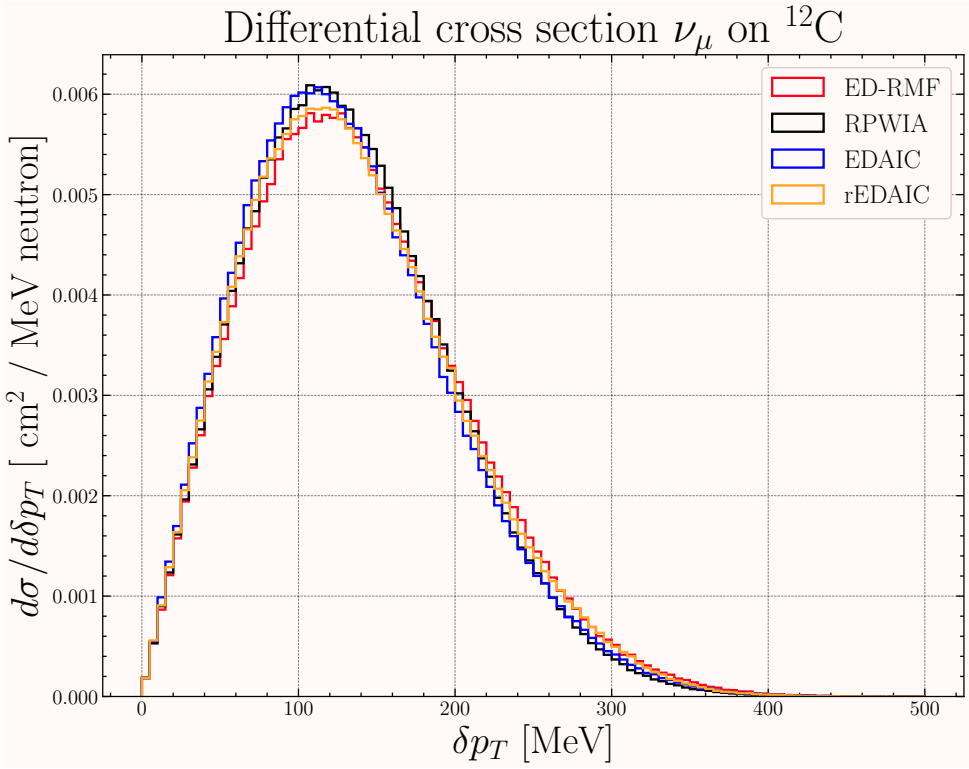

Figure 13.4: Differential cross section for the TKI variable δp_T. The differential cross section is normalised to unit area to show purely shape differences. The ED-RMF (red), RPWIA (black), EDAIC (blue) and rEDAIC (orange) models produced using a monochromatic neutrino energy of 250 MeV.

13.3 T2K flux

The ν_μ flux for T2K at ND280 is used to show the direct changes to the CCQE modelling in T2K. The T2K flux is shown alongside other experiment fluxes in Figure 1.6.

13.3.1 Comparison of ED-RMF to other NEUT CCQE models

Figure 13.5 shows the differential cross sections for the same variables for the ED-RMF, SF and N1p1h CCQE models. The E_l distribution shows a similar overall shape between the models. The $\cos(\theta_l)$ distribution shows that the SF model produces more events in the forward angle region. The ED-RMF and N1p1h models are more similar in angular distributions. The δp_T distribution shows clearly the difference in shapes between the models. The ED-RMF model, as previously seen, as a longer tail due to the elastic FSI present. The SF model has more of a tail than the N1p1h model due to the presence of SRC in the SF model. $\delta\alpha_T$ shows a relatively flat distribution for the N1p1h and SF models in comparison to the ED-RMF model which rises a lot towards higher angles due to elastic FSI. $\delta\phi_T$ shows the ED-RMF and SF models matching in the tail of the

distribution. The E_m distributions for all models are very different with the N1p1h model not showing any shell structure at all. The shapes of the ED-RMF and SF models show this structure but, as previously seen, differ in the positions and widths of the shells. p_N show the ED-RMF and SF models matching in the low and high p_N region. At high p_N, the distorted wave models tend to a plane wave model and therefore this is expected. The N1p1h model has a shifted peak in comparison to the SF and ED-RMF models.

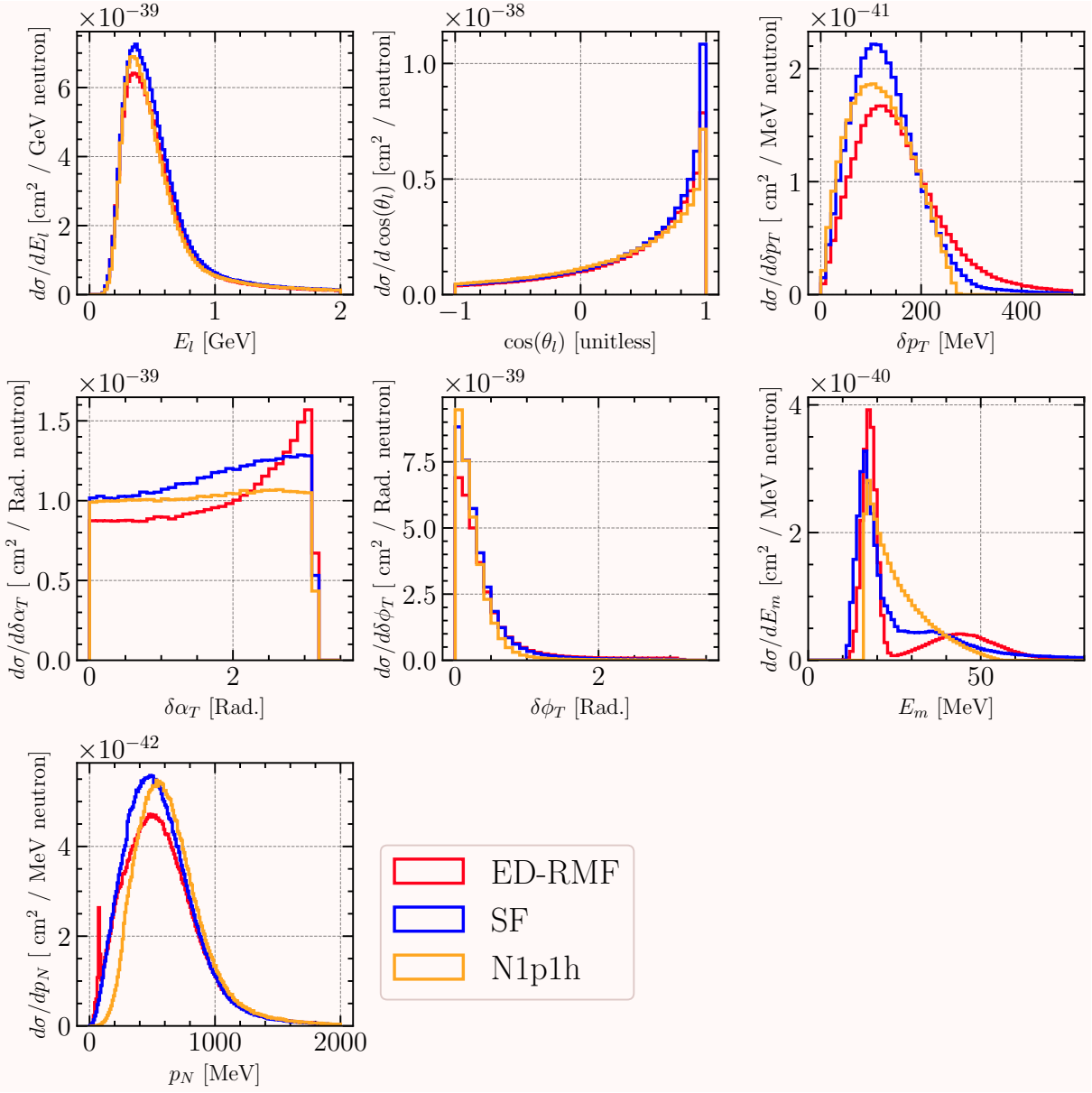

Figure 13.5: NEUT samples for the ED-RMF (red), SF (blue) and N1p1h (orange) models produced using the ν_μ forward horn current flux at ND280 in T2K. The scattered lepton energy E_l and angle $\cos(\theta_l)$, scattered nucleon momentum p_N, missing energy E_m and TKI variables δp_T, $\delta\alpha_T$ and $\delta\phi_T$ are shown.

13.3.2 Comparison of RDWIA models

Figure 13.6 shows the differential cross sections for the same variables for the different nuclear models. E_l shows a similar shape but differing normalisation for all models. $\cos(\theta_l)$ shows much higher strength in the forward scattering angles for the RPWIA model. δp_T again shows similar shapes that differ solely due to the total cross section and presence of elastic FSI. For all variables this theme is continued, however, p_N shows the peak of the distribution shifted to lower p_N values for the RPWIA and EDAIC models.

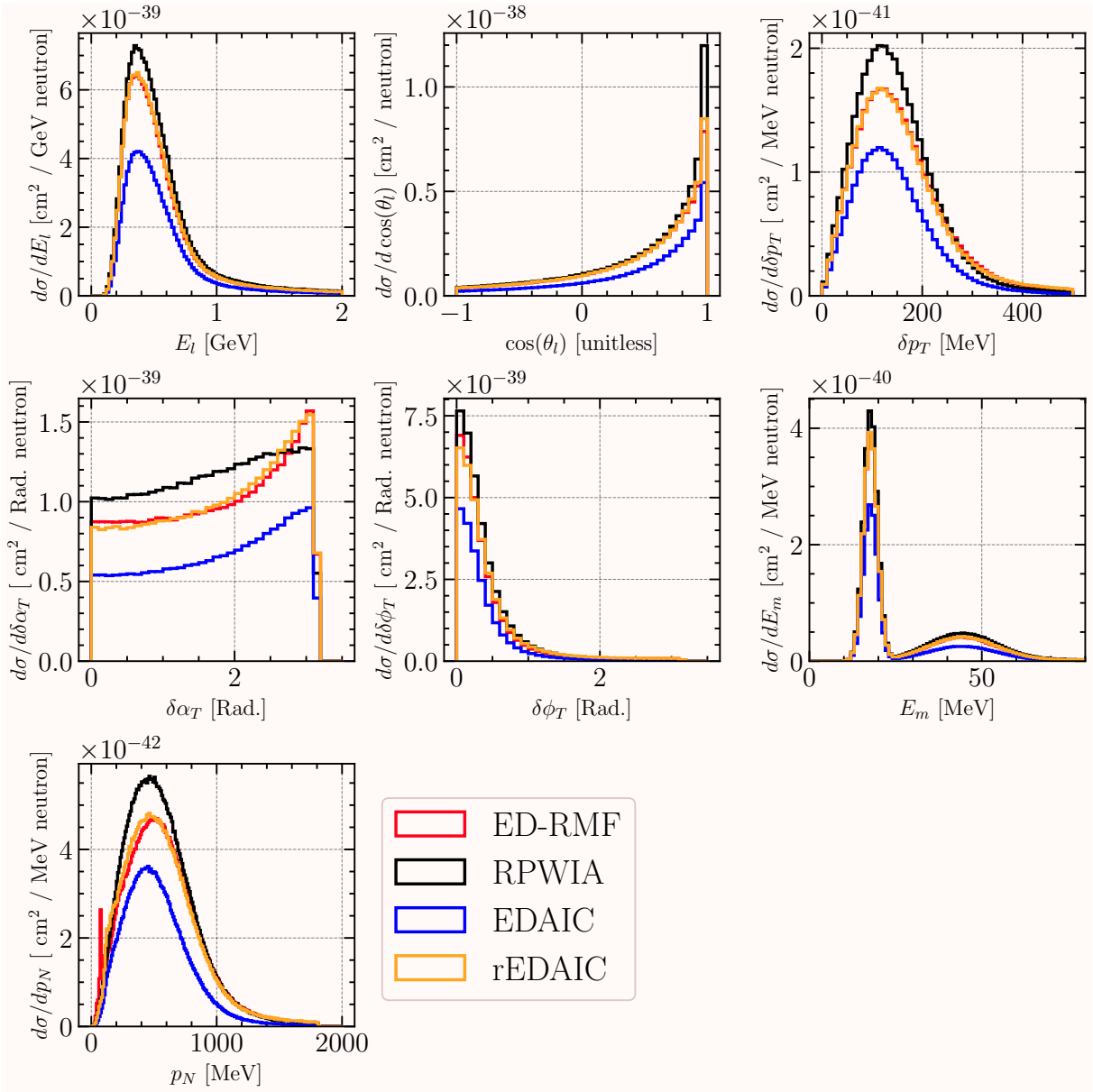

Figure 13.6: NEUT samples for the ED-RMF (red), RPWIA (black), EDAIC (blue) and rEDAIC (orange) models produced using the ν_μ forward horn current flux at ND280 in T2K. The scattered lepton energy E_l and angle $\cos(\theta_l)$, scattered nucleon momentum p_N, missing energy E_m and TKI variables δp_T, $\delta\alpha_T$ and $\delta\phi_T$ are shown.

Chapter 14

Comparison with neutrino and inclusive electron cross-section data

This chapter shows the benchmarking of the RMF-based CCQE model against neutrino cross-section data from the T2K, MINERvA and MicroBooNE experiments. The electron scattering RMF-based model is then benchmarked against inclusive electron scattering data and other NEUT electron scattering models. Finally, the neutrino model is compared to a Kaon decay-at-rest dataset that provides a differential cross section in terms of the missing energy.

14.1 Comparison with neutrino cross-section data

To benchmark the model implemented in this work, neutrino cross section data from the T2K [183], MINERvA [184, 185], and MicroBooNE experiments [186, 187, 188] were used. The data comparisons and results are written in my paper [140]. Data comparisons were performed using the NUISANCE framework [189]. The neutrino beams used by these experiments all primarily consist of ν_μ. As shown in Figure 1.6, the respective experiment fluxes are different; the T2K and MicroBooNE fluxes have a similar peak energy at around 0.5-0.6 GeV while the MINERvA flux has a higher peak energy at around 3 GeV. Because the T2K and MicroBooNE flux peak energies are similar, the primary interaction channel for both would be CCQE: ideal for benchmarking the RMF-based CCQE model. MINERvA however, will have more contributions from the pion-production channels since more energy is available in the interaction. The T2K and MINERvA experiments use hydrocarbon targets while MicroBooNE uses argon. Despite a hydrocarbon target having additional protons when compared to ^{12}C, NEUT simply combines a ^{12}C nucleus with free protons to construct the composite hydrocarbon nucleus. A ν_μ will not interact with a proton so the model in this work can still be applied.

14.1.1 NEUT samples

The RMF-based model is benchmarked against other NEUT CCQE models. The ED-RMF nuclear potential, with and without the cascade, and the full optical potential EDAI without the cascade are benchmarked. The EDAI model with carbon is denoted as EDAIC. The EDAI model represents the case where the struck nucleon experiences only elastic FSI and is expected to provide a lower bound for the CCQE channel. There is no existing optical potential for argon and so that of isobaric calcium is used. The coulomb contribution differences between $Z = 18$ and $Z = 20$ are added by hand when precomputing the hadron tensor tables. The other NEUT models used are the Rome spectral function (SF) implementation [51] and the Nieves *et. al.* model (N1p1h) presented in Ref. [180]. The SF model was generated with an axial mass of $M_A^{QE} = 1.03$ GeV while the N1p1h model was generated with $M_A^{QE} = 1.05$ GeV. NEUT 6.0.0 was used for the SF and RMF-based samples while NEUT 5.8.0 was used for the N1p1h samples. There is no SF available for argon in NEUT and so for the MicroBooNE results, only the N1p1h model is used. The NEUT cascade was applied to all samples apart from samples labelled "no cas". This was to directly study the effect of the NEUT cascade. NEUT was used with its default run mode, meaning that 2p2h, pion production and deep inelastic scattering channels are also produced. In NEUT, the 2p2h channel is based on Refs. [190, 180] and the pion production model is the Rein-Seghal model with added lepton mass corrections [191, 192, 193]. Contributions from 2p2h channels are shown with and without the π-absorption channels which are simulated in the NEUT cascade.

A χ^2 analysis is performed to quantify the level of agreement between the NEUT samples and the data. The χ^2 definition used in this work is given by

$$\chi^2 = \sum_{i,\ j} \big(D - M\big)_i \big(\mathrm{Cov}^{-1}\big)_{ij} \big(D - M\big)_j. \tag{14.1}$$

Here, i and j are matrix indices that indicate a value in a particular bin of a measurement. D and M represent the data and MC value in a given bin respectively. The inverse covariance matrix is given by Cov^{-1} and has dimensions $i_{\max} \times j_{\max}$. Using this definition, a low value of χ^2/N_{dof}, with N_{dof} being the number of degrees of freedom (histogram bins), indicates a good agreement with the data.

14.1.2 T2K results

The T2K data used are CC0πNp ("semi-inclusive") datasets [183]. The T2K measurement is presented in the unfolded truth space, the space that corresponds to the true particle kinematics after the detector resolution effects are included. It uses a standard regularisation procedure. The covariance matrix required for Equation 14.1 is part of the data release.

The kinematic selections applied in this dataset are in given in Table 14.1. The dataset is a triple-differential cross section from which double-differential and single-differential results are extracted. A χ^2 value is available only for the full triple-differential cross section and the TKI results, not the single- and double-differential measurements. The covariance matrix could be collapsed to produce this, but this is not part of the NUISANCE framework and, after discussions within T2K working groups, it was not performed in order to avoid "p-hacking". This is where the covariance matrix used in Equation 14.1 is not the same one used in the measurement and can bias the χ^2 value or p-value.

Kinematic Variable	CC0πNp	TKI
p_p	> 500 MeV	0.45 – 1 GeV
$\cos\theta_p$	...	> 0.4
p_μ	...	> 250 MeV
$\cos\theta_\mu$	...	> -0.6

Table 14.1: Kinematic selections applied in the T2K dataset. Here "..." indicate that there is no selection applied. In the T2K analysis, any number of protons are selected within the kinematic selections but only the highest momentum proton is used in the TKI and proton cross sections.

Single-differential sample

The single-differential cross section data comparison is given in Figure 14.1. The single-differential cross section is given against the cosine of the scattered muon angle, $\cos(\theta_\mu)$. In the low $\cos(\theta_\mu)$ region, the contribution from 2p2h and π-absorption contributions are low and CCQE dominates. These regions are important for quantifying differences between different CCQE models. The ED-RMF model with the NEUT cascade predicts below the data but is still consistent within experimental error. As $\cos(\theta_\mu)$ increases, the contributions from 2p2h and π-absorption increase, pushing MC predictions. As a result, ED-RMF with the cascade is then above data but within experimental data error. Due to the increase in 2p2h and π-absorption contributions, it is hard to discern whether this is due to the CCQE model or non-CCQE contributions. In contrast, the EDAIC model is consistently below the data. The SF is very similar to the ED-RMF model in the CCQE-dominated region. This makes sense since the initial-state nuclear model used is modelled to replicate the Rome SF.

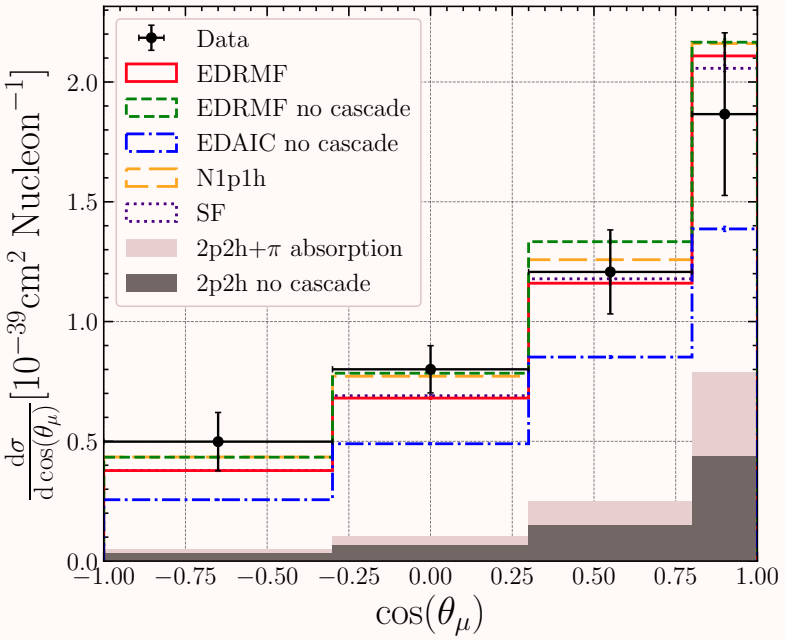

Figure 14.1: T2K ν_μ CC0πNp dataset on hydrocarbon. The single-differential cross section is given as a function of scattered lepton angle. The ED-RMF model with the cascade applied is represented by the solid red line, while the version without the cascade is shown as the dashed green line. The EDAIC model without the cascade is depicted by the blue dash-dotted line. The N1p1h model is indicated by the long dashed yellow line, and the SF model is shown as the purple dotted line. The 2p2h and π-absorption contributions are represented by the light gray filled bar, whereas the 2p2h-only contribution without the cascade is depicted by the dark gray filled bar.

Double- and triple-differential samples

The double-differential cross section as a function of the leading proton scattering angle in slices of the lepton scattering angle is shown in Figure 14.2. In the low $\cos(\theta_\mu)$, CCQE-dominated region, the ED-RMF model with the cascade agrees with data in the low $\cos(\theta_p)$ region but underestimates the data in the high $\cos(\theta_p)$ region. In the $-0.3 < \cos(\theta_\mu) < 0.3$ region, all models except the EDAIC model overestimates the data. Given the height of the data point in this final bin, it is not CCQE-dominated and could be because of 2p2h and π-absorption contributions. In the $0.8 < \cos(\theta_\mu) < 1.0$ region, at high $\cos(\theta_p)$, all models except the EDAIC model overestimate data, with the 2p2h and π-absorption contributions covering most of the data point and uncertainty. This suggests that the NEUT 2p2h or π-absorption is too strong in this region of phase space.

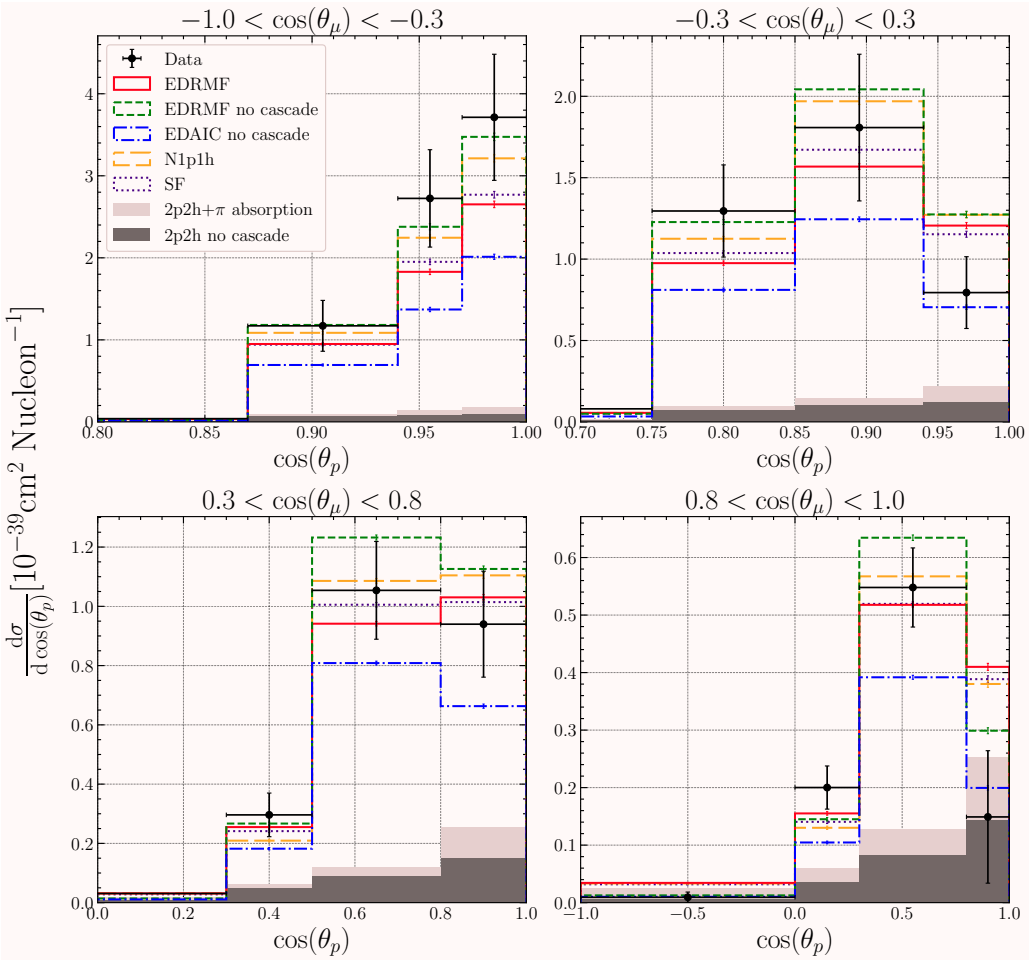

Figure 14.2: T2K ν_μ CC0πNp dataset on hydrocarbon. The differential cross section is given as a function of the scattered proton angle in slices of the scattered lepton angle starting from the top left. The histograms follow the same definition as Figure 14.1.

The triple-differential cross section as a function of the leading proton momentum, p_p, divided into slices based on the scattering angles of the leading proton and lepton is shown in Figure 14.3. At values of $p_p > 1.0$ GeV, all models overestimate the data despite negligible contributions from 2p2h and π-absorption processes. In this region, the ddataset contains few events and so it is statistically limited, perhaps contributing to this overestimation shown by all models. In the region $-0.3 < \cos(\theta_\mu) < 0.3$, $0.85 < \cos(\theta_p) < 0.94$ slice, for $p_p < 1.0$ GeV, no model replicates the shape seen in data.

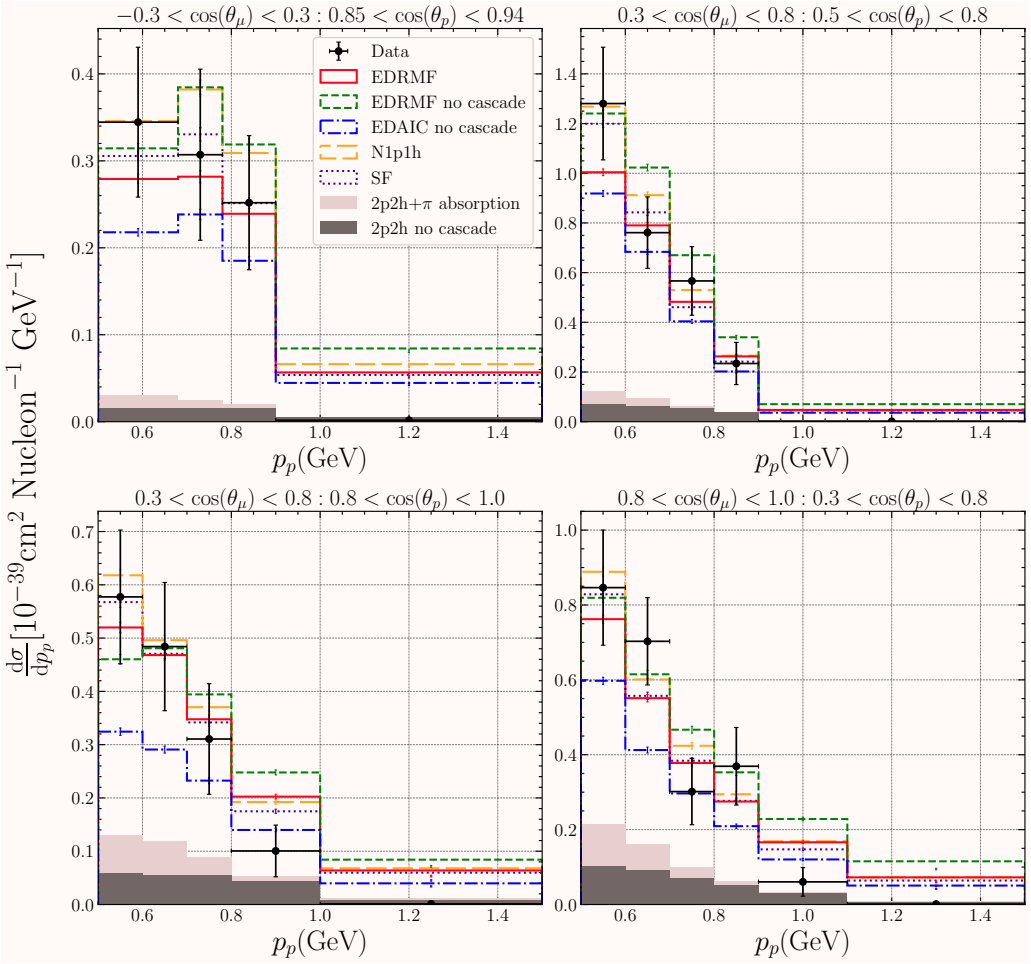

Figure 14.3: T2K ν_μ CC0πNp dataset on hydrocarbon. The differential cross section is given as a function of the scattered proton momentum in slices of the scattered lepton and nucleon angle starting from the top left. The histograms follow the same definition as Figure 14.1.

TKI samples

The differential cross section for the TKI variables are shown in Figure 14.4. The χ^2 values for the NEUT samples are given in Table 14.2. For the δp_T variable, the ED-RMF model with the cascade has the largest χ^2 value, this is likely due to the underprediction in the first bin at low δp_T. This is a CCQE-dominated region indicating that the ED-RMF model itself is underpredicting the data. It is interesting to see that the EDAIC model is the same as the ED-RMF model in this bin. The ED-RMF model without the cascade overestimates the data in the peak but then begins to underestimate the data in the high δp_T tail. This trend is also seen in the $\delta\phi_T$ variable. Here the ED-RMF model with the cascade also has the largest χ^2. For the $\delta\alpha_T$ variable, the χ^2 value for the ED-RMF model with the cascade shows an improved agreement with data in comparison to the other two

TKI variables and is similar to that of the SF and N1p1h models. The ED-RMF and EDAIC model without the cascade is flat across $\delta\alpha_T$ as expected. No models reproduces the oscillatory structure seen in the data between 1 and 2 radians.

Model	δp_T	$\delta\phi_T$	$\delta\alpha_T$
EDRMF cas	42.1/8	27.1/8	17.6/8
EDRMF no cas	60.4/8	51.2/8	27.5/8
N1p1h cas	5.62/8	12.6/8	31.3/8
SF cas	11.3/8	8.49/8	19.4/8
EDAIC no cas	24.6/8	19.3/8	18.8/8

Table 14.2: χ^2/N_{dof} values for each TKI variable for T2K. "cas" and "no cas" indicate where the cascade has and has not been applied respectively.

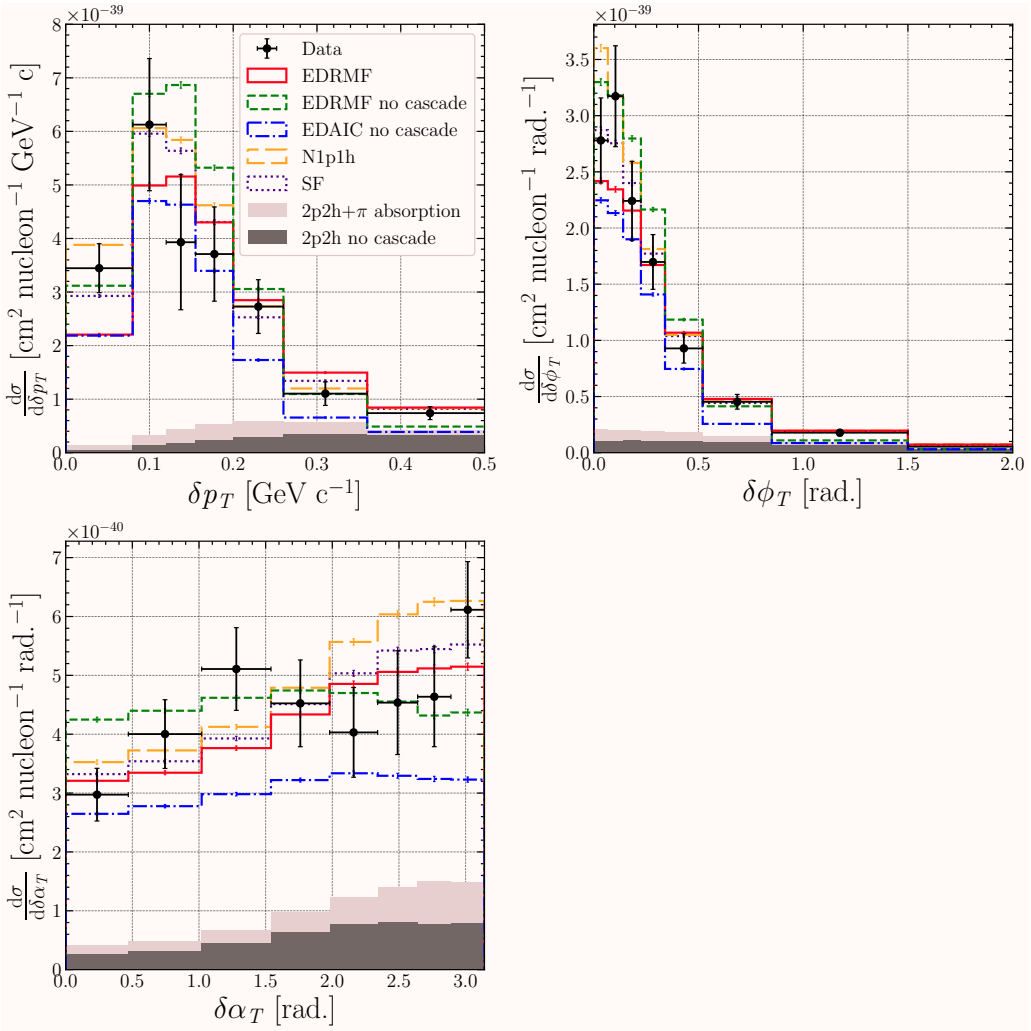

Figure 14.4: T2K ν_μ CC0πNp dataset on hydrocarbon. The TKI variables are defined in Equation 13.1. The histograms follow the same definition as Figure 14.1.

T2K TKI shape-only comparison

Shape-only comparisons are produced by NUISANCE [189]. Scale factors required to scale the overall normalisation of the MC are calculated by taking the ratio of the total cross section of the data distribution with that of the MC distribution. A scale factor close to 1.0 with a good shape agreement by eye indicates a good agreement with the data. A good shape with a scale factor that is not 1.0 indicates good agreement in shape but a difference in overall normalisation.

The TKI shape-only comparison is shown in Figure 14.5 with the scale factors given in Table14.3. For $\delta\phi_T$, all models show agreement from approximately 0.4 rad. For $\delta\alpha_T$, models with the cascade display a similar shape; likewise for models without the cascade. The ED-RMF model without the cascade and the EDAIC model have similar shapes for

all three TKI variables.

Model	δp_T	$\delta\phi_T$	$\delta\alpha_T$
EDRMF cas	1.00	1.02	1.05
EDRMF no cas	0.92	0.94	0.97
N1p1h cas	0.88	0.89	0.92
SF cas	0.95	0.97	1.00
EDAIC no cas	1.37	1.39	1.44

Table 14.3: Scale factors required to scale the MC to data for each TKI variable for T2K. "cas" and "no cas" indicate where the cascade has and has not been applied respectively.

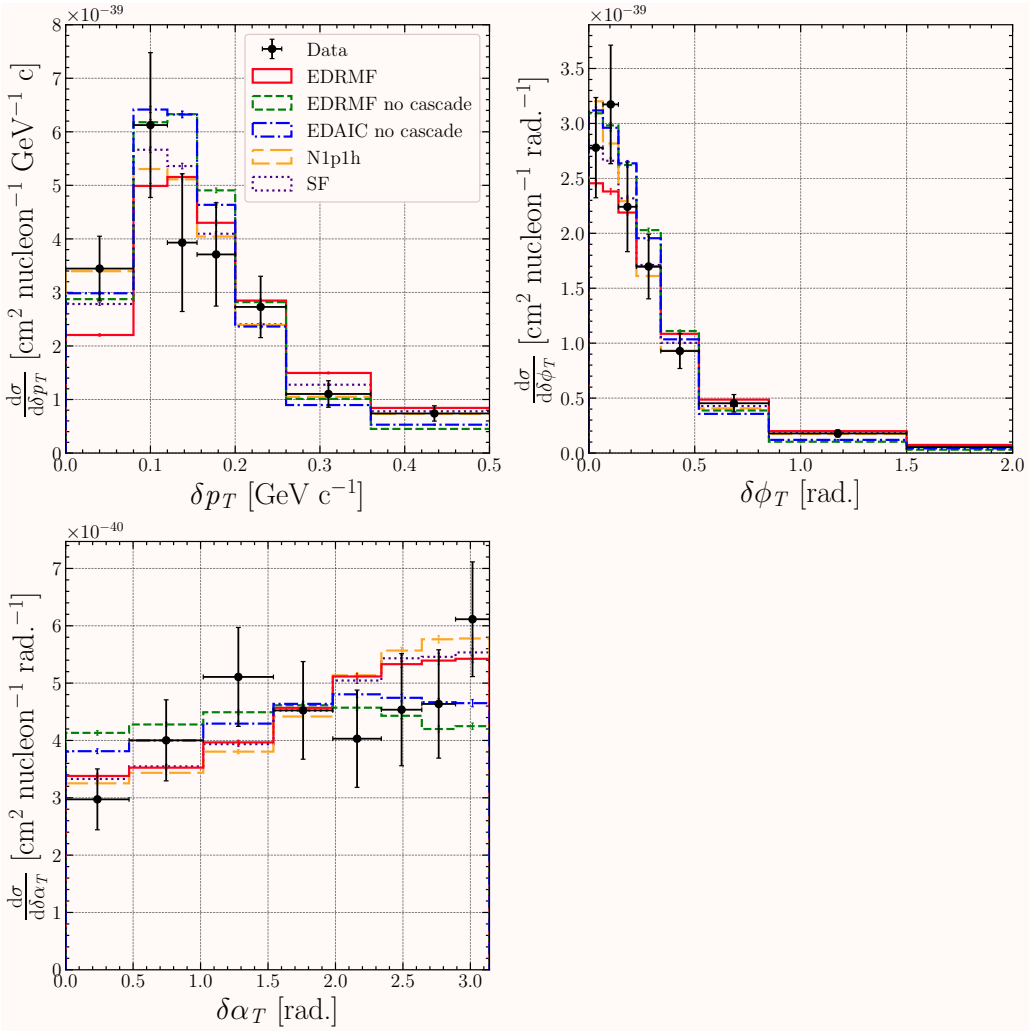

Figure 14.5: Shape-only differential cross sections for TKI variables defined in Equation 13.1 for T2K. The NEUT models are normalised to the measurement. The histograms follow the same definition as Figure 14.1.

14.1.3 MINERvA results

The MINERvA measurement is a CC0πNp dataset from Ref. [184] with a correction applied in Ref. [185]. Initially, the dataset within NUISANCE did not have this correction applied so I added this to NUISANCE. The dataset, like T2K, is presented in the unfolded truth space using the D'Agostini unfolding technique [185, 194]. Full covariance matrices are released alongside the dataset. The applied kinematic selections are given in Table 14.4.

Kinematic Variable	CC0πNp
p_p	0.45 – 1.2 GeV
$\cos\theta_p$	> 0.3420
p_μ	1.5 – 10 GeV
$\cos\theta_\mu$	> 0.9396

Table 14.4: Kinematic selections applied in the MINERvA dataset. In the MINERvA analysis, any number of protons are selected within the kinematic selections, but only the highest momentum proton is used in the TKI and proton cross sections. A higher momentum proton may fall outside of the kinematic selections, however.

Kinematic samples

The differential cross section for the scattered muon momentum, p_μ, leading scattered proton momentum, p_p, reconstructed initial neutron momentum, p_n, and leading proton scattering angle, θ_p are shown in Figure 14.6. The χ^2 values are given in Table 14.5. For the p_p, the ED-RMF model with the cascade shows the best agreement with the data, as indicated by the χ^2 value. This is not seen in the p_μ distribution, where surprisingly the EDAIC model has the best χ^2 value. For p_p, the ED-RMF model with the cascade has the best χ^2 value, showing a good agreement. For θ_p, the SF model shows the best agreement with the data based on the χ^2 value. In the larger θ_p region, where CCQE dominates, the ED-RMF model with the cascade has the lowest strength.

p_n is defined as given in Ref. [184]:

$$\begin{aligned} p_n &= \sqrt{\delta p_L^2 + \delta p_T^2} \\ \delta p_L &= \frac{1}{2}R - \frac{M_B^2 + \delta p_T^2}{2R} \\ R &= M_A + p_L^\mu + p_L^p - E^\mu - E^p. \end{aligned} \tag{14.2}$$

Here, L, B, μ and p indicate the longitudinal contribution, the residual nucleus, the muon and the proton respectively.

In electron scattering $(e, e'p)$ experiments, the differential cross section in terms of missing momentum is sensitive to the initial-state nuclear model and is related to the momentum of nucleons inside the nucleus. This allows for the contributions of the individual shells to be seen in the differential cross section. The missing momentum is analogous to p_n but in neutrino experiments, an average over neutrino energy is required, smearing the contributions from each peak and removing sensitivity. Despite this, the p_n differential cross section shows a clear two-peak structure. The region below 0.2 GeV is dominated by CCQE and the ED-RMF model with the cascade captures the peak well. 2p2h and π-absorption contributions increase above approximately 0.4 GeV, where there is now very little CCQE. This shows that p_n is a powerful tool for discerning between CCQE and non-CCQE events.

In the CCQE dominated region, the N1p1h model clearly overestimates the data. The ED-RMF with cascade, on the contrary, underestimates the data and provides a better description of the shape, having the best χ^2 value among all models.

Model	p_p	p_n	θ_p	p_μ
EDRMF cas	26.2/25	51.1/24	54.1/26	50.2/32
EDRMF no cas	36.9/25	112/24	68.6/26	43.9/32
N1p1h cas	43.2/25	105/24	66.6/26	41.6/32
SF cas	45.4/25	54.0/24	40.9/26	40.8/32
EDAIC no cas	33.4/25	52.4/24	46.8/26	37.1/32

Table 14.5: χ^2/N_{dof} values for each kinematic variable for MINERvA. "cas" and "no cas" indicate where the cascade has and has not been applied respectively.

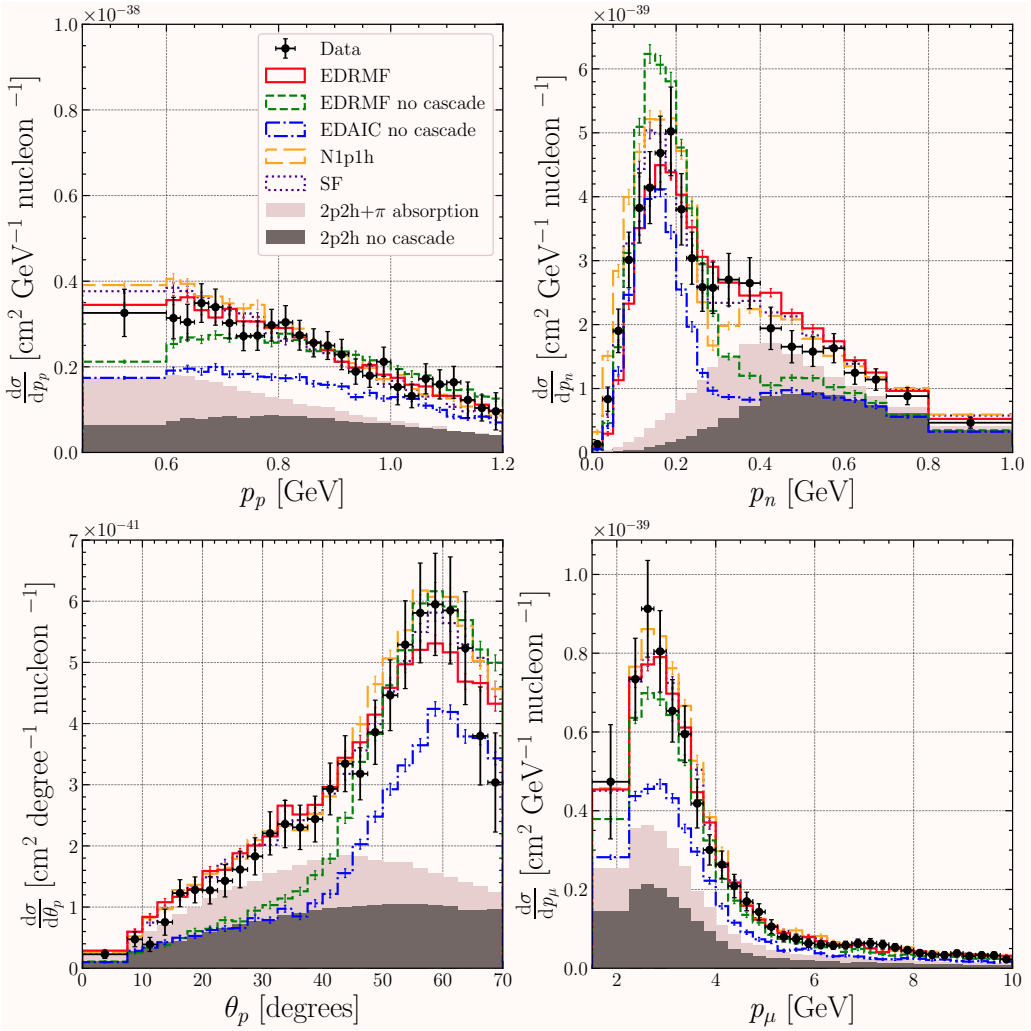

Figure 14.6: MINERvA ν_μ CC0πNp dataset on hydrocarbon. Differential cross sections for different kinematics are shown. Subscript p indicated a scattered proton kinematic; a subscript μ indicates a scattered lepton kinematic and a subscript n indicates a reconstructed initial neutron kinematic. The histograms follow the same definition as Figure 14.1.

TKI samples

The differential cross section for the TKI variables are shown in Figure 14.7. The χ^2 values are given in Table 14.6. The variables δp_T and p_n are slightly differing representations of the missing momentum, therefore they exhibit similar behaviour. The ED-RMF model with the cascade has a significantly improved χ^2 value compared to other NEUT models and captures the peak well, where CCQE dominates. The ED-RMF and EDAIC model without the cascade lack the elongated tail of the distribution that the cascade contributes to. In the end of the tail region, the 2p2h contribution is large and π-absorption is small, meaning that nucleon re-scattering FSI in the cascade is the only contribution. It is

clear that the cascade is necessary to not underestimate the data beyond approximately 0.3 GeV. Figure 14.8 shows the ED-RMF without the cascade plus the π-absorption contribution from the cascade. This clearly shows that nucleon re-scattering is important in reducing the strength in the peak and redistributing it to the tail. The RPWIA model with the cascade applied agrees with the ED-RMF model in the tail but differs in the peak. The only difference between these two models is the nuclear potential that is used to solve the final-state wavefunction. Hence, it is clear from this that the inclusion of the nuclear potential and the distortion of the plane wave is necessary to achieve the correct differential cross section strength in the CCQE-dominated peak.

For $\delta\phi_T$, the EDAIC model has a better χ^2 value, likely coming from the agreement in shape despite the normalisation being low to the eye. At low $\delta\phi_T$, when the angle between transverse p_p and $-p_\mu$ is small (indicating an almost back-to-back proton and muon), the N1p1h model significantly overestimates the data. For $\delta\alpha_T$, the ED-RMF model without the cascade exhibits a flat distribution. The ED-RMF model with the cascade yields a χ^2 value slightly higher than those of the existing models in NEUT. Notably, all models incorporating the cascade overestimate the last bin at large $\delta\alpha_T$. This could indicate that the NEUT cascade is providing too much strength to the differential cross section in this region.

Model	δp_T	$\delta\phi_T$	$\delta\alpha_T$
EDRMF cas	50.0/24	54.0/23	19.3/12
EDRMF no cas	154/24	102/23	38.6/12
N1p1h cas	182/24	81.6/23	18.5/12
SF cas	125/24	71.9/23	17.4/12
EDAIC no cas	72.3/24	46.7/23	30.7/12

Table 14.6: χ^2/N_{dof} values for each TKI variable for MINERvA. "cas" and "no cas" indicate where the cascade has and has not been applied respectively.

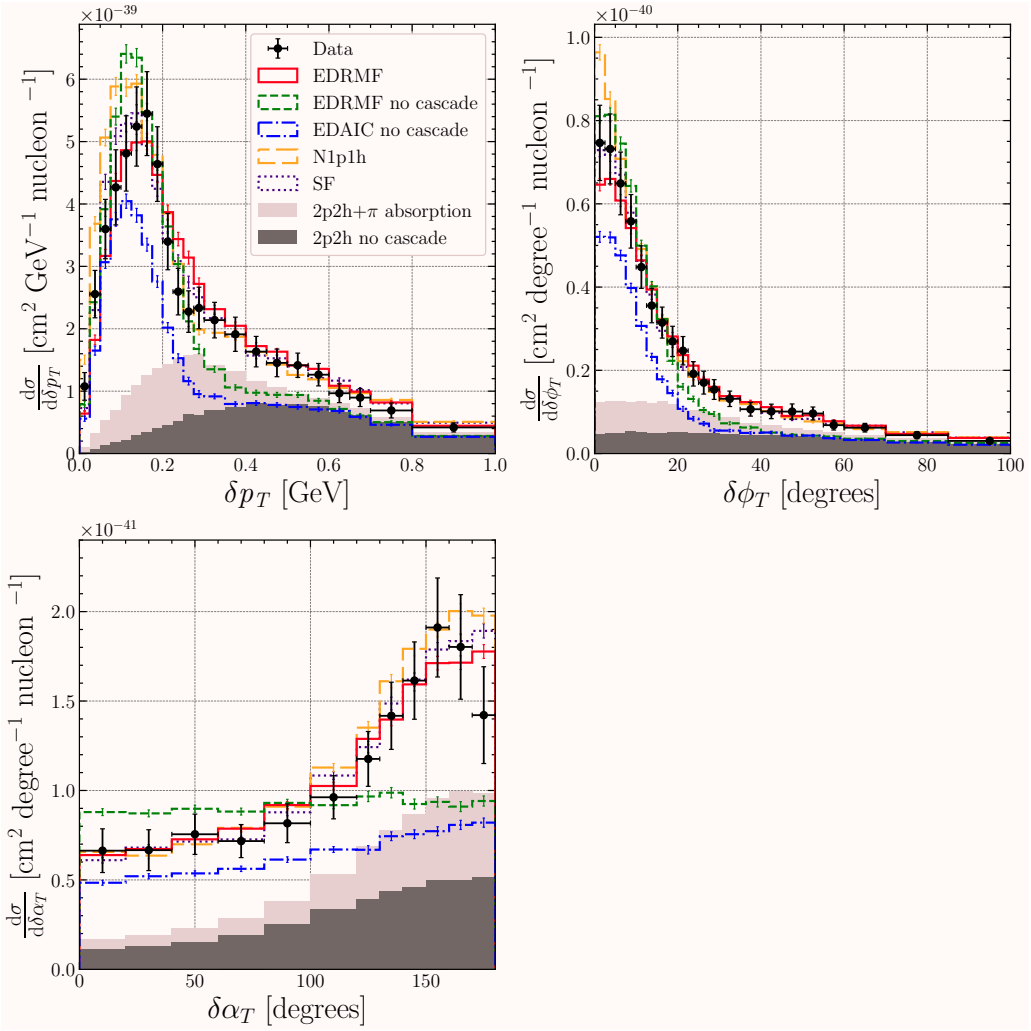

Figure 14.7: MINERvA ν_μ CC0πNp dataset on hydrocarbon. Differential cross sections for TKI variables defined in Eq. 13.1. The histograms follow the same definition as Figure 14.1.

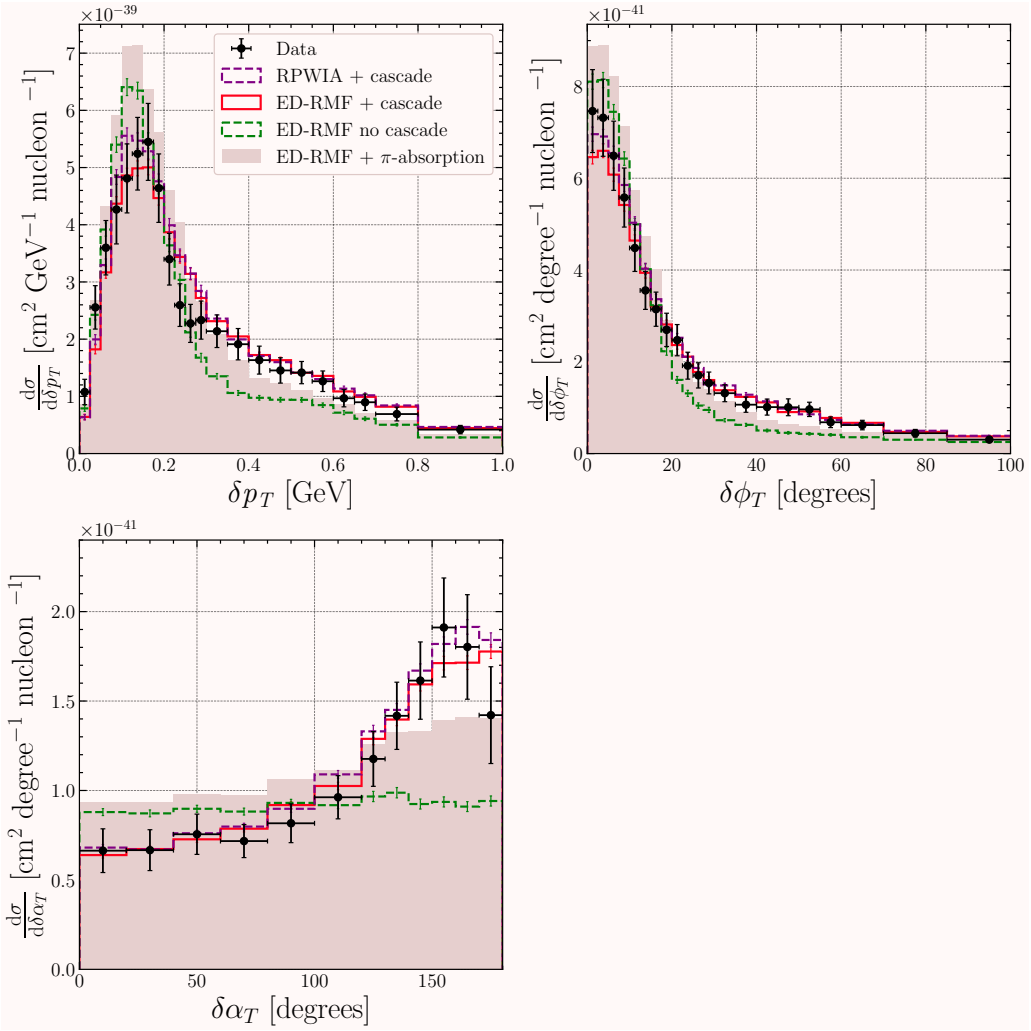

Figure 14.8: MINERvA ν_μ CC0πNp dataset on hydrocarbon. Differential cross sections for TKI variables defined in Equation 13.1. Here the ED-RMF model with and without the cascade are given by the solid red and dashed green lines respectively. The RPWIA model with the cascade is given by the dashed purple line. The ED-RMF model without the cascade but with the π-absorption from the NEUT cascade added is given by the grey shaded region. It is clear that it causes an overestimation in the peak of the distribution, demonstrating that nucleon re-scattering is important for redistributing the strength in the peak to the tail.

MINERvA kinematics shape-only comparison

The shape-only comparisons for the kinematics are given in Figure 14.9. The corresponding scale factors required to scale the MC to data are given in Table 14.7. For p_n, the peak is captured well by the SF and N1p1h models; however, the second peak around 0.3-0.4 GeV is captured only by the ED-RMF model with the cascade applied. For all variables, the ED-RMF model without the cascade and the EDAIC model agree in shape.

For p_μ, all models closely match the shape of the data. The peak is not captured by any of the models but is consistent within the error bar. This indicates that, in terms of cross section shape, all models differ mainly in the description of the hadron part of the interaction. For θ_p, all models with the cascade capture the shape at low angles, but at high angles the strength is lower, although consistent within the error.

Model	p_p	p_n	θ_p	p_μ
EDRMF cas	0.97	0.97	0.96	1.01
EDRMF no cas	1.13	1.12	1.11	1.17
N1p1h cas	0.91	0.91	0.90	0.95
SF cas	0.96	0.96	0.95	1.00
EDAIC no cas	1.63	1.62	1.61	1.69

Table 14.7: Scale factors required to scale the MC to data for each kinematic variable for MINERvA. "cas" and "no cas" indicate where the cascade has and has not been applied respectively.

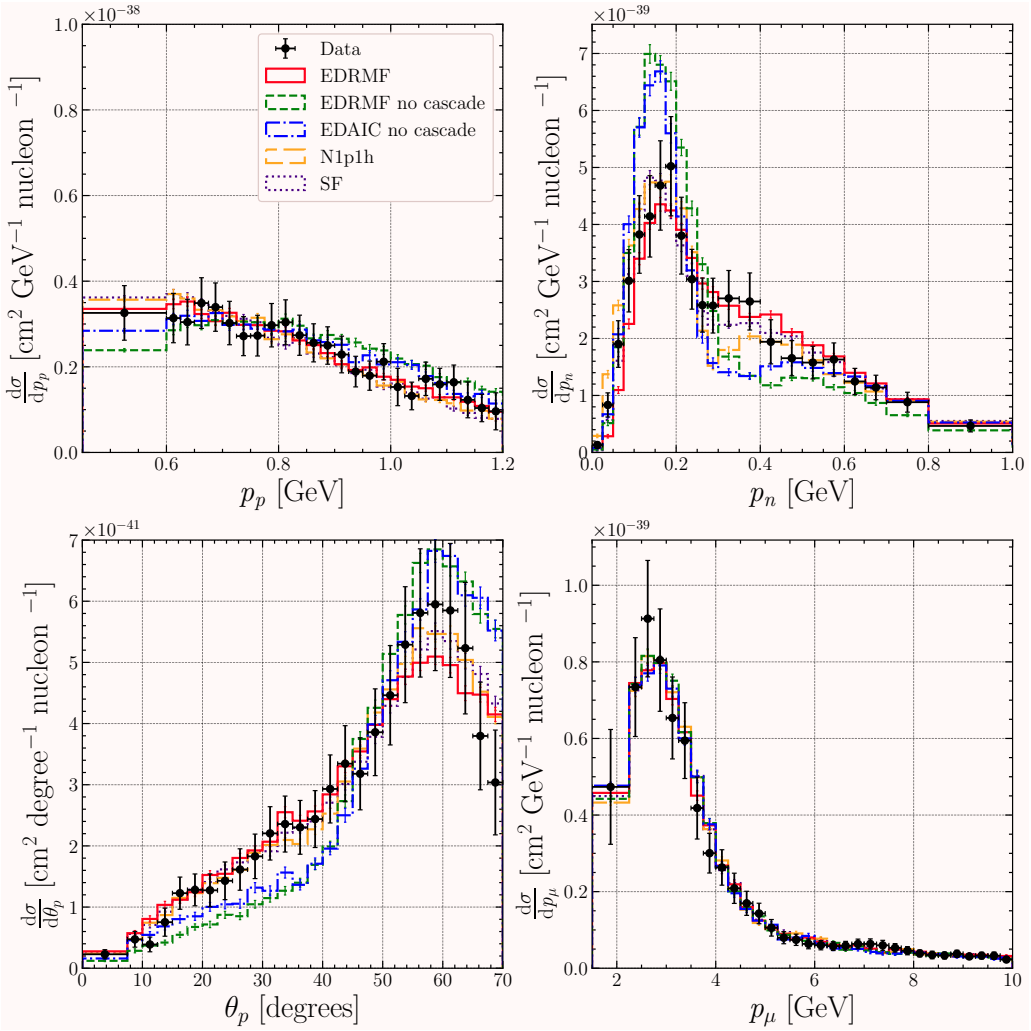

Figure 14.9: Shape-only differential cross sections for kinematic variables for MINERvA. The NEUT models are normalised to the measurement. The histograms follow the same definition as Figure 14.1.

MINERvA TKI shape-only comparison

The TKI shape-only comparisons are shown in Figure 14.10. The corresponding scale factors required to scale the MC to data are given in Table 14.8. For δp_T, the best shape agreement by eye is the SF model. For $\delta\phi_T$, all models with the cascade agree beyond approximately 10 degrees. The value of $\delta\phi_T$ at 0 degrees differs dramatically between the three models that employ the cascade. For $\delta\alpha_T$, all models with the cascade agree until around 100 degrees, differing at higher angles. In the case of $\delta\alpha_T$, the ED-RMF model and the EDAIC model without the cascade, do not agree in shape. The EDAIC model, due to the nuclear potential, has elastic FSI in the distorted wave; this causes the distribution to increase at higher $\delta\alpha_T$.

Model	δp_T	$\delta\phi_T$	$\delta\alpha_T$
EDRMF cas	0.96	0.97	0.97
EDRMF no cas	1.12	1.13	1.13
N1p1h cas	0.90	0.91	0.91
SF cas	0.95	0.96	0.96
EDAIC no cas	1.62	1.63	1.63

Table 14.8: Scale factors required to scale the MC to data for each TKI variable for MINERvA. "cas" and "no cas" indicate where the cascade has and has not been applied respectively.

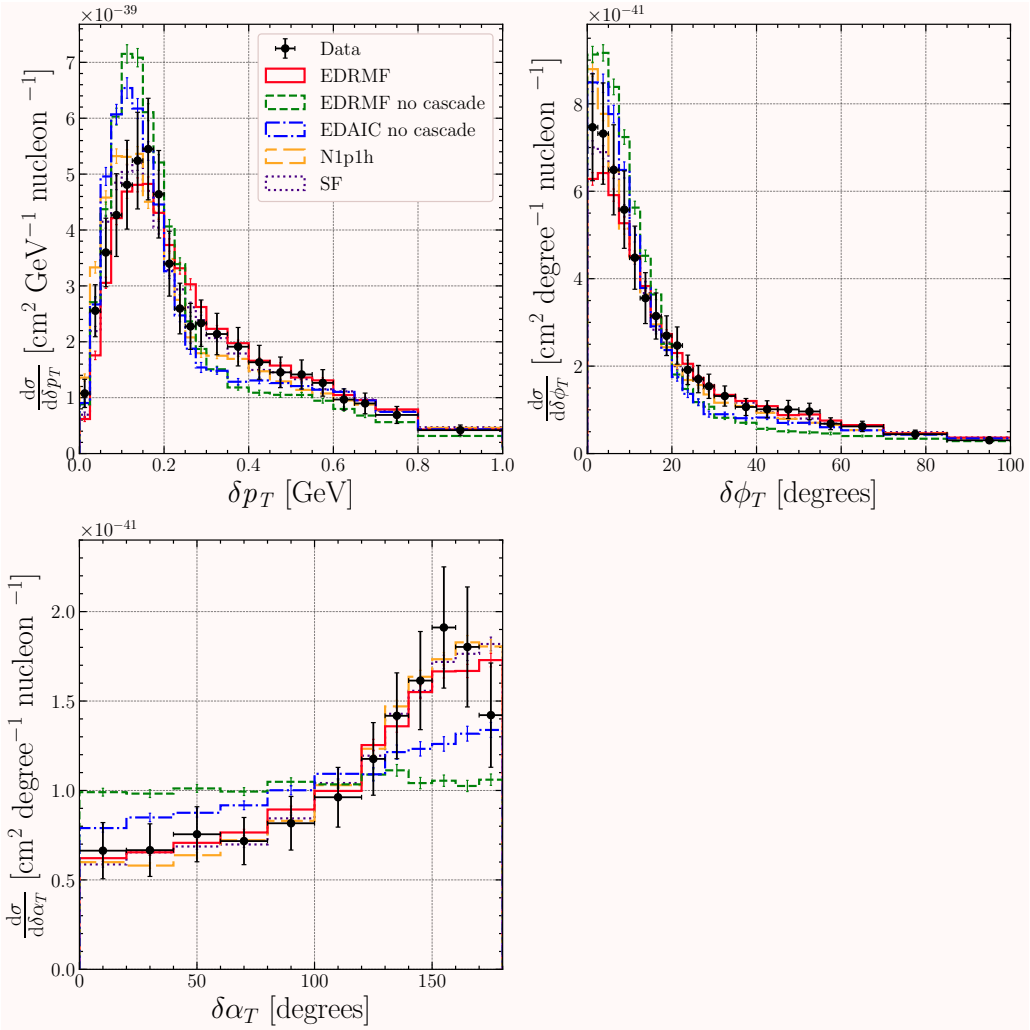

Figure 14.10: Shape-only differential cross sections for TKI variables defined in Equation 13.1 for MINERvA. The NEUT models are normalised to the measurement. The histograms follow the same definition as Figure 14.1.

14.1.4 MicroBooNE results

The MicroBooNE datasets are CC0π1p and CC0πNp datasets [187, 188, 186] and are interactions on argon. The applied kinematic selections are given in Table 14.9.

Kinematic Variable	CC0πNp	TKI
p_p	0.3 – 1.2 GeV	0.3 – 1 GeV
$\cos\theta_p$	...	...
p_μ	$>$ 0.1 GeV	0.1 – 1.2 GeV
$\cos\theta_\mu$	...	...

Table 14.9: Kinematic selections applied in the MicroBooNE dataset. Here "..." indicate that there is no selection applied. In the MicroBooNE analysis, only one proton is selected in the kinematic region for the TKI cross sections. This selected proton may not be the highest momentum proton in the event as this may be outside the kinematic region considered. Events with charged pions may pass selection criteria if their momentum is below 70 MeV. In the Np analysis, any number of protons can be selected, but only the highest momentum proton is used to calculate the proton cross sections. There are no pions or other mesons in the final state.

The MicroBooNE measurements in Refs. [187, 188] use an unfolding procedure based on Ref. [195], while Ref. [186] uses forward folding. Both procedures produce an additional smearing matrix that contains information about the amount of bias and regularisation of the measurement. Since this smearing matrix is applied to the published unfolded cross sections, it must also be applied to any theoretical predictions being compared to the measured cross sections [188]. The full covariance matrices and smearing matrices are released alongside the dataset.

Kinematic samples

The differential cross sections for the scattered muon momentum (p_μ), leading scattered proton momentum (p_p), muon scattering angle (θ_μ), leading proton scattering angle (θ_p), and the opening angle between the scattered proton and muon ($\theta_{p\mu}$) are shown in Figure 14.11. The corresponding χ^2 values are summarised in Table 14.10.

For p_μ, the EDAICa model achieves the lowest χ^2, indicating the best agreement with the data. Although the EDAICa model appears to have a lower normalisation by eye, high correlations in data can result in a relatively good χ^2 if the overall shape is well reproduced. In contrast, the other models have larger χ^2 values, suggesting poorer agreement with the data. Visual inspection shows that the ED-RMF model with cascade and the N1p1h model both provide a reasonable match to the data, although there is a slight

difference in the peak position. This level of agreement was less pronounced in comparisons with MINERvA and T2K data. For p_p, the ED-RMF model with the cascade and the N1p1h model has the best χ^2 value. Both of these models also show an increase in strength in the first bin. This is not seen in models that do not have the cascade applied indicating that the cascade may be increasing the strength too much in this first bin. The EDAICa model without the cascade applied has the lowest strength as expected.

For $\cos(\theta_\mu)$, the EDAICa model achieves the best χ^2 value. In the last bin, the N1p1h and ED-RMF models with the cascade overestimate the data and this could be a reason for the increased χ^2 value for those models. In the last bin, all models fail to replicate the drop in shape. It is however not possible to conclude whether this excess is due to the CCQE or to the non-CCQE contributions, which are quite large in the most forward bin. For $\cos(\theta_p)$, the ED-RMF model with the cascade is the best fit to data given the χ^2 and the EDAICa model without the cascade is the next best. It is also interesting to note that the EDRMF and EDAICa model without the cascade replicates the drop in the last bin, whilst models with the cascade does not. Similarly to $\cos(\theta_\mu)$, the last bin is overestimated by N1p1h and ED-RMF with the cascade. This indicates that the NEUT cascade is increasing the strength in the last $\cos(\theta_\mu)$ and $\cos(\theta_p)$ bins and could possibly be due to the non-CCQE contributions.

For the muon-proton opening angle, the EDAICa model without the cascade is the best fit to the data given the χ^2. Again, the strong correlations in the data may contribute to this outcome.

Model	p_μ	p_p	$\cos(\theta_\mu)$	$\cos(\theta_p)$	$\theta_{p\mu}$
EDRMF cas	26.7/6	7.74/10	21.9/12	7.57/9	10.6/6
EDRMF no cas	28.2/6	19.4/10	14.8/12	14.4/9	13.4/6
N1p1h cas	28.6/6	4.09/10	21.1/12	9.20/9	9.48/6
EDAICa no cas	10.7/6	17.4/10	8.34/12	8.17/9	5.73/6

Table 14.10: χ^2/N_{dof} values for each kinematic variable for MicroBooNE. "cas" and "no cas" indicate where the cascade has and has not been applied respectively.

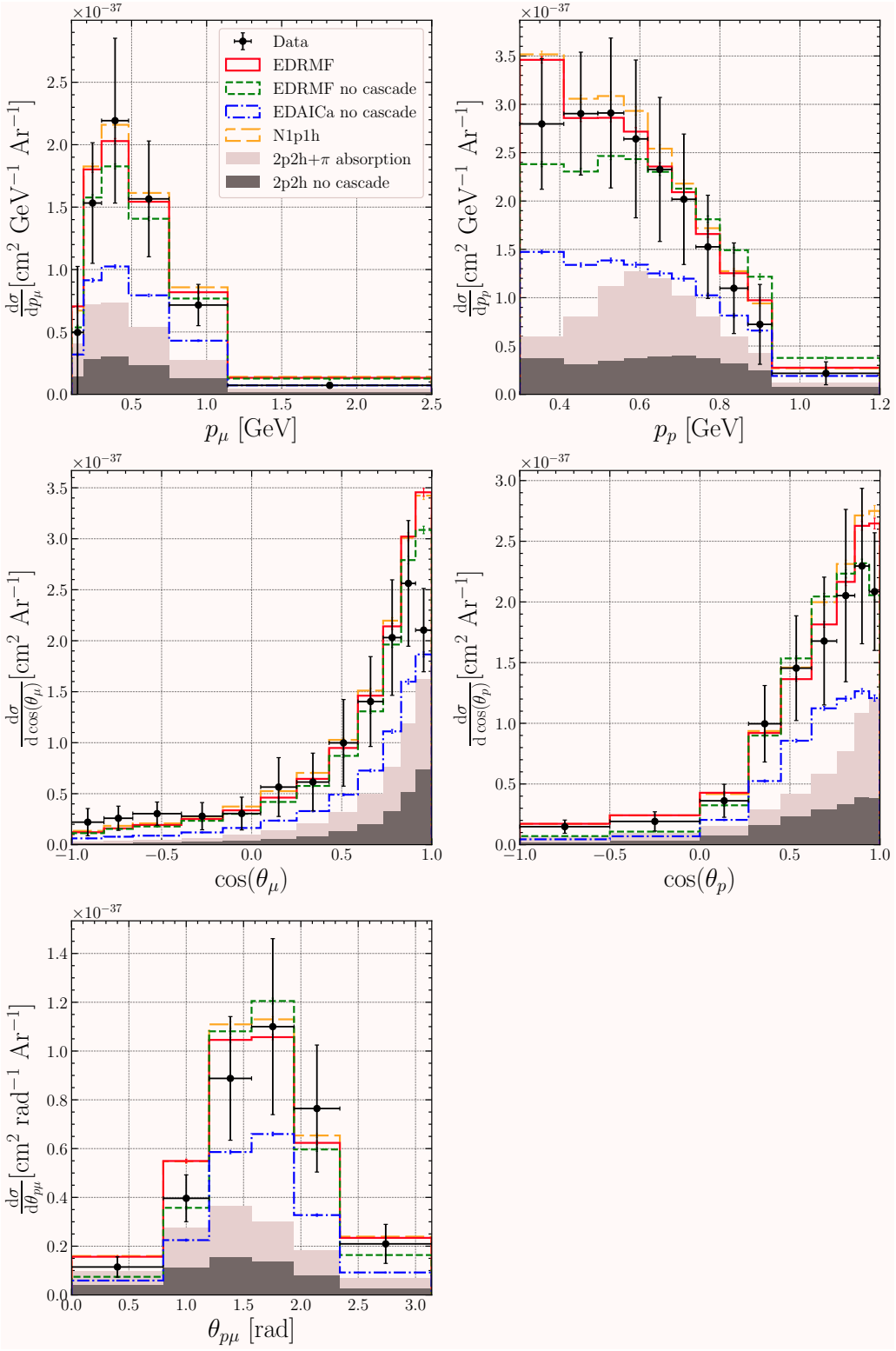

Figure 14.11: MicroBooNE ν_μ CC0πNp dataset on argon. Differential cross sections for different kinematics are shown. Subscript p indicated a scattered proton kinematic; a subscript μ indicates a scattered muon kinematic and the subscript $p\mu$ indicates the opening angle between the scattered proton and muon. The histograms follow the same definition as Figure 14.1 except the SF model is not included.

TKI samples

The differential for the TKI variables are shown in Figure 14.12. The corresponding χ^2 values are given in Table 14.11. For δp_T, the ED-RMF model with the cascade achieves the lowest χ^2 value, while the N1p1h model also shows good agreement with the data, as indicated by a reduced χ^2 slightly above 1. Both the ED-RMF and EDAICa models without the cascade show a high χ^2 value. It can be seen that all models except the ED-RMF without the cascade underestimate the data in all bins. The ED-RMF model, without the cascade, is consistent with data in the peak of the distribution and begins to underestimate the data in the sixth bin.

For $\delta\alpha_T$, both the N1p1h model and the ED-RMF model with the cascade show good agreement with the data based on their χ^2 values. For $\delta\phi_T$, the χ^2 values indicate that the ED-RMF model with the cascade provides the best agreement with the data, while the N1p1h model achieves the second-best agreement. The ED-RMF model without the cascade is more consistent with the data in the low-angle region compared to other models, all of which underestimate the data.

Model	δp_T	$\delta\phi_T$	$\delta\alpha_T$
EDRMF cas	11.0/13	12.0/12	8.34/7
EDRMF no cas	26.7/13	32.1/12	50.3/7
N1p1h cas	13.3/13	13.5/12	7.35/7
EDAICa no cas	26.1/13	38.3/12	31.6/7

Table 14.11: χ^2/N_{dof} values for each TKI variable for MicroBooNE. "cas" and "no cas" indicate where the cascade has and has not been applied respectively.

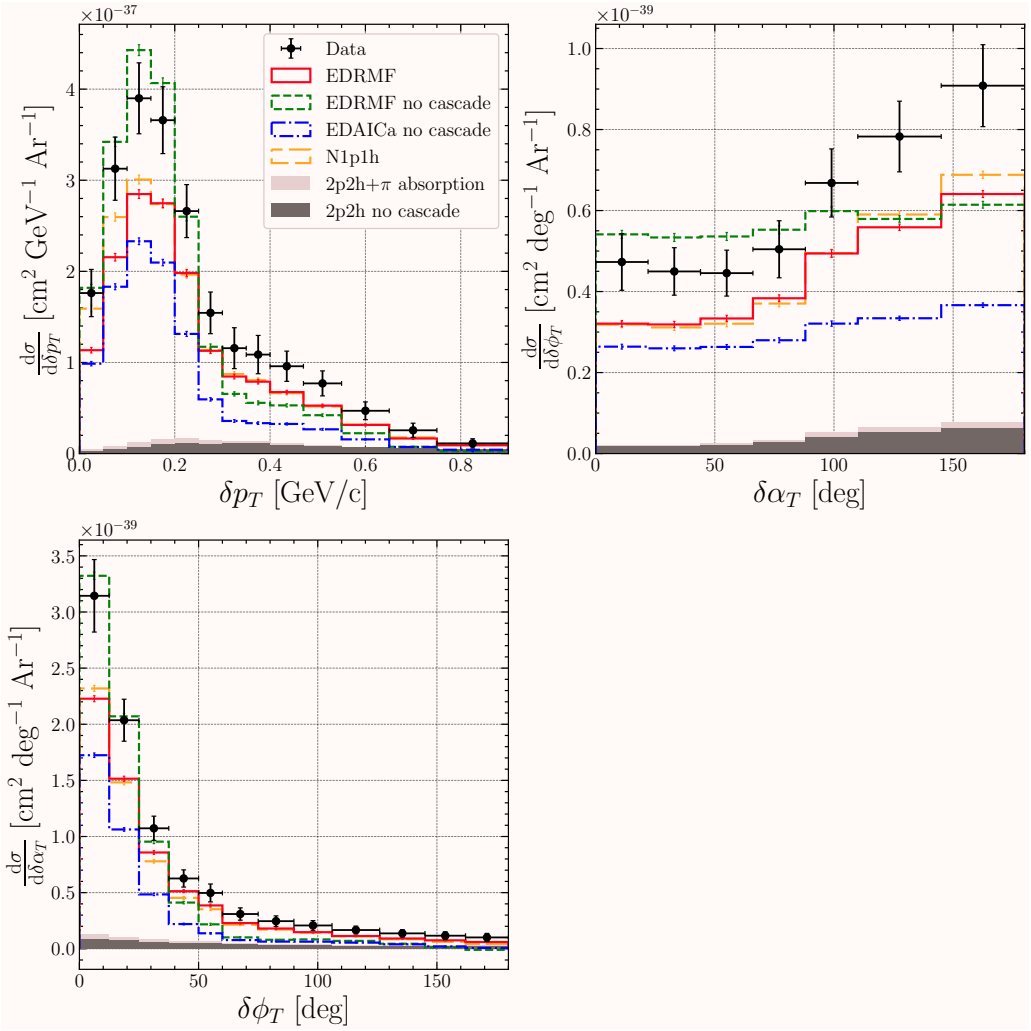

Figure 14.12: Differential cross sections for TKI variables defined in Equation 13.1 for MicroBooNE. The histograms follow the same definition as Figure 14.1 except the SF model is not included. Correlations in data lead to a visual normalisation difference between the MC and measurement.

MicroBooNE kinematics shape-only comparison

The shape-only comparisons for the kinematics are shown in Figure 14.13. The corresponding scale factors required to scale the MC to data are given in Table 14.12. For p_μ, all models agree in shape and are consistent with the data. A similar agreement is seen in $\cos(\theta_\mu)$, however, small shape disagreements are seen at $\cos(\theta_\mu) \approx 1.0$, indicating that at forward muon scattering angles, each model describes a different angular distribution. All models overestimate the final bin, where the measurement shows a drop.

For p_p, the ED-RMF model with the cascade and the N1p1h model agrees in shape and is consistent with data. The ED-RMF model without the cascade and the EDAICa

model have similar shapes but have lower strength at lower proton momentum and higher strength at higher proton momentum. Similarly, for $\cos(\theta_p)$, the ED-RMF model with the cascade and the N1p1h model agree in shape and with the data. The models without the cascade applied have slightly lower strength at lower $\cos(\theta_p)$ and slightly higher strength between $0.25 < \cos(\theta_p) < 0.8$ before having lower strength again in the final bin.

For $\theta_{p\mu}$, between 0 and 1 radians, models without the cascade have a better shape by eye before having a greater strength between 1 and 2 radians. The ED-RMF model with the cascade and the N1p1h model agree in shape and are consistent with the data.

Model	p_μ	p_p	$\cos(\theta_\mu)$	$\cos(\theta_p)$	$\theta_{p\mu}$
EDRMF cas	0.92	0.92	0.94	0.93	0.94
EDRMF no cas	1.01	1.01	1.04	1.02	1.03
N1p1h cas	0.88	0.88	0.90	0.89	0.90
EDAICa no cas	1.79	1.79	1.83	1.80	1.82

Table 14.12: Scale factors required to scale the MC to data for each kinematic variable for MINERvA. "cas" and "no cas" indicate where the cascade has and has not been applied respectively.

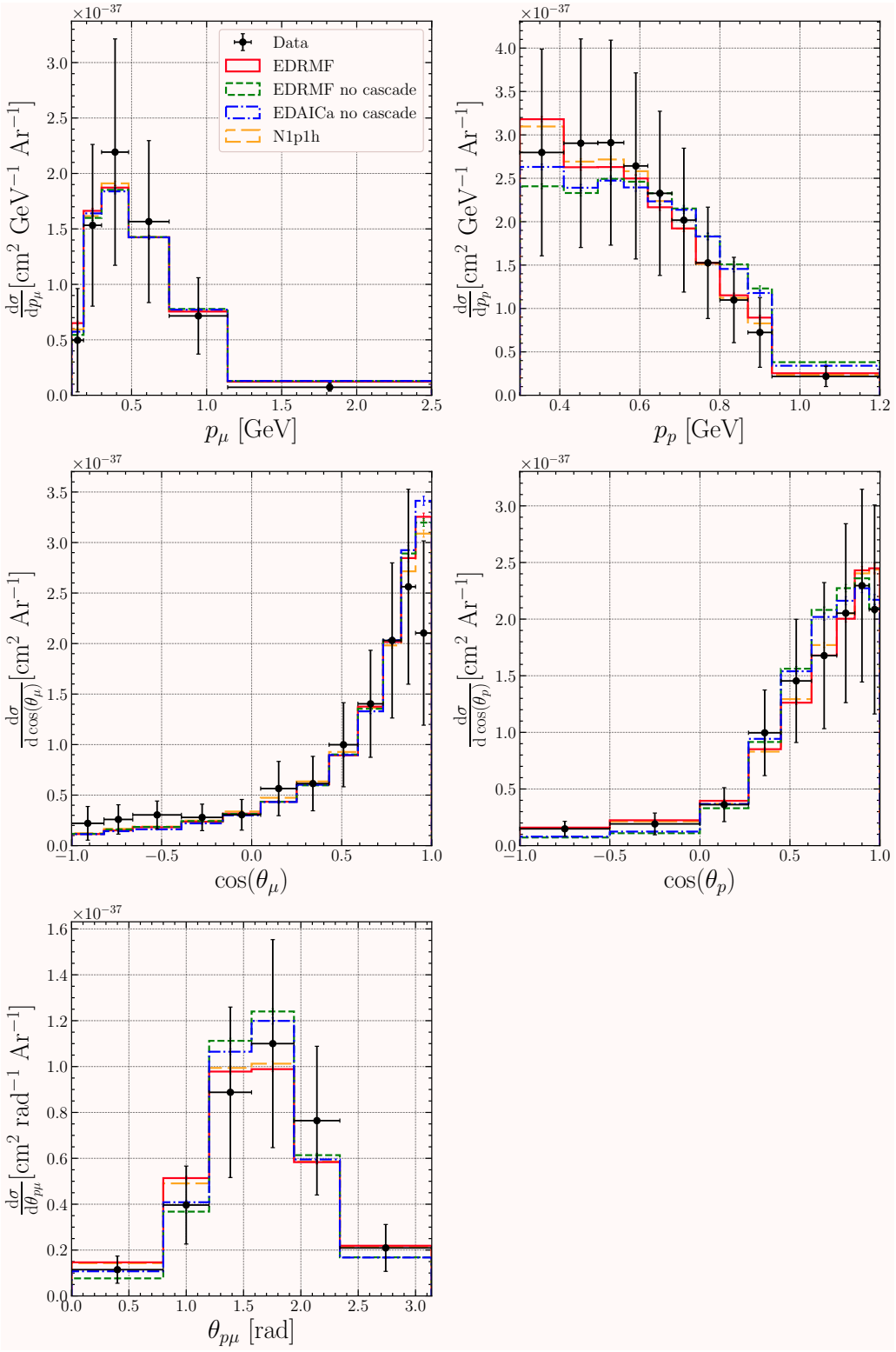

Figure 14.13: Shape-only differential cross sections for kinematic variables for MicroBooNE. The NEUT models are normalised to the measurement. The histograms follow the same definition as Figure 14.1 except the SF model is not included.

MicroBooNE TKI shape-only comparison

The shape-only comparisons for the TKI variables are shown in Figure 14.14. The corresponding scale factors required to scale the MC to data are given in Table 14.13. For all TKI variables, the N1p1h and ED-RMF model with the cascade agree to the data well and have almost identical shape. For δp_T and $\delta\phi_T$ it is interesting to note the agreement in shape for the ED-RMF model without the cascade and the EDAICa model, indicating that they differ mostly in normalisation.

Model	δp_T	$\delta\phi_T$	$\delta\alpha_T$
EDRMF cas	1.40	1.36	1.39
EDRMF no cas	1.12	1.21	1.12
N1p1h cas	1.31	1.40	1.36
EDAICa no cas	2.07	2.23	2.09

Table 14.13: Scale factors required to scale MC to data for each TKI variable for MicroBooNE. "cas" and "no cas" indicate where the cascade has and has not been applied respectively.

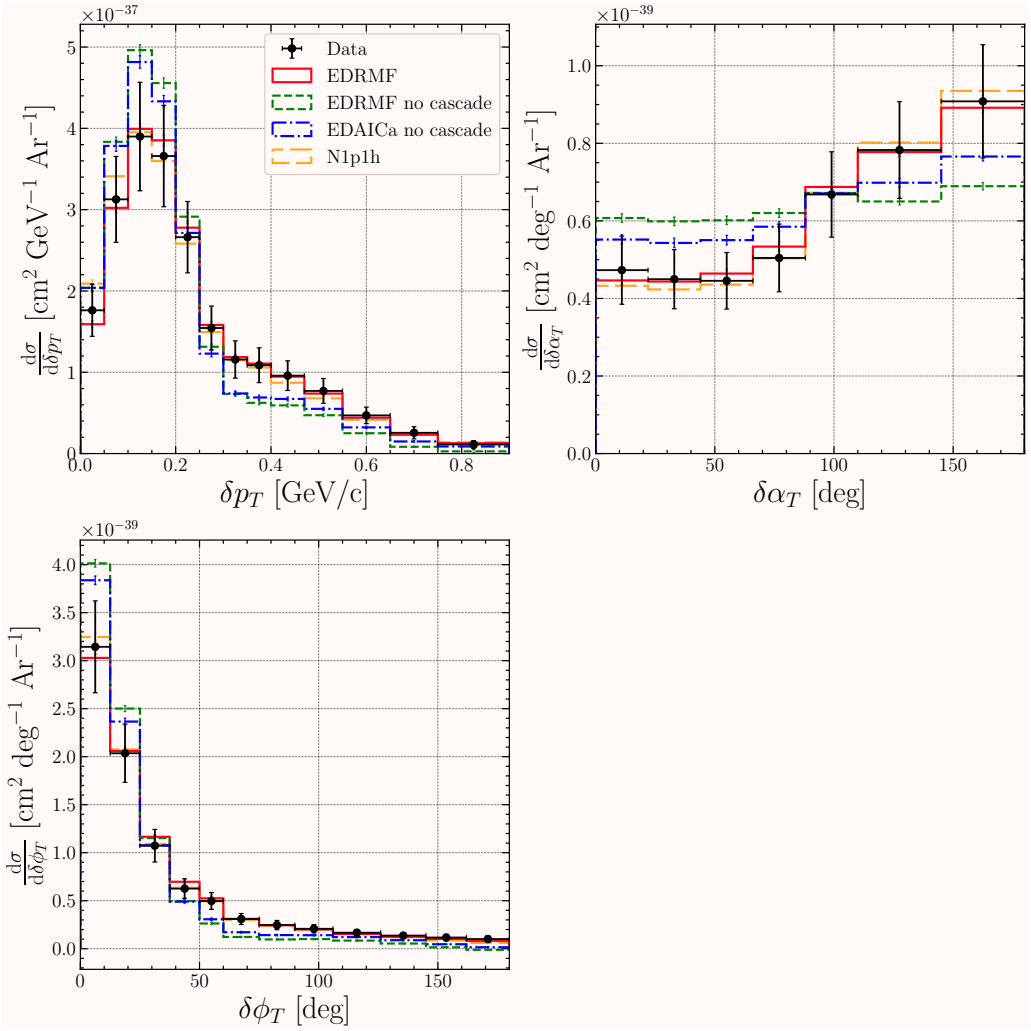

Figure 14.14: Shape-only differential cross sections for TKI variables defined in Equation 13.1 for MicroBooNE. The NEUT models are normalised to the measurement. The histograms follow the same definition as Figure 14.1 except the SF model is not included.

14.2 Comparison with inclusive electron scattering data

14.2.1 Comparison with different nuclear models

The ED-RMF electron scattering model implemented in NEUT is benchmarked against the nuclear models presented in Chapter 8. Figure 14.15 shows the gRFG (with binding energy correction), lRFG (with binding energy correction), SF and ED-RMF model against inclusive electron scattering data from Ref. [131, 196, 197]. The data is $(e, e')^{12}$C, meaning it contains contributions from QE, 2p2h and pion production channels. At low incident electron energies, the QE contribution dominates, but as the electron energy increases, the 2p2h and pion production contributions increase at higher ω. It is clear that at low incident electron energies, the gRFG and lRFG overestimate the data by a considerable amount and the peak is shifting significantly to higher ω. At higher electron energies, the gRFG model captures the shape of the QE peak well but can be shifted due to the constant binding energy correction applied. At lower electron energies, the SF model peak is shifted far to the right. This is not seen in the case of the ED-RMF model, which, at lower values of ω, has a peak value that better matches the data. At higher energies, like the SF, the ED-RMF model underestimates the data but matches the shape well, especially in the first rising slope of the data, where ED-RMF matches well but the SF model often underestimates. This is expected since the model contains only QE interactions and this leaves freedom in the model to include 2p2h and pion production contributions. The freedom to include 2p2h or MEC contributions in the model has been extensively explored in [168, 178].

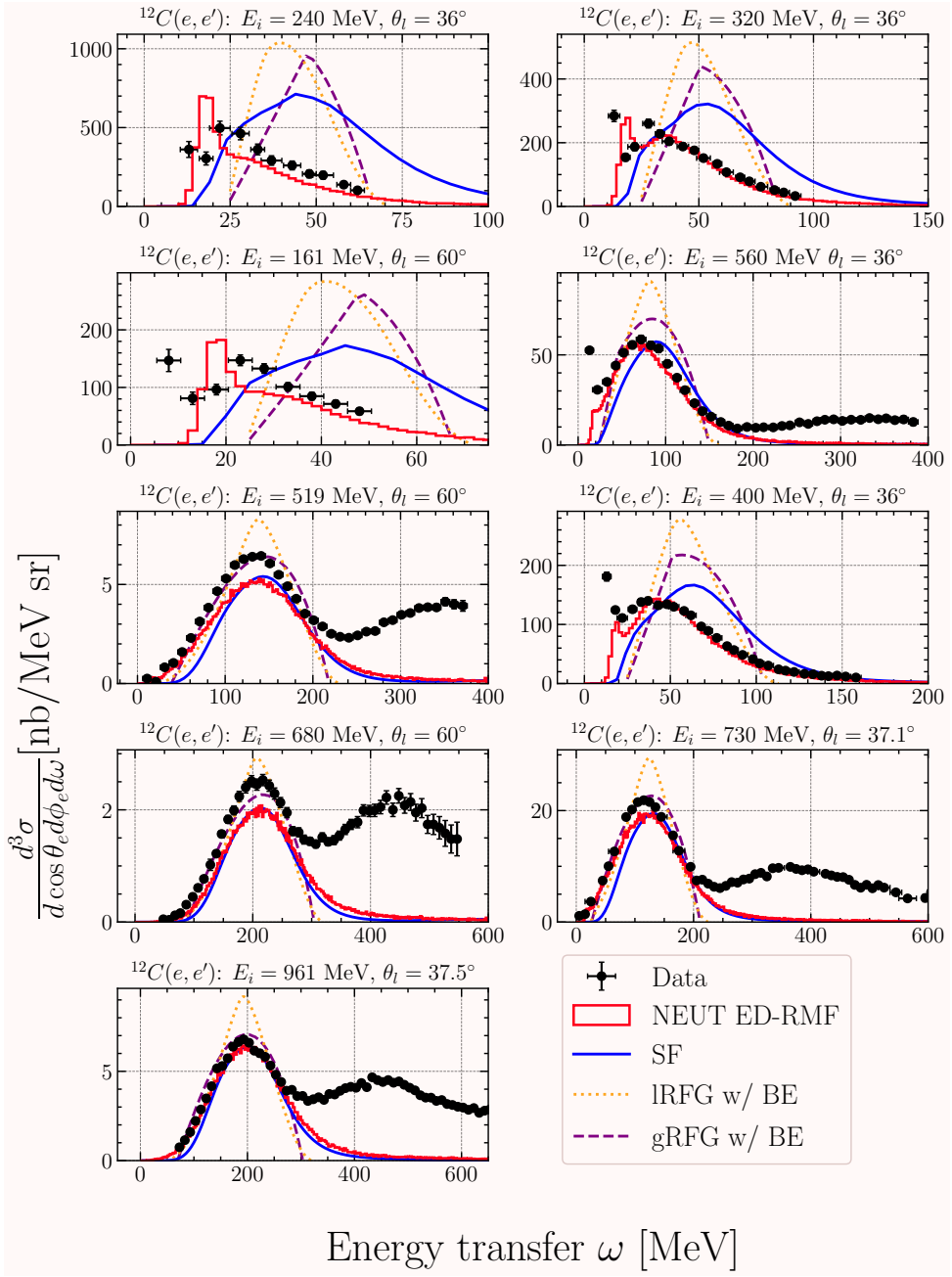

Figure 14.15: Comparison of a global relativistic Fermi gas (gRFG), local relativistic Fermi gas (lRFG), spectral function (SF) and energy-dependent relativistic mean field (ED-RMF) model against inclusive electron scattering data. Data from Refs. [131, 196, 197].

14.2.2 Comparison to other NEUT electron scattering models

A SF QE model and a dynamic coupled channel (DCC) pion production model [198, 199] were implemented in NEUT and were benchmarked against the experimental data in [200]. The SF model was based on the Rome spectral function like the neutrino scattering mode in NEUT. More recently, the spectral function from Ref. [201] (denoted SF*) was also implemented and a Coulomb correction for neutrons was also implemented. In this section, the SF and ED-RMF electron scattering models are benchmarked against the same data as in Figure 14.15.

Figure 14.16 shows the ED-RMF, SF and SF* QE models alongside the DCC pion production model against inclusive electron scattering data from Refs. [131, 196, 197]. Similarly to the previous section, at low electron energies and low ω, the SF models incorrectly calculate the position of the CCQE peak and are shifted to higher values of ω; this is not seen in the ED-RMF model. This indicates that the distortion of the outgoing wave is important at lower incident energies and that the PWIA is not a suitable approximation in this regime. At slightly higher electron energies, such as 320 MeV, the SF shift is reduced, but the peak is also overestimated. The shifted peak of the SF is present event at higher electron energies but the peak is then underestimated. The DCC contribution is only present after an ω of around 150 MeV. It is important to note that the SF-based NEUT models contain only the QE interaction, and therefore an overestimation of the data leaves no room for effects that are missing, such as meson-exchange currents (MEC). In the case of ED-RMF, the peak is often below the data and this leaves room for the MEC contributions shown in [168].

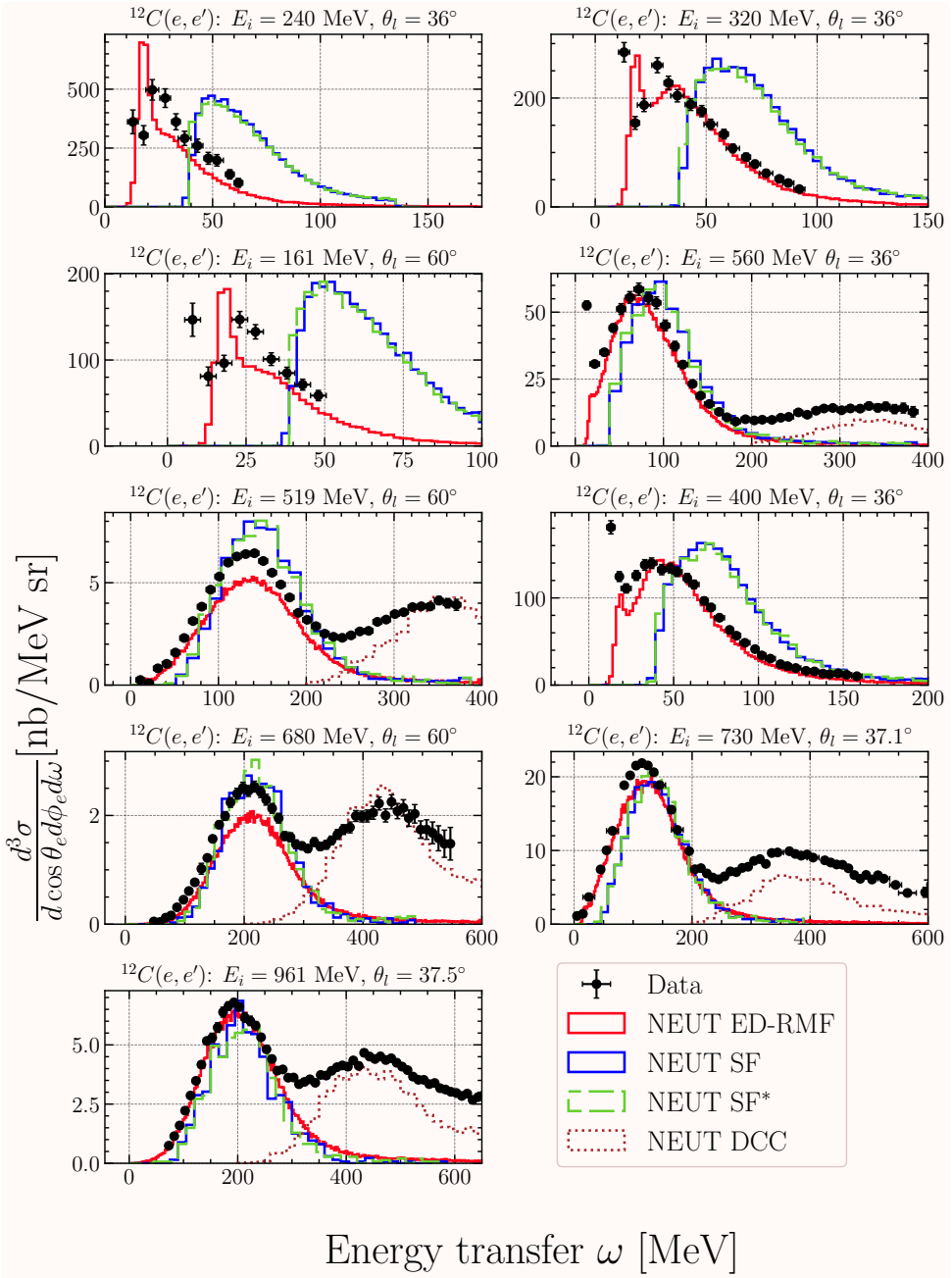

Figure 14.16: Comparison of the energy-dependent relativistic mean field potential model (ED-RMF), the spectral function (SF) model from Ref. [133, 200], the spectral function (SF*) model from Ref. [201] and the dynamic coupled channels (DCC) model from Ref. [200] against inclusive electron scattering data. Data from Refs. [131, 196, 197].

14.3 Comparison with JSNS KDAR

The results in this study are being prepared for publication [202].

14.3.1 Kaon decay-at-rest dataset

An ideal dataset to benchmark nuclear models would include a measurement of the missing energy, E_m itself. The E_m profile encodes information about the nuclear modelling such as the nuclear shell structure. In neutrino experiments, since E_m is not directly measurable due to the initial neutrino energy not being known and the inability to reconstruct nuclear recoil. However, if the neutrino energy is known, a "per event" E_m definition can be used. This is defined in Equation 8.24. A shape-only differential cross section of E_m using kaon decay-at-rest neutrinos at a monochromatic energy of 235.5 MeV on ^{12}C [203] is a unique dataset that allows such a comparison. The kaon can decay via $K^+ \to \mu^+\nu_\mu$ with a branching ratio of 63.6% [204, 203] producing a neutrino of single energy 235.5 MeV, ideal for calculating E_m. The measurement comes from the J-PARC Sterile Neutrino Search at the J-PARC Spallation Neutron Source liquid scintillator experiment.

In words, the definition of E_m is the energy that is transferred to the target nucleus minus the kinetic energy of the outgoing protons. In the absence of nuclear effects such as Fermi momenta and FSI, the E_m profile is expected to be zero. Thus, it is a powerful tool in investigating nuclear effects and benchmarking neutrino-nucleus interaction models and EGs. The definition of E_m used in this analysis is given below as

$$E_m = \omega - \sum T_p \tag{14.3}$$

where $\sum T_p$ is the sum of the kinetic energy of the final state protons. It is important to note that ν_μ CCQE events can also produce neutrons in the final state due to SRC events and FSI. In CCQE events, it is often the case that the recoil carbon nucleus is in an excited state of either ^{11}B* or ^{11}C*. The nuclear deexcitation step involves the emission of gammas or even other nucleons. While the authors of Ref. [203] do not take the energy of the emitted gamma rays into account in the definition of E_m, it can be added as

$$E_m = \omega - \sum T_p - \sum E_\gamma. \tag{14.4}$$

14.3.2 Results

For this study, 1×10^5 ν_μ events on ^{12}C at $E_\nu = 235.5$ MeV were produced using NEUT. The CCQE models used are the ED-RMF RDWIA model based on Ref. [140], the SF model based on Ref. [51] and the updated SF model based on Ref. [201] (denoted SF*). There are also different potentials available for the RDWIA models in NEUT, however, as shown in Section 10.4, they are all modelled with the same parameterised E_m profile.

The effect of nuclear deexcitation generation using NucDeEx [205, 206, 207] is also investigated, and in those cases, Equation 14.4 is used. The only selection cut applied to the NEUT samples is that it satisfies the CC0π criteria: a final-state muon and at least one final-state nucleon, but no final-state pions. The SF and SF* samples are produced with a M_A^{QE} of 1.21 GeV/c while the ED-RMF has a value of ≈ 1 GeV.

ED-RMF missing energy modelling

Figure 14.17 shows the E_m profiles of the SF, SF* and ED-RMF models inside NEUT. The SF and SF* models have a similar height in the first $1p_{3/2}$ nuclear shell but have quite different $1s_{1/2}$ shell modelling at higher E_m. This contrasts with the ED-RMF model which has significantly larger occupancies in the first $1p_{3/2}$ shell and then very low strength between that and the $1s_{1/2}$ shell.

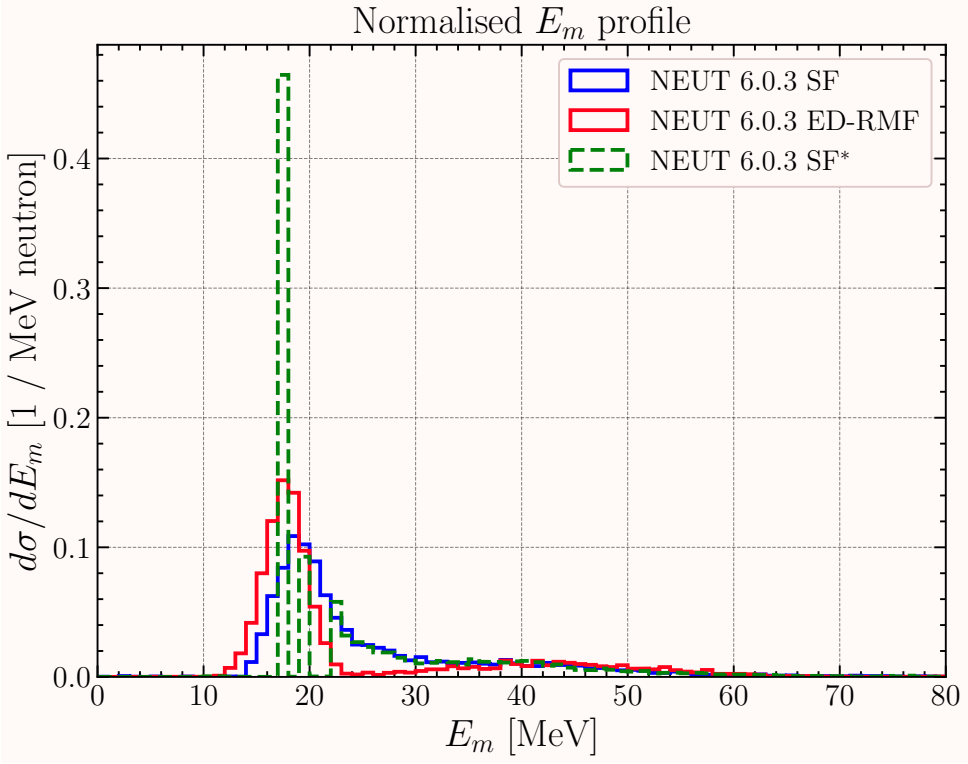

Figure 14.17: Missing energy (E_m) profiles of the SF (blue), SF* (green, dashed) and ED-RMF (red) models in NEUT 6.0.3. The SF* model incorporates nuclear deexcitation states at low E_m, leading to three pronounced peaks followed by a long tail; this is not present in the standard SF model.

Data comparison

Figure 14.18 shows the SF, SF* and ED-RMF models against the KDAR data [203]. The contribution from the NEUT cascade (denoted simply as "FSI") and nuclear deexcitation (denoted as "NucDeEx") are separated in a 2×2 grid. If the cascade or nuclear deexcitation contributions are not present, then "no FSI" or "no NucDeEx" is written. The χ^2 values are given in Table 14.14. The ED-RMF model has a significantly different shape to the data in all configurations, leading to a large χ^2 value. It is clear that the large occupancy in the $1p_{3/2}$ peak and dip before the broader $1s_{1/2}$ peak does not match the shape of the data. Without FSI or NucDeEx, it is surprising that the SF* also has a high χ^2 value (matching that of the ED-RMF model). This is likely due to the nuclear deexcitation peaks at low E_m as the bin width is large in comparison to the range at which these peaks are present. The SF model performs the best but the χ^2 value is still high. Introducing FSI but still without NucDeEx, all χ^2 values are improved; this will be an effect of the nucleon rescattering in the NEUT cascade, propagating events into the larger E_m region, bringing the MC samples closer to the data. Keeping only NucDeEx and not FSI, the E_m values will be lower since the energy of the emitted gamma rays are deducted, as shown in Equation 14.4. That being said, all χ^2 values are improved on the no FSI, no NucDeEx configuation. Once again, the SF model performs the best. Including both FSI and NucDeEx, The $1p_{3/2}$ peak of the ED-RMF model is now just in agreement with data. However, the bin before the peak is increased, leading to a larger χ^2 value. The SF* model reacts similarly. The SF model is again the best χ^2 value but this is not improved on the case where only one of FSI or NucDeEx is used.

Configuation	ED-RMF	SF	SF*
No FSI, no NucDeEx	178/16	98.8/16	178/16
FSI, no NucDeEx	120/16	53.2/16	94.2/16
no FSI, NucDeEx	109/16	54.3/16	99.8/16
FSI, NucDeEx	187/16	94.7/16	182/16

Table 14.14: χ^2 values for the ED-RMF, SF and SF* model.

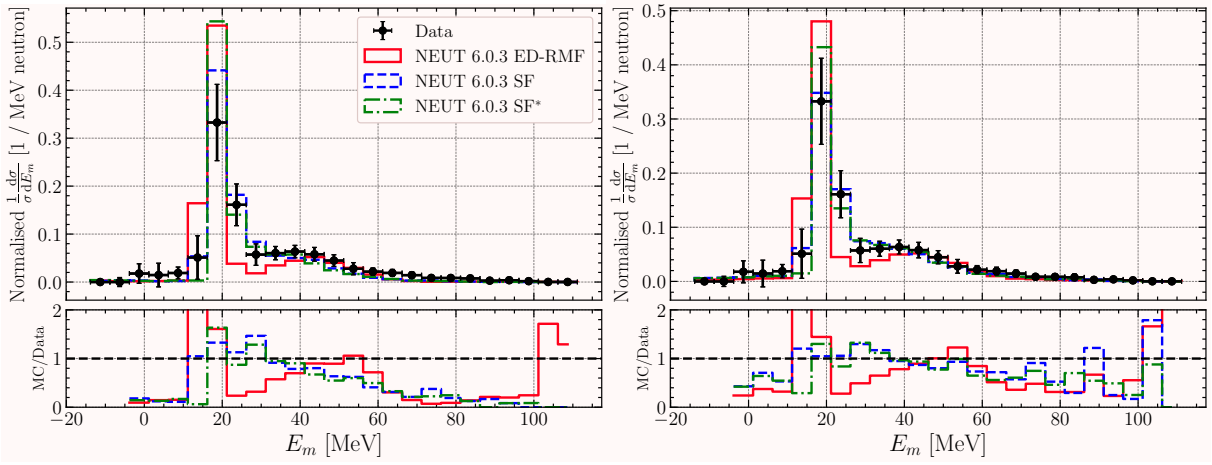

(a) Without FSI and without NucDeEx

(b) With FSI and without NucDeEx

(c) Without FSI but with NucDeEx

(d) With FSI and with NucDeEx

Figure 14.18: The normalised missing energy differential cross section for the ED-RMF, SF and SF* model in NEUT. With and without FSI and NucDeEx are shown separately to quantify the effect of each on the CCQE models. Data from [203].

Part IV

Investigating nuclear effects with the ND280 upgrade

Chapter 15

The SFGD and Nuclear Effects

Future long-baseline neutrino experiments, such as HK and DUNE, will bring neutrino oscillation studies into the high-statistics, high-precision era. Currently, the systematic errors due to nuclear mismodelling is the largest contributor to the overall systematic error for neutrino oscillation parameters [53]. Therefore, nuclear effects must be further understood before they become the limiting factor and inhibit the physics scope of the next generation experiments. The SFGD offers a unique insight into nuclear effects thanks to its modular and highly granular design. The SFGD offers a higher angular acceptance and lower proton tracking momentum threshold down to 250-300 MeV [71]. This, compared to the current T2K FGD detectors which have a proton tracking momentum threshold of around 500 MeV, a lot more phase space is accessible. This region of phase space is particularly important for nuclear effects that effect low-momentum interactions, such as Pauli blocking and the effects of RPWIA vs RDWIA.

Figure 15.1 shows the angular acceptance of ND280 and the SFGD. The ND280 FGD detectors are constructed such that particles travelling perpendicular to the beam direction are not reconstructed as well; this is seen in the Figure where the FGD1 and FGD2 have a drop in reconstruction efficiency at $\cos(\theta_\mu) = 0$. The SFGD, however, has uniformly increasing efficiency and, at the same point, has a 50% reconstruction efficiency. Figure 15.2 shows the full ND280 upgrade performance compared with the original ND280. The increase in angular acceptance is now very clear with $> 70\%$ across all $\cos(\theta)$. The tracking proton momentum is significantly improved at lower values of proton momentum.

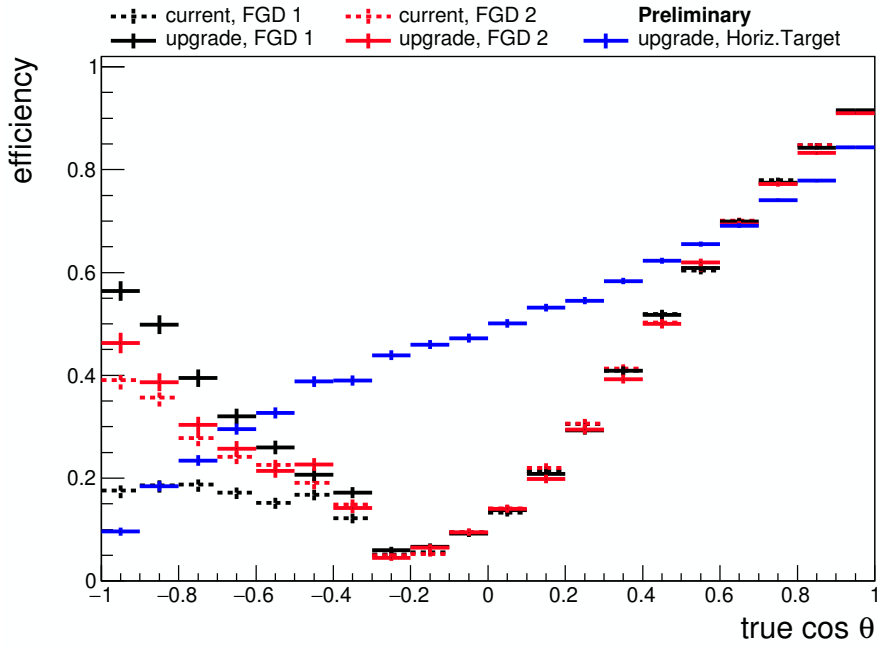

Figure 15.1: The angular efficiency for the ND280 FGDs and the SFGD as a function of the cosine of the muon scattering angle (from the beamline). The SFGD has a much wider angular acceptance thanks to its isotropic 3D readout design. Figure from Ref. [71].

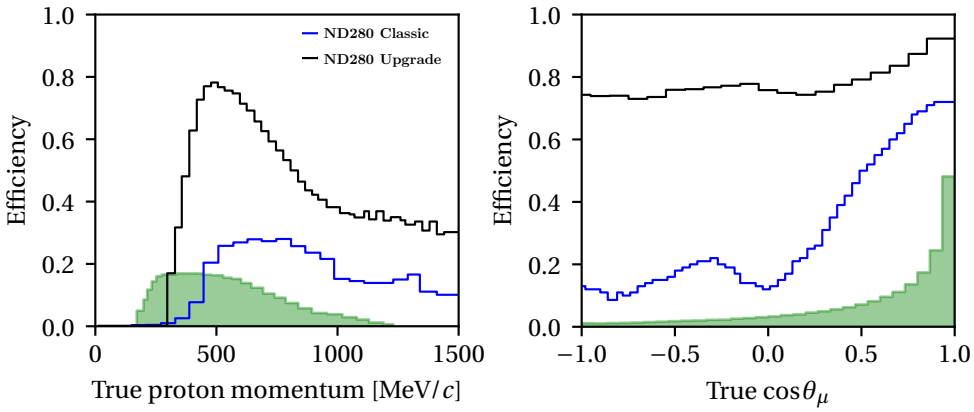

Figure 15.2: The angular acceptance and tracking proton momentum for the original ND280 and the ND280 upgrade. The upgrade has a much wider angular acceptance thanks to the 3D readout of the SFGD and positioning of the HA-TPCs. The upgrade also has a reduced proton tracking momentum threshold thanks to the granularity of the SFGD. The true distribution from NEUT is given by the green shaded region. Figure from Ref. [208].

15.1 Investigating the effects of Pauli blocking with the SFGD

Pauli blocking is more significant in interactions with lower momentum transfer. The region of phase space where it becomes significant is visible in Figure 15.3 which shows the differential cross section as a function of the momentum of the scattered nucleon. The ED-RMF model has some level of orthogonality between the initial and final states, resulting in Pauli blocking of states with too low momentum. However, the rEDAIC model does not. Since both potentials are real, the region where Pauli blocking becomes important is seen by the shift of the peak of the ED-RMF region in comparison to the rEDAIC. This region coincides well with the proton tracking momentum threshold of the ND280 upgrade. To further illustrate this, Figure 15.4 shows the same differential cross section but compares the ED-RMF, SF and N1p1h CCQE models in NEUT. The SFGD and FGD tracking proton momentum thresholds are shown by a black and grey arrow respectively. In NEUT, the SF model has a very simple implementation of Pauli blocking; it is a hard cut at a configurable scattered nucleon momentum (the default value in NEUT is 209 MeV). The N1p1h model, as described in Ref. [190], has an LFG-based implementation of Pauli blocking. Therefore, a differential cross section measurement as a function of momentum of the scattered nucleon with the SFGD should provide more insights into the application of Pauli blocking in different CCQE models.

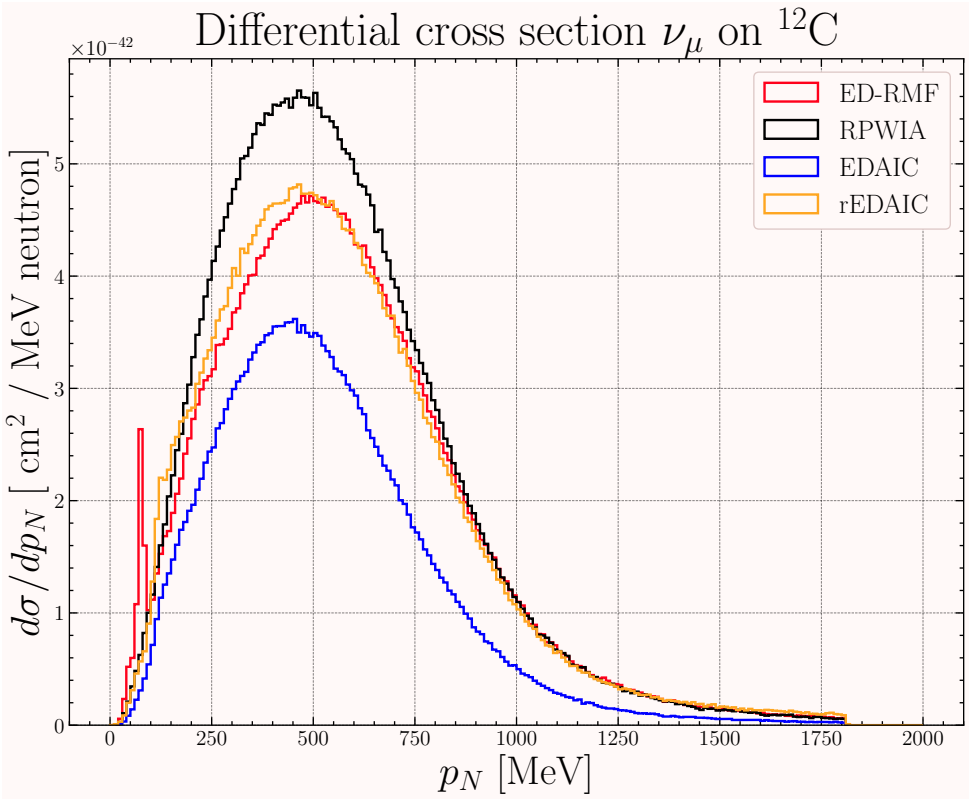

Figure 15.3: The differential cross section as a function scattered proton momentum for different RDWIA models.

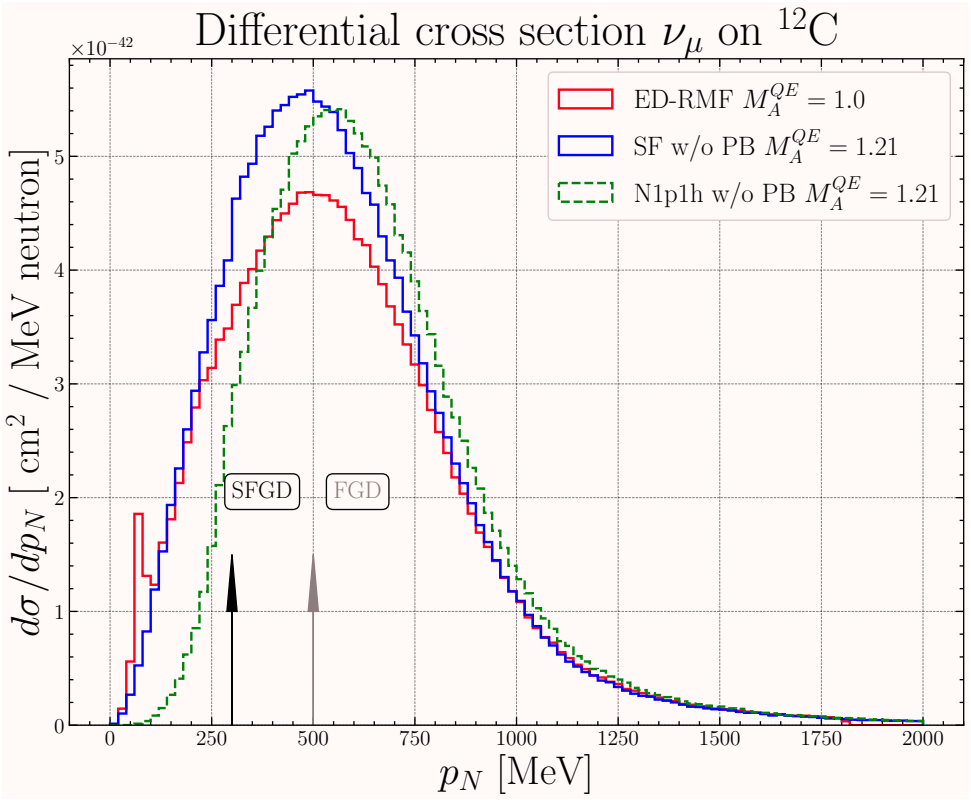

Figure 15.4: The differential cross section as a function scattered proton momentum for the energy-dependent relativistic mean field (ED-RMF), spectral function (SF) and Nieves *et. al.* (N1p1h) NEUT CCQE models.

15.2 Investigation of nuclear effects using TKI variables with the SFGD

As stated in Section 13.1, TKI variables are a sensitive probe when investigating nuclear effects. This is seen clearly when looking at their use in SFGD analyses and it shows clear model-discrimination potential. Figure 15.5 shows the δp_T TKI variable for an RFG, LFG and SF nuclear model. The bulk (peak region) of the distribution shows a clear difference between the nuclear models. Furthermore, "no FSI" samples show a clear discrimination between samples that use the cascade and samples that do not. This highlights the potential to benchmark the cascade that is used in T2K analyses. The tail region of the distribution show a clear separation between "no FSI" and "no 2p2h" interactions.

Figure 15.6 shows the differential cross section for the $\delta\alpha_T$ TKI variable for the same nuclear models. In this case, the nuclear models show similar shape distributions and only differ slightly by normalisation. In the "no FSI" case for the LFG, the shape is clearly different, as expected, as the distribution of $\delta\alpha_T$ in the absence of FSI is expected

to be isotropic. However, as shown in Ref. [71], $\delta\alpha_T$ can be used to further discriminate between nuclear models in the δp_T distribution by splitting it into three regions:

- $0 < \delta\alpha_T < \pi/3$: Low FSI region.
- $\pi/3 < \delta\alpha_T < 2\pi/3$: Intermediate FSI region.
- $2\pi/3 < \delta\alpha_T < \pi$: High FSI region.

Figure 15.7 shows the δp_T differential cross section for the LFG model (with and without FSI) split into the low and high $\delta\alpha_T$ regions. The low $\delta\alpha_T$ FSI region shows little difference between the FSI and no FSI cases. However, it is clear that the bulk of the distribution is populated by CCQE events with a slight tail being produced by 2p2h events. In the high $\delta\alpha_T$ FSI region, there is a clear difference in the FSI and no FSI case. The tail is now more populated by CCQE events that experience FSI. Therefore, the difference between the low and high $\delta\alpha_T$ FSI regions highlights a method of selecting a purer sample of CCQE events.

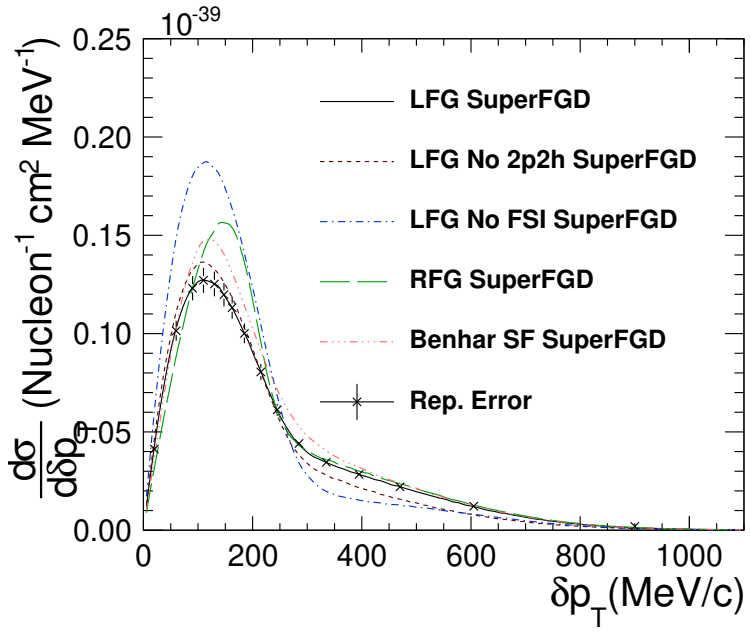

Figure 15.5: The δp_T TKI differential cross section for ν_μ interactions on hydrocarbon in a SFGD simulation. The RFG, LFG and SF nuclear models are used to highlight a clear difference between the nuclear models in the peak of the distribution. The tail of the distribution, however, separates interactions without FSI and 2p2h contributions. Figure from Ref. [71].

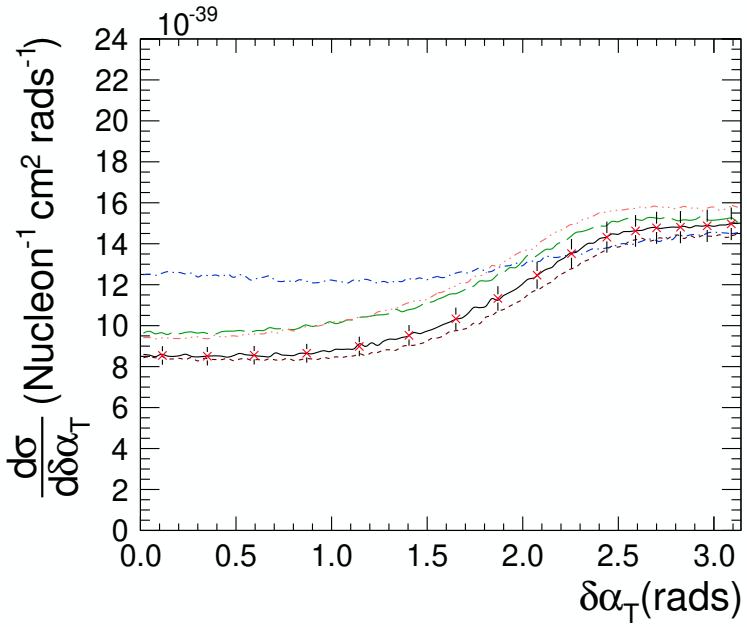

Figure 15.6: The $\delta\alpha_T$ TKI differential cross section for ν_μ interactions on hydrocarbon in a SFGD simulation. The nuclear models have similar shapes. Figure from Ref. [71]

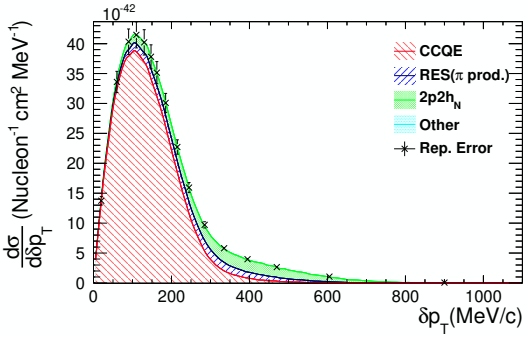

(a) LFG with FSI in low $\delta\alpha_T$ FSI region

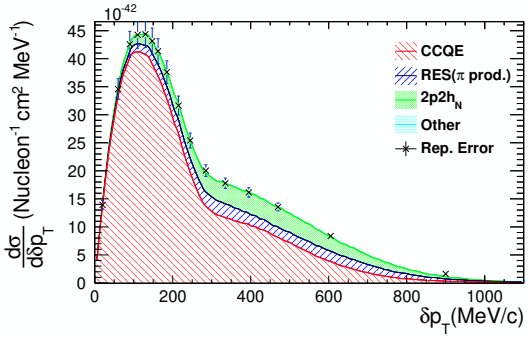

(b) LFG with FSI in high $\delta\alpha_T$ FSI region

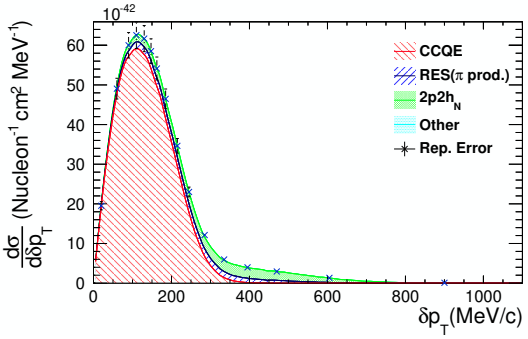

(c) LFG without FSI in low $\delta\alpha_T$ FSI region

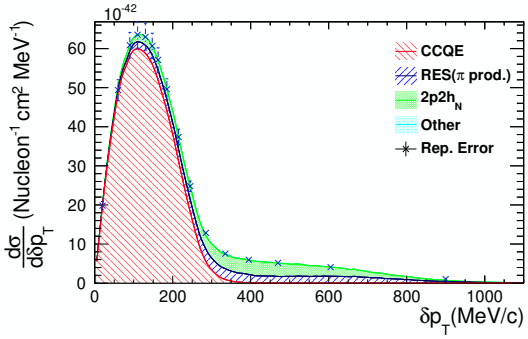

(d) LFG without FSI in high $\delta\alpha_T$ FSI region

Figure 15.7: Differential cross section of ν_μ events on hydrocarbon for the δp_T TKI variable with the LFG nuclear model. The differential cross section is split into the low and high FSI region defined by a $\delta\alpha_T$ slice. The upper row shows the full LFG model with FSI while the lower row shows without FSI. Figure taken from Ref. [71].

15.3 Investigating the ED-RMF model using the SFGD

For the ED-RMF model to be used more widely in T2K analyses, it is important to investigate what to expect when using the model compared to previously used models such as the N1p1h and the SF model. In this section, 1×10^5 ν_μ CCQE events on ^{12}C were simulated using NEUT. The SF model and the N1p1h model both have the NEUT Pauli blocking turned on and are generated using an M_A^{QE} of 1.21 GeV. The ED-RMF samples do not use the NEUT Pauli blocking. A sample of the ED-RMF model is also generated with SRC contributions for events with $E_m > 80$ MeV. The NEUT cascade is turned off for all samples to get an initial benchmark for how the base models compare. The samples were then converted into a format that is accepted by the T2K ND280 detector simulation [109]. The ND280 detector simulation applies electronics simulation, detector simulation using GEANT4 and reconstruction algorithms on the produced NEUT samples. The events were placed in the center of the SFGD to start the simulation. The CC0π selection criteria in the Highland2 software [109] was then used to apply the CC0π selection that is used for ND280 upgrade samples. Although this analysis may not be the

final CC0π analysis that is used for future ND280 upgrade samples, the results allow us to gain an idea of what SFGD would see for the different CCQE models.

15.3.1 Kinematic distributions

The main difference between the N1p1h, SF and ED-RMF models is the treatment of the final-state nucleon. Therefore, the event distributions of the true (raw NEUT event information) and reconstructed (reco) proton momenta are analysed. Figure 15.8 shows the event distributions for the true and reco information given a final-state muon and proton that are detected by the SFGD. If the final state contains multiple protons, the leading proton is used. Comparing the true and reco information, it is clear that the detector reconstruction introduces a slight redistribution of strengths across the bins; This is known as "detector smearing effects". The SF model has the tallest peak both in the true and the reco distributions; this is not such a surprise since this is also seen in Figure 15.4. However, the N1p1h model has an overall normalisation similar to the ED-RMF model that is not seen in the same Figure. The ED-RMF model does not show any particular region that has an excess or deficit of events compared to other models. Including SRC contributions in the ED-RMF model brings it closer to the SF model in shape, especially in reco information. There is likely a mismatch in the amount of SRC due to the SRC thresholds of the SF and ED-RMF model.

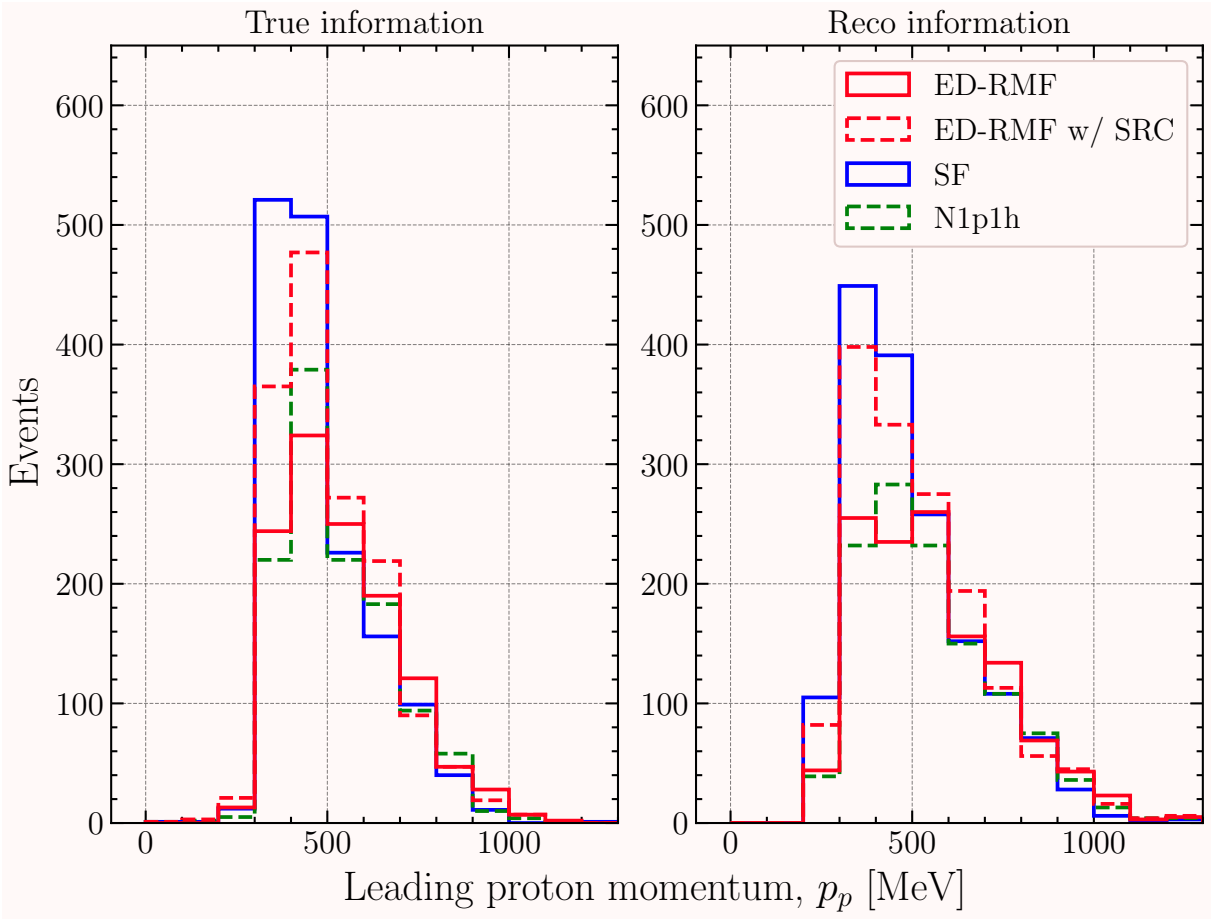

Figure 15.8: The event distribution for the leading proton momentum for the ED-RMF (red, solid), ED-RMF with SRC (red, dashed), SF (blue, solid) and N1p1h (green, dashed) NEUT CCQE models. In these samples a muon and a proton are both detected within the SFGD.

15.3.2 TKI variables

The difference in treatment of the final states should also be seen in the TKI variables. Figure 15.9 shows the event distribution for the δp_T variable. In both the true and reco distributions, the ED-RMF, SF and N1p1h models have distinct shapes. In the true information, the ED-RMF model has a tall peak and a small tail leading up to around 600 MeV. The SF model has a much broader tail extending to around 1000 MeV. The tail is not seen in the N1p1h model. Crossing to the reco information, all peaks are reduced, and the tails are smeared considerably. The SF model has a broader tail distribution meaning more events are seen at higher δp_T. This is matched very closely by the ED-RMF model with SRC.

Figure 15.10 shows the event distribution for the $\delta\alpha_T$ variable. Since the cascade is not

applied for these MC samples, the $\delta\alpha_T$ distribution should be roughly flat. This is seen in the N1p1h and ED-RMF case. This shows that, despite the ED-RMF model having additional elastic FSI that causes a rise in $\delta\alpha_T$ that is seen in Figure 13.5, once smeared by detector and reconstruction effects, this is not visible. The SF model, however, has a steep rise towards high $\delta\alpha_T$. This is also seen in the ED-RMF model with SRC contributions and so the rise at high $\delta\alpha_T$ can be attributed to the SRC contribution breaking the isotropy of the variable.

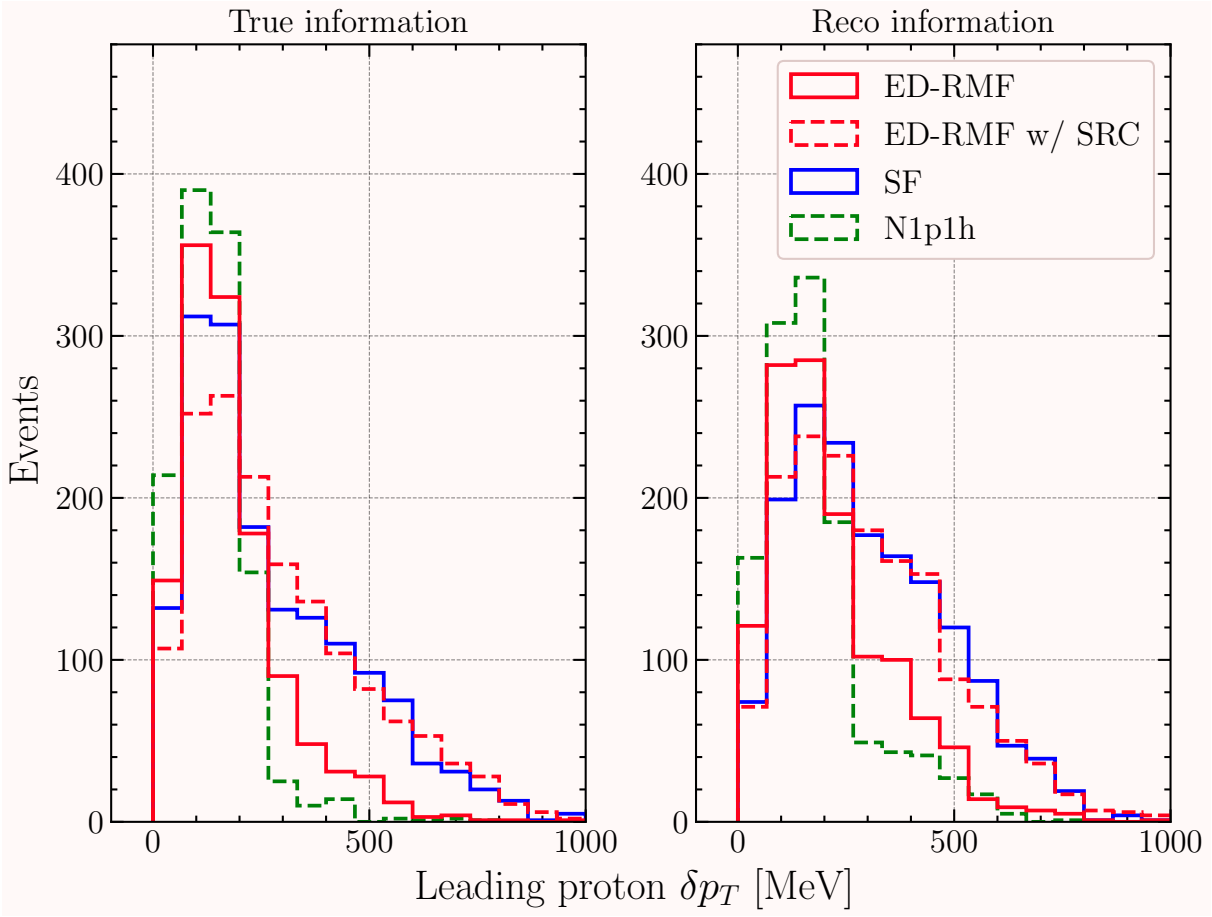

Figure 15.9: The event distribution for δp_T for the leading proton for the ED-RMF (red, solid), ED-RMF with SRC (red, dashed), SF (blue, solid) and N1p1h (green, dashed) NEUT CCQE models. In these samples a muon and a proton are both detected within the SFGD.

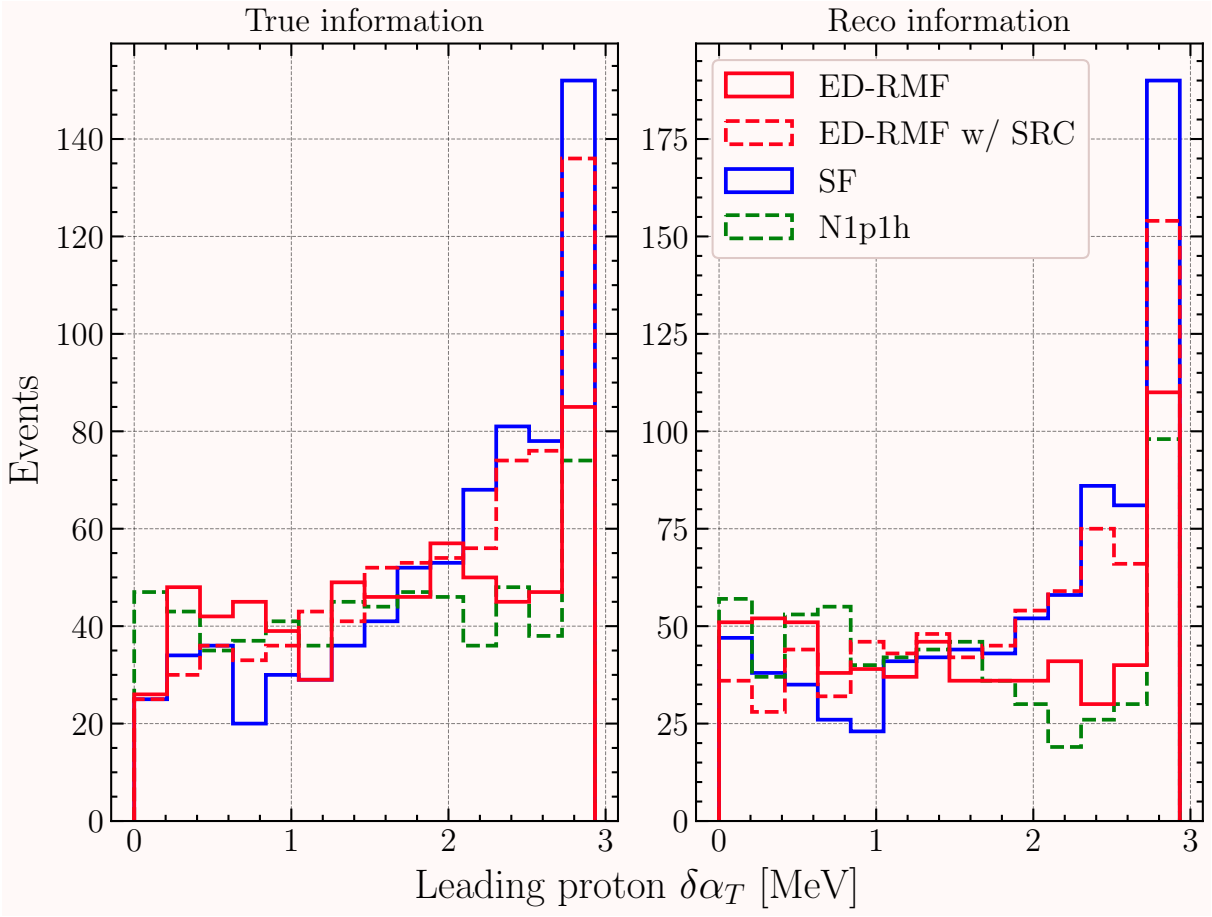

Figure 15.10: The event distribution for $\delta\alpha_T$ for the leading proton for the ED-RMF (red, solid), ED-RMF with SRC (red, dashed), SF (blue, solid) and N1p1h (green, dashed) NEUT CCQE models. In these samples a muon and a proton are both detected within the SFGD.

Chapter 16

Conclusions and future prospects

The T2K experiment is a long-baseline neutrino oscillation experiment based at J-PARC in Japan. It produces a beam of muon (anti)neutrinos at J-PARC that is then sent at a 2.5° off-axis angle to ND280 and SK. Nuclear mismodelling in the T2K analyses is one of the largest contributions to the overall systematic uncertainty. As next-generation experiments such as the T2K upgrade, HK and DUNE begin to take data and enter the precision era, these nuclear mismodelling uncertainties will become the limiting factor in the overall physics scope of these experiments.

The work presented in this thesis introduces a new highly granular detector, the SFGD, that is now in operation and taking data in T2K, and a new microscopic CCQE interaction model to use in the NEUT neutrino event generator. The SFGD will increase neutrino interaction statistics, reduce the proton tracking momentum threshold, improve momentum, spatial and timing resolution, and provide an insight into nuclear effects. The work in this thesis presented the construction, commissioning, and characterisation of the SFGD. In addition, the work done to ensure the correct calibration of SFGD data is shown. This culminated in many pieces of software being written that is now being utilised by T2K to run, monitor, and calibrate the SFGD.

The CCQE model presented in this work is significantly different to other CCQE models in current neutrino event generators. It is the first time a distorted wave impulse approximation model has been implemented into a neutrino event generator. There were significant challenges initially; however, it has been improved and shaped into a polished model that is ready for T2K analyses. In addition to the model, implementation and validation details that are shown, the model is also benchmarked against CC0π neutrino cross-section data from the T2K, MINERvA and MicroBooNE experiments. It showed an improved agreement with data for final-state nucleon kinematic variables. In addition to this, the model often sits below the data in the CCQE-dominated region, leaving room for future endeavors to include MEC contribution.

Comparison to inclusive electron scattering data highlighted the necessity of the distorted

wave and showed that the SF model is unsuitable at low incident electron energies and low energy transfers. The comparison to the Kaon decay-at-rest dataset, however, showed the difference in initial-state missing energy modelling between the RMF-based models and the SF model. This highlights potential improvements that can be made to the RMF-based model.

The potential use of the SFGD to investigate nuclear effects is then shown. The samples produced using different NEUT CCQE models were processed with the ND280 detector simulation and event reconstruction software before being processed by the CC0π selection algorithms that are built for the SFGD. This clearly showed the different outputs for the different CCQE models.

Looking forward, the RMF-based CCQE models are being finalised in order to be used in T2K official Monte Carlo productions. This will be the first step in T2K using a new CCQE model in official neutrino oscillation analyses. The nuclear mismodelling systematic uncertainty will be re-evaluated given the inclusion of this new model. It is likely that, in order to cover the various model predictions, the systematic uncertainty will be initially inflated. The RMF-based models themselves will also undergo changes in the near future. A change in the design of the hadronic tensor tables will mean that the value of M_A^{QE} can be changed; this will be invaluable for systematic uncertainty studies within T2K. In addition to this, the inclusion of MEC into the model will bring it one step closer to being complete. The use of hadronic tensor tables, however, is still a rigid approach that offers less freedoms when it comes to developing systematic uncertainties based on the theoretical parameters of the model. An approach using a tabulated final-state spinor would allow the parameters in the RMF initial-state model to be changed, leading to more theoretically robust systematic uncertainties. Future T2K analyses will benefit from these model improvements.

However, there are parameters in the model that can be altered. These parameters come from the missing energy density parameterisation. Namely, the Gaussian centres, widths and the occupancies of the shells. Although changing these parameters can alter the model's agreement with inclusive electron scattering data, it provides T2K with the ability to model many different missing energy densities and nuclear models. This work is already being done within the T2K nuclear interactions working group.

A further future goal is to include the pion production interaction in the same nuclear framework. While this introduces new challenges, especially the curse of dimensionality, a simple, tabulated approach could show the benefits of having pion elastic FSI and a CCQE model that is consistent with the pion production model.

Bibliography

[1] J. Chadwick. The intensity distribution in the magnetic spectrum of β particles from radium (B + C). In: *Verh. Phys. Gesell.* 16 (1914), pp. 383–391.

[2] W. Pauli. Dear radioactive ladies and gentlemen. In: *Phys. Today* 31N9 (1978), p. 27.

[3] J. Chadwick. Possible Existence of a Neutron. In: *Nature* 129 (1932), p. 312. DOI: 10.1038/129312a0.

[4] E. Fermi. An attempt of a theory of beta radiation. 1. In: *Z. Phys.* 88 (1934), pp. 161–177. DOI: 10.1007/BF01351864.

[5] C. L. Cowan et al. Detection of the Free Neutrino: a Confirmation. In: *Science* 124.3212 (1956), pp. 103–104. DOI: 10.1126/science.124.3212.103. eprint: https://www.science.org/doi/pdf/10.1126/science.124.3212.103. URL: https://www.science.org/doi/abs/10.1126/science.124.3212.103.

[6] Raymond Davis Jr. Attempt to detect the antineutrinos from a nuclear reactor by the Cl37(anti-nu,e-) A37 reaction. In: *Phys. Rev.* 97 (1955), pp. 766–769. DOI: 10.1103/PhysRev.97.766.

[7] G. Danby et al. Observation of High-Energy Neutrino Reactions and the Existence of Two Kinds of Neutrinos. In: *Phys. Rev. Lett.* 9 (1 1962), pp. 36–44. DOI: 10.1103/PhysRevLett.9.36. URL: https://link.aps.org/doi/10.1103/PhysRevLett.9.36.

[8] M. L. Perl et al. Evidence for Anomalous Lepton Production in $e^+ - e^-$ Annihilation. In: *Phys. Rev. Lett.* 35 (22 1975), pp. 1489–1492. DOI: 10.1103/PhysRevLett.35.1489. URL: https://link.aps.org/doi/10.1103/PhysRevLett.35.1489.

[9] S. Navas et al. Review of Particle Physics. In: *Phys. Rev. D* 110 (3 2024), p. 030001. DOI: 10.1103/PhysRevD.110.030001. URL: https://link.aps.org/doi/10.1103/PhysRevD.110.030001.

[10] K. Kodama et al. Observation of tau neutrino interactions. In: *Physics Letters B* 504.3 (Apr. 2001), 218–224. ISSN: 0370-2693. DOI: 10.1016/s0370-2693(01)00307-0. URL: http://dx.doi.org/10.1016/S0370-2693(01)00307-0.

[11] C. S. Wu et al. Experimental Test of Parity Conservation in Beta Decay. In: *Phys. Rev.* 105 (4 1957), pp. 1413–1415. DOI: 10.1103/PhysRev.105.1413. URL: https://link.aps.org/doi/10.1103/PhysRev.105.1413.

[12] Schael. S et al. In: *Physics Reports* 427.5–6 (May 2006), 257–454. ISSN: 0370-1573. DOI: 10.1016/j.physrep.2005.12.006. URL: http://dx.doi.org/10.1016/j.physrep.2005.12.006.

[13] B. Pontecorvo. Mesonium and anti-mesonium. In: *Sov. Phys. JETP* 6 (1957), p. 429.

[14] B. Pontecorvo. Neutrino Experiments and the Problem of Conservation of Leptonic Charge. In: *Zh. Eksp. Teor. Fiz.* 53 (1967), pp. 1717–1725.

[15] Ziro Maki, Masami Nakagawa, and Shoichi Sakata. Remarks on the Unified Model of Elementary Particles. In: *Progress of Theoretical Physics* 28.5 (Nov. 1962), pp. 870–880. ISSN: 0033-068X. DOI: 10.1143/PTP.28.870. eprint: https://academic.oup.com/ptp/article-pdf/28/5/870/5258750/28-5-870.pdf. URL: https://doi.org/10.1143/PTP.28.870.

[16] Y. Fukuda et al. Evidence for Oscillation of Atmospheric Neutrinos. In: *Phys. Rev. Lett.* 81 (8 1998), pp. 1562–1567. DOI: 10.1103/PhysRevLett.81.1562. URL: https://link.aps.org/doi/10.1103/PhysRevLett.81.1562.

[17] S.M. Bilenky, C. Giunti, and W. Grimus. Phenomenology of neutrino oscillations. In: *Progress in Particle and Nuclear Physics* 43 (Jan. 1999), 1–86. ISSN: 0146-6410. DOI: 10.1016/s0146-6410(99)00092-7. URL: http://dx.doi.org/10.1016/S0146-6410(99)00092-7.

[18] C. Giganti, S. Lavignac, and M. Zito. Neutrino oscillations: The rise of the PMNS paradigm. In: *Progress in Particle and Nuclear Physics* 98 (Jan. 2018), 1–54. ISSN: 0146-6410. DOI: 10.1016/j.ppnp.2017.10.001. URL: http://dx.doi.org/10.1016/j.ppnp.2017.10.001.

[19] Luis Salvador Miranda et al. *Searching for non-unitary neutrino oscillations in the present T2K and NOνA data*. 2021. arXiv: 1911.09398 [hep-ph]. URL: https://arxiv.org/abs/1911.09398.

[20] L. Wolfenstein. Neutrino oscillations in matter. In: *Phys. Rev. D* 17 (9 1978), pp. 2369–2374. DOI: 10.1103/PhysRevD.17.2369. URL: https://link.aps.org/doi/10.1103/PhysRevD.17.2369.

[21] S. P. Mikheyev and A. Yu. Smirnov. Resonance Amplification of Oscillations in Matter and Spectroscopy of Solar Neutrinos. In: *Sov. J. Nucl. Phys.* 42 (1985), pp. 913–917.

[22] J. N. Bahcall et al. Solar Neutrino Flux. In: 137 (Jan. 1963), pp. 344–346. DOI: 10.1086/147513.

[23] Raymond Davis, Don S. Harmer, and Kenneth C. Hoffman. Search for Neutrinos from the Sun. In: *Phys. Rev. Lett.* 20 (21 1968), pp. 1205–1209. DOI: 10.1103/PhysRevLett.20.1205. URL: https://link.aps.org/doi/10.1103/PhysRevLett.20.1205.

[24] B. Pontecorvo. Inverse beta process. In: *Camb. Monogr. Part. Phys. Nucl. Phys. Cosmol.* 1 (1991), pp. 25–31.

[25] K. S. Hirata et al. Observation of ^{8}B solar neutrinos in the Kamiokande-II detector. In: *Phys. Rev. Lett.* 63 (1 1989), pp. 16–19. DOI: 10.1103/PhysRevLett.63.16. URL: https://link.aps.org/doi/10.1103/PhysRevLett.63.16.

[26] J.N. Abdurashitov et al. Results from SAGE (The Russian-American gallium solar neutrino experiment). In: *Physics Letters B* 328.1 (1994), pp. 234–248. ISSN: 0370-2693. DOI: https://doi.org/10.1016/0370-2693(94)90454-5. URL: https://www.sciencedirect.com/science/article/pii/0370269394904545.

[27] M. Cribier. Results of the whole GALLEX experiment. In: *Nucl. Phys. B Proc. Suppl.* 70 (1999). Ed. by A. Bottino, Alessandra Di Credico, and Piero Monacelli, pp. 284–291. DOI: 10.1016/S0920-5632(98)00438-1.

[28] A. Bellerive et al. The Sudbury Neutrino Observatory. In: *Nuclear Physics B* 908 (July 2016), 30–51. ISSN: 0550-3213. DOI: 10.1016/j.nuclphysb.2016.04.035. URL: http://dx.doi.org/10.1016/j.nuclphysb.2016.04.035.

[29] M. P. Decowski. KamLAND's precision neutrino oscillation measurements. In: *Nucl. Phys. B* 908 (2016), pp. 52–61. DOI: 10.1016/j.nuclphysb.2016.04.014.

[30] K. S. Hirata et al. Observation of a small atmospheric muon-neutrino / electron-neutrino ratio in Kamiokande. In: *Phys. Lett. B* 280 (1992), pp. 146–152. DOI: 10.1016/0370-2693(92)90788-6.

[31] C. Simpson et al. Sensitivity of Super-Kamiokande with Gadolinium to Low Energy Antineutrinos from Pre-supernova Emission. In: *The Astrophysical Journal* 885.2 (Nov. 2019), p. 133. ISSN: 1538-4357. DOI: 10.3847/1538-4357/ab4883. URL: http://dx.doi.org/10.3847/1538-4357/ab4883.

[32] K. Abe et al. The T2K Experiment. In: *Nucl. Instrum. Meth. A* 659 (2011), pp. 106–135. DOI: 10.1016/j.nima.2011.06.067. arXiv: 1106.1238 [physics.ins-det].

[33] A. Habig. The NOvA Experiment. In: *Nucl. Phys. B Proc. Suppl.* 229-232 (2012). Ed. by George S. Tzanakos, pp. 460–460. DOI: 10.1016/j.nuclphysbps.2012.09.097.

[34] T. Wester et al. Atmospheric neutrino oscillation analysis with neutron tagging and an expanded fiducial volume in Super-Kamiokande I–V. In: *Phys. Rev. D* 109 (7 2024), p. 072014. DOI: 10.1103/PhysRevD.109.072014. URL: https://link.aps.org/doi/10.1103/PhysRevD.109.072014.

[35] P. Adamson et al. Precision Constraints for Three-Flavor Neutrino Oscillations from the Full MINOS+ and MINOS Dataset. In: *Phys. Rev. Lett.* 125 (13 2020), p. 131802. DOI: 10.1103/PhysRevLett.125.131802. URL: https://link.aps.org/doi/10.1103/PhysRevLett.125.131802.

[36] M. A. Acero et al. Improved measurement of neutrino oscillation parameters by the NOvA experiment. In: *Phys. Rev. D* 106 (3 2022), p. 032004. DOI: 10.1103/PhysRevD.106.032004. URL: https://link.aps.org/doi/10.1103/PhysRevD.106.032004.

[37] K. Abe et al. Measurements of neutrino oscillation parameters from the T2K experiment using

$$3.6 \times 10^{21}$$

protons on target. In: *The European Physical Journal C* 83.9 (Sept. 2023). ISSN: 1434-6052. DOI: 10.1140/epjc/s10052-023-11819-x. URL: http://dx.doi.org/10.1140/epjc/s10052-023-11819-x.

[38] R. Abbasi et al. Measurement of atmospheric neutrino mixing with improved IceCube DeepCore calibration and data processing. In: *Phys. Rev. D* 108 (1 2023), p. 012014. DOI: 10.1103/PhysRevD.108.012014. URL: https://link.aps.org/doi/10.1103/PhysRevD.108.012014.

[39] K. Abe et al. Improved constraints on neutrino mixing from the T2K experiment with 3.13×10^{21} protons on target. In: *Phys. Rev. D* 103 (11 2021), p. 112008. DOI: 10.1103/PhysRevD.103.112008. URL: https://link.aps.org/doi/10.1103/PhysRevD.103.112008.

[40] K. Abe et al. Updated T2K measurements of muon neutrino and antineutrino disappearance using 3.6×10^{21} protons on target. In: *Phys. Rev. D* 108.7 (2023), p. 072011. DOI: 10.1103/PhysRevD.108.072011. arXiv: 2305.09916 [hep-ex].

[41] T. Wester et al. Atmospheric neutrino oscillation analysis with neutron tagging and an expanded fiducial volume in Super-Kamiokande I–V. In: *Physical Review D* 109.7 (Apr. 2024). ISSN: 2470-0029. DOI: 10.1103/physrevd.109.072014. URL: http://dx.doi.org/10.1103/PhysRevD.109.072014.

[42] K. Abe et al. First Joint Oscillation Analysis of Super-Kamiokande Atmospheric and T2K Accelerator Neutrino Data. In: *Phys. Rev. Lett.* 134 (1 2025), p. 011801. DOI: 10.1103/PhysRevLett.134.011801. URL: https://link.aps.org/doi/10.1103/PhysRevLett.134.011801.

[43] Tomas Nosek. T2K+NOvA Joint Measurement of Neutrino Oscillation Parameters. In: *PoS* ICHEP2024 (2025), p. 153. DOI: 10.22323/1.476.0153.

[44] K. Abe et al. Sensitivity of the Hyper-Kamiokande experiment to neutrino oscillation parameters using acceleration neutrinos. In: (May 2025). arXiv: 2505.15019 [hep-ex].

[45] Maury Goodman. The Deep Underground Neutrino Experiment. In: *Adv. High Energy Phys.* 2015 (2015), p. 256351. DOI: 10.1155/2015/256351.

[46] Matthias Raphael Stock. *Status and Prospects of the JUNO Experiment*. 2024. arXiv: 2405.07321 [physics.ins-det]. URL: https://arxiv.org/abs/2405.07321.

[47] Ivan Esteban et al. NuFit-6.0: updated global analysis of three-flavor neutrino oscillations. In: *Journal of High Energy Physics* 2024.12 (Dec. 2024). ISSN: 1029-8479. DOI: 10.1007/jhep12(2024)216. URL: http://dx.doi.org/10.1007/JHEP12(2024)216.

[48] E. D. Bloom and F. J. Gilman. Scaling and the Behavior of Nucleon Resonances in Inelastic Electron-Nucleon Scattering. In: *Phys. Rev. D* 4 (9 1971), pp. 2901–2916. DOI: 10.1103/PhysRevD.4.2901. URL: https://link.aps.org/doi/10.1103/PhysRevD.4.2901.

[49] A. Bodek and U.K. Yang. Modeling deep inelastic cross sections in the few GeV region. In: *Nuclear Physics B - Proceedings Supplements* 112.1–3 (Nov. 2002), 70–76. ISSN: 0920-5632. DOI: 10.1016/s0920-5632(02)01755-3. URL: http://dx.doi.org/10.1016/S0920-5632(02)01755-3.

[50] M. Khachatryan et al. Electron-beam energy reconstruction for neutrino oscillation measurements. In: *Nature* 599.7886 (2021), pp. 565–570. DOI: 10.1038/s41586-021-04046-5.

[51] Artur M. Ankowski, Omar Benhar, and Makoto Sakuda. Improving the accuracy of neutrino energy reconstruction in charged-current quasielastic scattering off nuclear targets. In: *Phys. Rev. D* 91 (3 2015), p. 033005. DOI: 10.1103/PhysRevD.91.033005. URL: https://link.aps.org/doi/10.1103/PhysRevD.91.033005.

[52] R. Acciarri et al. Design and Construction of the MicroBooNE Detector. In: *JINST* 12.02 (2017), P02017. DOI: 10.1088/1748-0221/12/02/P02017. arXiv: 1612.05824 [physics.ins-det].

[53] K. Abe et al. Measurements of neutrino oscillation parameters from the T2K experiment using 3.6×10^{21} protons on target. In: *The European Physical Journal C* 83.9 (Sept. 2023). ISSN: 1434-6052. DOI: 10.1140/epjc/s10052-023-11819-x. URL: http://dx.doi.org/10.1140/epjc/s10052-023-11819-x.

[54] L. Aliaga et al. Design, calibration, and performance of the MINERvA detector. In: *Nuclear Instruments and Methods in Physics Research Section A: Accelerators, Spectrometers, Detectors and Associated Equipment* 743 (Apr. 2014), 130–159. ISSN: 0168-9002. DOI: 10.1016/j.nima.2013.12.053. URL: http://dx.doi.org/10.1016/j.nima.2013.12.053.

[55] K. Abe et al. Indication of Electron Neutrino Appearance from an Accelerator-Produced Off-Axis Muon Neutrino Beam. In: *Phys. Rev. Lett.* 107 (4 2011), p. 041801. DOI: 10.1103/PhysRevLett.107.041801. URL: https://link.aps.org/doi/10.1103/PhysRevLett.107.041801.

[56] K. Abe et al. Constraint on the matter–antimatter symmetry-violating phase in neutrino oscillations. In: *Nature* 580.7803 (2020), 339–344. ISSN: 1476-4687. DOI: 10.1038/s41586-020-2177-0. URL: http://dx.doi.org/10.1038/s41586-020-2177-0.

[57] K. Abe et al. J-PARC Neutrino Beamline Upgrade Technical Design Report. In: (Aug. 2019). arXiv: 1908.05141 [physics.ins-det].

[58] K. Abe et al. Measurement of the intrinsic electron neutrino component in the T2K neutrino beam with the ND280 detector. In: *Physical Review D* 89.9 (May 2014). ISSN: 1550-2368. DOI: 10.1103/physrevd.89.092003. URL: http://dx.doi.org/10.1103/PhysRevD.89.092003.

[59] Tatsuya Kikawa. "Measurement of Neutrino Interactions and Three Flavor Neutrino Oscillations in the T2K Experiment". In: 2015.

[60] Japan Atomic Energy Agency (JAEA) J-PARC Center High Energy Accelerator Research Organization (KEK). Significant Increase in Beam Power and Electric Power Efficiency of the J-PARC Main Ring Accelerator - A Powerful Driving Force for Neutrino Research -. 2024. URL: https://j-parc.jp/c/en/press-release/2024/01/17001276.html (visited on 02/03/2025).

[61] Kunio Koseki. Development of the 320kA pulsed magnetic horn power supply with a novel energy recovery system for the T2K experiment. In: *Nuclear Instruments and Methods in Physics Research Section A: Accelerators, Spectrometers, Detectors and Associated Equipment* 735 (2014), pp. 633–639. ISSN: 0168-9002. DOI: https://doi.org/10.1016/j.nima.2013.10.040. URL: https://www.sciencedirect.com/science/article/pii/S0168900213014216.

[62] K. Matsuoka et al. Design and performance of the muon monitor for the T2K neutrino oscillation experiment. In: *Nuclear Instruments and Methods in Physics Research Section A: Accelerators, Spectrometers, Detectors and Associated Equipment* 624.3 (Dec. 2010), 591–600. ISSN: 0168-9002. DOI: 10.1016/j.nima.2010.09.074. URL: http://dx.doi.org/10.1016/j.nima.2010.09.074.

[63] D Beavis et al. *Long baseline neutrino oscillation experiment at the AGS. Physics design report*. Tech. rep. Brookhaven National Lab. (BNL), Upton, NY (United States), Apr. 1995. DOI: 10.2172/52878. URL: https://www.osti.gov/biblio/52878.

[64] N. Abgrall et al. Pion emission from the T2K replica target: Method, results and application. In: *Nuclear Instruments and Methods in Physics Research Section A: Accelerators, Spectrometers, Detectors and Associated Equipment* 701 (2013), pp. 99–114. ISSN: 0168-9002. DOI: https://doi.org/10.1016/j.nima.2012.10.079. URL: https://www.sciencedirect.com/science/article/pii/S016890021201234X.

[65] K. Abe et al. T2K neutrino flux prediction. In: *Phys. Rev. D* 87 (1 2013), p. 012001. DOI: 10.1103/PhysRevD.87.012001. URL: https://link.aps.org/doi/10.1103/PhysRevD.87.012001.

[66] K. Abe et al. Measurements of the T2K neutrino beam properties using the INGRID on-axis near detector. In: *Nuclear Instruments and Methods in Physics Research Section A: Accelerators, Spectrometers, Detectors and Associated Equipment* 694 (2012), 211–223. ISSN: 0168-9002. DOI: 10.1016/j.nima.2012.03.023. URL: http://dx.doi.org/10.1016/j.nima.2012.03.023.

[67] Hamamatsu Photonics. MPPC® (SiPMs) / SPADs. URL: https://www.hamamatsu.com/eu/en/product/optical-sensors/mppc.html (visited on 02/07/2025).

[68] M. Yokoyama et al. Performance of multi-pixel photon counters for the T2K near detectors. In: *Nuclear Instruments and Methods in Physics Research Section A: Accelerators, Spectrometers, Detectors and Associated Equipment* 622.3 (Oct. 2010), 567–573. ISSN: 0168-9002. DOI: 10.1016/j.nima.2010.07.070. URL: http://dx.doi.org/10.1016/j.nima.2010.07.070.

[69] J-PARC neutrino review committee. Technical review report on the ND280. URL: https://j-parc.jp/researcher/Hadron/en/pac_0701/JNRC_report.pdf. (accessed 30/06/2022).

[70] A Blondel, M Yokoyama, and M Zito. *The T2K-ND280 upgrade proposal*. Tech. rep. This proposal is the follow-up of the Expression of Interest EOI-15 submitted to SPSC in January 2017. Geneva: CERN, 2018. URL: https://cds.cern.ch/record/2299599.

[71] K. Abe et al. *T2K ND280 Upgrade – Technical Design Report*. 2020. arXiv: 1901.03750 [physics.ins-det].

[72] S. Assylbekov et al. The T2K ND280 off-axis pi–zero detector. In: *Nuclear Instruments and Methods in Physics Research Section A: Accelerators, Spectrometers, Detectors and Associated Equipment* 686 (Sept. 2012), 48–63. ISSN: 0168-9002. DOI: 10.1016/j.nima.2012.05.028. URL: http://dx.doi.org/10.1016/j.nima.2012.05.028.

[73] D Allan et al. The electromagnetic calorimeter for the T2K near detector ND280. In: *Journal of Instrumentation* 8.10 (Oct. 2013), P10019–P10019. ISSN: 1748-0221. DOI: 10.1088/1748-0221/8/10/p10019. URL: http://dx.doi.org/10.1088/1748-0221/8/10/P10019.

[74] Particle Data Group. Atomic and nuclear properties of lead (Pb). URL: https://pdg.lbl.gov/2015/AtomicNuclearProperties/HTML/lead_Pb.html (visited on 02/07/2025).

[75] S. Aoki et al. The T2K Side Muon Range Detector (SMRD). In: *Nuclear Instruments and Methods in Physics Research Section A: Accelerators, Spectrometers, Detectors and Associated Equipment* 698 (Jan. 2013), 135–146. ISSN: 0168-9002. DOI: 10.1016/j.nima.2012.10.001. URL: http://dx.doi.org/10.1016/j.nima.2012.10.001.

[76] P. A. Amaudruz et al. The T2K Fine-Grained Detectors. In: *Nucl. Instrum. Meth. A* 696 (2012), pp. 1–31. DOI: 10.1016/j.nima.2012.08.020. arXiv: 1204.3666 [physics.ins-det].

[77] T2K ND280 TPC collaboration. *Time Projection Chambers for the T2K Near Detectors*. 2010. arXiv: 1012.0865 [physics.ins-det]. URL: https://arxiv.org/abs/1012.0865.

[78] T Ovsiannikova et al. The new experiment WAGASCI for water to hydrocarbon neutrino cross section measurement using the J-PARC beam. In: *Journal of Physics: Conference Series* 675.1 (2016), p. 012030. DOI: 10.1088/1742-6596/675/1/012030. URL: https://dx.doi.org/10.1088/1742-6596/675/1/012030.

[79] M. Antonova et al. Baby MIND: a magnetized segmented neutrino detector for the WAGASCI experiment. In: *Journal of Instrumentation* 12.07 (July 2017), C07028–C07028. ISSN: 1748-0221. DOI: 10.1088/1748-0221/12/07/c07028. URL: http://dx.doi.org/10.1088/1748-0221/12/07/C07028.

[80] H. Oshima et al. First measurement using a nuclear emulsion detector of the ν_μ charged-current cross section on iron around the 1 GeV energy region. In: *PTEP* 2021.3 (2021), p. 033C01. DOI: 10.1093/ptep/ptab027. arXiv: 2012.05221 [hep-ex].

[81] S. Fukuda et al. The Super-Kamiokande detector. In: *Nuclear Instruments and Methods in Physics Research Section A: Accelerators, Spectrometers, Detectors and Associated Equipment* 501.2 (2003), pp. 418–462. ISSN: 0168-9002. DOI: https://doi.org/10.1016/S0168-9002(03)00425-X. URL: https://www.sciencedirect.com/science/article/pii/S016890020300425X.

[82] M. Shiozawa et al. Search for Proton Decay via $p \to e^+\pi^0$ in a Large Water Cherenkov Detector. In: *Phys. Rev. Lett.* 81 (16 1998), pp. 3319–3323. DOI: 10.1103/PhysRevLett.81.3319. URL: https://link.aps.org/doi/10.1103/PhysRevLett.81.3319.

[83] Y. Fukuda et al. Evidence for Oscillation of Atmospheric Neutrinos. In: *Physical Review Letters* 81.8 (Aug. 1998), 1562–1567. ISSN: 1079-7114. DOI: 10.1103/physrevlett.81.1562. URL: http://dx.doi.org/10.1103/PhysRevLett.81.1562.

[84] K. Abe et al. Evidence for the Appearance of Atmospheric Tau Neutrinos in Super-Kamiokande. In: *Physical Review Letters* 110.18 (2013). DOI: 10.1103/physrevlett.110.181802. URL: https://doi.org/10.1103%2Fphysrevlett.110.181802.

[85] Mark Thomson. Modern particle physics. New York: Cambridge University Press, Oct. 2013. ISBN: 978-1-107-03426-6, 978-1-139-52536-7. DOI: 10.1017/CBO9781139525367.

[86] K. Abe et al. First gadolinium loading to Super-Kamiokande. In: *Nuclear Instruments and Methods in Physics Research Section A: Accelerators, Spectrometers, Detectors and Associated Equipment* 1027 (Mar. 2022), p. 166248. ISSN: 0168-9002. DOI: 10.1016/j.nima.2021.166248. URL: http://dx.doi.org/10.1016/j.nima.2021.166248.

[87] D. Attié et al. Performances of a resistive Micromegas module for the Time Projection Chambers of the T2K Near Detector upgrade. In: *Nuclear Instruments and Methods in Physics Research Section A: Accelerators, Spectrometers, Detectors and Associated Equipment* 957 (2020), p. 163286. ISSN: 0168-9002. DOI: https://doi.org/10.1016/j.nima.2019.163286. URL: https://www.sciencedirect.com/science/article/pii/S0168900219315426.

[88] D. Attié et al. Analysis of test beam data taken with a prototype of TPC with resistive Micromegas for the T2K Near Detector upgrade. In: *Nuclear Instruments and Methods in Physics Research Section A: Accelerators, Spectrometers, Detectors and Associated Equipment* 1052 (July 2023), p. 168248. ISSN: 0168-9002. DOI: 10.1016/j.nima.2023.168248. URL: http://dx.doi.org/10.1016/j.nima.2023.168248.

[89] Eljen Technology. GENERAL PURPOSE EJ-200, EJ-204, EJ-208, EJ-212. 2021. URL: https://eljentechnology.com/products/plastic-scintillators/ej-200-ej-204-ej-208-ej-212 (visited on 02/18/2025).

[90] A. Korzenev et al. A 4π time-of-flight detector for the ND280/T2K upgrade. In: *Journal of Instrumentation* 17.01 (Jan. 2022), P01016. ISSN: 1748-0221. DOI: 10.1088/1748-0221/17/01/p01016. URL: http://dx.doi.org/10.1088/1748-0221/17/01/P01016.

[91] John Nugent. ND280 Upgrade. URL: https://www.ppe.gla.ac.uk/~jnugent/nd280upgrade_nufact19_2nddraft.pdf. (accessed 30/06/2022).

[92] Claudio (LPNHE Paris) Giganti, Thorsten (IFAE Barcelona) Lux, and Masashi (University of Tokyo) Yokoyama. *NP07: ND280 Upgrade project*. Tech. rep. Geneva: CERN, 2020. URL: http://cds.cern.ch/record/2713578.

[93] A. Blondel et al. A fully-active fine-grained detector with three readout views. In: *Journal of Instrumentation* 13.02 (Feb. 2018), P02006–P02006. ISSN: 1748-0221. DOI: 10.1088/1748-0221/13/02/p02006. URL: http://dx.doi.org/10.1088/1748-0221/13/02/P02006.

[94] Kuraray Co. Wavelength Shifting Fibers. URL: http://kuraraypsf.jp/psf/ws.html (visited on 02/22/2025).

[95] Hamamatsu Photonics. MPPC S13360-1325PE. URL: https://www.hamamatsu.com/eu/en/product/optical-sensors/mppc/mppc_mppc-array/S13360-1325PE.html (visited on 02/25/2025).

[96] Tatsuya Kikawa. The SuperFGD for the upgraded T2K near detector - operation and performance. URL: https://www-he.scphys.kyoto-u.ac.jp/member/kikawa/tmp/vci_2025_sfgd.pdf (visited on 02/25/2025).

[97] Olivier Drapier. The SK2HK Rise European grant. URL: https://indico.in2p3.fr/event/20582/contributions/79191/attachments/57176/76261/OD-Reunion-Groupe.pdf (visited on 02/25/2025).

[98] Yusuke Furui. Status of the LED calibration system. URL: https://www.t2k.org/nd280/calib/Meetings/2023/20230206/Status%20of%20the%20LED%20calibration%20system (visited on 02/24/2025).

[99] Weeroc. Citiroc 1A Scientific instrumentation SiPM read-out chip. URL: https://www.weeroc.com/read_out_chips/citiroc-1a/ (visited on 02/25/2025).

[100] Team Midas. The Maximum Integrated Data Acquisition System (MIDAS) git repository. URL: https://bitbucket.org/tmidas/midas (visited on 02/25/2025).

[101] Shunta Arimoto. The DAQ system development for the T2K new near detector Super-FGD. URL: https://indico.cern.ch/event/1291157/contributions/5876973/attachments/2899278/5083850/20240719_ICHEP2024_v4.pdf (visited on 02/25/2025).

[102] O. Mineev et al. Beam test results of 3D fine-grained scintillator detector prototype for a T2K ND280 neutrino active target. In: *Nuclear Instruments and Methods in Physics Research Section A: Accelerators, Spectrometers, Detectors and Associated Equipment* 923 (Apr. 2019), 134–138. ISSN: 0168-9002. DOI: 10.1016/j.nima.2019.01.080. URL: http://dx.doi.org/10.1016/j.nima.2019.01.080.

[103] Hamamatsu Photonics. S12571-025, -050, -100C/P. URL: https://hamamatsu.su/files/uploads/pdf/3_mppc/s12571-025_050_100_c_p_kapd1042e.pdf (visited on 02/27/2025).

[104] A. Blondel et al. The SuperFGD Prototype charged particle beam tests. In: *Journal of Instrumentation* 15.12 (Dec. 2020), P12003–P12003. ISSN: 1748-0221. DOI: 10.1088/1748-0221/15/12/p12003. URL: http://dx.doi.org/10.1088/1748-0221/15/12/P12003.

[105] Hamamatsu Photonics. MPPC S13360-3025CS. URL: https://www.hamamatsu.com/eu/en/product/optical-sensors/mppc/mppc_mppc-array/S13360-3025CS.html (visited on 02/27/2025).

[106] I. Alekseev et al. SuperFGD prototype time resolution studies. In: *Journal of Instrumentation* 18.01 (Jan. 2023), P01012. ISSN: 1748-0221. DOI: 10.1088/1748-0221/18/01/p01012. URL: http://dx.doi.org/10.1088/1748-0221/18/01/P01012.

[107] A. Agarwal et al. Total neutron cross-section measurement on CH with a novel 3D-projection scintillator detector. In: *Physics Letters B* 840 (May 2023), p. 137843. ISSN: 0370-2693. DOI: 10.1016/j.physletb.2023.137843. URL: http://dx.doi.org/10.1016/j.physletb.2023.137843.

[108] Hamamatsu Photonics. MPPC - Technical guide to silicon photomultipliers (MPPC). URL: https://www.hamamatsu.com/content/dam/hamamatsu-photonics/sites/documents/99_SALES_LIBRARY/ssd/mppc_kapd9005e.pdf (visited on 06/20/2025).

[109] T2K. ND280 Software Gitlab. 2025. URL: https://git.t2k.org/nd280 (visited on 04/05/2025).

[110] Yoshi Uchida. ND280 Upgrade: Software. 2018. URL: https://indico.cern.ch/event/698927/contributions/2884828/attachments/1594677/2525177/20180205-YoshiU-ND280UpgradeSoftware-upload.pdf (visited on 06/22/2025).

[111] F. Halzen and Alan D. Martin. QUARKS AND LEPTONS: AN INTRODUCTORY COURSE IN MODERN PARTICLE PHYSICS. 1984. ISBN: 978-0-471-88741-6.

[112] W. Greiner and J. Reinhardt. Quantum electrodynamics. 1992. ISBN: 978-3-540-87560-4.

[113] James D. Bjorken and Sidney D. Drell. Relativistic Quantum Mechanics. International Series In Pure and Applied Physics. New York: McGraw-Hill, 1965. ISBN: 978-0-07-005493-6.

[114] James J. Kelly. Gauge ambiguities in $(\vec{e}, e'\vec{N})$ reactions. In: *Phys. Rev. C* 56 (5 1997), pp. 2672–2687. DOI: 10.1103/PhysRevC.56.2672. URL: https://link.aps.org/doi/10.1103/PhysRevC.56.2672.

[115] J E Amaro et al. Electron- versus neutrino-nucleus scattering. In: *Journal of Physics G: Nuclear and Particle Physics* 47.12 (2020), p. 124001. DOI: 10.1088/1361-6471/abb128. URL: https://dx.doi.org/10.1088/1361-6471/abb128.

[116] Kaushik Borah et al. Parametrization and applications of the low-Q^2 nucleon vector form factors. In: *Phys. Rev. D* 102 (7 2020), p. 074012. DOI: 10.1103/PhysRevD.102.074012. URL: https://link.aps.org/doi/10.1103/PhysRevD.102.074012.

[117] C. Patrignani. Review of Particle Physics. In: *Chinese Physics C* 40.10 (2016), p. 100001. DOI: 10.1088/1674-1137/40/10/100001. URL: https://dx.doi.org/10.1088/1674-1137/40/10/100001.

[118] N. J. Baker et al. Quasielastic neutrino scattering: A measurement of the weak nucleon axial-vector form factor. In: *Phys. Rev. D* 23 (11 1981), pp. 2499–2505. DOI: 10.1103/PhysRevD.23.2499. URL: https://link.aps.org/doi/10.1103/PhysRevD.23.2499.

[119] T. Kitagaki et al. High-energy quasielastic $\nu_\mu n \to \mu^- p$ scattering in deuterium. In: *Phys. Rev. D* 28 (3 1983), pp. 436–442. DOI: 10.1103/PhysRevD.28.436. URL: https://link.aps.org/doi/10.1103/PhysRevD.28.436.

[120] T. Kitagaki et al. Study of $\nu d \to \mu^- p p_s$ and $\nu d \to \mu^- \Delta^{++}(1232) n_s$ using the BNL 7-foot deuterium-filled bubble chamber. In: *Phys. Rev. D* 42 (5 1990), pp. 1331–1338. DOI: 10.1103/PhysRevD.42.1331. URL: https://link.aps.org/doi/10.1103/PhysRevD.42.1331.

[121] W. A. Mann et al. Study of the Reaction $\nu + n \to \mu^- + p$. In: *Phys. Rev. Lett.* 31 (13 1973), pp. 844–847. DOI: 10.1103/PhysRevLett.31.844. URL: https://link.aps.org/doi/10.1103/PhysRevLett.31.844.

[122] S. J. Barish et al. Study of neutrino interactions in hydrogen and deuterium: Description of the experiment and study of the reaction $\nu + d \to \mu^- + p + p_s$. In: *Phys. Rev. D* 16 (11 1977), pp. 3103–3121. DOI: 10.1103/PhysRevD.16.3103. URL: https://link.aps.org/doi/10.1103/PhysRevD.16.3103.

[123] K. L. Miller et al. Study of the reaction $\nu_\mu d \to \mu^- pp_s$. In: *Phys. Rev. D* 26 (3 1982), pp. 537–542. DOI: 10.1103/PhysRevD.26.537. URL: https://link.aps.org/doi/10.1103/PhysRevD.26.537.

[124] T. Cai et al. Measurement of the axial vector form factor from antineutrino–proton scattering. In: *Nature* 614.7946 (2023), pp. 48–53. ISSN: 1476-4687. DOI: 10.1038/s41586-022-05478-3. URL: https://doi.org/10.1038/s41586-022-05478-3.

[125] Richard J. Hill and Gil Paz. Model-independent extraction of the proton charge radius from electron scattering. In: *Phys. Rev. D* 82 (11 2010), p. 113005. DOI: 10.1103/PhysRevD.82.113005. URL: https://link.aps.org/doi/10.1103/PhysRevD.82.113005.

[126] Oleksandr Tomalak, Rajan Gupta, and Tanmoy Bhattacharya. *Confronting axial-vector form factor from lattice QCD with MINERvA antineutrino-proton data*. 2023. arXiv: 2307.14920 [hep-lat]. URL: https://arxiv.org/abs/2307.14920.

[127] Geoffrey F. Chew and Gian Carlo Wick. The Impulse Approximation. In: *Phys. Rev.* 85 (4 1952), pp. 636–642. DOI: 10.1103/PhysRev.85.636. URL: https://link.aps.org/doi/10.1103/PhysRev.85.636.

[128] M. Duer et al. Probing high-momentum protons and neutrons in neutron-rich nuclei. In: *Nature* 560 (2018), pp. 617–621. DOI: 10.1038/s41586-018-0400-z. URL: https://doi.org/10.1038/s41586-018-0400-z.

[129] W. Pauli. Über den Zusammenhang des Abschlusses der Elektronengruppen im Atom mit der Komplexstruktur der Spektren. In: *Z. Phys.* 31.1 (1925), pp. 765–783. DOI: 10.1007/BF02980631.

[130] Raúl González Jiménez. Relativistic Quantum Theory and Weak Interactions. Notes from the Interuniversity Master's Degree in Nuclear Physics and Erasmus Mundus Master's Degree in Nuclear Physics. 2024.

[131] P. Barreau et al. Deep-inelastic electron scattering from carbon. In: *Nuclear Physics A* 402.3 (1983), pp. 515–540. ISSN: 0375-9474. DOI: https://doi.org/10.1016/0375-9474(83)90217-8. URL: https://www.sciencedirect.com/science/article/pii/0375947483902178.

[132] Tina J. Leitner. "Neutrino-nucleus interactions in a coupled-channel hadronic transport model". Other thesis. Oct. 2009.

[133] Omar Benhar, Donal Day, and Ingo Sick. Inclusive quasielastic electron-nucleus scattering. In: *Rev. Mod. Phys.* 80 (1 2008), pp. 189–224. DOI: 10.1103/RevModPhys.80.189. URL: https://link.aps.org/doi/10.1103/RevModPhys.80.189.

[134] A. Nikolakopoulos et al. Electron versus Muon Neutrino Induced Cross Sections in Charged Current Quasielastic Processes. In: *Phys. Rev. Lett.* 123 (5 2019), p. 052501. DOI: 10.1103/PhysRevLett.123.052501. URL: https://link.aps.org/doi/10.1103/PhysRevLett.123.052501.

[135] K. Langanke, Joachim A. Maruhn, and S. E. Koonin, eds. Computational Nuclear Physics 1. Nuclear Structure. Springer, 1991. ISBN: 978-3-642-76358-8, 978-3-642-76356-4. DOI: 10.1007/978-3-642-76356-4.

[136] P G Reinhard. The relativistic mean-field description of nuclei and nuclear dynamics. In: *Reports on Progress in Physics* 52.4 (1989), p. 439. DOI: 10.1088/0034-4885/52/4/002. URL: https://dx.doi.org/10.1088/0034-4885/52/4/002.

[137] P. Ring et al. The time-dependent relativistic mean-field theory and the random phase approximation. In: *Nuclear Physics A* 694.1–2 (Nov. 2001), 249–268. ISSN: 0375-9474. DOI: 10.1016/s0375-9474(01)00986-1. URL: http://dx.doi.org/10.1016/S0375-9474(01)00986-1.

[138] Brian D. Serot and John Dirk Walecka. The Relativistic Nuclear Many Body Problem. In: *Adv. Nucl. Phys.* 16 (1986), pp. 1–327.

[139] M.M. Sharma, M.A. Nagarajan, and P. Ring. Rho meson coupling in the relativistic mean field theory and description of exotic nuclei. In: *Physics Letters B* 312.4 (1993), pp. 377–381. ISSN: 0370-2693. DOI: https://doi.org/10.1016/0370-2693(93)90970-S. URL: https://www.sciencedirect.com/science/article/pii/037026939390970S.

[140] J. McKean et al. *Implementation of a relativistic distorted wave impulse approximation model into the NEUT event generator*. 2025. arXiv: 2502.10629 [hep-ex]. URL: https://arxiv.org/abs/2502.10629.

[141] Max Born. Quantenmechanik der Stoßvorgänge. In: *Zeitschrift fur Physik* 38.11-12 (Nov. 1926), pp. 803–827. DOI: 10.1007/BF01397184.

[142] L. D. Landau and E. M. Lifshitz. Quantum mechanics: non-relativistic theory. Pergamon press, 1965.

[143] J. M. Udías et al. Relativistic versus nonrelativistic optical potentials in A(e,e'p)B reactions. In: *Phys. Rev. C* 51 (6 1995), pp. 3246–3255. DOI: 10.1103/PhysRevC.51.3246. URL: https://link.aps.org/doi/10.1103/PhysRevC.51.3246.

[144] E. D. Cooper, S. Hama, and B. C. Clark. Global Dirac optical potential from helium to lead. In: *Phys. Rev. C* 80 (3 2009), p. 034605. DOI: 10.1103/PhysRevC.80.034605. URL: https://link.aps.org/doi/10.1103/PhysRevC.80.034605.

[145] R. González-Jiménez et al. Nuclear effects in electron-nucleus and neutrino-nucleus scattering within a relativistic quantum mechanical framework. In: *Phys. Rev. C* 100 (4 2019), p. 045501. DOI: 10.1103/PhysRevC.100.045501. URL: https://link.aps.org/doi/10.1103/PhysRevC.100.045501.

[146] R. González-Jiménez et al. Constraints in modeling the quasielastic response in inclusive lepton-nucleus scattering. In: *Phys. Rev. C* 101 (1 2020), p. 015503. DOI: 10.1103/PhysRevC.101.015503. URL: https://link.aps.org/doi/10.1103/PhysRevC.101.015503.

[147] J. M. Udías et al. Spectroscopic factors in ^{40}Ca and ^{208}Pb from (e,e'p): Fully relativistic analysis. In: *Phys. Rev. C* 48 (6 1993), pp. 2731–2739. DOI: 10.1103/PhysRevC.48.2731. URL: https://link.aps.org/doi/10.1103/PhysRevC.48.2731.

[148] C. Giusti et al. Quasifree $(e, e'p)$ reactions on nuclei with neutron excess. In: *Phys. Rev. C* 84 (2 2011), p. 024615. DOI: 10.1103/PhysRevC.84.024615. URL: https://link.aps.org/doi/10.1103/PhysRevC.84.024615.

[149] A. V. Butkevich. Quasi-elastic neutrino charged-current scattering off medium-heavy nuclei: ^{40}Ca and ^{40}Ar. In: *Phys. Rev. C* 85 (6 2012), p. 065501. DOI: 10.1103/PhysRevC.85.065501. URL: https://link.aps.org/doi/10.1103/PhysRevC.85.065501.

[150] Hana Gil, Chang Ho Hyun, and Kyungsik Kim. Quasielastic electron scattering with the KIDS nuclear energy density functional. In: *Phys. Rev. C* 104 (4 2021), p. 044613. DOI: 10.1103/PhysRevC.104.044613. URL: https://link.aps.org/doi/10.1103/PhysRevC.104.044613.

[151] R. González-Jiménez et al. Extensions of superscaling from relativistic mean field theory: The SuSAv2 model. In: *Phys. Rev. C* 90 (3 2014), p. 035501. DOI: 10.1103/PhysRevC.90.035501. URL: https://link.aps.org/doi/10.1103/PhysRevC.90.035501.

[152] G. D. Megias et al. Inclusive electron scattering within the SuSAv2 meson-exchange current approach. In: *Phys. Rev. D* 94 (1 2016), p. 013012. DOI: 10.1103/PhysRevD.94.013012. URL: https://link.aps.org/doi/10.1103/PhysRevD.94.013012.

[153] Andrea Meucci et al. Inclusive electron scattering in a relativistic Green's function approach. In: *Phys. Rev. C* 67 (5 2003), p. 054601. DOI: 10.1103/PhysRevC.67.054601. URL: https://link.aps.org/doi/10.1103/PhysRevC.67.054601.

[154] G. Garino et al. Proton propagation in nuclei studied in the (e,e'p) reaction. In: *Phys. Rev. C* 45 (2 1992), pp. 780–790. DOI: 10.1103/PhysRevC.45.780. URL: https://link.aps.org/doi/10.1103/PhysRevC.45.780.

[155] M. Holtrop et al. Measurement of the interference structure function R_{LT} for the ^{12}C$(e, e'p)$ reaction in the quasielastic region. In: *Phys. Rev. C* 58 (6 1998), pp. 3205–3211. DOI: 10.1103/PhysRevC.58.3205. URL: https://link.aps.org/doi/10.1103/PhysRevC.58.3205.

[156] D. Dutta et al. Quasielastic $(e, e^{'}p)$ reaction on ^{12}C,^{56} Fe, and ^{197}Au. In: *Phys. Rev. C* 68 (6 2003), p. 064603. DOI: 10.1103/PhysRevC.68.064603. URL: https://link.aps.org/doi/10.1103/PhysRevC.68.064603.

[157] L. Jiang et al. Determination of the argon spectral function from $(e, e'p)$ data. In: *Phys. Rev. D* 105 (11 2022), p. 112002. DOI: 10.1103/PhysRevD.105.112002. URL: https://link.aps.org/doi/10.1103/PhysRevD.105.112002.

[158] L. Jiang et al. Determination of the titanium spectral function from $(e, e'p)$ data. In: *Phys. Rev. D* 107 (1 2023), p. 012005. DOI: 10.1103/PhysRevD.107.012005. URL: https://link.aps.org/doi/10.1103/PhysRevD.107.012005.

[159] K. G. Fissum et al. Dynamics of the quasielastic ^{16}O$(e, e'p)$ reaction at $Q^2 \approx 0.8$ (GeV/c)^2. In: *Phys. Rev. C* 70 (3 2004), p. 034606. DOI: 10.1103/PhysRevC.70.034606. URL: https://link.aps.org/doi/10.1103/PhysRevC.70.034606.

[160] G.J. Kramer et al. Proton ground-state correlations in ^{40}Ca studied with the reaction ^{40}Ca(e,e'p)^{49}K. In: *Physics Letters B* 227.2 (1989), pp. 199–203. ISSN: 0370-2693. DOI: https://doi.org/10.1016/S0370-2693(89)80022-X. URL: https://www.sciencedirect.com/science/article/pii/S037026938980022X.

[161] Y. Yasuda et al. Spectroscopic factors and strength distributions for the deeply bound orbitals in ^{40}Ca obtained from the $(\vec{p}, 2p)$ reaction at 392 MeV. In: *Phys. Rev. C* 81 (4 2010), p. 044315. DOI: 10.1103/PhysRevC.81.044315. URL: https://link.aps.org/doi/10.1103/PhysRevC.81.044315.

[162] S. S. Volkov et al. (p,2p) and (p,pn) quasielastic scattering reactions at 1-GeV and deformation properties of the d shell nuclei. (In Russian). In: *Sov. J. Nucl. Phys.* 52 (1990), pp. 848–857.

[163] M. C. Atkinson et al. Validity of the distorted-wave impulse-approximation description of ^{40}Ca$(e, e'p)^{39}$K data using only ingredients from a nonlocal dispersive optical model. In: *Phys. Rev. C* 98 (4 2018), p. 044627. DOI: 10.1103/PhysRevC.98.044627. URL: https://link.aps.org/doi/10.1103/PhysRevC.98.044627.

[164] R. González-Jiménez et al. Neutrino energy reconstruction from semi-inclusive samples. In: *Phys. Rev. C* 105 (2 2022), p. 025502. DOI: 10.1103/PhysRevC.105.025502. URL: https://link.aps.org/doi/10.1103/PhysRevC.105.025502.

[165] O. Benhar et al. Spectral function of finite nuclei and scattering of GeV electrons. In: *Nuclear Physics A* 579.3 (1994), pp. 493 –517. ISSN: 0375-9474. DOI: https://doi.org/10.1016/0375-9474(94)90920-2. URL: http://www.sciencedirect.com/science/article/pii/0375947494909202.

[166] Omar Benhar et al. Electron- and neutrino-nucleus scattering in the impulse approximation regime. In: *Phys. Rev. D* 72 (5 2005), p. 053005. DOI: 10.1103/PhysRevD.72.053005. URL: https://link.aps.org/doi/10.1103/PhysRevD.72.053005.

[167] J. M. Franco-Patino et al. Final state interactions in semi-inclusive neutrino-nucleus scattering: Applications to the T2K and MINERνA experiments. In: *Phys. Rev. D* 106 (11 2022), p. 113005. DOI: 10.1103/PhysRevD.106.113005. URL: https://link.aps.org/doi/10.1103/PhysRevD.106.113005.

[168] T. Franco-Munoz et al. Relativistic two-body currents for one-nucleon knockout in electron-nucleus scattering. In: *Physical Review C* 108.6 (Dec. 2023). ISSN: 2469-9993. DOI: 10.1103/physrevc.108.064608. URL: http://dx.doi.org/10.1103/PhysRevC.108.064608.

[169] J. M. Franco-Patino et al. New model comparison for semi-inclusive charged-current electron and muon neutrino scattering by ^{40}Ar in the energy range of the MicroBooNE experiment. In: *Phys. Rev. D* 109 (1 2024), p. 013004. DOI: 10.1103/PhysRevD.109.013004. URL: https://link.aps.org/doi/10.1103/PhysRevD.109.013004.

[170] K. S. Egiyan et al. Measurement of Two- and Three-Nucleon Short-Range Correlation Probabilities in Nuclei. In: *Phys. Rev. Lett.* 96 (8 2006), p. 082501. DOI: 10.1103/PhysRevLett.96.082501. URL: https://link.aps.org/doi/10.1103/PhysRevLett.96.082501.

[171] Yoshinari Hayato and Luke Pickering. The NEUT neutrino interaction simulation program library. In: *The European Physical Journal Special Topics* 230.24 (Oct. 2021), 4469–4481. ISSN: 1951-6401. DOI: 10.1140/epjs/s11734-021-00287-7. URL: http://dx.doi.org/10.1140/epjs/s11734-021-00287-7.

[172] T. Golan, J. T. Sobczyk, and J. Zmuda. NuWro: the Wroclaw Monte Carlo Generator of Neutrino Interactions. In: *Nucl. Phys. B Proc. Suppl.* 229-232 (2012). Ed. by George S. Tzanakos, pp. 499–499. DOI: 10.1016/j.nuclphysbps.2012.09.136.

[173] Costas Andreopoulos et al. *The GENIE Neutrino Monte Carlo Generator: Physics and User Manual*. 2015. arXiv: 1510.05494 [hep-ph]. URL: https://arxiv.org/abs/1510.05494.

[174] Joshua Isaacson et al. Introducing a novel event generator for electron-nucleus and neutrino-nucleus scattering. In: *Physical Review D* 107.3 (Feb. 2023). ISSN: 2470-0029. DOI: 10.1103/physrevd.107.033007. URL: http://dx.doi.org/10.1103/PhysRevD.107.033007.

[175] O. Buss et al. Transport-theoretical description of nuclear reactions. In: *Physics Reports* 512.1–2 (Mar. 2012), 1–124. ISSN: 0370-1573. DOI: 10.1016/j.physrep.2011.12.001. URL: http://dx.doi.org/10.1016/j.physrep.2011.12.001.

[176] Hugo W. Bertini. Nonelastic Interactions of Nucleons and π Mesons with Complex Nuclei at Energies Below 3 GeV. In: *Phys. Rev. C* 6 (2 1972), pp. 631–659. DOI: 10.1103/PhysRevC.6.631. URL: https://link.aps.org/doi/10.1103/PhysRevC.6.631.

[177] L.L. Salcedo et al. Computer simulation of inclusive pion nuclear reactions. In: *Nuclear Physics A* 484.3 (1988), pp. 557–592. ISSN: 0375-9474. DOI: https://doi.org/10.1016/0375-9474(88)90310-7. URL: https://www.sciencedirect.com/science/article/pii/0375947488903107.

[178] T Franco-Munoz, R González-Jiménez, and J M Udías. Effects of two-body currents in the one-particle one-hole electromagnetic responses within a relativistic model. In: *Journal of Physics G: Nuclear and Particle Physics* 52.2 (2025), p. 025103. DOI: 10.1088/1361-6471/ad9eca. URL: https://dx.doi.org/10.1088/1361-6471/ad9eca.

[179] Seisho Abe. Implementation and investigation of electron-nucleus scattering in the neut neutrino event generator. In: *Phys. Rev. D* 111 (3 2025), p. 033006. DOI: 10.1103/PhysRevD.111.033006. URL: https://link.aps.org/doi/10.1103/PhysRevD.111.033006.

[180] J. Nieves, I. Ruiz Simo, and M.J. Vicente Vacas. The nucleon axial mass and the MiniBooNE quasielastic neutrino–nucleus scattering problem. In: *Physics Letters B* 707.1 (2012), pp. 72–75. ISSN: 0370-2693. DOI: https://doi.org/10.1016/j.physletb.2011.11.061. URL: https://www.sciencedirect.com/science/article/pii/S0370269311014407.

[181] X.-G. Lu et al. Measurement of nuclear effects in neutrino interactions with minimal dependence on neutrino energy. In: *Physical Review C* 94.1 (July 2016). ISSN: 2469-9993. DOI: 10.1103/physrevc.94.015503. URL: http://dx.doi.org/10.1103/PhysRevC.94.015503.

[182] K. Abe et al. T2K ND280 Upgrade - Technical Design Report. In: (Jan. 2019). arXiv: 1901.03750 [physics.ins-det].

[183] K. Abe et al. Characterization of nuclear effects in muon-neutrino scattering on hydrocarbon with a measurement of final-state kinematics and correlations in charged-current pionless interactions at T2K. In: *Phys. Rev. D* 98 (3 2018), p. 032003. DOI: 10.1103/PhysRevD.98.032003. URL: https://link.aps.org/doi/10.1103/PhysRevD.98.032003.

[184] X.-G. Lu et al. Measurement of Final-State Correlations in Neutrino Muon-Proton Mesonless Production on Hydrocarbon at $<E_\nu> = 3$ GeV. In: *Phys. Rev. Lett.* 121 (2 2018), p. 022504. DOI: 10.1103/PhysRevLett.121.022504. URL: https://link.aps.org/doi/10.1103/PhysRevLett.121.022504.

[185] T. Cai et al. Nucleon binding energy and transverse momentum imbalance in neutrino-nucleus reactions. In: *Phys. Rev. D* 101 (9 2020), p. 092001. DOI: 10.1103/PhysRevD.101.092001. URL: https://link.aps.org/doi/10.1103/PhysRevD.101.092001.

[186] P. Abratenko et al. Measurement of differential cross sections for ν_μ-Ar charged-current interactions with protons and no pions in the final state with the MicroBooNE detector. In: *Phys. Rev. D* 102 (11 2020), p. 112013. DOI: 10.1103/PhysRevD.102.112013. URL: https://link.aps.org/doi/10.1103/PhysRevD.102.112013.

[187] P. Abratenko et al. First Double-Differential Measurement of Kinematic Imbalance in Neutrino Interactions with the MicroBooNE Detector. In: *Phys. Rev. Lett.* 131 (10 2023), p. 101802. DOI: 10.1103/PhysRevLett.131.101802. URL: https://link.aps.org/doi/10.1103/PhysRevLett.131.101802.

[188] P. Abratenko et al. Multidifferential cross section measurements of ν_μ-argon quasielasticlike reactions with the MicroBooNE detector. In: *Phys. Rev. D* 108 (5 2023), p. 053002. DOI: 10.1103/PhysRevD.108.053002. URL: https://link.aps.org/doi/10.1103/PhysRevD.108.053002.

[189] P. Stowell et al. NUISANCE: a neutrino cross-section generator tuning and comparison framework. In: *JINST* 12.01 (2017), P01016. DOI: 10.1088/1748-0221/12/01/P01016. arXiv: 1612.07393 [hep-ex].

[190] J. Nieves, I. Ruiz Simo, and M. J. Vicente Vacas. Inclusive charged-current neutrino-nucleus reactions. In: *Phys. Rev. C* 83 (4 2011), p. 045501. DOI: 10.1103/PhysRevC.83.045501. URL: https://link.aps.org/doi/10.1103/PhysRevC.83.045501.

[191] Dieter Rein and Lalit M. Sehgal. Neutrino Excitation of Baryon Resonances and Single Pion Production. In: *Annals Phys.* 133 (1981), pp. 79–153. DOI: 10.1016/0003-4916(81)90242-6.

[192] Ch. Berger and L. M. Sehgal. Lepton mass effects in single pion production by neutrinos. In: *Phys. Rev. D* 76 (11 2007), p. 113004. DOI: 10.1103/PhysRevD.76.113004. URL: https://link.aps.org/doi/10.1103/PhysRevD.76.113004.

[193] Krzysztof M. Graczyk and Jan T. Sobczyk. Lepton mass effects in weak charged current single pion production. In: *Phys. Rev. D* 77 (5 2008), p. 053003. DOI: 10.1103/PhysRevD.77.053003. URL: https://link.aps.org/doi/10.1103/PhysRevD.77.053003.

[194] G. D'Agostini. A multidimensional unfolding method based on Bayes' theorem. In: *Nuclear Instruments and Methods in Physics Research Section A: Accelerators, Spectrometers, Detectors and Associated Equipment* 362.2 (1995), pp. 487–498. ISSN: 0168-9002. DOI: https://doi.org/10.1016/0168-9002(95)00274-X. URL: https://www.sciencedirect.com/science/article/pii/016890029500274X.

[195] W. Tang et al. Data Unfolding with Wiener-SVD Method. In: *Journal of Instrumentation* 12.10 (Oct. 2017), P10002–P10002. ISSN: 1748-0221. DOI: 10.1088/1748-0221/12/10/p10002. URL: http://dx.doi.org/10.1088/1748-0221/12/10/P10002.

[196] R. M. Sealock et al. Electroexcitation of the $\Delta(1232)$ in nuclei. In: *Phys. Rev. Lett.* 62 (12 1989), pp. 1350–1353. DOI: 10.1103/PhysRevLett.62.1350. URL: https://link.aps.org/doi/10.1103/PhysRevLett.62.1350.

[197] J. S. O'Connell et al. Electromagnetic excitation of the delta resonance in nuclei. In: *Phys. Rev. C* 35 (3 1987), pp. 1063–1071. DOI: 10.1103/PhysRevC.35.1063. URL: https://link.aps.org/doi/10.1103/PhysRevC.35.1063.

[198] S. X. Nakamura, H. Kamano, and T. Sato. Dynamical coupled-channels model for neutrino-induced meson productions in resonance region. In: *Phys. Rev. D* 92 (7 2015), p. 074024. DOI: 10.1103/PhysRevD.92.074024. URL: https://link.aps.org/doi/10.1103/PhysRevD.92.074024.

[199] Noemi Rocco et al. Electroweak pion production on nuclei within the extended factorization scheme. In: *Phys. Rev. C* 100 (4 2019), p. 045503. DOI: 10.1103/PhysRevC.100.045503. URL: https://link.aps.org/doi/10.1103/PhysRevC.100.045503.

[200] Seisho Abe. Implementation and investigation of electron-nucleus scattering in the neut neutrino event generator. In: *Physical Review D* 111.3 (Feb. 2025). ISSN: 2470-0029. DOI: 10.1103/physrevd.111.033006. URL: http://dx.doi.org/10.1103/PhysRevD.111.033006.

[201] Artur M. Ankowski, Omar Benhar, and Makoto Sakuda. Determination of the proton spectral function of ^{12}C from $(e, e^{'}p)$ data. In: *Phys. Rev. C* 110 (5 2024), p. 054612. DOI: 10.1103/PhysRevC.110.054612. URL: https://link.aps.org/doi/10.1103/PhysRevC.110.054612.

[202] J McKean, S Abe, and L. Munteanu. *In preparation.* 2025.

[203] E. Marzec et al. First Measurement of Missing Energy due to Nuclear Effects in Monoenergetic Neutrino Charged-Current Interactions. In: *Phys. Rev. Lett.* 134 (8 2025), p. 081801. DOI: 10.1103/PhysRevLett.134.081801. URL: https://link.aps.org/doi/10.1103/PhysRevLett.134.081801.

[204] Particle Data Group et al. Review of Particle Physics. In: *Progress of Theoretical and Experimental Physics* 2020.8 (Aug. 2020), p. 083C01. ISSN: 2050-3911. DOI: 10.1093/ptep/ptaa104. eprint: https://academic.oup.com/ptep/article-pdf/2020/8/083C01/34673722/ptaa104.pdf. URL: https://doi.org/10.1093/ptep/ptaa104.

[205] Seisho Abe. Nuclear Deexcitation Event Generator (NucDeEx). URL: https://github.com/SeishoAbe/NucDeEx (visited on 07/20/2025). Github repository.

[206] Seisho Abe. Nuclear deexcitation simulator for neutrino interactions and nucleon decays of ^{12}C and ^{16}O based on TALYS. In: *Phys. Rev. D* 109 (3 2024), p. 036009. DOI: 10.1103/PhysRevD.109.036009. URL: https://link.aps.org/doi/10.1103/PhysRevD.109.036009.

[207] Arjan Koning, Stephane Hilaire, and Stephane Goriely. TALYS: modeling of nuclear reactions. In: *The European Physical Journal A* 59.6 (2023), p. 131. ISSN: 1434-601X. DOI: 10.1140/epja/s10050-023-01034-3. URL: https://doi.org/10.1140/epja/s10050-023-01034-3.

[208] L. Berns et al. T2K future sensitivity studies. 2024. URL: https://www.t2k.org/docs/technotes/480/v3p1 (visited on 07/14/2025). Private T2K Technical Note.

Appendix A

A.1 Four vectors

In 3D space, one uses standard vectors to denote objects which have both magnitude and direction. This can be represented mathematically as a column vector with three elements.

$$\mathbf{v} = \begin{bmatrix} v_1 \\ v_2 \\ v_3 \end{bmatrix} \tag{A.1}$$

In tensor notation, this can be expressed as v^i where $i = 1, 2, 3$ for v_1, v_2 and v_3 respectively. Note that for 3D vectors using tensor notation, the choice of letter for the subscript is arbitrary but should not be a Greek letter as this is reserved to denote four-dimensional vectors in Special Relativity (four vectors). In 4D spacetime, four vectors are used to denote a 3D vector, with an additional zeroth component to denote the time component. This can be expressed in tensor notation as X^μ where $\mu = 0, 1, 2, 3$. The scalar product can be taken using four vectors and this thesis uses the following convention.

$$\begin{aligned} X \cdot X &= X^\mu g_{\mu\nu} X^\nu \\ &= X^\mu X_\mu \\ &= X^0 X_0 - X^1 X_1 - X^2 X_2 - X^3 X_3 \end{aligned} \tag{A.2}$$

where X is a four vector and $g_{\mu\nu}$ is the metric tensor of Minkowski spacetime and is represented as

$$g_{\mu\nu} = \begin{pmatrix} 1 & 0 & 0 & 0 \\ 0 & -1 & 0 & 0 \\ 0 & 0 & -1 & 0 \\ 0 & 0 & 0 & -1 \end{pmatrix} \tag{A.3}$$

A.2 Dirac equation

The free Dirac equation is given by

$$(i\gamma^{\mu}\partial_{\mu} - m)\Psi(x) = 0, \tag{A.4}$$

with positive energy solutions

$$\Psi^{(+)}(x) = \sqrt{\frac{m}{VE}}\,\mathcal{U}(\mathbf{p}, s)e^{-ip\cdot x} \tag{A.5}$$

and negative energy solutions;

$$\Psi^{(-)}(x) = \sqrt{\frac{m}{VE}}\,\mathcal{V}(\mathbf{p}, s)e^{ip\cdot x}. \tag{A.6}$$

Here, M is the mass of the particle, s is the spin of the particle ($\pm$ 1/2), V is the volume, E is the energy of the particle, $\mathbf{p}$ is the three momenta of the particle, p is the four momentum and x is the four position of the particle. The spinors, $\mathcal{U}$ and $\mathcal{V}$, can be expressed as

$$\mathcal{U}(\mathbf{p}, s) = \sqrt{E + m}\begin{pmatrix}\chi^{(s)} \\ \frac{\boldsymbol{\sigma}\cdot\mathbf{p}}{E+m}\chi^{(s)}\end{pmatrix}, \tag{A.7}$$

and

$$\mathcal{V}(\mathbf{p}, s) = \sqrt{E + m}\begin{pmatrix}\frac{\boldsymbol{\sigma}\cdot\mathbf{p}}{E+m}\chi^{(s)} \\ \chi^{(s)}\end{pmatrix}. \tag{A.8}$$

The two-component spinors, χ^s are given as

$$\chi^{(+1/2)} = \begin{pmatrix}1\\0\end{pmatrix}, \quad \chi^{(-1/2)} = \begin{pmatrix}0\\1\end{pmatrix}. \tag{A.9}$$

The Pauli spin matrices, $\boldsymbol{\sigma}$ are given as

$$\sigma^1 = \begin{pmatrix}0 & 1\\1 & 0\end{pmatrix}, \quad \sigma^2 = \begin{pmatrix}0 & -i\\i & 0\end{pmatrix}, \quad \sigma^3 = \begin{pmatrix}1 & 0\\0 & -1\end{pmatrix}. \tag{A.10}$$

A.3 Gamma matrices

The gamma matrices are given as

$$\gamma^0 = \begin{pmatrix} 1 & 0 & 0 & 0 \\ 0 & 1 & 0 & 0 \\ 0 & 0 & -1 & 0 \\ 0 & 0 & 0 & -1 \end{pmatrix} \quad \gamma^1 = \begin{pmatrix} 0 & 0 & 0 & 1 \\ 0 & 0 & 1 & 0 \\ 0 & -1 & 0 & 0 \\ -1 & 0 & 0 & 0 \end{pmatrix}$$
$$\gamma^2 = \begin{pmatrix} 0 & 0 & 0 & -i \\ 0 & 0 & i & 0 \\ 0 & -i & 0 & 0 \\ i & 0 & 0 & 0 \end{pmatrix} \quad \gamma^3 = \begin{pmatrix} 0 & 0 & 1 & 0 \\ 0 & 0 & 0 & -1 \\ -1 & 0 & 0 & 0 \\ 0 & 1 & 0 & 0 \end{pmatrix}. \tag{A.11}$$

The trace theorems for gamma matrices are

$$\mathrm{Tr}[\gamma^\mu \gamma^\nu] = 4g^{\mu\nu} \tag{A.12}$$
$$\mathrm{Tr}[\gamma^\mu \gamma^\nu \gamma^\rho \gamma^\sigma] = 4\left(g^{\mu\nu} g^{\rho\sigma} - g^{\mu\rho} g^{\nu\sigma} + g^{\mu\sigma} g^{\nu\rho}\right) \tag{A.13}$$
$$\mathrm{Tr}[\gamma^\mu \gamma^\nu \gamma^\rho] = 0. \tag{A.14}$$

A.4 Four-dimensional Dirac delta function

The definition of the one-dimensional Dirac delta function is given as

$$\delta(x) = \begin{cases} +\infty & \text{if } x = 0 \\ 0 & \text{if } x \neq 0 \end{cases} \tag{A.15}$$

where δ is the Dirac delta function.

It can be defined by integrating over an exponential function from $-\infty$ to $+\infty$.

$$\delta(x - y) = \int_{-\infty}^{+\infty} \exp^{-k(x-y)}\, dk \tag{A.16}$$

When using four vectors, the four-dimensional Dirac delta function can be defined in an analogous way. For given four momenta, P and P', and four position, X,

$$\int \exp^{i(P-P')\cdot X}\, dX = (2\pi)^4 \delta^4(P' - P) \tag{A.17}$$

where the limits of the integral has been removed for brevity knowing that the integral is performed across the whole space.

A.4.1 Dirac delta identities

The two following identities are useful and pertinent to calculating cross-section expressions.

$$[(2\pi)^4\delta^4(P-P')]^2 = VT(2\pi)^4\delta^4(P-P'). \tag{A.18}$$

$$\delta(f(x)) = \sum_i \frac{\delta(x-x_i)}{|\partial f(x)/\partial x|}\bigg|_{x=x_i} \tag{A.19}$$

Appendix B

B.1 Explicit lepton tensor derivation

The expression for the lepton current and tensor are

$$j_\mu \stackrel{\text{def}}{=} \bar{\mathcal{U}}(\mathbf{k_f}, s_f)\gamma_\mu \mathcal{U}(\mathbf{k_i}, s_i) \tag{B.1}$$

and

$$L'_{\mu\nu} = \frac{1}{2}\sum_{s_i}\sum_{s_f}(j_\mu)^* j_\nu. \tag{B.2}$$

Substituting the definition for the current into Equation B.2, we see that the terms involving Dirac spinors are heavily involved.

$$(j_\mu)^* j_\nu = \Big[\bar{\mathcal{U}}(\mathbf{k_f}, s_f)\gamma_\mu \mathcal{U}(\mathbf{k_i}, s_i)\Big]^* \Big[\bar{\mathcal{U}}(\mathbf{k_f}, s_f)\gamma_\nu \mathcal{U}(\mathbf{k_i}, s_i)\Big] \tag{B.3}$$

Lemma B.1.1 $\big[\bar{\mathcal{U}}_a \,\Gamma\, \mathcal{U}_b\big]^* = \big[\bar{\mathcal{U}}_b \,\overline{\Gamma}\, \mathcal{U}_a\big]$

We consider a general operator Γ, which can represent e.g. γ^μ. All Lorentz and spin indices are removed here for brevity but assume an operator always carries a Lorentz index and a spinor always carries a spin index unless otherwise specified.

The expressions that contain the spinors and the Dirac matrices are complex numbers and so taking the complex conjugate and adjoint are the equivalent.

$$\big[\bar{\mathcal{U}}_a \,\Gamma\, \mathcal{U}_b\big]^* = \big[\bar{\mathcal{U}}_a \,\Gamma\, \mathcal{U}_b\big]^\dagger \tag{B.4}$$

The definition of the adjoint, $\bar{\mathcal{U}}_a = \mathcal{U}_a^\dagger \gamma^0$, can be used to show that

$$\big[\mathcal{U}_a^\dagger \mathcal{U}_a \gamma^0 \,\Gamma\, \mathcal{U}_b\big]^\dagger = \big[\mathcal{U}_b^\dagger \,\Gamma^\dagger\, (\gamma^0)^\dagger\, \mathcal{U}_a\big]. \tag{B.5}$$

The fact $(\gamma^0)^\dagger = \gamma^0$ can now be used along with the identity relation $\mathbb{I} = \gamma^0\gamma^0$. And, using the fact that for general operators $\overline{\Gamma} = (\Gamma)^\dagger$, it can be shown that

$$\big[\mathcal{U}_b^\dagger \;\Gamma^\dagger\; \mathcal{U}_a\big] = \big[\mathcal{U}_b^\dagger \;\overline{\Gamma}\, \mathcal{U}_a\big], \tag{B.6}$$

which is simply

$$\left[\bar{\mathcal{U}}_b \,\overline{\Gamma}\, \mathcal{U}_a\right] \blacksquare \tag{B.7}$$

When using the normal gamma matrices as an operator, the Dirac adjoint is simply the gamma matrix itself, $\bar{\gamma^\mu} = \gamma^\mu$

Lemma B.1.2 *Comepleteness relation for Dirac spinors is given by the sum over the spins*

$$\sum_{s_A} \mathcal{U}(\mathbf{p_A}, s_A)\, \bar{\mathcal{U}}(\mathbf{p_A}, s_A) = \frac{1}{2M_A}(\not{P}_A + M_A) = \frac{1}{2M_A}(\gamma^\mu P_{\mu,A} + M_A) \tag{B.8}$$

Lemma B.1.3 *Trace theorems for Dirac spinors and operators in QED.*

The trace theorems are convenient theorems that turn expressions seen above in Equation B.3 into more easily manageable mathematical expressions. To show this, it is convenient to now write the explicit Lorentz indices and the matrix indices. Lorentz indices are given by Greek letters and in this section the matrix indices are given by alphabetic letters. The benefit of writing the matrix indices is that is reduces the quantities to numbers and so can be rearranged without worry of commutation relations.
Beginning with

$$\sum_s \sum_{a,b} \bar{\mathcal{U}}_a(\mathbf{k}, s)\ \gamma^\mu_{ab}\ \mathcal{U}_b(\mathbf{k}, s), \tag{B.9}$$

we can rearrange it to be

$$\sum_s \sum_{a,b} \mathcal{U}_b(\mathbf{k}, s)\bar{\mathcal{U}}_a(\mathbf{k}, s)\ \gamma^\mu_{ab}, \tag{B.10}$$

where one can now use Lemma B.1.2.

$$\sum_s \sum_{a,b} \mathcal{U}_b(\mathbf{k}, s)\bar{\mathcal{U}}_a(\mathbf{k}, s)\ \gamma^\mu_{ab} = \frac{1}{2M} \sum_{a,b} (\gamma^\lambda p_\lambda + M)_{ba}\ \gamma^\mu_{ab}. \tag{B.11}$$

This is now a trace of a matrix.

$$\frac{1}{2M} \sum_{a,b} (\gamma^\lambda p_\lambda + M)_{ba}\ \gamma^\mu_{ab} = \frac{1}{2M} \sum_b [(\gamma^\lambda p_\lambda + M)\gamma^\mu]_{bb} = \frac{1}{2M} \mathrm{Tr}[(\gamma^\lambda p_\lambda + M)\gamma^\mu]. \tag{B.12}$$

As a general rule for cases such as $\bar{\mathcal{U}}_a \Gamma_1 \mathcal{U}_b\, \bar{\mathcal{U}}_b\, \Gamma_2 \mathcal{U}_a$, one can use the aforementioned Lemmas and the completeness theorem to show that it results in

$$\frac{1}{(2M)^2} \mathrm{Tr}\left[(\gamma^\sigma p_\sigma + M)\Gamma_1^\mu\, (\gamma^\lambda p_\lambda + M)\Gamma_2^\nu\right] \tag{B.13}$$

B.1.1 Derivation

Armed with the previous Lemmas and results, we can now explicitly derive the lepton tensor.

Beginning with Equation B.2,

$$L'_{\mu\nu} = \frac{1}{2}\sum_{s_i}\sum_{s_f}(j_\mu)^* j_\nu = \frac{1}{2}\sum_{s_i}\sum_{s_f}\Big[\bar{\mathcal{U}}(\mathbf{k_f}, s_f)\gamma_\mu \mathcal{U}(\mathbf{k_i}, s_i)\Big]^*\Big[\bar{\mathcal{U}}(\mathbf{k_f}, s_f)\gamma_\nu \mathcal{U}(\mathbf{k_i}, s_i)\Big], \quad \text{(B.14)}$$

we can use Lemma B.1.1 to rewrite it as

$$= \frac{1}{2}\sum_{s_i}\sum_{s_f}\Big[\bar{\mathcal{U}}(\mathbf{k_i}, s_i)\gamma_\mu \mathcal{U}(\mathbf{k_f}, s_f)\Big]\Big[\bar{\mathcal{U}}(\mathbf{k_f}, s_f)\gamma_\nu \mathcal{U}(\mathbf{k_i}, s_i)\Big], \quad \text{(B.15)}$$

$$= \frac{1}{2}\sum_{s_i}\Big[\bar{\mathcal{U}}(\mathbf{k_i}, s_i)\gamma_\mu \frac{1}{2m_f}(\gamma^\lambda K_{f,\lambda} + m_f)\gamma_\nu \mathcal{U}(\mathbf{k_i}, s_i)\Big], \quad \text{(B.16)}$$

using Lemma B.1.2. We can now use Lemma B.1.3 to employ traces

$$= \frac{1}{2}\frac{1}{4m_i m_f}\mathrm{Tr}\Big[(\gamma^\sigma K_{i,\sigma} + m_i)\gamma_\mu(\gamma^\lambda K_{f,\lambda} + m_f)\gamma_\nu\Big]. \quad \text{(B.17)}$$

Expanding out the term inside the brackets, we get

$$\underbrace{\gamma_\sigma K_i^\sigma \gamma_\mu \gamma_\lambda K_f^\lambda \gamma_\nu}_{\text{Term A}} + \overbrace{\gamma_\sigma K_i^\sigma \gamma_\mu m_f \gamma_\nu}^{\text{Term B}} + \underbrace{m_i \gamma_\mu \gamma_\lambda K_f^\lambda \gamma_\nu}_{\text{Term C}} + \overbrace{m_i m_f \gamma_\mu \gamma_\nu}^{\text{Term D}}. \quad \text{(B.18)}$$

Now employing the trace to each term (the trace acts only on the spinor indices), we get:

1. Term A:

$$K_i^\sigma K_f^\lambda \mathrm{Tr}\big[\gamma_\sigma \gamma_\mu \gamma_\lambda \gamma_\nu\big] = 4K_i^\sigma K_f^\lambda\big[g_{\sigma\mu}g_{\lambda\nu} - g_{\sigma\lambda}g_{\mu\nu} + g_{\sigma\nu}g_{\mu\lambda}\big] \quad \text{(B.19)}$$

2. Term B:

$$m_f K_i^\sigma \mathrm{Tr}\big[\gamma_\sigma \gamma_\mu \gamma_\nu\big] = 0 \quad \text{(B.20)}$$

3. Term C:

$$m_i K_f^\lambda \mathrm{Tr}\big[\gamma_\mu \gamma_\lambda \gamma_\nu\big] = 0 \quad \text{(B.21)}$$

4. Term D:

$$m_i m_f \mathrm{Tr}\big[\gamma_\mu \gamma_\nu\big] = 4m_i m_f g_{\mu\nu} \quad \text{(B.22)}$$

Finally

$$L'_{\mu\nu} = \frac{1}{2}\frac{1}{4m_i m_f}\Big[K_{i,\mu}K_{f,\nu} + K_{i,\nu}K_{f,\mu} - g_{\mu\nu}(K_i \cdot K_f - m_i m_f)\Big], \tag{B.23}$$

where it is often convention to multiply by the lepton masses to get

$$L_{\mu\nu} \overset{def}{=} m_i m_f L'_{\mu\nu} = \frac{1}{2}\Big[K_{i,\mu}K_{f,\nu} + K_{i,\nu}K_{f,\mu} - g_{\mu\nu}(K_i \cdot K_f - m_i m_f)\Big]. \tag{B.24}$$

B.2 Explicit hadron tensor derivation

The expression for the hadron current and tensor are

$$J^\nu = \bar{\mathcal{U}}(\mathbf{p_N}, s_N)\Gamma^\nu(Q^2)\mathcal{U}(\mathbf{p_i}, s) \tag{B.25}$$

and

$$H^{\mu\nu} \overset{\text{def}}{=} \frac{1}{2}\sum_s\sum_{s_N}(J^\mu)^* J^\nu. \tag{B.26}$$

Substituting the definition for the current into the tensor and using the same trace theorems as B.1.3, we get

$$H^{\mu\nu} = \frac{1}{2}\mathrm{Tr}\Big[\frac{\gamma^\lambda p_\lambda + M}{2M}\bar{\Gamma}^\mu_{\text{EM|CC1}}\frac{\gamma^\sigma p_{N,\sigma} + M}{2M}\Gamma^\nu_{\text{EM|CC1}}\Big]. \tag{B.27}$$

Recall the operator $\Gamma^\mu_{\text{EM|CC1}}$ is given by

$$\Gamma^\mu_{\text{EM|CC1}} = (F_1 + F_2)\gamma^\mu - (\frac{F_2}{2M})(p + p_N)^\mu. \tag{B.28}$$

We can treat the conjugate $\bar{\Gamma}^\mu = \Gamma^\mu$ and let $A^\mu = (F_1 + F_2)\gamma^\mu$ and $B^\mu = \left(\frac{F_2}{2M}\right)(p + p_N)^\mu$. Then, on expanding Equation B.27, we obtain four terms.

$$\begin{aligned}(\gamma^\lambda p_\lambda + M)[A^\mu - B^\mu](\gamma^\sigma p_{N,\sigma} + M)[A^\nu - B^\nu] = \\ +(\gamma^\lambda p_\lambda + M)A^\mu(\gamma^\sigma p_{N,\sigma} + M)A^\nu \\ -(\gamma^\lambda p_\lambda + M)A^\mu(\gamma^\sigma p_{N,\sigma} + M)B^\nu \\ -(\gamma^\lambda p_\lambda + M)B^\mu(\gamma^\sigma p_{N,\sigma} + M)A^\nu \\ +(\gamma^\lambda p_\lambda + M)B^\mu(\gamma^\sigma p_{N,\sigma} + M)B^\nu\end{aligned} \tag{B.29}$$

Term 1

The first term is

$$(\gamma^\lambda p_\lambda + M)A^\mu(\gamma^\sigma p_{N,\sigma} + M)A^\nu, \tag{B.30}$$

which, when using Lemma B.1.3, becomes

$$\mathrm{Tr}\Big[(\gamma^\lambda p_\lambda + M)(F_1 + F_2)\gamma^\mu(\gamma^\sigma p_{N,\sigma} + M)(F_1 + F_2)\gamma^\nu\Big]. \tag{B.31}$$

Expanding out the brackets yields

$$(F_1 + F_2)^2\ \mathrm{Tr}\Big[\gamma^\lambda p_\lambda \gamma^\mu \gamma^\sigma p_{N,\sigma}\gamma^\nu + M\gamma^\lambda p_\lambda \gamma^\mu \gamma^\nu + M\gamma^\mu\gamma^\sigma p_{N,\sigma}\gamma^\nu + M^2\gamma^\mu\gamma^\nu\Big], \tag{B.32}$$

where the second and third terms within the trace is 0 due to taking the trace of an odd number of gamma matrices. This leaves

$$\begin{aligned} &4(F_1 + F_2)^2\ \mathrm{Tr}\Big[p_\lambda p_{N,\sigma}\ (g^{\lambda\mu}g^{\sigma\nu} - g^{\lambda\sigma}g^{\mu\nu} + g^{\lambda\nu}g^{\mu\sigma}) + M^2 g^{\mu\nu}\Big] \\ &= 4(F_1 + F_2)^2\ \Big[p^\mu p_N^\nu + p^\nu p_N^\mu - g^{\mu\nu}(P \cdot P_N) + M^2 g^{\mu\nu}\Big] \\ &= 4(F_1 + F_2)^2\ \Big[p^\mu p_N^\nu + p^\nu p_N^\mu + (M^2 - P \cdot P_N)g^{\mu\nu}\Big] \end{aligned} \tag{B.33}$$

Term 2

The second term is

$$(\gamma^\lambda p_\lambda + M)A^\mu(\gamma^\sigma p_{N,\sigma} + M)B^\nu \tag{B.34}$$

which becomes

$$\mathrm{Tr}\ \Big[(\gamma^\lambda p_\lambda + M)(F_1 + F_2)\gamma^\mu(\gamma^\sigma p_{N,\sigma} + M)\big(\frac{F_2}{2M}\big)(p + p_N)^\nu\Big]. \tag{B.35}$$

Through similar manipulations, the second term simplifies to

$$\frac{4F_2(F_1 + F_2)}{2}\big(p + p_N\big)^\mu\big(p + p_N\big)^\nu \tag{B.36}$$

B.2.1 Term 3

The third term is

$$(\gamma^\lambda p_\lambda + M)B^\mu(\gamma^\sigma p_{N,\sigma} + M)A^\nu \tag{B.37}$$

which becomes

$$(\gamma^\lambda p_\lambda + M)(\frac{F_2}{2M})(p + p_N)^\mu(\gamma^\sigma p_{N,\sigma} + M)(F_1 + F_2)\gamma^\nu. \tag{B.38}$$

Through similar manipulations, the third term simplifies to

$$\frac{4F_2(F_1 + F_2)}{2}\big(p + p_N\big)^\mu\big(p + p_N\big)^\nu, \tag{B.39}$$

which is identical to the second term.

B.2.2 Term 4

The final term is

$$(\gamma^{\lambda}p_{\lambda} + M)B^{\mu}(\gamma^{\sigma}p_{N,\sigma} + M)B^{\nu} \tag{B.40}$$

which becomes

$$(\gamma^{\lambda}p_{\lambda} + M)(\frac{F_2}{2M})(p + p_N)^{\mu}(\gamma^{\sigma}p_{N,\sigma} + M)(\frac{F_2}{2M})(p + p_N)^{\nu}. \tag{B.41}$$

Through similar manipulations, the fourth term simplifies to

$$4\Big(\frac{F_2}{2M}\Big)^2(P \cdot P_N + M^2)(p + p_N)^{\mu}(p + p_N)^{\nu}. \tag{B.42}$$

B.2.3 All terms

The hadron tensor is given by Equation B.29, which after substituting the simplified forms of all terms, yields

$$\begin{aligned} H^{\mu\nu} = \frac{1}{2M^2}\Bigg\{ & (F_1 + F_2)^2\big[p^{\mu}p_N^{\nu} + p^{\nu}p_N^{\mu} + g^{\mu\nu}(M^2 - P \cdot P_N)\big] \\ & + \Big[\big(\frac{F_2}{2M}\big)^2(P \cdot P_N + M^2) - (F_1 + F_2)F_2\Big](p + p_N)^{\mu}(p + p_N)^{\nu}\Bigg\}. \end{aligned} \tag{B.43}$$

Appendix C

C.1 Electromagnetic and quark currents

The EM current, J_μ^{EM}, can be described in terms of quark fields (a vector of quark fields), f, as

$$J_\mu^{\mathrm{EM}} = Q_q \bar{q} \gamma_\mu q, \tag{C.1}$$

where γ_μ are the Dirac matrices and Q_q is the quark charge matrix. Considering only the u and d quarks, Q_q is given by

$$Q_q = \begin{pmatrix} +\frac{2}{3} & 0 \\ 0 & -\frac{1}{3} \end{pmatrix}, \tag{C.2}$$

and $q = \begin{pmatrix} u \\ d \end{pmatrix}$. Therefore, J_μ^{EM} can be expressed as

$$J_\mu^{\mathrm{EM}} = \frac{2}{3}\bar{u}\gamma^\mu u - \frac{1}{3}\bar{d}\gamma_\mu d. \tag{C.3}$$

In two-flavour QCD, the quarks form an $SU(2)$ doublet as written above. The $SU(2)$ group has three generators given by the Pauli spin matrices, σ^i. From this the isovector currents can be defined as

$$V_\mu^i = \frac{1}{2}\bar{q}\gamma_\mu \sigma^i q \ ; \quad i = 1, 2, 3. \tag{C.4}$$

The EM interaction does not change quark flavour, therefore it does not change isospin. Only the third Pauli spin matrix has this property, meaning only the third isovector current contributes to the EM interaction. This is given explicitly as

$$V_\mu^3 = \frac{1}{2}\begin{pmatrix} \bar{u} & \bar{d} \end{pmatrix} \gamma_\mu \begin{pmatrix} 1 & 0 \\ 0 & -1 \end{pmatrix} \begin{pmatrix} u \\ d \end{pmatrix} = \frac{1}{2}(\bar{u}\gamma_\mu u - \bar{d}\gamma_\mu d). \tag{C.5}$$

The quarks also form a singlet isoscalar state with the generator given by the identity matrix. Since this also conserves isospin, it contributes to the EM current. This is given

explicitly as

$$V_\mu^0 = \begin{pmatrix} \bar{u} & \bar{d} \end{pmatrix} \gamma_\mu \begin{pmatrix} 1 & 0 \\ 0 & 1 \end{pmatrix} \begin{pmatrix} u \\ d \end{pmatrix} = \bar{u}\gamma_\mu u + \bar{d}\gamma_\mu d. \tag{C.6}$$

The isoscalar and isovector currents can be used as a basis (known as the isospin basis) to describe the EM current. This is done by writing

$$\begin{aligned} \bar{u}\gamma_\mu u &= \frac{1}{2}(V_\mu^0 + 2V_\mu^3) \\ \bar{d}\gamma_\mu d &= \frac{1}{2}(V_\mu^0 - 2V_\mu^3), \end{aligned} \tag{C.7}$$

therefore,

$$J_\mu^{\mathrm{EM}} = \frac{1}{6}V_\mu^0 + V_\mu^3. \tag{C.8}$$

From this we can deduce that the EM interaction is mediated mostly by isovector contributions, with some isoscalar contributions. This naturally leads to the isoscalar and isovector form factor descriptions of the EM current. The isoscalar and isovector form factors are given as

$$\begin{aligned} \langle N | V_\mu^0 | N \rangle &\to F_i^{\mathrm{isoscalar}}(Q^2) = F_i^p + F_i^n \\ \langle N | V_\mu^3 | N \rangle &\to F_i^{\mathrm{isovector}}(Q^2) = F_i^p - F_i^n, \end{aligned} \tag{C.9}$$

where N is a free nucleon state and Q^2 is the transferred four momentum.

C.2 Charged-current and quark currents

In a manner similar to the EM current, the weak CC current can be described in terms of a vector of quark fields. The weak CC current changes isospin by a factor of 1 by changing the quark field $u \to d$ (mediated by a W^+ boson) or $d \to u$ (mediated by a W^- boson). The weak CC current also has an axial-vector component. The weak CC current can be written as

$$J_\mu^{\mathrm{CC}} = J_\mu^{\mathrm{CC},+} + J_\mu^{\mathrm{CC},-}, \tag{C.10}$$

with

$$\begin{aligned} J_\mu^{\mathrm{CC},+} &= \bar{u}\gamma_\mu(1-\gamma_5)d \\ J_\mu^{\mathrm{CC},-} &= \bar{d}\gamma_\mu(1-\gamma_5)u. \end{aligned} \tag{C.11}$$

The vector and vector-axial currents can be written explicitly as

$$\begin{aligned} V_\mu^a &= \frac{1}{2}\bar{q}\gamma_\mu\sigma^a q \\ A_\mu^a &= \frac{1}{2}\bar{q}\gamma_\mu\gamma_5\sigma^a q. \end{aligned} \tag{C.12}$$

By forming isospin ladder operators from $\sigma^{\pm} = \sigma^1 \pm i\sigma^2$, the following vector and axial-vector operators can be written:

$$\begin{aligned} V_\mu^{\pm} &= \frac{1}{2}\bar{q}\gamma_\mu\sigma^{+}q \\ A_\mu^{\pm} &= \frac{1}{2}\bar{q}\gamma_\mu\gamma_5\sigma^{+}q. \end{aligned} \tag{C.13}$$

These ladder operators mediate the isospin change. Writing each operator out explicitly, we see

$$\begin{aligned} V_\mu^{+} &= \frac{1}{2}\bar{q}\gamma_\mu\sigma^{+}q = \bar{u}\gamma_\mu d, \\ V_\mu^{-} &= \frac{1}{2}\bar{q}\gamma_\mu\sigma^{-}q = \bar{d}\gamma_\mu u, \\ A_\mu^{+} &= \frac{1}{2}\bar{q}\gamma_\mu\gamma_5\sigma^{+}q = \bar{u}\gamma_\mu\gamma_5 d, \\ A_\mu^{-} &= \frac{1}{2}\bar{q}\gamma_\mu\gamma_5\sigma^{-}q = \bar{d}\gamma_\mu\gamma_5 u. \end{aligned} \tag{C.14}$$

From this, it is clear that

$$\begin{aligned} J_\mu^{\mathrm{CC}} &= (V_\mu^{+} + V_\mu^{-}) - (A_\mu^{+} + A_\mu^{-}) \\ &= \bar{q}\gamma_\mu(1-\gamma_5)\sigma^1 q. \end{aligned} \tag{C.15}$$

C.2.1 Conserved vector current hypothesis

The conserved vector current (CVC) hypothesis relates the isovector component of the EM current to the vector component of the weak current. In the isospin limit (assuming $m_u = m_d$), then the CVC states that

$$\partial^\mu V_\mu^a = 0. \tag{C.16}$$

Since nucleons can be placed into an isospin doublet based on I and I_3, the Wigner-Eckart theorem allows one to relate the EM isovector operator to the CC ladder vector operators and finds that they are part of the same isotriplet. The full theorem states that the reduced matrix elements are the same up to Clebsch–Gordan coefficients.

C.3 Neutral-current and quark currents

In a manner similar to the EM current, the NC current can be described in terms of a vector of quark fields. Although this is not the focus of this thesis, the relation between the NC and EM currents is relevant. The NC current can be written as

$$J_\mu^{\mathrm{NC}} = \bar{q}\gamma_\mu(I_3 - 2Q_q \sin^2\theta_W)q \tag{C.17}$$

for two-flavour QCD. Here I_3 is the third component of isospin ($\pm\frac{1}{2}$ for left and right handed fermions respectively) and θ_W is the weak mixing angle (the Weinberg angle). Writing in the explicit values of I_3 and Q_q, the NC current can be written as

$$J_\mu^{\mathrm{NC}} = \bar{u}\gamma_\mu(\frac{1}{2} - \frac{4}{3}\sin^2\theta_W)u + \bar{d}\gamma_\mu(-\frac{1}{2} + \frac{2}{3}\sin^2\theta_W)d \tag{C.18}$$

, which, after regrouping by weak mixing angle dependence, can be written as

$$J_\mu^{\mathrm{NC}} = \underbrace{\frac{1}{2}(\bar{u}\gamma_\mu u - \bar{d}\gamma_\mu d)}_{V_\mu^3} - \sin^2\theta_W \underbrace{(\frac{2}{3}\bar{u}\gamma_\mu u - \frac{1}{3}\bar{d}\gamma_\mu d)}_{J_\mu^{\mathrm{EM}}}. \tag{C.19}$$

Therefore, we arrive at

$$J_\mu^{\mathrm{NC}} = V_\mu^3 - \sin^2\theta_W J_\mu^{\mathrm{EM}}, \tag{C.20}$$

which, after rewriting in terms of the isospin basis, is

$$J_\mu^{\mathrm{NC}} = (1 - \sin^2\theta_W)V_\mu^3 - \frac{1}{6}\sin^2\theta_W V_\mu^0. \tag{C.21}$$

From this we deduce that the isoscalar and isovector currents contribute to the NC current. This is expected as the NC channel does not change the flavour of the quarks and therefore does not change the isospin.

The form factors that describe the NC channel can therefore be expressed in terms of the isoscalar and isovector form factors. Until now, the two-flavour QCD approximation has been used. In reality, there is a contribution from the s quark. The form factors for the NC current can be written as:

$$F_i^{\mathrm{NC}} = (1 - \sin^2\theta_W)F_i^{\mathrm{isovector}} - \frac{1}{6}\sin^2\theta_W F_i^{\mathrm{isoscalar}} - \frac{1}{2}F_i^s, \tag{C.22}$$

where F_i^s are the strange form factors.

Appendix D

D.1 Total cross section for carbon

The total cross section for the ED-RMF, RPWIA, EDAI and rEDAI models are given for all neutrino flavours and helicities in Figure D.1.

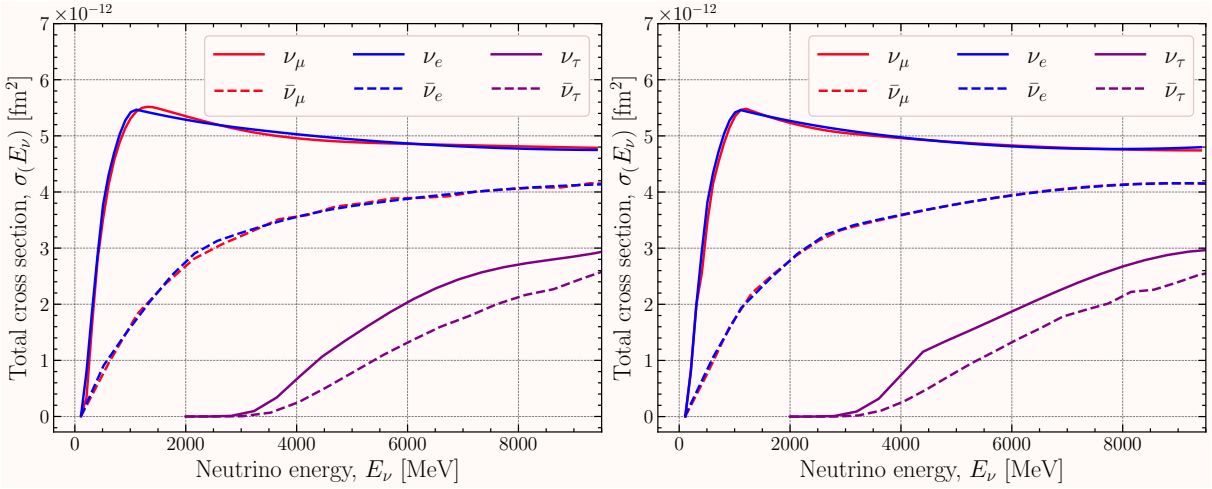

(a) ED-RMF on ^{12}C

(b) rEDAI on ^{12}C

(c) EDAI on ^{12}C

(d) RPWIA on ^{12}C

Figure D.1: Total cross section for ED-RMF, EDAI, rEDAI and RPWIA model on ^{12}C.

D.2 Total cross section for oxygen

The total cross section for the ED-RMF, RPWIA, EDAI and rEDAI models are given for all neutrino flavours and helicities in Figure D.2.

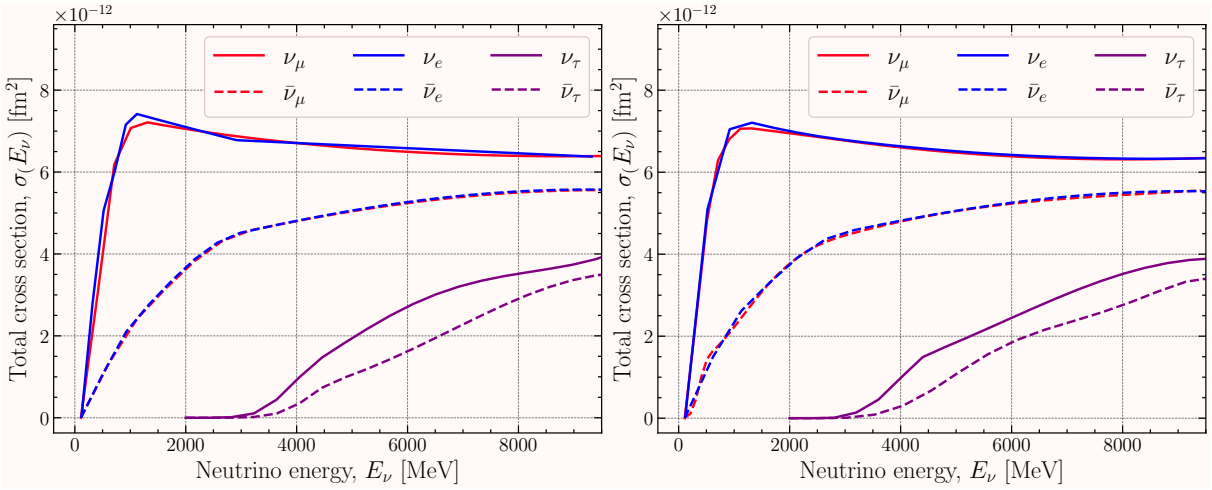

(a) ED-RMF on ^{16}O

(b) rEDAI on ^{16}O

(c) EDAI on ^{16}O

(d) RPWIA on ^{16}O

Figure D.2: Total cross section for ED-RMF, EDAI, rEDAI and RPWIA model on ^{16}O.

D.3 Maximum differential cross section for carbon

The maximum six-fold differential cross section for the ED-RMF, RPWIA, EDAI and rEDAI models are given for all neutrino flavours and helicities in Figure D.3.

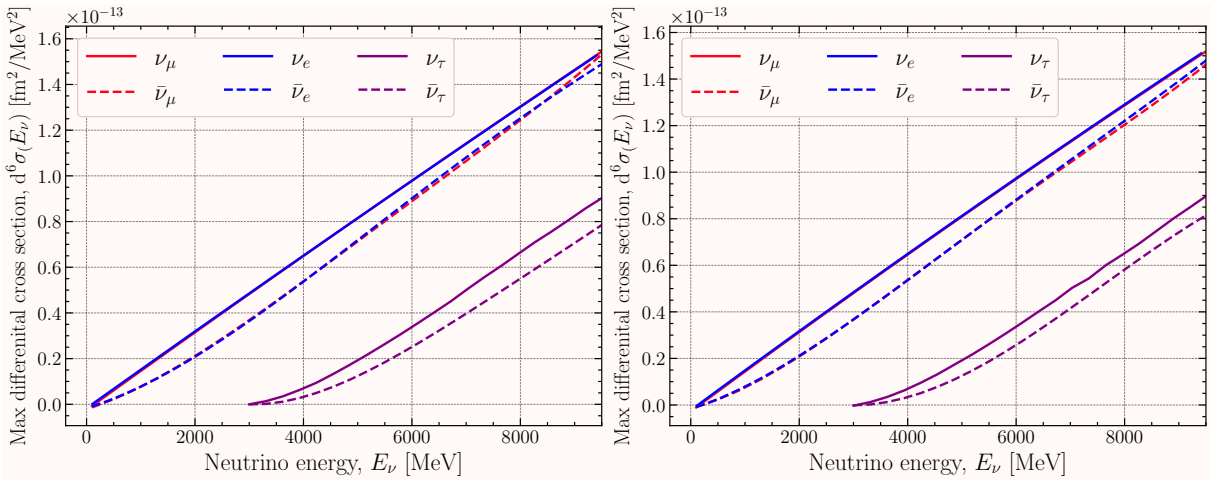

(a) ED-RMF on ^{12}C

(b) rEDAI on ^{12}C

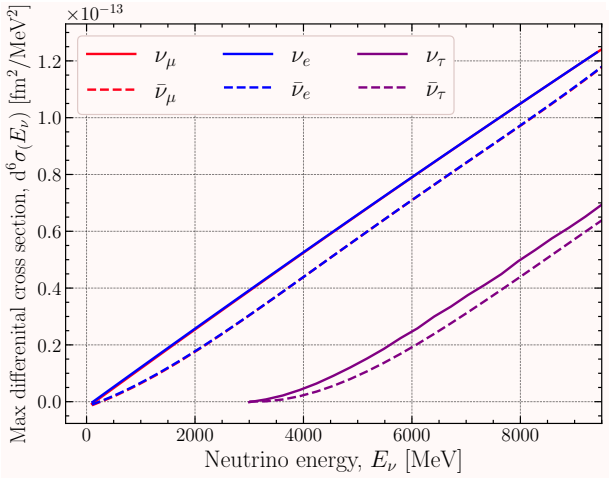

(c) EDAI on ^{12}C

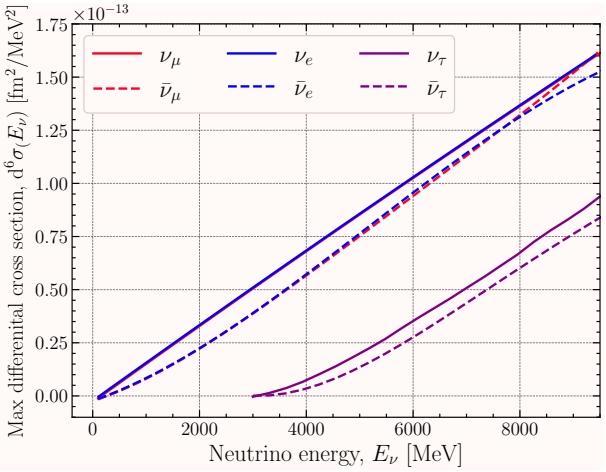

(d) RPWIA on ^{12}C

Figure D.3: Maximum six-fold differential cross section for ED-RMF, EDAI, rEDAI and RPWIA model on ^{12}C.

D.4 Maximum differential cross section for oxygen

The maximum six-fold differential cross section for the ED-RMF, RPWIA, EDAI and rEDAI models are given for all neutrino flavours and helicities in Figure D.4.

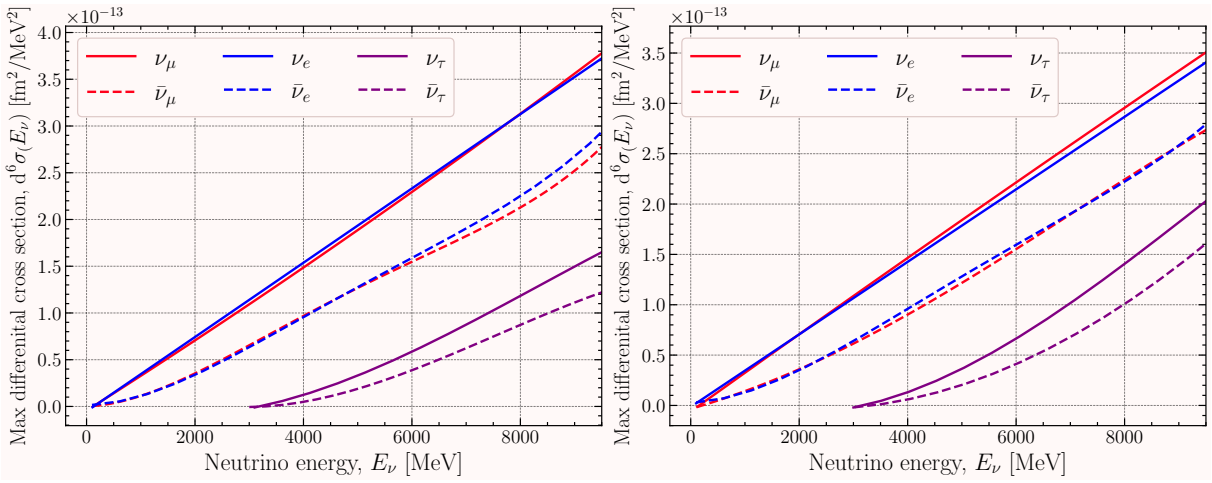

(a) ED-RMF on ^{16}O

(b) rEDAI on ^{16}O

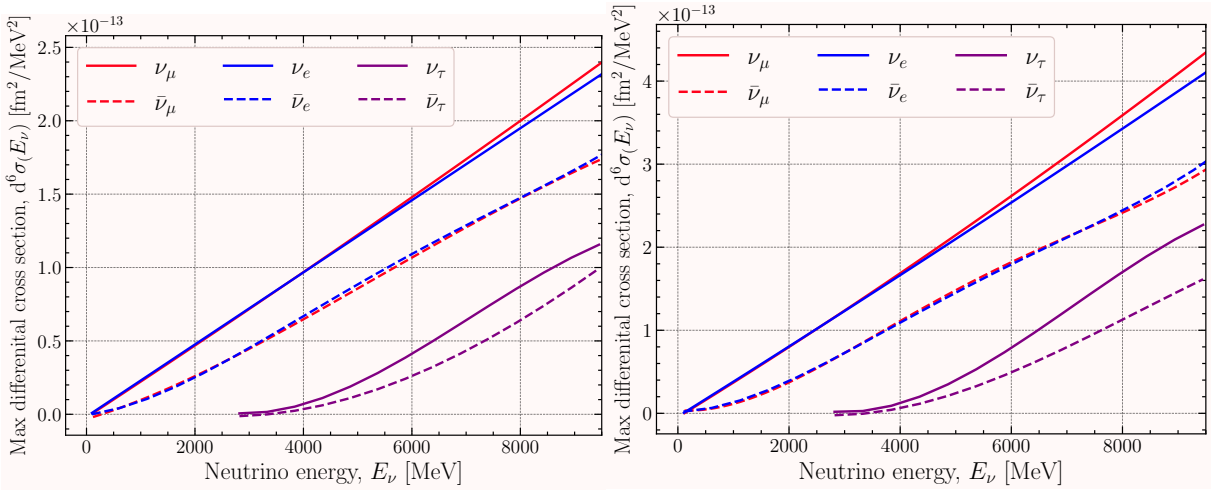

(c) EDAI on ^{16}O

(d) RPWIA on ^{16}O

Figure D.4: Maximum six-fold differential cross section for ED-RMF, EDAI, rEDAI and RPWIA model on ^{16}O.

Appendix E

E.1 RPWIA model validation

E.1.1 Normalised single differential cross section on Carbon

Carbon ν_μ

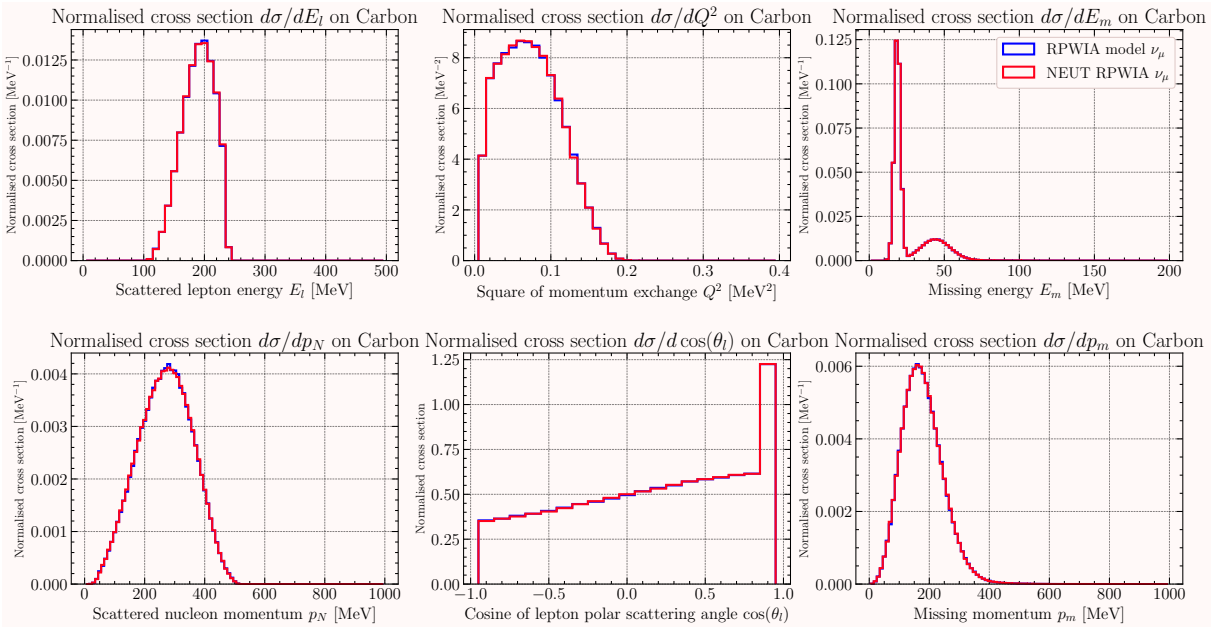

Carbon ν_e

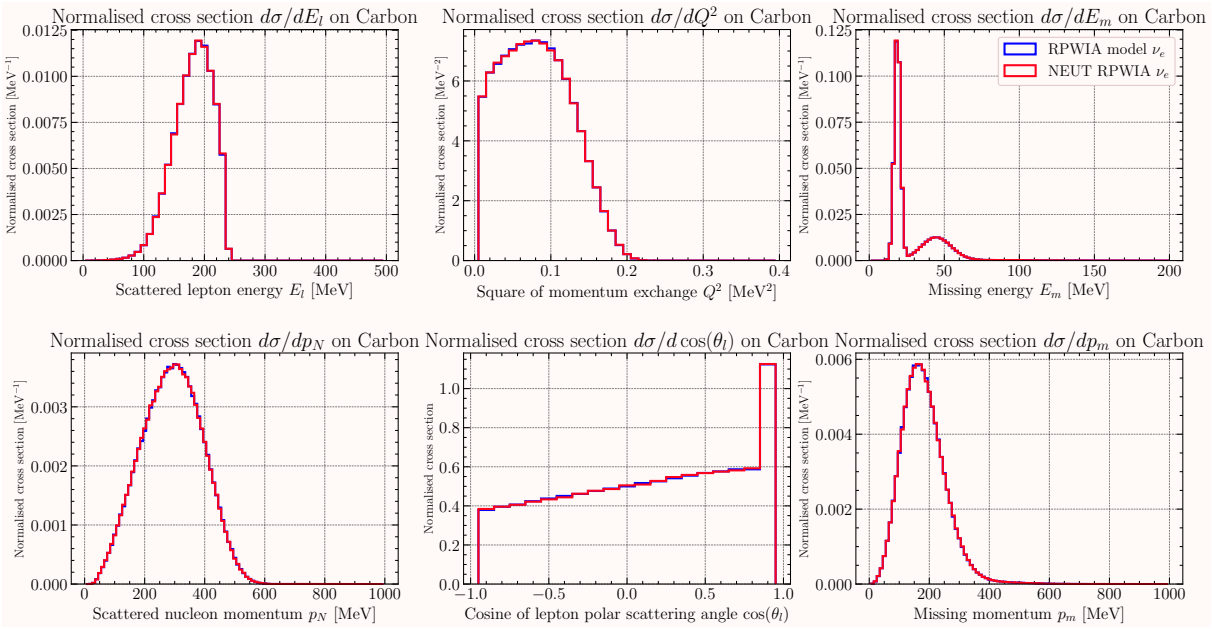

Carbon $\bar{\nu}_\mu$

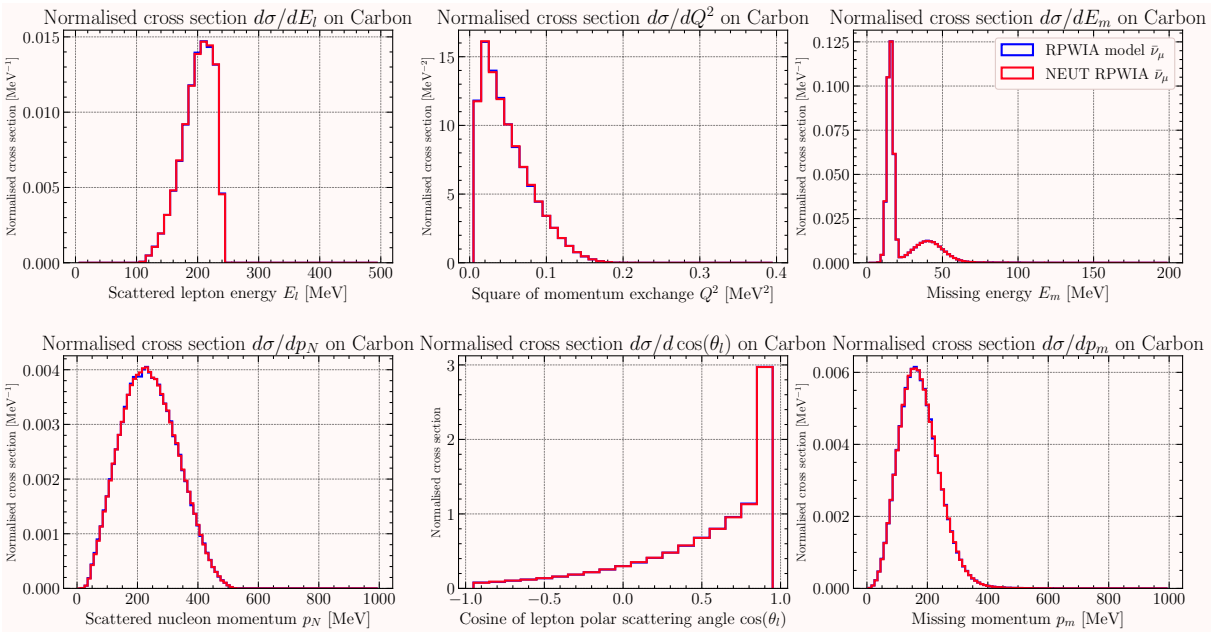

Carbon $\bar{\nu}_e$

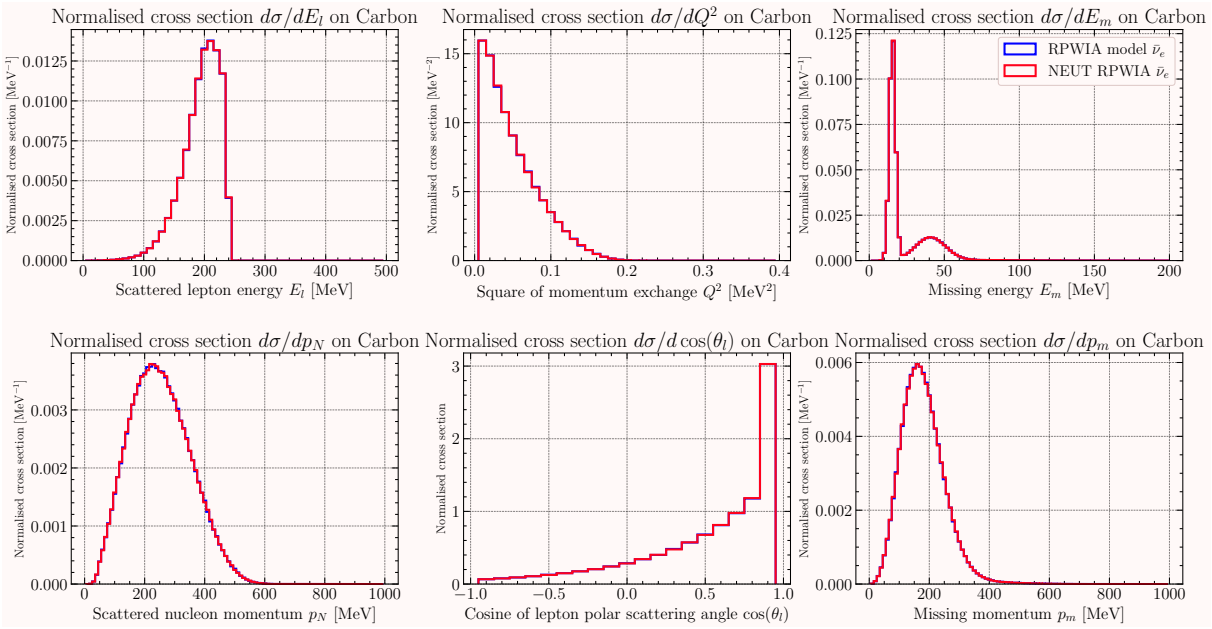

E.1.2 Normalised single differential cross section on Oxygen

Oxygen ν_μ

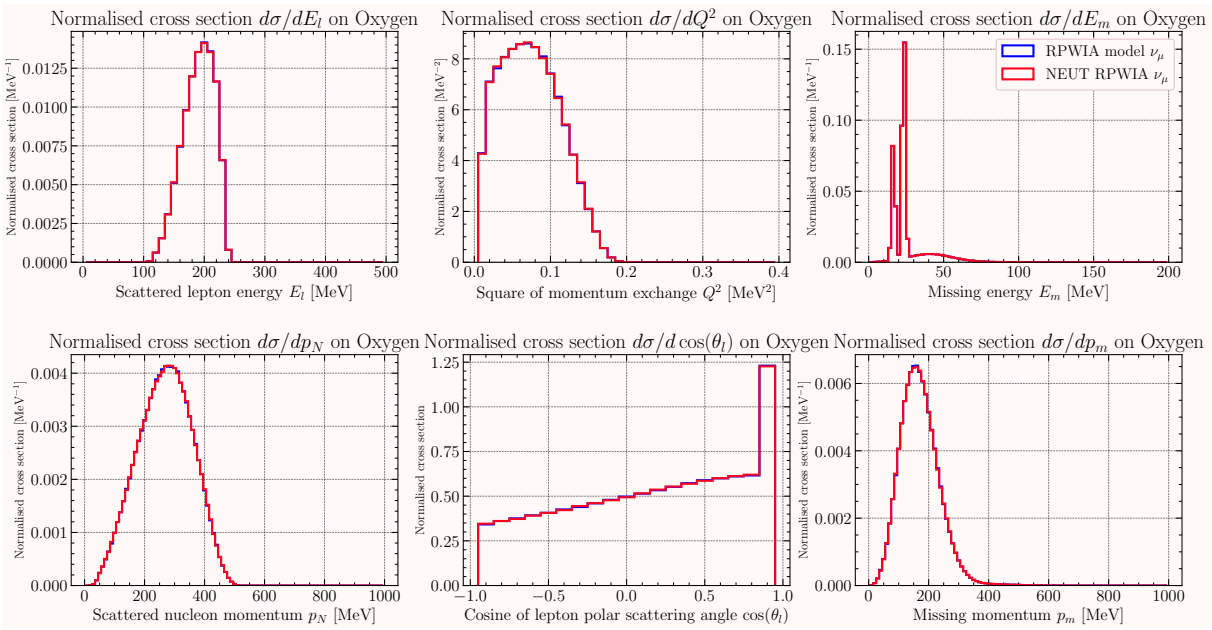

Oxygen ν_e

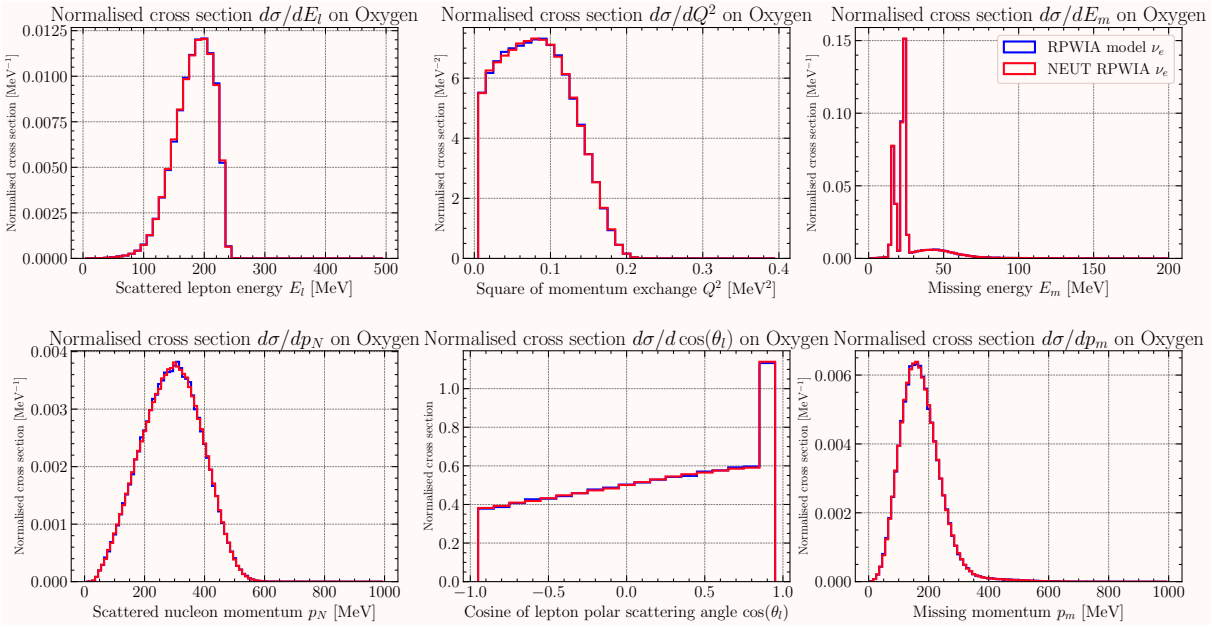

Oxygen $\bar{\nu}_\mu$

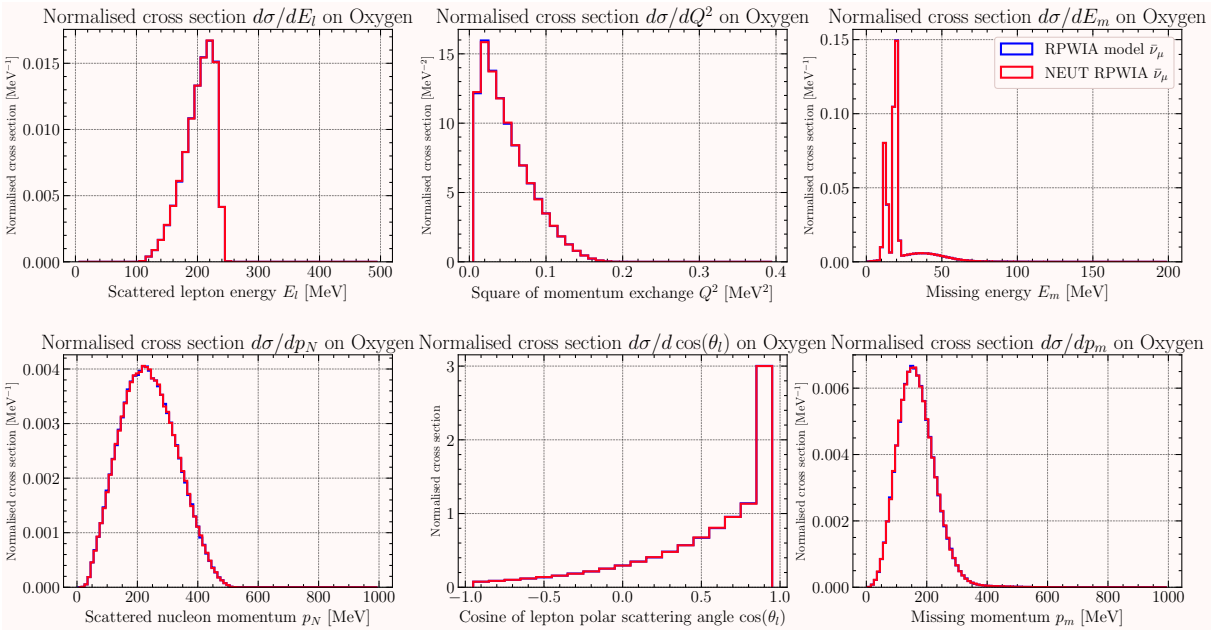

Oxygen $\bar{\nu}_e$

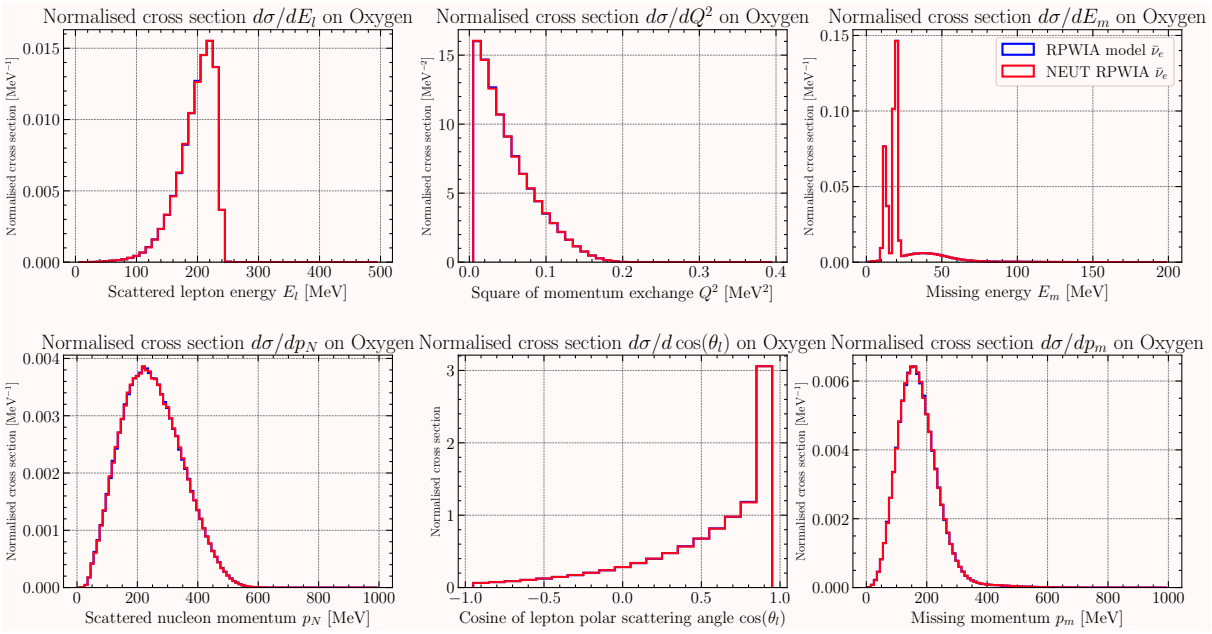

E.2 EDAI model validation

E.2.1 Normalised single differential cross section on Carbon

Carbon ν_μ

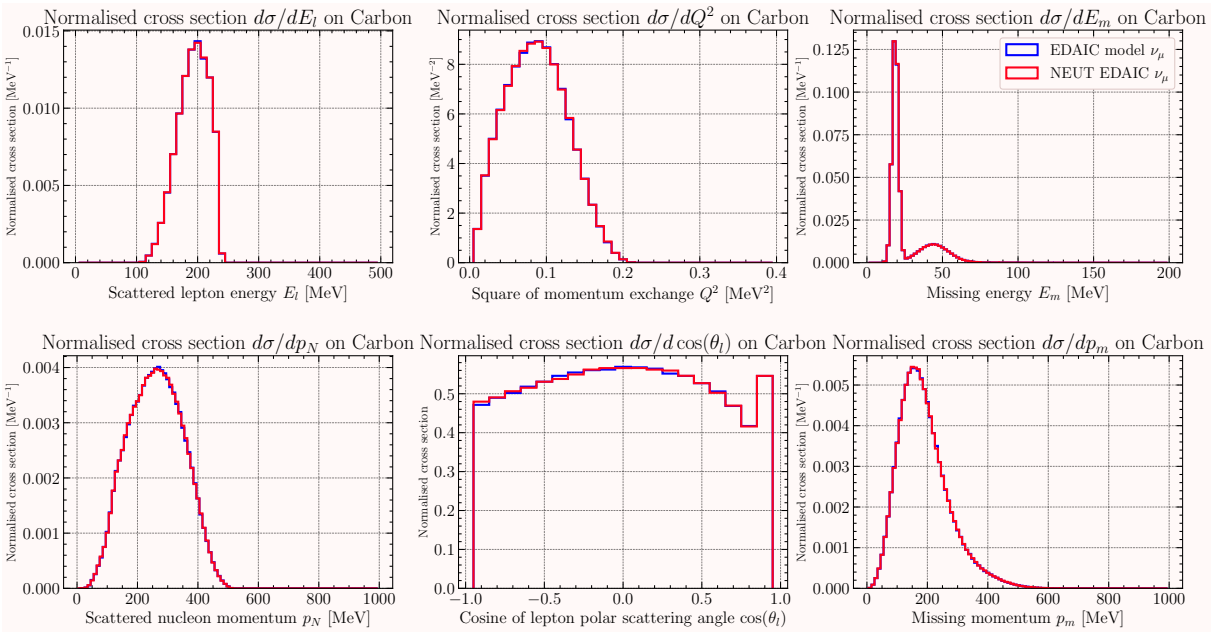

Carbon ν_e

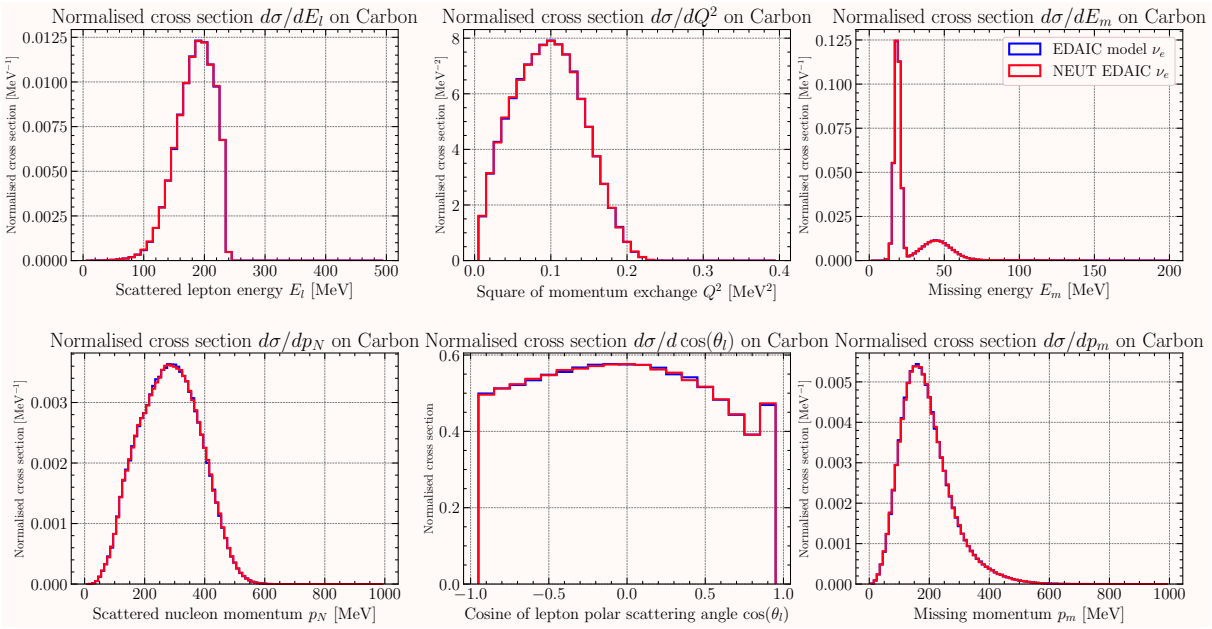

Carbon $\bar{\nu}_\mu$

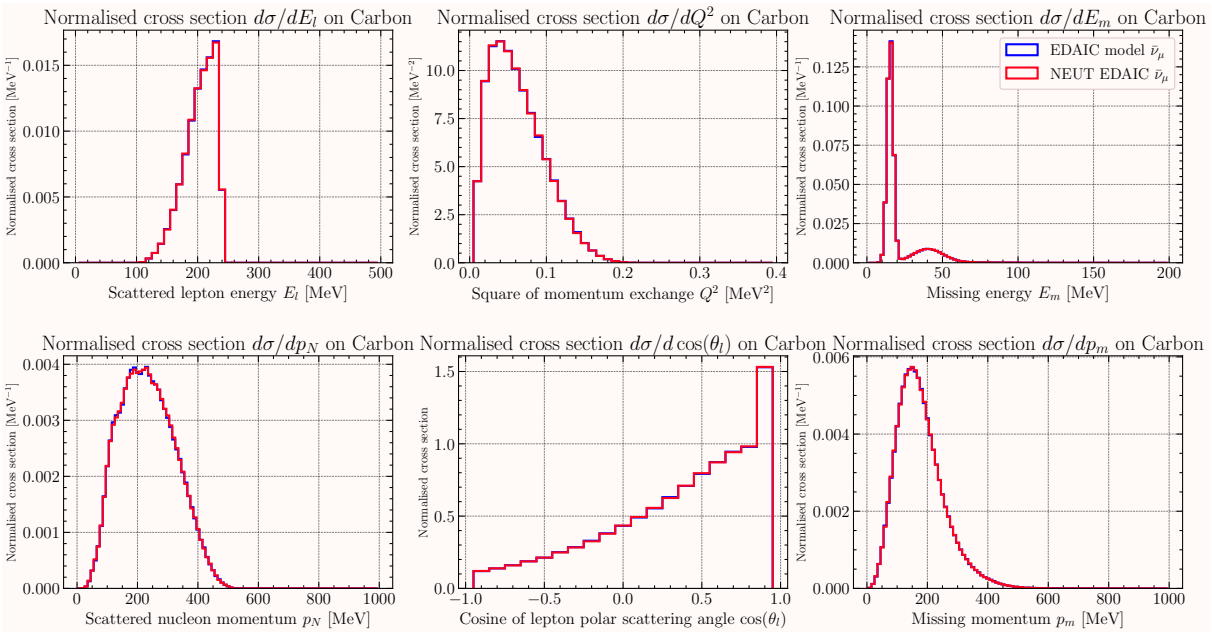

Carbon $\bar{\nu}_e$

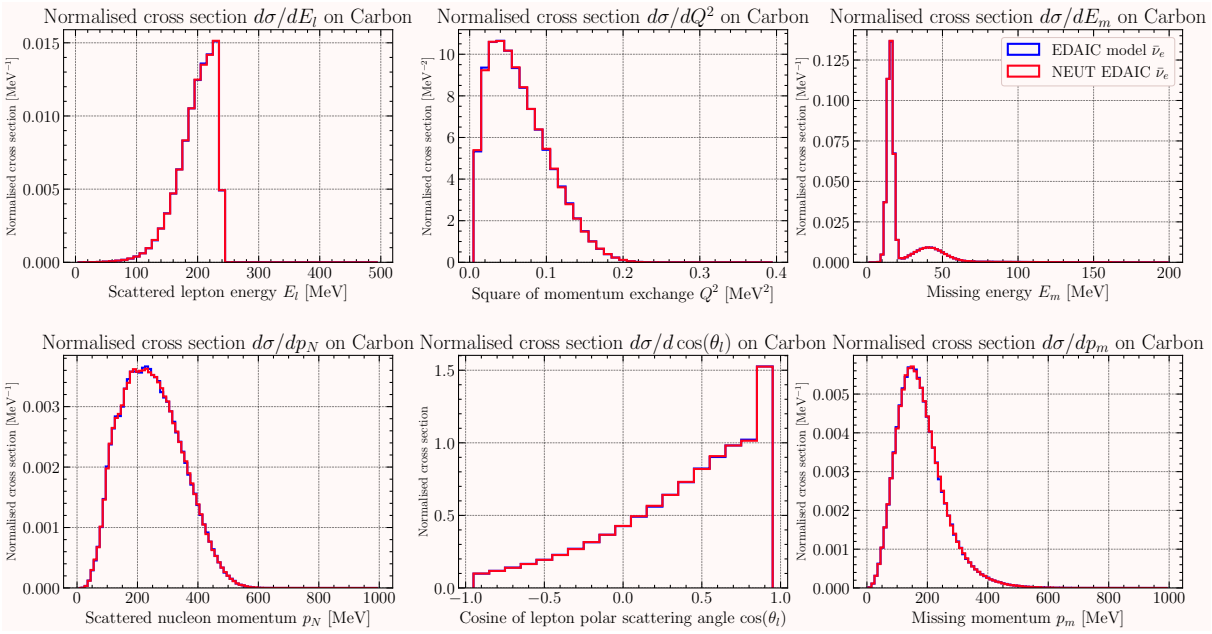

E.2.2 Normalised single differential cross section on Oxygen

Oxygen ν_μ

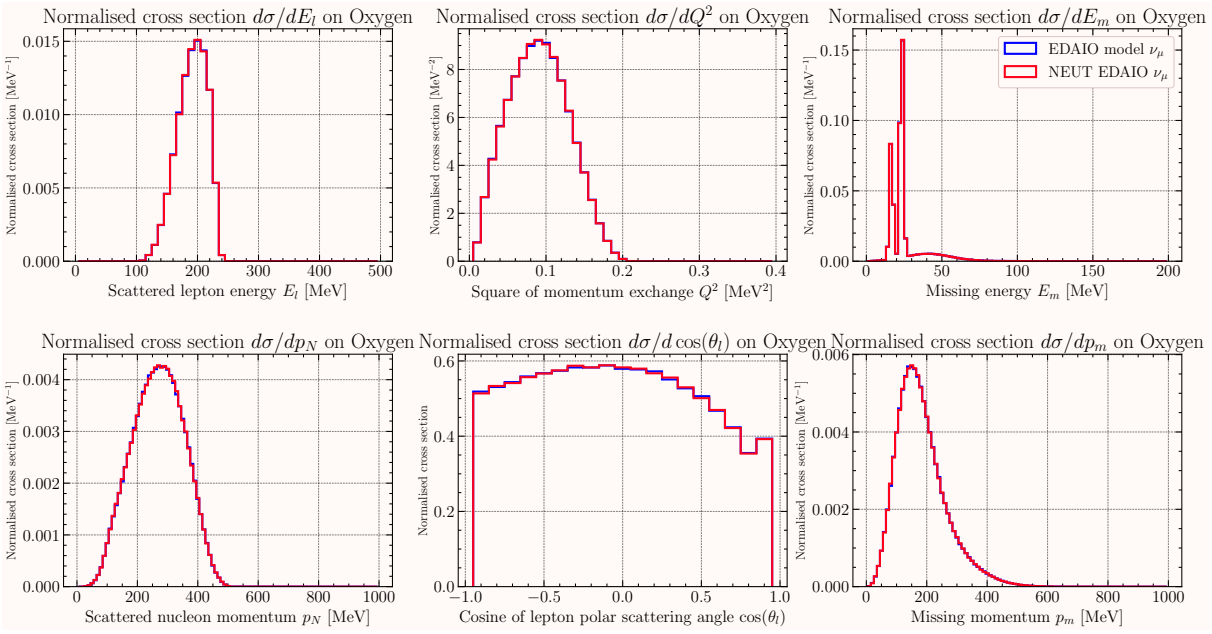

Oxygen ν_e

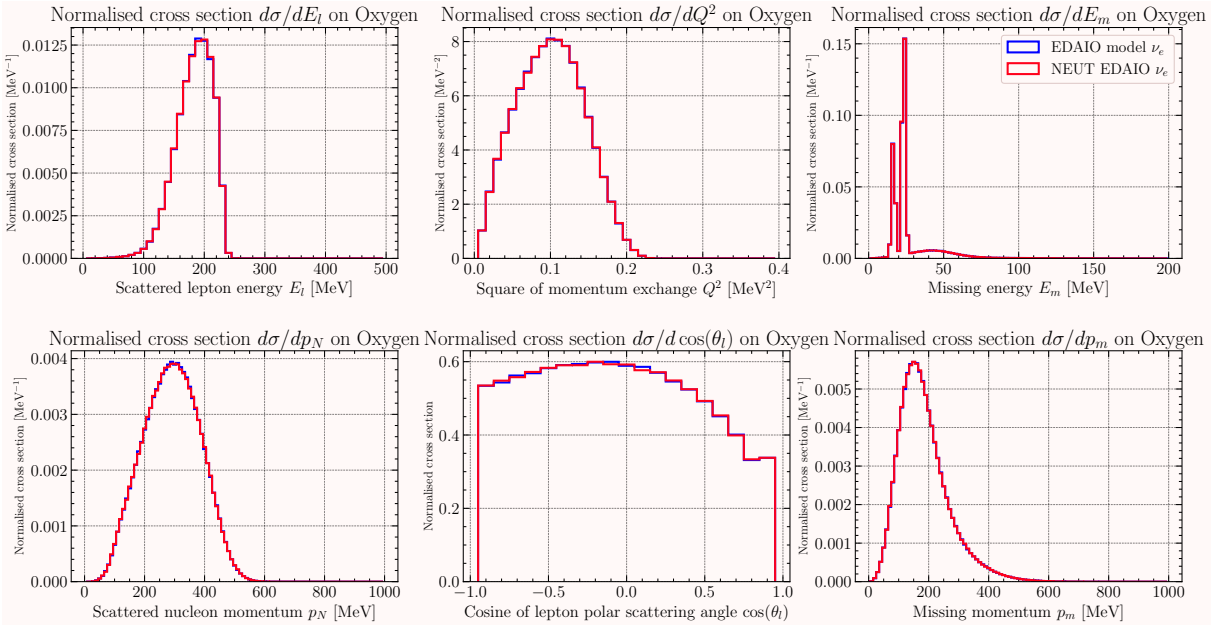

Oxygen $\bar{\nu}_\mu$

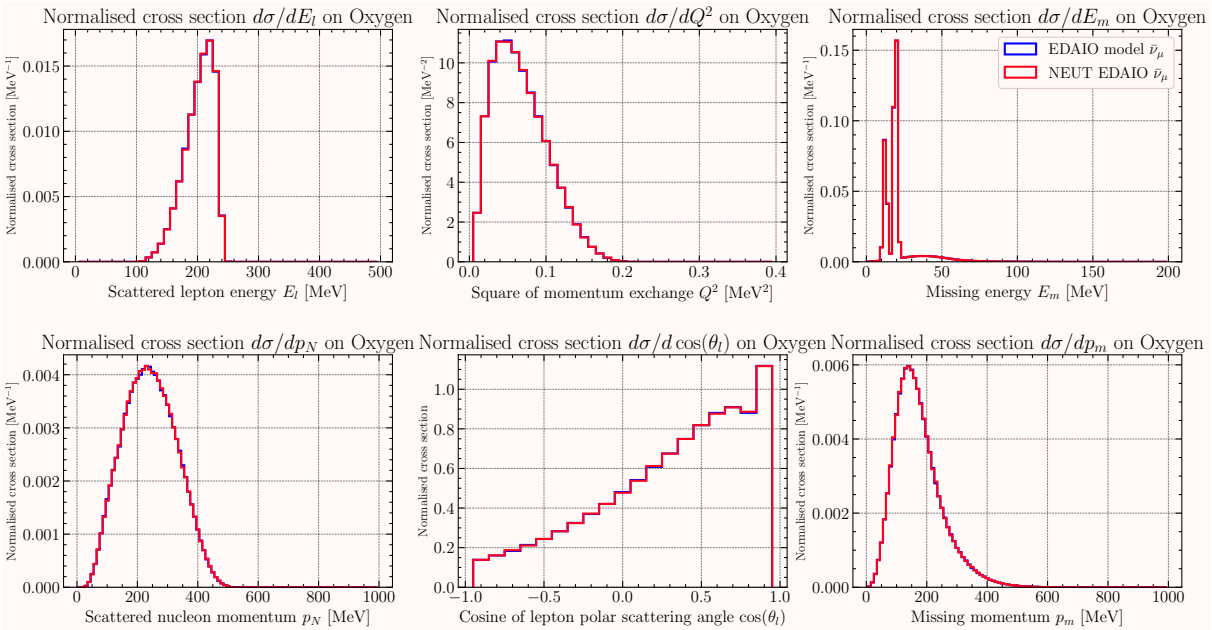

Oxygen $\bar{\nu}_e$

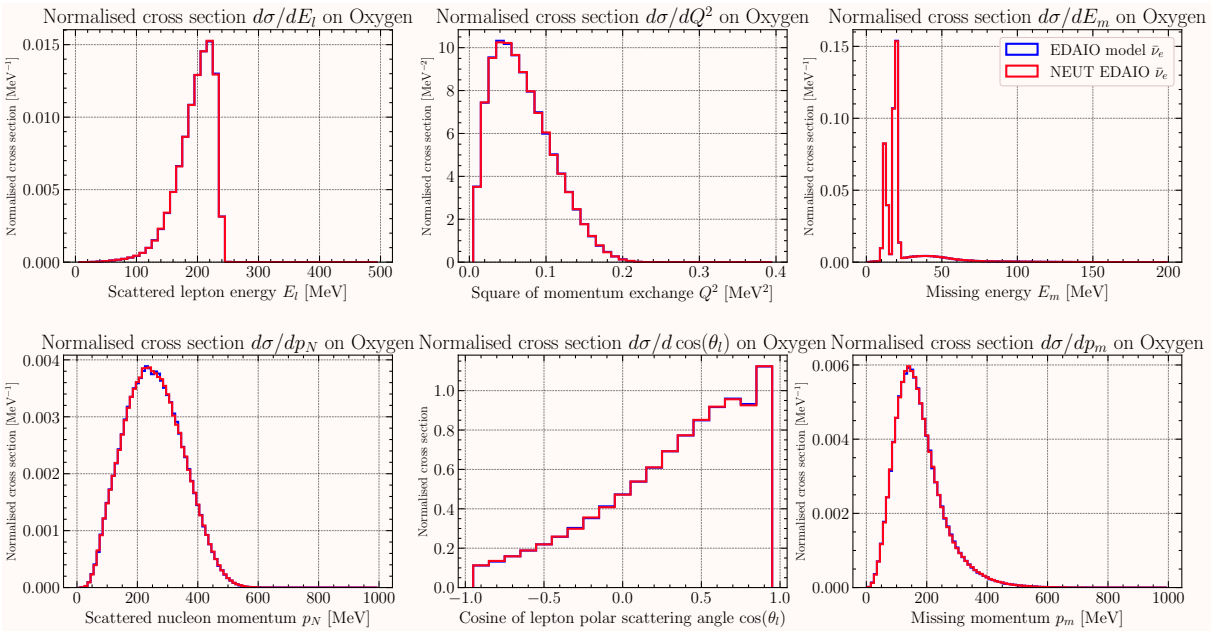

E.3 rEDAI model validation

E.3.1 Normalised single differential cross section on Carbon

Carbon ν_μ

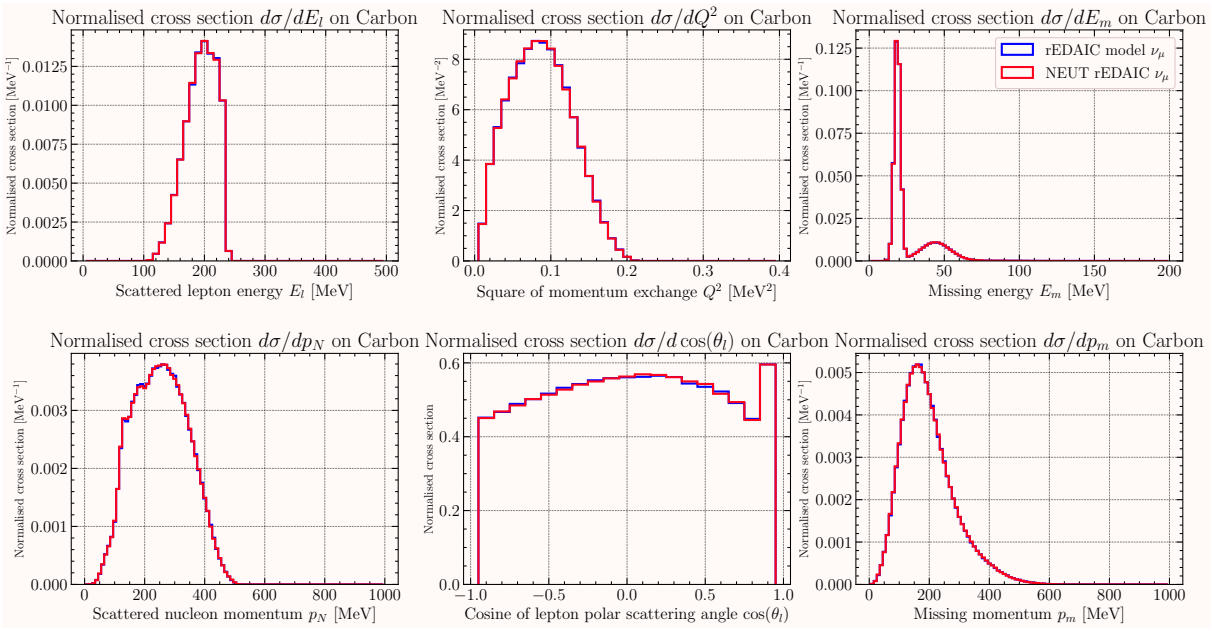

Carbon ν_e

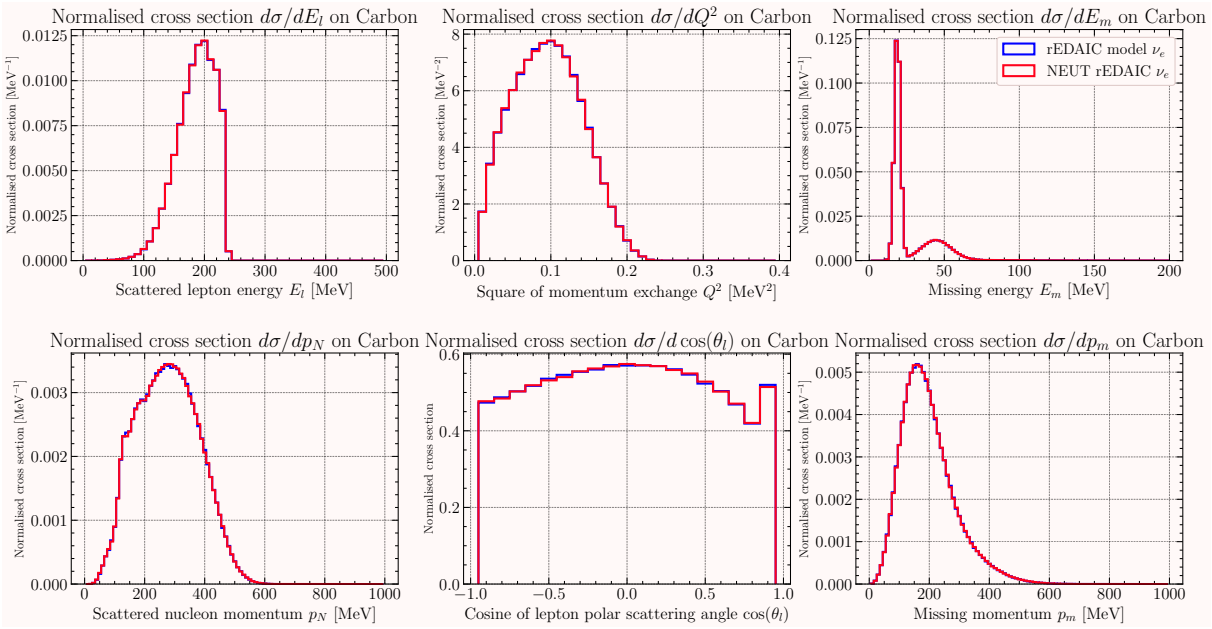

Carbon $\bar{\nu}_\mu$

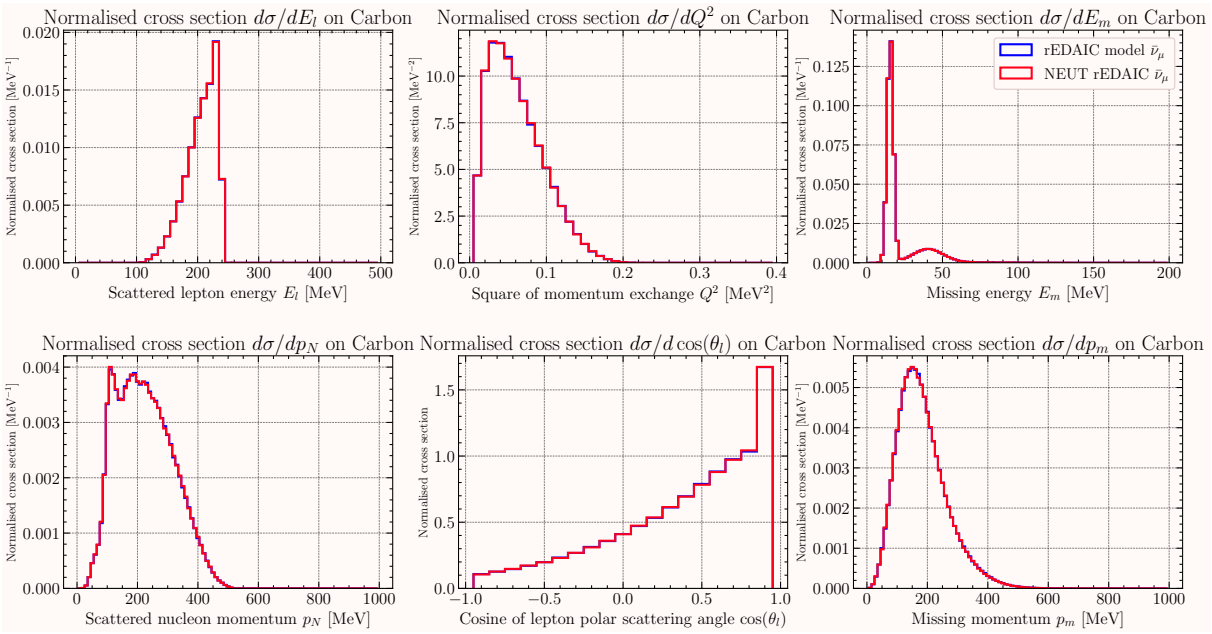

Carbon $\bar{\nu}_e$

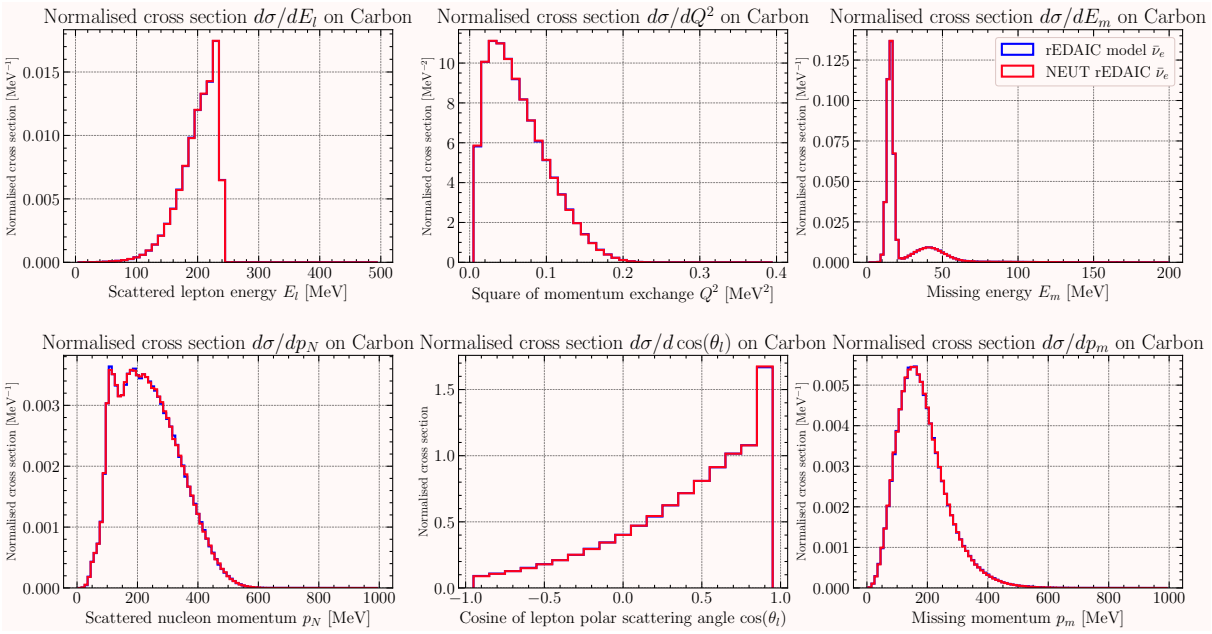

E.3.2 Normalised single differential cross section on Oxygen

Oxygen ν_μ

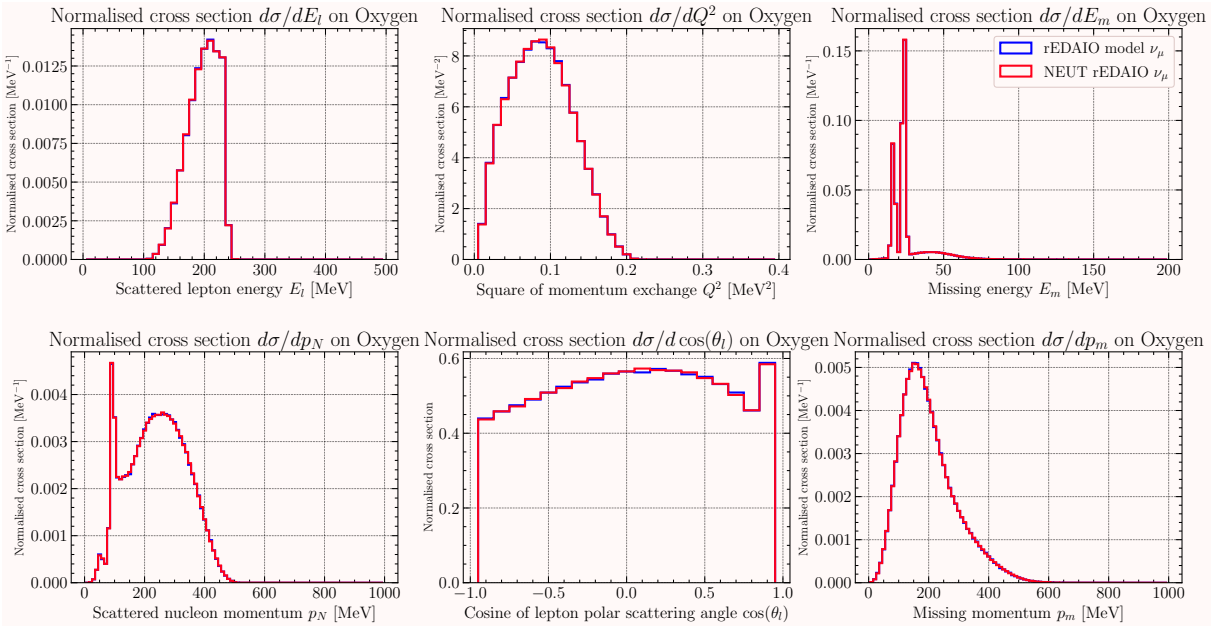

Oxygen ν_e

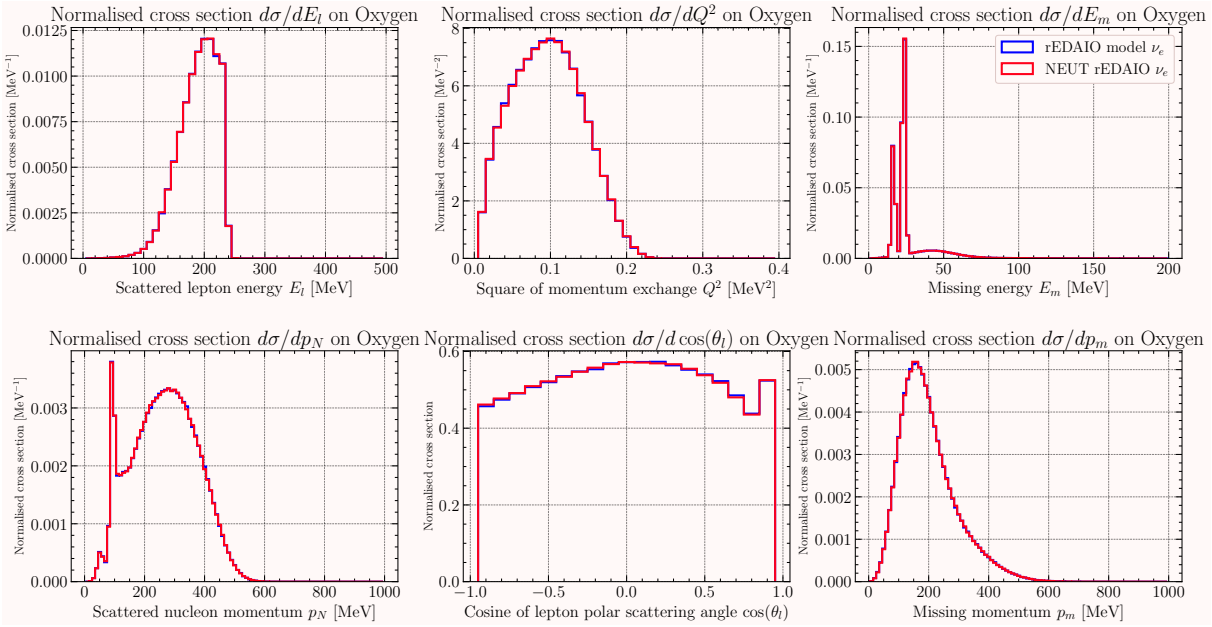

Oxygen $\bar{\nu}_\mu$

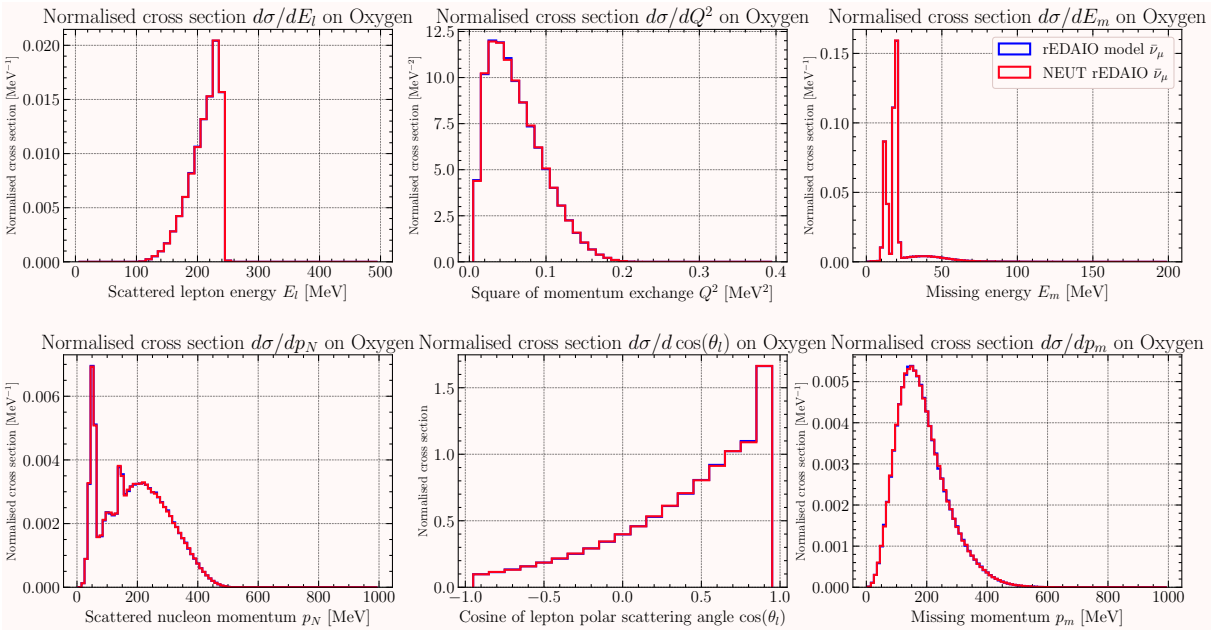

Oxygen $\bar{\nu}_e$

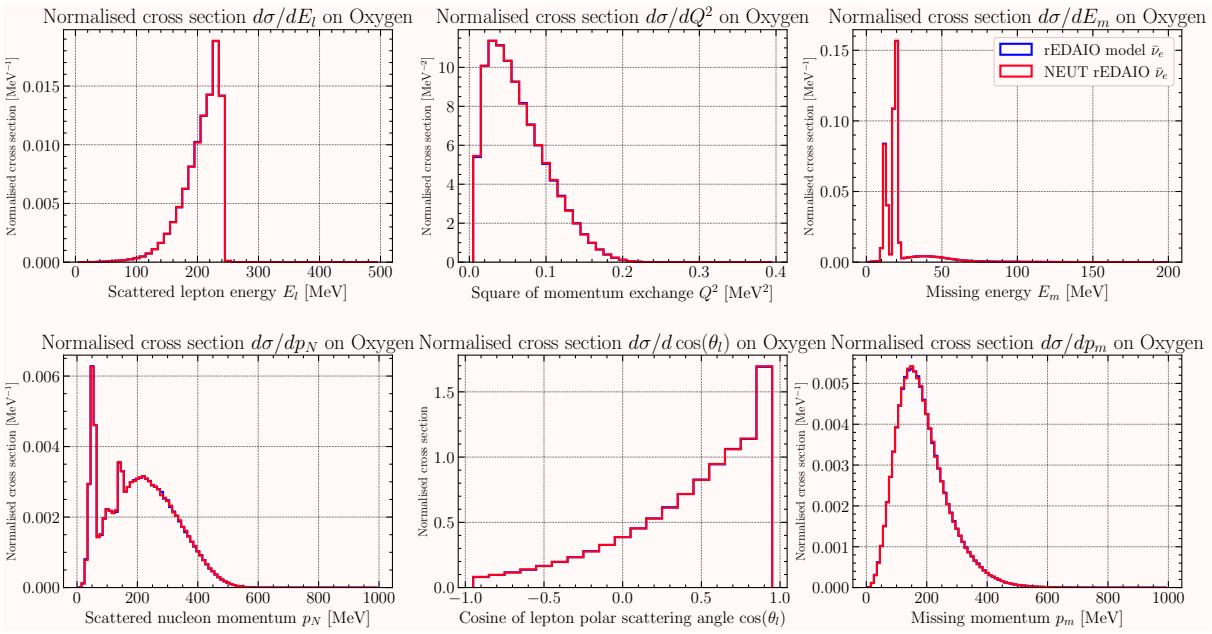
Normalised cross section $d\sigma/dE_l$ on Oxygen
Normalised cross section [MeV^{-1}]
Scattered lepton energy E_l [MeV]
Normalised cross section $d\sigma/dQ^2$ on Oxygen
Normalised cross section [MeV^{-2}]
Square of momentum exchange Q^2 [MeV^2]
Normalised cross section $d\sigma/dE_m$ on Oxygen
rEDAIO model $\bar{\nu}_e$
NEUT rEDAIO $\bar{\nu}_e$
Normalised cross section [MeV^{-1}]
Missing energy E_m [MeV]
Normalised cross section $d\sigma/dp_N$ on Oxygen
Normalised cross section [MeV^{-1}]
Scattered nucleon momentum p_N [MeV]
Normalised cross section $d\sigma/d\cos(\theta_l)$ on Oxygen
Normalised cross section
Cosine of lepton polar scattering angle $\cos(\theta_l)$
Normalised cross section $d\sigma/dp_m$ on Oxygen
Normalised cross section [MeV^{-1}]
Missing momentum p_m [MeV]